Imperial College London
Hamlyn Centre for Robotic Surgery
Department of Computing

High-resolution fluorescence endomicroscopy for rapid evaluation of breast cancer margins

Khushi Vyas

October, 2018

Supervised by:
Professor Guang-Zhong Yang
Second supervisors: Mr. Daniel Leff and Dr. Michael Hughes

Submitted in part fulfilment of the requirements for the degree of
Doctor of Philosophy in Computing of Imperial College London
and the Diploma of Imperial College London

Declaration of Originality

The work in this thesis is solely that of the author, other than the following exceptions:

- The Line-scan confocal laser endomicroscopy system (LS-CLE), operating at 488 nm, used for experiments in Chapter 3 has been developed by Dr. Michael Hughes.
- The original Labview software to acquire LS-CLE images was developed by Dr. Michael Hughes.
- The original Matlab routine to generate mosaics was written by Dr. Michael Hughes and Dr. Petros Giataganas.
- The robotic scanner used in Chapter 5 for large-area endomicroscopic imaging has been developed by Dr. Chris Payne and Dr. Petros Giataganas.
- The piezoelectric scanner driving circuit used in Chapter 6 was designed and assembled by Dr. Bruno Gil Rosa.

I herewith certify that all material in this dissertation which is not my own work has been properly acknowledged.

Khushi Vyas

Copyright Declaration

Abstract

Breast cancer is a major public health problem world-wide and the second leading cause of cancer-related female deaths. Breast conserving surgery (BCS), in the form of wide local excision (WLE), allows complete tumour resection while maintaining acceptable cosmesis. It is the recommended treatment for a large number of patients with early stage disease or, in more advanced cases, following neoadjuvant chemotherapy. About 30% of patients undergoing BCS require one or more re-operative interventions, mainly due to the presence of positive margins. The standard of care for surgical margin assessment is post-operative examination of histopathological tissue sections. However, this process is invasive, introduces sampling errors and does not provide real-time assessment of the tumour status of radial margins. The objective of this thesis is to improve intra-operative assessment of margin status by performing optical biopsy in breast tissue.

This thesis presents several technical and clinical developments related to confocal fluorescence endomicroscopy systems for real-time characterisation of different breast morphologies. The imaging systems discussed employ flexible fibre-bundle based imaging probes coupled to high-speed line-scan confocal microscope set-up. A preliminary study on 43 unfixed breast specimens describes the development and testing of line-scan confocal laser endomicroscope (LS-CLE) to image and classify different breast pathologies. LS-CLE is also demonstrated to assess the intra-operative tumour status of whole WLE specimens and surgical excisions with high diagnostic accuracy. A third study demonstrates the development and testing of a bespoke LS-CLE system with methylene blue (MB), an US Food and Drug Administration (FDA) approved fluorescent agent, and integration with robotic scanner to enable large-area *in vivo* imaging of breast cancer.

The work also addresses three technical issues which limit existing fibre-bundle based fluorescence endomicroscopy systems: i) Restriction to use single fluorescence agent due to low-speed, single excitation and single fluorescence spectral band imaging systems; ii) Limited Field of view (FOV) of fibre-bundle endomicroscopes due to small size of the fibre tip and iii) Limited spatial resolution of fibre-bundle endomicroscopes due to the spacing between the individual fibres leading to fibre-pixelation effects.

Details of design and development of a high-speed dual-wavelength LS-CLE system suitable for high-resolution multiplexed imaging are presented. Dual-wavelength imaging is achieved by sequentially switching between 488 nm and 660 nm laser sources for alternate frames, avoiding spectral bleed-through, and providing an effective frame rate of 60 Hz. A combination of hand-held or robotic scanning with real-time video mosaicking, is demonstrated to enable large-area imaging while still maintaining microscopic resolution. Finally, a miniaturised piezoelectric transducer based fibre-shifting endomicroscope is developed to enhance the resolution over conventional fibre-bundle based imaging systems. The fibre-shifting endomicroscope provides a two-fold improvement in resolution, and coupled to a high-speed LS-CLE scanning system, provides real-time imaging of biological samples at 30 fps. These investigations furthered the utility and applications of the fibre-bundle based fluorescence systems for rapid imaging and diagnosis of cancer margins.

Acknowledgements

I am very grateful to Professor Guang-Zhong Yang for accepting me into the PhD programme and providing me with constant guidance, support and supervision throughout my PhD. Your futuristic vision, enthusiasm and dedication towards making healthcare - simple, affordable and accessible to all has always inspired me. Your constant encouragement and excellent guidance are primarily responsible for the progress I could make during my project period. Thank you for providing me with multiple opportunities to collaborate with very talented and skilled people within and outside the Hamlyn Centre.

I would like to express my immense gratitude to my second supervisor Dr. Michael Hughes. Your technical abilities, work attitude and never ending support have encouraged me to realise my full potential and take pride in my research. You have taught me many essential research skills, enhance my technical knowledge and showed ways to think critically, all which have been instrumental in my development as an independent researcher. Thank you for proof-reading my thesis too.

I am also very grateful to Mr. Daniel Leff for being my clinical supervisor, sharing your knowledge about breast surgery and guiding me on how to effectively translate my work to clinical practice. Thank you for all the support without which these clinical studies would not have been possible. Further, I would like to thank my project collaborators from Charing Cross hospital including Professor Sami Shousha and Dr Rathi Ramakrishnan from the Histopathology Department. I shall forever remember the support and generosity received from you. A big thanks to all the members of Imperial College Tissue bank for providing me with clinical samples for this thesis and for guiding me through the ethical documentation at every step. A special thanks to members of iKnife team, especially Brook, for helping me with tissue collection. I am grateful to all the patients, surgeons and histopathologists who took part in these studies and for being so willing and sparing their time. I am also grateful to the Charing Cross Hospital staff for being so helpful.

I would like to thank Dr. Petros Giataganas for developing the robotic scanning system used in the methylene blue imaging study. Thank you for your continuous support and help with software framework, CAD modelling, and experiments during various stages of this

thesis work. I would like to thank Dr. Bruno Gil-Rosa for your help with making the PZT driver circuit. I wish to thank the Hamlyn Centre research team especially Christina, Carlo, Bruno, Yun, Mali, Maura, Burak, Ning, Piyamate, Haojie and Alex for sharing their knowledge, resources and valuable technical discussions. I extend my gratitude to Ms. Raphaele Raupp for your time and support with managing all the administrative tasks. I would also like thank all the researchers and staff of the Hamlyn Centre for their friendliness and cooperation.

Finally, I would like to thank my family, especially my in-laws Mr. Amal Lavsi and Mrs. Shreya Lavsi, my parents Mr. Kishan Vyas and Mrs. Anju Vyas and my brother Hrudesh for being unconditionally supportive, understanding and encouraging. You are my role models, thank you for giving me this opportunity. Without your support none of this would have been possible. This thesis is for you. A special thanks to Smitha, Vikki and Christina for being such amazing friends and for all the fun, advice and care. I extend my gratitude to all family members and friends for your support, patience, love and encouragement at every stage.

Last but not the least, my biggest thanks to my husband, Ashray, who is the most supportive, understanding, and loving person I have ever known. Thank you for believing in me and for your constant motivation and encouragement as well as patience during the last several years. Also, thank you for proof-reading my thesis. I could not have done this without you by my side.

Contents

List of Figures

List of Tables

Abbreviations

3D-PSF three-dimensional point spread function.

ADH atypical ductal hyperplasia.

AH acriflavine hydrochloride.

ALH atypical lobular hyperplasia.

ASTRO American Society for Radiation Oncology.

BBD benign breast diseases.

BCS breast conserving surgery.

CB core biopsy.

CCD charged-coupled device.

CFM confocal fluorescence microscopy.

CLE confocal laser endomicroscopy.

CMOS complementary metal-oxide-semiconductor.

COBALT clinical outcomes in patients with primary biliary cholangitis.

CSM confocal strip-mosaicking microscope.

DCIS ductal carcinoma *in situ*.

DESI desorption electrospray ionization.

DH ductal hyperplasia.

DLSM digital scanned laser light-sheet fluorescence microscope.

DMD digital micro-mirror device.

DT Delaunay triangulation.

eCLE endoscope based confocal laser endomicroscopy.

ESS elastic scattering spectroscopy.

FDA food and drug administration.

FEM fibre-bundle endomicroscopy.

FFT fast fourier transform.

FNAC fine needle aspiration cytology.

FOV field of view.

FWHM full width half maximum.

GFP green fluorescent protein.

GI gastrointestinal.

GRIN gradient refractive index.

H&E hematoxylin and eosin.

HE histogram equalisation.

HR high resolution.

HRME high resolution microendoscopy.

HWHM half width half maximum.

ICG indocyanine green.

IDC invasive ductal carcinoma.

IHC histopathology and immunohistochemistry.

ILC invasive lobular carcinoma.

IMA intra-operative margin assessment.

IOUS intra-operative ultrasound.

LCIS lobular carcinoma *in situ*.

LR low resolution.

LS-CLE line-scan confocal laser endomicroscopy.

MB methylene blue.

MEMS microelectromechanical system.

MFD mode field diameter.

MIS minimally-invasive surgery.

MPM multiphoton microscopy.

MRI magnetic resonance imaging.

NA numerical aperture.

NCC normalised cross-correlation.

NICE National Institute for Health and Care Excellence.

NPV negative predictive value.

OCT optical coherence tomography.

OPM oblique plane microscope.

p-SR pixel super resolution.

pCLE probe-based confocal laser endomicroscopy.

PMT photomultiplier tube.

PPV positive predictive value.

PZT lead zirconate titanate.

REIMS rapid evaporative ionisation mass spectrometry.

SFM scanning force microscopy.

SIM structured illumination microscopy.

SLM spatial light modulators.

SNR signal-to-noise.

SPIM selective plane illumination microscopy.

SSO Society of Surgical Oncology.

SURF speeded up robust features.

TDLU terminal duct lobular unit.

USAF United States air force.

WLE wide local excision.

Chapter 1

Introduction

1.1 Motivation

The efforts of humankind to see and understand things far smaller than what could be perceived by the naked eye dates back to more than 2000 years when the ancient civilisations starting to study the magnifying properties of glass, rock-crystal and water. Originally the word 'microscope' was used for optical magnifiers or 'lenses' (glass that was thick in the centre and thin on the edges). The early microscopes were magnifying lenses with only one power, usually 3×-10×. However these 'magnifiers' were not used for biological research until the advent of the first compound light microscope in the end of the 16th century by Dutch spectacle makers Hans and Zacharias Janssen [4]. By the 17th century Robert Hooke had employed his version of Janssen's compound microscope to observe organisms, such as fossils, diatoms, and was credited with the historic milestone of discovering the basic unit of life, 'cell'. Towards the end of the 17th century, Anton van Leeuwenhoek built the first real single-lens microscope and made possible studies to see bacteria and single cells, Fig.1.1.

Figure 1.1: Optical Microscope time-line

Since then, technical innovations and sophisticated optics have allowed for substantial improvements in resolution, magnification and image contrast, making microscopy to be one of the most important tools for discovery in the history of life sciences. The last few decades have witnessed a plethora of new optical microscopy techniques that could surpass the ultimate resolution limit due to diffraction of light (∼200 nm) and enable super-resolution cellular, molecular and genetic imaging [5].

1.1.1 Intra-operative imaging in minimally-invasive surgery

The developments in microscopy and fluorescence imaging have greatly influenced the ascendance of histological techniques in the late 19th century. This enabled the tissue slides to be fixed, stained and stored for months and examined repeatedly with hitherto indiscernible details and contrast. While the static nature of histology facilitated longitudinal imaging of cellular architecture, it was the incessant desire to make biology a more exact science that led to the development of new methods to visualise the physiology of the cells in their living state. The rise of live-cell imaging in the past decade has been meteoric with intense technical innovation both in the development of new fluorescent probes for molecular imaging and in the microscopy techniques to facilitate imaging with higher resolution and magnification [6–8].

An area of research where these developments could be particularly advantageous is for intra-operative imaging during minimally-invasive surgery (MIS) procedures [9]. One of the many challenges a surgeon faces in the operating theatre is the inability to recognise indistinguishable disease on the tissues being operated on. In the case of breast conserving surgery (BCS), tumour cells might be missed resulting in positive margins, tumour recurrence and high re-operation rates [10–13]. Serial sectioning of excised specimens followed by histopathology imaging is currently the gold standard for the assessment of breast margin status. While the process results in high diagnostic accuracy, it is very slow, invasive and introduces the possibility of sampling errors.

Thin coherent waveguides such as optical fibres and fibre-bundles have played a key role in bridging the gap between microscopes and endoscopes and providing a route to non-invasive cellular-level visualisation of tissue morphology [3, 14]. They have been used as compact endomicroscopic optical biopsy probes for various high-resolution imaging modalities including epi-fluorescence microscopy [15,16], fluorescence confocal microscopy [17–19] optical coherence tomography [20, 21] and two-photon microscopy [22]. In applications where conventional histology is still required to confirm a diagnosis, endomicroscopy is particularly beneficial as a guide in the selection of excision sites by targeting suspicious regions and minimising the number of random biopsies.

1.1.2 Optical biopsy with confocal endomicroscopy

Fluorescence based confocal laser endomicroscopy (CLE) is one such popular optical biopsy technique that translates conventional confocal fluorescence microscopy into a real-time *in vivo* clinical modality [19,23,24]. Flexible optical fibre-bundles are used as small diameter imaging probes to acquire images at confined sites within the body. These probes can be inserted into the working channels of conventional endoscopes enabling fast and non-invasive classification of a tissue's histopathological status. Preliminary pre-clinical and clinical studies on CLE were conducted on upper and lower gastrointestinal (GI) tract for visualisation of Barrett's oesophagus, gastric neoplasia and for screening colonoscopy. CLE has since been also explored in the imaging of the respiratory and urinary tract for cancer diagnosis and has recently found use in hepatobiliary and intra-abdominal endomicroscopy applications [3,19,23,25–28].

Currently, CLE systems have demonstrated promising sensitivity and specificity in small clinical studies primarily conducted by academics in research settings [3,24,28]. However, progression of CLE as an intra-operative tool for surgical applications has not reached its maximum potential. This may be due to various factors like safety profile of the staining agent, high cost, varied operator experience, proficiency in interpretation of the image features and technical limitations. Technical limitations include reduction in penetration depth, low acquisition rate and substantially low resolution as compared to the diagnostic 'gold standard' excision histology. The technical challenges and clinical applications of CLE form the basis of this thesis. While the methodology sought is generic, the imaging of morphological features from non-neoplastic and neoplastic breast regions following BCS serves as a clinical case study for the project. This work aims to recognise (and attempt to address) the main challenges to CLEs development for evaluating breast margins, and in doing so, identify new niches for its advancement.

1.2 Structure of thesis

A summary of the chapters of this thesis follows:

Chapter 1 provides the motivation and significance of this work including the key scientific contributions and a list of academic achievements generated from this thesis.

Chapter 2 presents the clinical and technical background for this thesis, beginning with an overview of breast anatomy and types of breast cancers. The importance of surgical margin evaluation is highlighted and several existing intra-operative approaches in the literature to assess the margin status are discussed. Subsequently, the theory of fluorescence imaging is presented followed by a review of existing single-photon fluorescence microscopy techniques that have potential to be miniaturised for breast tissue imaging. In

particular, this chapter focuses on fluorescence based confocal endomicroscopy techniques and reviews relevant challenges such as limited spatial resolution, speed, miniaturisation and cost. The clinical impact of these challenges for intra-operative assessment of margins during BCS is discussed.

Chapter 3, presents a feasibility study on identification and characterisation of non-neoplastic and neoplastic breast features in images acquired with high speed line-scan confocal laser endomicroscopy (LS-CLE) system, developed in the Hamlyn Centre at Imperial College London. Detailed steps for specimen preparation, staining protocol, image acquisition, processing and histology correlation are presented. For this study, 43 unfixed breast tissue specimens with non-neoplastic and neoplastic pathologies are examined and a taxonomy of different breast tissue features imaged with LS-CLE is developed. Large-area mosaics are created by registering and stitching the image frames as the probe moves across the tissue. The same specimens are also imaged with a commercial Cellvizio system and side-by-side comparisons are made. A more detailed description of design, image acquisition and operation of the LS-CLE system is provided since it will be adapted for other technical developments in this thesis.

Chapter 4, describes the results of a prospective and observational study that was carried out on 27 freshly excised wide local specimens and margin excisions from 13 patients undergoing BCS. Utilising acriflavine hydrochloride as the fluorescent agent and histology slides of the corresponding sections for gold standard comparison, morphological features of invasive and non-invasive breast cancers were readily visualised and distinguished on LS-CLE images. Selected areas on each margin are evaluated prior to any histopathological processing, with overall imaging time restricted to 40 minutes from excision. After correlation with histopathology findings, an overall accuracy of 87% is achieved. These results demonstrate the potential of LS-CLE as a real-time method for rapid margin assessment in BCS.

The potential of LS-CLE to perform high-resolution diagnostic imaging of excised breast specimens has motivated advances in LS-CLE technology for *in vivo* breast cavity imaging. **Chapter 5** describes a custom high-speed LS-CLE system at 660 nm that enables high-resolution histomorphological imaging of breast tissue stained with methylene blue (MB), an alternative fluorescent stain for localising sentinel nodes during breast surgery. High quality and long mosaics are generated by using the MB aided LS-CLE system operating at 120 fps which otherwise would be challenging. Preliminary results of imaging 24 unfixed human breast tissue specimens are presented, demonstrating the potential of MB aided rapid LS-CLE to determine the oncological status of surgical margins *in vivo*.

The chapter also reports on new developments of LS-CLE towards dual-wavelength imaging and robotic scanning applications. Dual-wavelength imaging is achieved by

switching between 488 nm and 660 nm laser sources for alternate frames, avoiding bleed-through and providing an effective frame rate of 60 Hz. Preliminary images with a resolution of 2.2 μm are presented from fluorescent stained phantoms and *ex vivo* tissue, demonstrating the clinical feasibility of the technique. Robot-assisted LS-CLE is demonstrated using a portable, robotic scanning probe and applications towards large area imaging of breast tissue are demonstrated.

Chapter 6 details the development of a compact and rapid piezoelectric transducer based bundle-shifting endomicroscopy system in which a pixel super-resolution image is restored from multiple pixelation-limited images. A miniaturised lead zirconate titanate (PZT) tube actuates the fibre bundle behind a gradient refractive index (GRIN) microlens and a Delaunay triangulation based algorithm reconstructs an enhanced resolution image. To enable real-time cellular-level imaging, imaging is performed using LS-CLE with a raw frame rate of 120 fps, delivering up to 2$\times$ spatial resolution improvement for a field of view (FOV) of 350 μm at a net frame rate of 30 fps. The resolution enhancement is confirmed using resolution phantoms and *ex vivo* fluorescence endomicroscopy imaging of human breast specimens is demonstrated.

Chapter 7 provides a summary of the major results presented in this thesis and recommended future directions for this project.

1.3 Contributions of the thesis

The contributions of this thesis fall under two categories - technical novelties and clinical applications. Key contributions are summarised as follows:

1. Critical comparison between commercial Cellvizio and in-house LS-CLE systems for imaging unfixed breast tissue specimens with normal, benign and neoplastic breast tissue morphologies.

2. The confirmation that high quality and long mosaics of normal and neoplastic breast morphologies can be generated using the LS-CLE system operating at 120 fps.

3. The development of a novel classification system to guide interpretation of neoplastic and non-neoplastic breast morphology on LS-CLE images.

4. The first description of LS-CLE images of neoplastic and non-neoplastic changes on radial margins of whole wide local excisions following BCS; and the resulting scientific interests towards rapid intra-operative assessment.

5. The description of neoplastic and non-neoplastic changes on glandular and stromal components of the breast on LS-CLE images with methylene blue staining; and the

resulting scientific interests towards *in vivo* hand-held and robotic cavity scanning applications.

6. Design and development of a high-speed dual-wavelength fluorescence endomicroscopy system suitable for multiplexed morphological and molecular imaging applications using 488 nm and 660 nm laser sources.

7. Design and development of a miniature 2-axis fibre-shifting endomicroscope that enhances lateral resolution of existing fibre-bundle fluorescence endomicroscopy systems by a factor of 2.

1.4 List of publications

The work presented in this thesis has resulted in the following peer reviewed publications, presentations and conference proceedings:

REFEREED JOURNAL PAPERS

- **Khushi Vyas**, Michael Hughes, Bruno Gil Rosa, and Guang-Zhong Yang, "Fiber bundle shifting endomicroscopy for high-resolution imaging," Biomed. Opt. Express 9, 4649-4664 (2018)

- **Khushi Vyas**, Michael Hughes, Daniel R. Leff, Guang-Zhong Yang, "Methylene-blue aided rapid confocal laser endomicroscopy of breast cancer," J. Biomed. Opt. 22(2) 020501 (2017)

PRESENTATIONS AND CONFERENCE PROCEEDINGS

- **Khushi Vyas**, Michael Hughes, Daniel R. Leff, Guang-Zhong Yang, "Robot-assisted Endomicroscopic Imaging Of Breast Cancer: Instrumentation And Applications," Poster presentation at Advanced Biophotonics workshop, Hamlyn Symposium on Medical Robotics (2018)

- **Khushi Vyas**, Michael R. Hughes, Guang-Zhong Yang, "A dual-wavelength line-scan confocal endomicroscopy system for rapid molecular imaging (Conference Presentation-Oral)," Proc. SPIE 10470, Endoscopic Microscopy XIII, 104700V (2018)

- **Khushi Vyas**, Michael Hughes, Guang-Zhong Yang, "Fiber-shifting endomicroscopy for enhanced resolution imaging," in Frontiers in Optics 2017, OSA Technical Digest (online) (2017), paper JTu2A.79.

- **Khushi Vyas**, Michael Hughes, Daniel R. Leff, Guang-Zhong Yang, "Microscale imaging of surgical margins in breast cancer using confocal laser endomicroscopy – a clinical study," (Conference Presentation-Oral), London Surgical Symposium, (2017)

- Piyamate Wisanuvej, **Khushi Vyas**, Petros Giataganas, Konrad Leibrandt, Jindong Liu, Michael Hughes, Guang-Zhong Yang, "Three-dimensional Robotic-assisted Endomicroscopy with a Force Adaptive Robotic Arm," Robotic challenge at Hamlyn Symposium on Medical Robotics (2017)

- **Khushi Vyas**, Michael Hughes, Daniel R. Leff, Guang-Zhong Yang, "Endomicroscopic Imaging Of Breast Cancer: Instrumentation And Applications," Poster presentation at Biophotonics and Imaging Graduate Summer School (2016) (Poster prize- honorary mention)

- **Khushi Vyas**, Michael Hughes, Guang-Zhong Yang, "Establishing imaging protocol for evaluation of breast cancer margins using high-speed confocal endomicroscopy and methylene blue," Poster presentation at Hamlyn Symposium on Medical Robotics (2016)

Other relevant peer reviewed publications and conference proceedings (not included in the thesis)

- Yun Gu, **Khushi Vyas**, Jie Yang and Guang-Zhong Yang, Transfer Recurrent Feature Learning for Endomicroscopy Image Classification, IEEE Transactions on Medical Imaging, 2018.

- Yun Gu, **Khushi Vyas**, Jie Yang and Guang-Zhong Yang, Weakly-supervised Reperesentation Learning for Endomicroscopy Image Analysis, MICCAI, 2018 (Student Travel Award).

- Yun Gu, **Khushi Vyas**, Jie Yang and Guang-Zhong Yang, Unsupervised Feature Learning for Endomicroscopy Image Retrieval, MICCAI, 2017.

- **Khushi Vyas**, Michael Hughes, Daniel R. Leff, Guang-Zhong Yang, "Towards intraoperative visualization of breast tumour margins using low-cost epi-fluorescence endomicroscopy (Conference Presentation-Oral)," Proc. SPIE, Diagnosis and Treatment of Diseases in the Breast and Reproductive System II (2016)

Chapter 2

Fluorescence microscopy imaging of breast cancer

2.1 Introduction

This chapter provides the clinical and technical background to support this thesis. It is intended to introduce the diagnosis and surgical treatment of breast cancer for the non-clinical reader. It highlights the clinical relevance of breast cancer cases followed by the description of breast anatomy and histology, and the types of breast diseases. The diagnostic process is briefly summarised with particular attention being paid to the fluorescence imaging of breast cancer, since these images provide the basis for the work described in later chapters.

Almost inevitably, surgery is offered as the first line of treatment plan. This chapter outlines the current surgical practice and challenges in the excision of breast cancer, related to either removal of the whole breast (mastectomy) or removal of the cancerous lump and a portion of the breast tissue around it (lumpectomy) while keeping the rest of the breast intact. Lumpectomy or BCS operations often have high re-operation rates because of the presence of positive margins [29]. The definition and significance of radial margins is briefly reviewed as it motivates the need for an intra-operative imaging technique to achieve clear margins during surgery.

The ultimate goal of the work described in this thesis is to develop a rapid intra-operative assessment tool that could detect breast margin non-destructively and with microscopic resolution. In pursuing this goal, a review of existing single-photon fluorescence microscopy techniques that have potential to be miniaturised for accurate assessment of fresh breast tissue morphology is presented. Current challenges relevant to these techniques such as limited spatial resolution, speed, miniaturisation and cost are reviewed and their clinical

impact for intra-operative assessment of margin status during BCS is discussed.

2.2 Breast anatomy

Breast tissue is heterogeneous and contains many complex structures such as ducts, lobules, stroma, fat and blood vessels. Fig.2.1 illustrates the anatomy of a normal human breast. Each breast consists of a single mammary gland formed from 15-20 sections called lobes [30, 31], which in-turn contain smaller lobules which can produce milk. Recent studies have identified breasts with 7-10 ductal orifices [32, 33] which are are linked by tubes called ducts that begin at the nipple, branch into smaller ducts and end in the terminal duct lobular unit (TDLU). The TDLU is composed of a terminal duct and many small ductules (or acini) which are lined by an inner layer of cuboidal to columnar epithelial cells and an outer layer of myoepithelial cells forming the glandular tissue. Spaces around the lobules and ducts are filled with adipose tissue, ligaments and connective tissue. The pectoralis major muscles lie under each breast and cover the ribs. Each breast contains blood vessels and lymph vessels which lead to the lymph nodes found in the axilla, above the clavicle and in the chest.

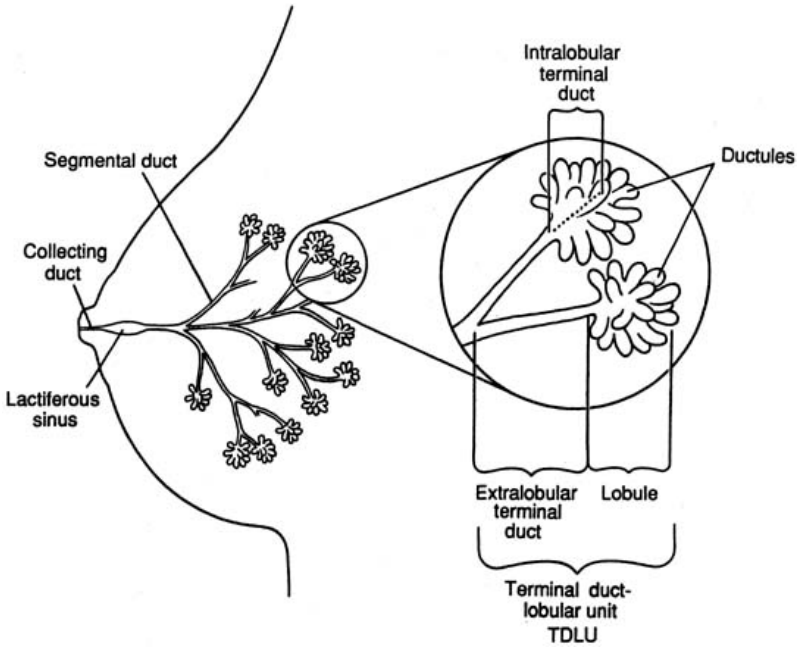

Figure 2.1: Diagram of the normal breast showing ductal and lobular architecture (Breast care: a clinical guidebook for women's primary health care providers, Development and growth of the breast, 1999, p. 34, Figure 3.7, WH Hindle, ©Springer-Verlag New York 1999. Used with permission of Springer [1]).

The epithelium and lobular stroma are hormonally responsive causing significant changes in the molecular structure and composition of the breast from early adolescence to menopause [34–36]. In the early years, the breasts are mainly composed of fatty tissue and connective tissue [31]. During puberty, an increase in the hormones estrogen and progesterone cause the breast to develop and mature in size and the ductal system starts to grow [32, 33]. The mature, non-lactating female breast is composed of approximately equal amounts of glandular and adipose tissue. During pregnancy, there is a marked proliferation of ductules resulting in an increase in the number of lobules. Additionally, the epithelial cells have abundant cytoplasm filled with secretory vacuoles [37, 38]. During menopause, the estrogen and progesterone levels start decreasing leading to a reduced quantity of glandular tissue. Thus post-menopause, the breast shrinks in size and is primarily composed of adipose tissue and collagen [39].

2.3 Breast diseases

Breast cancer is one of the leading causes of cancer in women, accounting for 23% of the total cancer cases and 14% of all cancer-related female deaths [40]. In 2012 there were an estimated 464,000 new cases of female breast cancer and 131,000 deaths in Europe [41]. It is estimated that one in 8 women will develop breast cancer in their lifetime [42]. A woman diagnosed with breast cancer today has an estimated 80% chance of surviving for 5 years and a 64% chance of surviving for 20 years [43]. These survival rates have continually improved over the past 20 years. This is likely due to not only the improved treatments, but also to the earlier detection of cancer resulting from initiatives such as the NHS Breast Screening Programme [44].

Normal breast ducts are composed of a basement membrane and a layer of luminal epithelial and myoepithelial cells. The transition from normal to malignant breast tissue is a complex process [45, 46]. There are many ways that breast cancer can develop but it typically develops in the ducts from the epithelial cells which line the TDLU [47]. Fig.2.2 illustrates the steps in breast cancer progression through sequentially defined stages, starting from benign ductal hyperplasia (DH) and atypical ductal hyperplasia (ADH), followed by ductal carcinoma *in situ* (DCIS) and finally progressing to invasive ductal carcinoma (IDC). DH is a benign condition that occurs when normal epithelial cells lining the ducts increase in number and develop unusual shapes. ADH is considered as one of the early precursor lesion to high-risk malignant conditions. DCIS is an increasingly commonly diagnosed non-invasive neoplasm that presents a high risk of developing into IDC. IDC occurs when malignant ductal epithelial cells invade past the basement membrane into the stromal tissue of the breast.

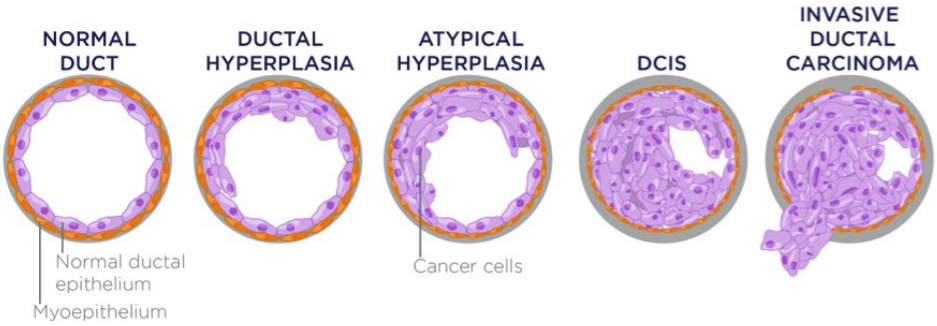

Figure 2.2: Illustration of breast cancer progression showing schematic view of normal, hyperplastic, in situ and invasive carcinoma

2.3.1 Benign breast disease

Breast diseases, both benign and malignant, are prevalent. benign breast diseases (BBD) are the most common cause of breast problems in females and at least 10 times more frequent than the malignant ones [48]. BBD encompasses a heterogeneous group of lesions that may present a wide range of symptoms or may be detected as incidental microscopic findings. BBDs in the epithelium are commonly classified histologically into three categories: non-proliferative, proliferative without atypia, and atypical hyperplasia [49–51]. Non-proliferative breast lesions such as cysts, apocrine metaplasia, fibrosis, DH, and fibroadenomas do not increase the future risk of developing breast cancer. Examples of proliferative lesions without atypia include florid hyperplasia, sclerosing adenosis, and intraductal papillomatosis which offer a moderate risk of developing breast cancer. When the proliferative lesion is associated with atypia the risk for breast cancer is even higher. These fibrocystic lesions include either an ADH or atypical lobular hyperplasia (ALH). The relative risk is also found to increase if a strong family history is present.

2.3.2 Malignant breast conditions

Malignant breast cancers can be divided into two sub-groups: the carcinomas and the sarcomas. Carcinomas are cancers that arise from the epithelial cells that line the organs and tissue in the body and comprise of the vast majority of all breast cancers. Most breast carcinomas are adenocarcinoma which start in epithelial cells lining the glandular tissue of the breast like the lobules and terminal ducts. Under normal conditions, these epithelial cells are responsible for making milk. Sarcomas are rare cancers that arise from the stromal (connective tissue) components of the breast. These stromal cells include myofibroblasts and blood vessel cells, and cancers arising from these cells include phyllodes tumours and angiosarcoma. Sarcomas account for less than 1% of primary breast cancers.

Based on histopathological analysis, the carcinomas are further classified as non-invasive (or *in situ*) and invasive cancers. Non-invasive cancers refer to abnormal cells that are present but have not grown beyond their site of origin into neighbouring tissue. Such cells remain within the basement membrane of the ducts and lobules. Examples include DCIS, which accounts for over 20% of all diagnosed breast cancers and lobular carcinoma *in situ* (LCIS) which is an uncommon condition [52].

Invasive or infiltrating carcinoma refer to cancer that has started in a duct or lobule and has invaded nearby tissue and possibly to the lymph nodes and other parts of the body. IDC is the most common form of breast cancer, making up between 70% and 85% of all breast cancers [53]. invasive lobular carcinoma (ILC) is another common cancer condition accounting for 5-10% of all breast cancers [54, 55]. Other types of invasive carcinomas include medullary (2%) [56], mucinous (2%) [57] and tubular (2%) [58].

2.4 Diagnosing breast cancer

The breast triple assessment is the current gold standard-of-care hospital-based assessment that allows for the early and rapid detection of breast cancer, both for cancers detected by a screening programme as well as during symptomatic clinics. This consists of a combination of clinical examination, imaging and pathology to detect and allow for the early intervention in the treatment of breast cancer [59, 60]. At each stage of the triple assessment, the suspicion for malignancy is graded to create an overall risk index.

Clinical examination

The first test consists of clinical history and examination performed by a breast surgeon focusing on breast palpation to detect regions of abnormality such as discrete mass, lumps or areas of asymmetric nodularity.

Imaging

The clinical imaging of the breast tissue during triple assessment is performed by a trained radiologist to determine the lesion type, size, location and margin features. Since early diagnosis plays a significant role in increasing the survival time for cancer patients, numerous breast cancer screening and diagnosis techniques have been developed and are routinely used in clinical practice. The mainstay of breast imaging techniques include Mammography, ultrasound and magnetic resonance imaging (MRI) [61–73].

The most-widely used breast screening and diagnosis technique is mammography which is the X-ray examination of the breast [61–66]. Screening mammography typically involves taking two views of the breast (oblique and craniocaudal) allowing for the detection of

mass lesions and micro-calcifications. It has been shown to reduce breast cancer mortality in population-based screening programs with an overall sensitivity of 85%. However, in women with dense breast tissue the sensitivity is reduced to 47.8% from 64.4% [65]. Further, about 15% of cancers do not show up on mammograms especially for women with dense breasts who are at a higher risk of developing breast cancer [66].

Ultrasound is another common imaging technique which uses high frequency sound waves to clinically analyse breast tissue and used mainly to distinguish between solid and fluid-filled lumps [67–70]. It is increasingly being used as a supplementary screening tool to mammography due to its low-cost, wide-availability, small foot-size and non-ionising radiation exposure. However, its sensitivity depends on factors like patient age and breast density as well as on the ability and expertise of the radiologist performing the examination.

MRI has superior sensitivity to mammography and ultrasound in the detection of invasive cancer and has been shown to be effective in some high-risk groups e.g. dense breasts or familial or genetic predisposition to breast cancer [71–73]. However, MRI screening is rarely used and often criticised for decreased specificity, high cost, and prompting biopsy or follow up imaging.

Histopathology analysis

If a suspicious mass or lesion is detected during imaging, a non-excision biopsy sample is acquired to be sent to the laboratory for detailed histopathology and immunohistochemistry (IHC) analysis. Depending on the tissue condition, biopsies can be taken in different ways, with or without use of mammographic or ultrasound guidance. fine needle aspiration cytology (FNAC) involves aspirating the suspicious area or lump [74–76]. If the syringe fills with fluid and the lump collapses this effect is typical of a cyst. A solid lump may be a benign tumour like a fibroadenoma or a breast cancer. Alternately, a core biopsy (CB) provides full histology (as opposed to FNAC which only provides cytology), allowing differentiation between invasive and *in situ* carcinoma. CB takes out a small piece of breast tissue for analysis and provides histological information [77–79]. The test can generate important information about tumour grading and staging and has a higher sensitivity and specificity than FNAC for detecting breast cancer.

However, such invasive approaches lead to several limitations like significant sampling errors, trauma and tissue damage. Moreover, cyto-histopathology analysis requires special preparation of the dissected tissue (fixation, slicing and staining) prior to its examination under a microscope, thus making the final diagnosis time-consuming and dependent on the skill and experience of trained specialists.

2.5 Breast cancer treatment

Based on results from clinical, radiological and pathological investigations the diagnosis of the type of breast lesion is established and steps towards the treatment are outlined below. There are several procedures available for the treatment of breast cancer. These include surgery, radiotherapy, chemotherapy as well as others like hormone and targeted (biological) therapy. The choice of the surgical procedure and follow up treatment depends on the size and stage of the tumour, its locality as well as patients' preference. Surgery is the first line of treatment plan offered for excision of malignant lesions by either removing the whole breast (Mastectomy) or by removing the cancerous lesion and a portion of the breast tissue around it (Lumpectomy), while keeping the rest of the breast intact [10, 80].

In addition to removing the tumour the surgeon would remove one (in the case of sentinel node biopsies) or more axillary lymph nodes for pathological assessment. Presence of cancer in one of these nodes indicate that cancer may have spread to other parts of the body. The breast tissue and nodes once excised are sent for histopathology examination for detailed tissue pathology and disease diagnosis.

Lumpectomy or BCS is often the treatment of choice for patients with early-stage breast cancer as it allows for complete tumour excision whilst maintaining acceptable cosmesis. Studies have shown that BCS followed by radiotherapy is as successful as total mastectomy for treating early-stage breast cancer [81–83]. However, choice may not be offered if the lesion is too large, multi-focal, lobular or, in the surgeon's opinion, so close to the nipple that it is likely to cause distortion. In such cases, the entire breast is removed by having mastectomy along with sentinel lymph node biopsy. Surgery is usually followed by chemotherapy or radiotherapy or, in some cases depending on the type and stage of cancer, hormone or biological therapy, or a combination of these treatments to eliminate any residual cancer cells.

2.6 Recurrence and high re-operative rates

In a mastectomy all breast tissue is removed, therefore the surgeon can be relatively confident that all of a primary breast cancer has been removed. However, whilst BCS in combination with adjuvant radiotherapy has been demonstrated to have a similar overall survival rate to mastectomy [81], there are still concerns that conservative resection may not provide complete tumour excision. Various patient factors, treatment factors and pathologic factors have been reported to be associated with an increased risk of recurrence after BCS treatment for invasive breast cancer and DCIS [10, 84–86].

Arguably, the most important of these is the status of the microscopic margins of excision

of the resected breast specimen [11, 29, 87–89]. What constitutes an adequate surgical margin is highly debated with evidence supporting all opinions [90]. American Society for Radiation Oncology (ASTRO) and Society of Surgical Oncology (SSO) have defined an adequate margin as no microscopic disease touching the inked surface of the resection specimen [91]. The National Institute for Health and Care Excellence (NICE) guidelines define a negative margin as >2 mm normal tissue surrounding the tumour [92] as illustrated in Fig.2.3(a).

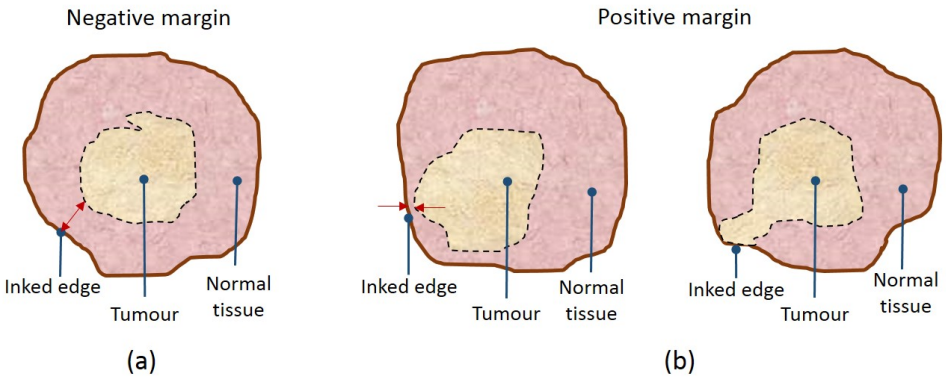

Figure 2.3: Definitions of surgical margin status. (a) Negative surgical margin means that the microscopic tumour within 2 mm from resection margins. (b) Positive surgical margin is defined as when tumour cells are found close or on the inked edge on the resection margin.

Positive/close margins, illustrated in Fig.2.3(b), are defined as invasive carcinoma or DCIS at or close to an inked tissue edge. Positive margin rates vary between institutions and definitions but typically range between 12.4%-43.1% and have a significant association with risk factors such as large tumour size, young age and presence of an intraductal component [10–13]. In a review by Singletary et al., accumulating data from over 15,000 patients from 34 studies, positive margins were found to significantly increase the likelihood of local recurrence of breast cancer in comparison to negative margins regardless whether the latter was defined as >1 mm or > 2 mm (P=0.006 and P=0.008 respectively) [29].

The rate of positive margins is undesirably high and consequently, a large proportion of patients undergoing BCS require re-excision to further remove microscopic disease. Every 1 in 5 women are reported to require re-operation within 3 months, including both mastectomy and a second BCS, and of those, 1 in 7 women who undergo a second BCS require a third operation [10]. This high rate of re-operation for both primary and secondary BCS indicates the importance of obtaining negative surgical margins, not only for the cosmetic outcomes but also to decrease the rate of local and distant recurrence associated with re-operation, hospital costs and patient trauma.

2.7 Intra-operative margin assessment

There are two possible approaches to intra-operative margin assessment (IMA). One option is to examine the surfaces of the resection cavity *in vivo* and the second approach is to assess the margin status of the resected specimen in a timely manner. The latter is more common for margin assessment and is conventionally done by histopathological analysis of the resection specimens worldwide. In this approach, the whole resection specimen is orientated to a clock face coordinate system using sutures and clips such that short suture and single clip mark the super margin and the long suture and double clip mark the lateral margin. Co-ordinates are recorded based on their position around the clock face and distance (in mm) from the margin. Tissue sections (5-20 μm) are cut from these locations for staining and histopathological examination. While such a post-operative pathology technique provides high diagnostic accuracy, it is labour-intensive and slow adding approximately one hour to the duration of the operation and therefore the examination is not truly 'intra-operative'.

A small number of hospitals that perform BCS currently utilise cytologic or frozen-section analysis of IMA [13, 93–99]. Touch-preparation cytology is a technique in which cells on the surface of the tissue are transferred to glass slides by touching the specimen to the glass and are then stained for pathologic observation. For frozen section analysis, the tissue is frozen and selected microscopically thin sections are cut from the specimen for further pathologic observation. A study on 181 diseased and 188 control patients, with and without frozen section, evaluation was carried out and reduction in reexcision rates by 34 percentage points (from 48.9% to 14.9%) and re-operation rates by 36 percentage points (from 55.3% to 19.3%) was observed [99]. A much smaller fraction of the tumour margin is sampled in frozen section than in post-operative pathology, as a result although the specificity is high (>95%), the sensitivity is often low. Further, both procedures are time consuming and require special expertise by a pathologist at the time of surgery. Sampling issues are also a problem since the entire specimen cannot be evaluated.

Many surgeons perform intra-operative radiological assessment of excised impalpable lesions using portable X-ray devices [100,101] and intra-operative ultrasound (IOUS) [102–107]. McCornick et al. found that use of intra-operative specimen radiography more than halved the rates of positive margins [102] whilst Layfield et al. reported that use of intra-operative specimen radiography for palpable breast cancer led to a reduction in the mean specimen weight without increasing re-excision rates and was associated with improved cosmesis [103]. The clinical outcomes in patients with primary biliary cholangitis (COBALT) study, a prospective multicentre trial, addressed the hypothesis that the use of IOUS for wide local excision (WLE) of palpable breast cancers had 80% power to

detect an 18% reduction in the re-excision rates [106]. However, compared to pathological techniques they have inferior accuracy and hence do not parallel the observed reductions in re-operation rates.

Due to the limitations of contemporary IMA techniques, a plethora of innovative devices are under development aiming to provide a tool that limits workflow disruption, gives rapid results, optimises margin control and reduces re-operation rates. Systems like MarginProbe™ (Dune Medical Devices, Caesarea, Israel) [108–110] and ClearEdge™ [111] that rely on measuring tissue-specific electric properties propose a significant reduction in re-operative rates with promising preliminary data (Margin probe: sensitivity and specificity 70% and ClearEdge: sensitivity 85%, specificity 80%). Mass spectrometry imaging based systems like rapid evaporative ionisation mass spectrometry (REIMS) [112, 113] and desorption electrospray ionization (DESI) [114], ionisation technique that utilises the aerosol by-product of electrosurgical tools, have shown promising results for detection of positive resection margins intra-operatively (REIMS: sensitivity and specificity 94%).

Various studies have applied different optical spectroscopy techniques such as elastic scattering spectroscopy (ESS) [115], diffuse reflectance spectroscopy [116] and Raman spectroscopy [117, 118] that measure light scattering at different wavelengths to provide both morphological and biochemical contrast between healthy and tumour tissues. Whilst preliminary results are promising, and molecular contrast can be achieved with tissue sectioning and staining, these probes rely on single-point spectral measurements which make the system extremely slow (more than 5 hour/mm^2) and suffers from large sampling errors. Preliminary studies on using optical coherence tomography (OCT) techniques with near IR illumination have also been carried out to assess breast margins and lymph nodes [119–124]. From a study performed on 37 patients using bench-top OCT, Nguyen et al. reported a sensitivity of 100% and a specificity of 82% for assessment of positive and negative tumour margins [120], whilst using a hand-held OCT probe, Zysk et al. performed a multicenter, prospective study on 46 patients undergoing BCS and positive margins were identified in 5/8 (63%) patients [123].

On the other-hand, several advances have been made in optical fluorescence microscopy with surgeons being able to accurately distinguish neoplastic lesions from normal breast tissues based on cellular and sub-cellular imaging features. These devices are either probe based for potential *in vivo* cavity scanning or bench-top system for high-resolution large-area imaging of whole resected specimens.

The next sections provide a detailed overview of fluorescence microscopy for rapid breast tissue characterisation with a focus on single-photon fluorescence microscopy techniques like epi-fluorescence and confocal microscopy that are central to this thesis and demon-

strate a potential to be miniaturised for *in vivo* application.

2.8 Fluorescence and fluorescence imaging

Fluorescence microscopy, now a mainstream tool for 3D cellular imaging, was invented almost a century ago when microscopists were experimenting with ultraviolet light to achieve higher resolutions. In the very beginning, observations were limited to specimens that naturally fluoresce. Rapidly, fluorescent dyes for staining tissues and cells were investigated and landmark evolution in the field was marked in 1994 with success in expressing green fluorescent protein (GFP) in living organisms [125].

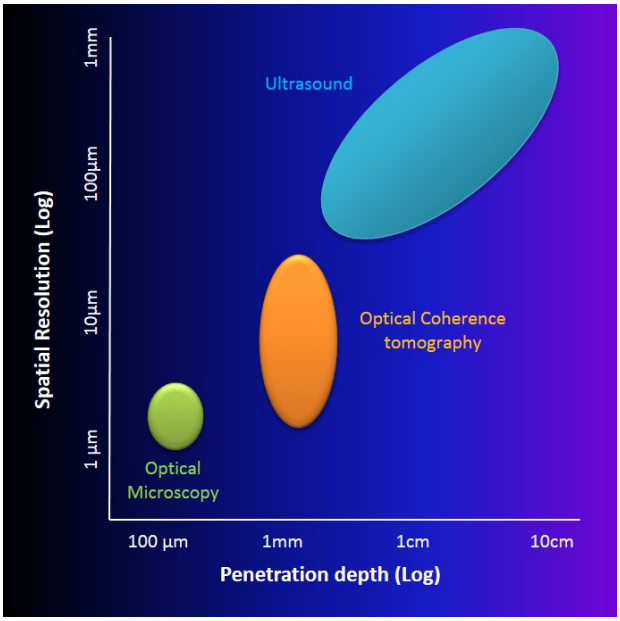

Figure 2.4: Spatial Resolution vs. penetration depth

Techniques like epi-fluorescence and confocal fluorescence microscopy have become powerful tools for thick tissue imaging. A plot of image resolution versus the penetration depth for these modalities as compared to X-ray, OCT and ultrasound imaging is shown in Fig.2.4. Fluorescence microscopy methods offer micron-level resolution whilst maintaining lower penetration depths of about 100-120 μm.

Even though the penetration depth is lower as compared to OCT and ultrasound techniques, these length scales are adequate for surgical imaging and characterisation of superficial lesions. Since most breast carcinomas start in the epithelial cells lining the glandular tissue, the shallow penetration depth of fluorescence microscopy systems ($\sim$ 60 μm) is sufficient to acquire diagnostic information during BCS without the need for surgical excisions.

2.8.1 Principle of fluorescence

Fluorescence is a phenomenon by which a molecule, upon illumination at a specific wavelength, re-emits light at another (typically longer) wavelength [126]. A molecule that has the ability to fluoresce is called a fluorophore. A Jablonski diagram, as shown is Fig.2.5, is commonly used to illustrate the physics of fluorescence. A molecule can exist in a variety of energetic states, which, for the most part, are determined by the configuration of its electrons and the vibrational agitation of its atomic nuclei. If a single photon with sufficient energy is absorbed by a fluorophore the latter moves from its ground state to an excited electronic state. Fluorescence occurs when the excited molecule returns to the ground state by releasing energy through emission of a photon. Two or more incident photons can also excite a fluorophore in a process called multi-photon excitation. Unlike single-photon excitation, this process scales non-linearly with intensity as it relies on the chance of two or more photons coinciding on a fluorophore at the same time.

As some of the energy gained during excitation is converted to heat, the emitted photon has a lower energy (hence, longer wavelength) than the absorbed photon. This results in the difference in wavelength which is known as the Stokes shift. Fluorophores whose spectra present a large Stokes shift are usually preferred since their emitted light is easier to separate from the excitation light using optical dichroic filters.

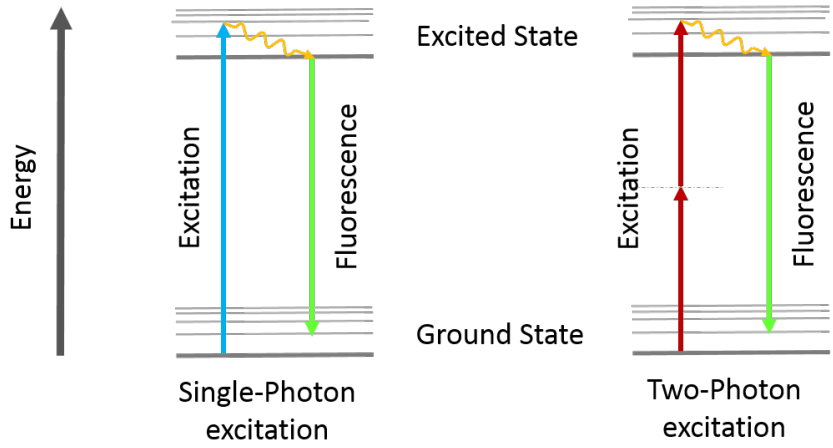

Figure 2.5: Jablonski diagram for single-photon and two-photon excitation

2.8.2 The wide-field fluorescence microscope

Wide-field fluorescence microscopy has emerged as a widely-used simple in-expensive technique for biological imaging. It is based on the paradigm proposed by Köhler to generate uniform illumination at the sample plane. A typical wide-field fluorescence microscope

based on epi-illumination * geometry is shown in Fig.2.6. Köhler illumination describes a system that is configured in a way that the source and the back-focal plane of the objective lens are at conjugate planes (shown as blue lines) [127]. Excitation light sources like LEDs or lamps are used to illuminate the sample and the emitted light is separated by a dichroic mirror towards the camera. To excite fluorescence at a particular wavelength, an excitation filter is positioned after the light source. An emission filter is placed after the dichroic mirror to image fluorescence in a specific wavelength range while rejecting background noise and excitation light. Typically, the image plane is recorded by a charged-coupled device (CCD) detector or viewed by the user through the microscope eye piece.

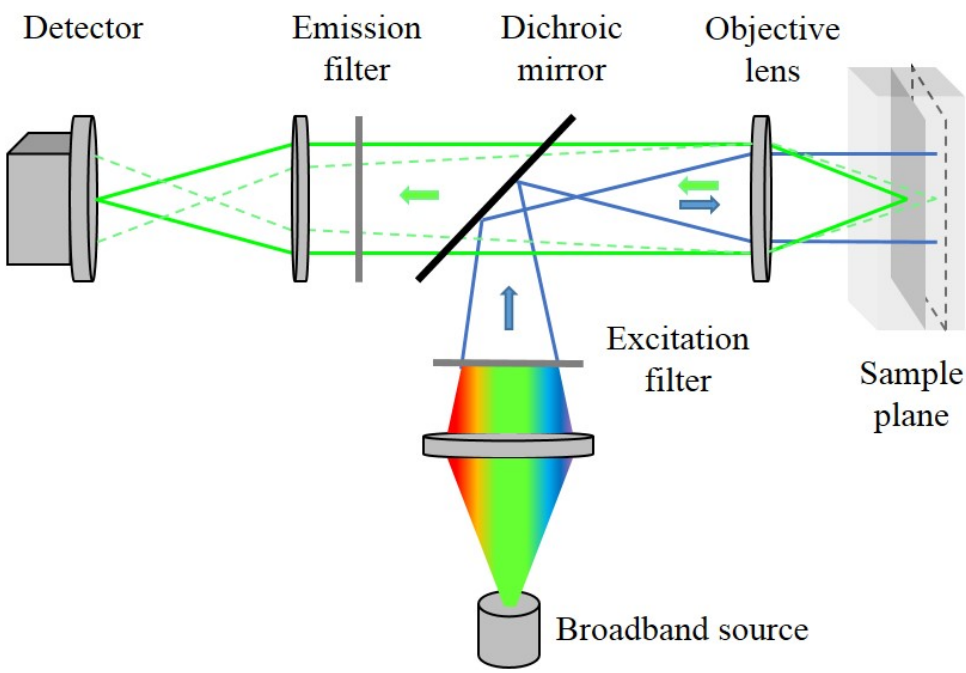

Figure 2.6: Working principle of wide-field epi-fluorescence microscope.

The epi-fluorescence microscope acquires signal from all pixels in parallel to provide the highest acquisition speeds. However, for optically thick specimens, light from different tissue layers contributes to image formation and out-of-focus light cannot be rejected (shown as dashed green lines).

Resolution or resolving power of a fluorescence microscope is defined as the minimum distance between two points that results in a certain level of contrast between them such that they can still be distinguished as two separate points [128]. The three-dimensional

*Epi-illumination describes an illumination method in which the objective lens is used as both the illumination condenser and the fluorescent light collector.

point spread function (3D-PSF) describes the three-dimensional diffraction pattern of light emitted from an infinitely small point source as traverses the optical system. Lateral/Transverse resolution can be characterised by measuring the width of the intensity profile of the 3D-PSF of the microscope. If a point source is focused by an objective lens on the screen, a 2D diffraction pattern will be visible on the screen and its central bright spot is called 'Airy disk', and the whole distribution including the concentric rings of light around it, is called the 'Airy pattern', as shown in Fig.2.7. The Airy disk, which gives minimum spot size to which a beam of light can be focused, can be calculated as:

$$d_{XY,Airy} = 2.44\frac{f\lambda}{D} \tag{2.1}$$

where f is the focal length of the lens, D is the diameter of the lens and λ is the wavelength of light.

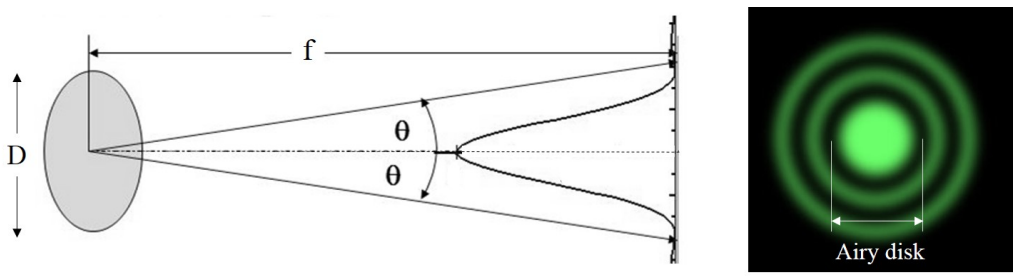

Figure 2.7: Airy disk seen as bright central spot in Airy pattern.

Using Abbe's formula, the diffraction-limited resolution of the optical system can be obtained as function of the wavelength of the incident light and numerical aperture (NA)[†] of the objective lens [129]. The lateral resolution of the microscope, given by the smallest period of intensity spatial frequency component that can be resolved, is expressed as:

$$d_{XY,Abbe} = 0.5\frac{\lambda}{NA} \tag{2.2}$$

where λ is the wavelength of light, n is the refractive index of the medium, θ is the semi aperture-angle of the microscope objective lens and NA is the numerical aperture of the lens, such that $NA = nsin\theta$.

Eq.2.2 has been further refined to provide different definitions of resolution given by the Rayleigh criteria, Sparrow criteria and full width half maximum (FWHM). The most commonly used definition for resolution in microscopy is the Rayleigh criterion that describes

[†]The NA of a microscope objective is a measure of its ability to gather light and resolve fine specimen detail while working at a fixed object (or specimen) distance.

the minimum resolvable distance of two point sources as the situation in which the central maximum of Airy pattern of one point source just overlaps with the first radial minimum of the Airy pattern of the other point source. The Rayleigh resolution is defined as:

$$d_{XY,Rayleigh} = 0.61\frac{\lambda}{NA} \tag{2.3}$$

Alternatively, according to the Sparrow criteria, the lateral resolution is defined as the distance at which the centre maximum of the diffraction image of two point sources just disappears and the image exhibits a constant brightness across the region between the central peaks. The Sparrow resolution limit is defined as:

$$d_{XY,Sparrow} = 0.47\frac{\lambda}{NA} \tag{2.4}$$

Another frequently used definition for resolution is the FWHM of the Airy disk which is the diameter of the central spot where the intensity drops to its half maximum (50%). The lateral FWHM resolution is expressed as:

$$d_{XY,FWHM} = 0.51\frac{\lambda}{NA} \tag{2.5}$$

And the axial FWHM resolution is expressed as:

$$d_{Z,FWHM} = 0.89\frac{\lambda}{n - \sqrt{n^2 - (NA)^2}} \tag{2.6}$$

The concept of image contrast is often used to quantify resolution experimentally. For two objects of equal intensity, the contrast is defined as the difference between maximum and minimum intensity occurring in the space between them. Image resolution is calculated as the minimum separation distance between two points that results in a certain level of contrast between them.

The conventional resolution limits and their definitions using point-like objects are illustrated in Fig.2.8. By using the Rayleigh criteria, the first minimum of one Airy profile overlaps the maximum of the second Airy, with the sum of the two profiles showing a distinct dip and the contrast value is about 26.4%. For the Abbe limit, a small dip is still discernible between the two maxima whereas for the Sparrow criterion, the sum of the two Airy patterns produces a flat intensity profile and the contrast becomes zero.

High resolution can be obtained by using high NA objectives or by reducing the illumination wavelength. For a 450 nm light source and an NA of 1.4, the highest possible Rayleigh resolution for conventional light microscopy is about 200 nm.

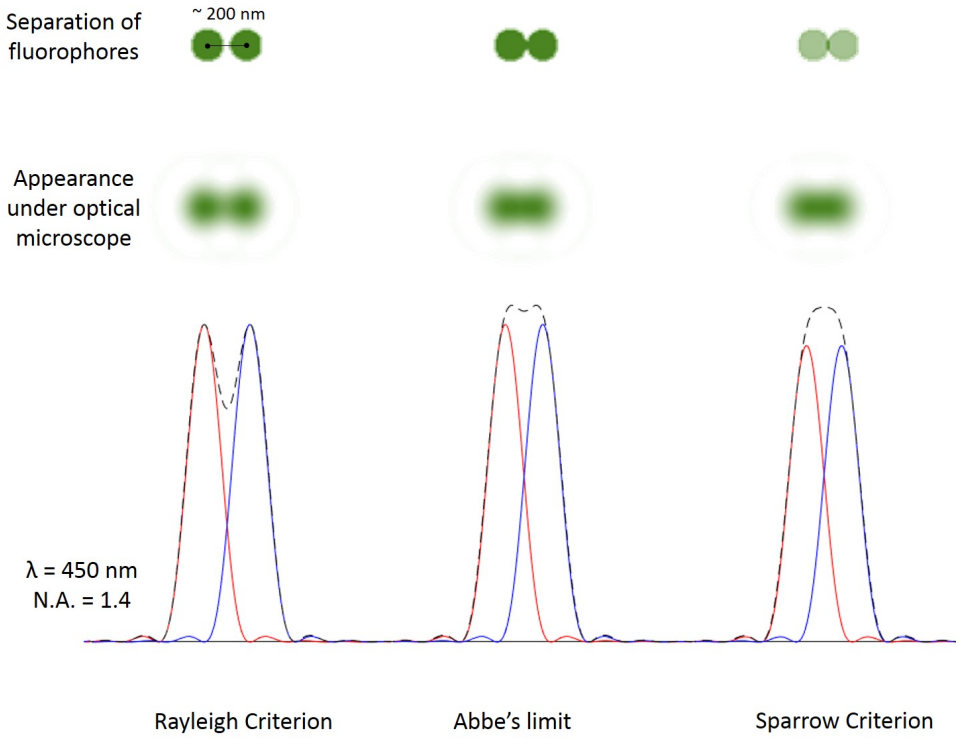

Figure 2.8: Various conventional resolution limits and their definitions. In the Rayleigh convention, the first minimum of one Airy profile overlaps the maximum of the second Airy profile, with the sum of the two profiles showing a distinct dip. In the Abbe limit, a small dip is still discernible between the two maxima while in the Sparrow criterion, the sum of the two Airy patterns produces a flat intensity profile.

2.8.3 Contrast agents

Since fluorescence microscopy mainly relies on induced fluorescence, it is imperative to use staining agents that have a safety profile for clinical application and selective contrast to distinguish between normal and malignant tissue. Fluorescence images based on contrast are generated due to endogenous agents, autofluorescence or exogenous dyes. Endogenous fluorescence arises from intrinsic biomarkers such as NADH and FAD which play an important role in the physiological processes taking place in the cells. Autofluorescence signal arises mainly from elastin, keratin, melanin and collagen but the emitted fluorescence signal is often low.

The majority of work on fluorescence microscopy imaging is conducted using exogenous staining agents administered either intravenously or topically. Non-specific agents like fluorescein, methylene blue and indocyanine green diffuse into the blood or the lymphatic system following intravenous administration. Staining occurs as a consequence of dye retention in a particular organ or tissue. For example, methylene-blue has been

used for mapping and localisation of non-palpable lesions and sentinel lymph node during breast surgeries [130–132]. Alternatively staining dyes like acridine orange, acriflavine and proflavine for nuclear-staining, Hypericin and 5-ALA for tumour targeting as well as a range of Alexa flour dyes are used for topical applications. Such agents require minimum preparation time and hence are often used for rapid *ex vivo* imaging applications of freshly excised specimens. Fluorescein, acriflavine hydrochloride, acridine orange and proflavine are commonly used as markers for analysis of tissue morphology as their excitation and emission spectra matches the source wavelength of common 488nm lasers. Acriflavine hydrochloride, a compound containing both proflavine and euflavine, has been used in a number of GI imaging studies [19, 133]. The topical stains are applied either by dipping the whole specimen into stain solution or by spraying the tissue surface using a spray catheter.

2.9 Optical sectioning microscopy

Images of biological specimen thicker than the microscope objective's depth of field have contributions from both the in-focus and out-of-focus planes. This reduces the contrast and resolution when imaged with the conventional wide-field system. The need to image optically thick specimens gave rise to optical sectioning microscopes that are able to isolate the light originating from the in-focus plane independently of its position into a thick sample. As a result, most of the out-of-focus light is rejected without the need for physically sectioning the sample. Optical sectioning can be achieved optically (eg. Confocal and Light-sheet microscopy), computationally (eg. Deconvolution microscopy) or using a combination of optical and computational methods (eg. Structured-illumination microscopy).

2.9.1 Confocal fluorescence microscopy

confocal fluorescence microscopy (CFM) was first invented by M. Minsky in 1957 [134] to enhance standard wide-field fluorescence microscopes by optically eliminating the out-of-focus light due to scattering from thick specimens. A CFM employs single point illumination, using a low-power laser source or a pinhole in front of a wide source, to focus light to a small point in the sample plane. Most confocal imaging systems rather than using a condenser lens for illuminating the object use epi-illumination in which objective serves both as condenser and objective lens, as illustrated in Fig.2.9. For image formation a spatial filter, usually a pinhole aperture, is placed in the detector plane conjugate to the sample plane. As a result, the detector collects light only from the illuminated focused spot and rejects all the other out-of-focus light from the sample. This ability to reject out-

of-focus light, known as spatial filtering, enables the CFM to image thin slices through a sample without physically sectioning it. When using a point source and point detector, it is possible to image only one spot of the sample at a time. To create a 2D image, the laser spot is typically scanned point-by-point in raster-scan or spiral-scan patterns using a scan mirror. Such a microscope is called a confocal laser scanning microscope [128, 135–139]. The sample is often moved mechanically in the axial direction to reconstruct a 3D volume from a stack of depth-resolved 2D confocal images.

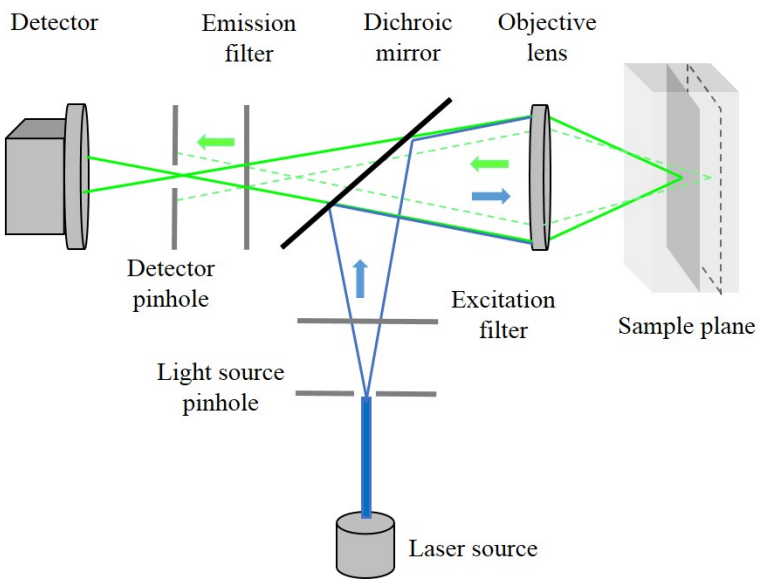

Figure 2.9: Simplified diagram of point-scanning confocal fluorescence microscope.

For fluorescence imaging applications signal levels are often very low, hence the sensitivity and noise performance of the detector are of great importance. A range of different photodetectors are available for CFM. In most scanning CFMs with detection pinhole aperture, a photomultiplier tube (PMT) is usually used due to its high sensitivity and signal to noise ratio. A PMT consists of a photocathode and a series of dynodes in which the number of photoelectrons is multiplied. As a result, the initial input optical signal is amplified largely by conversion to electric signal and mapped to a grayscale value for a pixel in the image. The main limitation of the PMT is its low quantum efficiency, typically less than 30%, meaning that only 30% of the incoming photons are effectively "converted" into electrons. Cooled CCD cameras are also used as detectors in scanning confocal systems due to higher quantum efficiency of 70% or more and small sensor readout noise of several electrons per pixel. A point of the image is recorded at a time and then this is swept across the CCD array to build a 2D image.

For point-scanning CFM, the 3D-PSF is the product of the independent illumination intensity and detection aperture intensity PSFs, resulting in about 28% reduction in the width of the PSF as compared to conventional wide-field microscopes. Because of narrower PSFs and improved contrast, there is a gain of resolution ($\sim \sqrt{2}\times$ over conventional case) [137]. However, the resolution is still diffraction-limited. For infinitely small pinhole size, the lateral and axial resolution limits for confocal microscope are expressed as:

$$d_{XY,Rayleigh\text{-}confocal} = 0.5\frac{\lambda}{NA} \tag{2.7}$$

$$d_{XY,Sparrow\text{-}confocal} = 0.34\frac{\lambda}{NA} \tag{2.8}$$

$$d_{XY,FWHM\text{-}confocal} = 0.37\frac{\lambda}{NA} \tag{2.9}$$

$$d_{Z,FWHM\text{-}confocal} = 0.64\frac{\lambda}{n - \sqrt{n^2 - (NA)^2}} \tag{2.10}$$

where λ is the emission wavelength, n is the refractive index of the medium and NA is the numerical aperture of the objective lens.

Although confocal microscopy enhances the optical resolution and contrast as compared to conventional microscopes, it does have several drawbacks. The point-scanning mechanism reduces the overall image acquisition rate of the system, thus making imaging of live or moving samples impractical. The small pinhole size reduces the number of photons that arrive at the detector, often requiring to raise the intensity and/or exposure time of the excitation light, resulting in photo-toxicity and photo-bleaching of the sample.

Various extensions have been developed to overcome these limitations of point-scanning confocal microscopes. Line-scanning confocal systems have been developed to accelerate the scanning process [140–146]. In a typical configuration, the pinhole detector is replaced with a slit or linear camera while the illumination is provided by focusing illumination (usually a laser) onto the sample with a cylindrical lens. In the case of an incoherent illumination source, a slit aperture is placed in the image plane in front of the light source, however this greatly reduces the total number of photons transmitted to the sample. The focused line is scanned only in one dimension perpendicular to the slit, rather than having to scan the diffraction-limited spot in two directions for a point-scanning setup. The line-scan mechanism improves the acquisition speed and the signal-to-noise ratio (SNR) compared to a point-scanning system by increasing pixel dwell times, but reduces the optical sectioning, especially far from focus [140].

The size of the confocal pinhole/slit relative to that of the Airy disk in the detector plane is an important parameter in determining the spatial resolution of the confocal

system [140]. If the width is too large, the confocal property is lost and if it is too small then not enough signal will be transmitted to the detector. By decreasing the size of the pinhole ($< d_{XY,Airy}/5$), the axial resolution of the microscope can be improved but at the cost of reducing the signal level. Although the slit system gives a stronger signal than a pinhole of diameter equal to the slit width, however, the axial resolution is degraded resulting in poorer sectioning performance. As a result, the line-scan systems are often referred to as semi-confocal. For wide-field diffraction-limited resolution, the radius of the pinhole/slit is chosen to be same as, or slightly smaller than $d_{XY,Airy}$.

Multiple point scanning confocal microscopy is another approach that attempts to facilitate high speed confocal imaging by scanning multiple pinholes in parallel. This is achieved by using a Nipkow-disk system - spinning disk with multiple pinholes in it, generally arranged in an Archimedean spiral pattern [147, 148]. These pinholes are placed at the primary image plane so they are imaged onto the sample and also act as detection pinholes for returning fluorescence. Using the Nipkow disk the 2-D illumination pattern can be shifted across the sample, allowing video rate imaging of moving and live samples with reduced photo-bleaching. A major limitation of this, however, is the trade-off in terms of achievable axial resolution, due to crosstalk between the different detection pinholes.

2.9.2 Light-sheet microscopy

A conceptually simpler method for providing optical sectioning in a fluorescence microscope is light-sheet microscopy [149–153]. A thin sheet of light is produced to illuminate a single plane at once rather than illuminating the whole sample which is fluorescently labelled. The emitted fluorescence is collected using a second microscope objective, which is most often in an orthogonal direction to the excitation sheet, such that its focal plane coincides with the plane of the light-sheet, as shown in Fig.2.10. The collected light is then re-imaged onto a camera and, typically, the light-sheet or the specimen is scanned in the axial direction to allow for rapid 3D imaging.

The first versions of the light-sheet microscope used a cylindrical lens to create a light-sheet in one direction and were referred to as selective plane illumination microscopy (SPIM) [149]. Since only the plane of interest is illuminated during a single exposure, the biological specimens could be imaged for a longer time with reduced photo-bleaching. The lateral resolution is solely dependent on the NA of the detection objective whereas the axial resolution is determined by a combination of the NA of the detection optics and the width of the generated light-sheet. Recent enhancements to the original SPIM technique focus on minimising the trade-off between optical sectioning, imaging speed and FOV.

The digital scanned laser light-sheet fluorescence microscope (DLSM) that uses laser scanner to generate virtual light sheets of uniform intensity, rather than using cylindri-

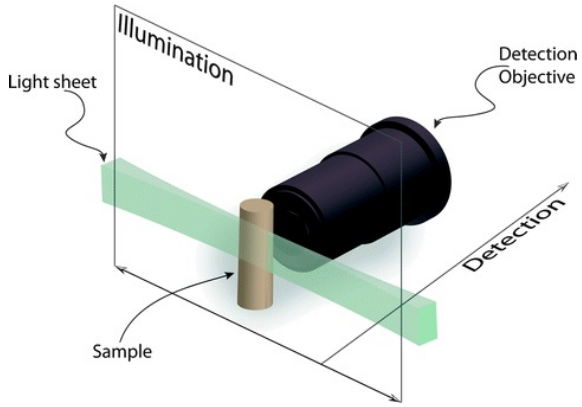

Figure 2.10: Simplified diagram of the light-sheet fluorescence microscope. (Tomer, Raju, Khaled Khairy, and Philipp J. Keller. "Light sheet microscopy in cell biology." Cell Imaging Techniques. Humana Press, Totowa, NJ, 2012, p. 124, Figure 1, WH Hindle, © Springer Science+Business Media, LLC 2013. Used with permission of Springer [2]).

cal optics, has been developed for high speed imaging of large specimens. The digitally scanned light sheets based on advanced beams such as Bessel, lattices, and Airy beams have been also constructed to overcome scattering and provide large field of view imaging [154–156]. By coupling the light-sheet into the objective at an angle of 60°, an oblique plane microscope (OPM) has also been constructed where the light-sheet is produced by the same objective used to detect fluorescence [157]. This allows for imaging live samples without the need to move the entire sample and refocus each time. Another approach to increasing image depth and signal contrast with regards to imaging thick or scattering samples is to combine this technique with two-photon excitation.

2.9.3 Deconvolution microscopy

Deconvolution is a computational approach to achieve optical sectioning by numerically reversing the effect of blur due to out-of-focus fluorescence in 3D stacks of wide-field microscope images. Different deconvolution methods have been designed over the years [136, 158–162]. Two popular deconvolution methods include deblurring algorithms and image restoration algorithms. The deblurring algorithms operate on the 2D images of the image stack by using the PSF to estimate the blur due to out-of-focus plane and subtracting it from the in-focus plane. The image restoration algorithms operate simultaneously on every pixel in a 3D image stack either by blind 3D deconvolution or by utilising knowledge of the point spread function (PSF) of the imaging system. A computational model of the blurring process, based on the convolution of a point object and its PSF, can be used to deconvolve or reassign the blurred light back to its in-focus location instead of subtracting it.

Several deconvolution algorithms have been used as an adjunct to 3D confocal microscopy [136, 161], however, they are often more complex and time consuming to compute than the simpler methods, suffer from artefacts when imaging planar fluorescent structures whose Fourier transformation falls into the missing cone region and usually require multiple rounds of iterative approximation to the reconstructed image.

2.9.4 Structured illumination microscopy

A common adaptation for wide-field microscope to reject out-of-focus light and improve image contrast is structured illumination microscopy (SIM) [163–165]. SIM consists of modifying the Köhler illumination by superimposing a predefined spatially varying pattern on the sample. It relies on illuminating the specimen with a periodic light pattern typically using 1-D grid pattern or non-periodic patterns like random speckles at the primary image plane of the microscope. Several images are captured by translating or rotating the light pattern and are computationally combined to reconstruct a whole-field image with optical sectioning.

Typically, three images shifted by $1/3^{rd}$ of the period of the grid are recombined to reconstruct an optically sectioned image using the following equation:

$$I_{SIM} = \sqrt{[(I_1 - I_2)^2 \ + \ (I_2 - I_3)^2 \ + \ (I_3 - I_1)^2]} \tag{2.11}$$

where I_{SIM} represents the intensity of the final image and $I_1,\ I_2,\ I_3$ are images which are shifted from each other by a phase of 0, $(2\pi/3)$ and $(4\pi/3)$ respectively [163].

Piezo elements, micromirror arrays and galvanometers have been conventionally used to generate precise grid shifts for accurate reconstruction. Grid artefacts and low image acquisition speeds are a major limiting factors for this methodology. Recent work has been focused on developing novel strategies to suppress these artefacts and facilitate high-resolution, fast deep tissue imaging for various biological applications. The SIM frame-rate can be increased by using programmable LED arrays [166], liquid crystal spatial light modulators (SLM) [167,168] and digital micro-mirror device (DMD) [169–171] which have the advantage of generating and controlling the fringe patterns accurately and quickly.

2.10 Endomicroscopes for *in vivo* imaging

Combining miniaturised and flexible optical fibres with these powerful microscopy modalities have facilitated their translation into optical biopsy methods for *in vivo* imaging applications [172,173]. The integrated instrument that bridges 'endoscopy' with 'microscopy' is referred to as 'endomicroscope'. The terms 'endomicroscope' and 'microendoscope' have been used interchangeably in literature. To remove ambiguity from the terminology, in the

rest of the thesis we adopt the term 'endomicroscopy' for an instrument used to acquire microscopic images from inside the body [3].

2.10.1 Optical fibres

The integration of fibre optics enables the separation of the imaging arm from the source and detector for *in vivo* scanning and reduction in the overall cost and complexity of the system. Endomicroscopes typically employ flexible single-mode optical fibres or fibre bundles to relay light to and from the sample, thus facilitating live imaging of tissue micro-architecture and cellular features.

Single mode fibres have a single small diameter core (<10 μm) surrounded by a lower refractive index cladding material with diameter typically 125 μm. Total internal reflection occurs when rays of light enter the fibre core and strike the core-cladding interface with an incident angle greater than the critical angle[‡]. This effect is used in optical fibres to confine light in the core and guide it along the fibre length. The small core size of such fibres support the propagation of a single spatial mode of light. As a result they can be focused to a near diffraction-limited spot in the specimen plane and can act as confocal pinhole aperture [174,175]. This has led to the development of various fibre-optic confocal systems where single-mode fibres are used for illumination, detection or both [17,19,173]. The focused spot has to be scanned across the sample to acquire full images. Recent work constitutes the development of high-speed and miniaturised distal scanning mechanisms for confocal systems which will be discussed in the next section.

A widely used method for fibre optic fluorescence endomicroscopy is to use multiple optical fibres arranged in a bundle, instead of a single fibre. Such optical fibre bundles consist of tens of thousands of step-index fibres surrounded by low refractive index material, and are typically packaged in hexagonal lattice. In a coherent bundle, the individual fibres preserve their relative spatial relationships. Ideally each core is considered to act as an individual wave guide transmitting one pixel of information in the image. This enables miniaturisation of the distal tip by allowing proximal scanning mechanisms using large and less expensive scanning devices. Fibre-bundles are commercially available by companies like Fujikura, Schott and Sumitomo which currently dominate the market for coherent fibre bundles and have been widely demonstrated for various biomedical and industrial applications.

Imaging fibre bundles are manufactured both in silica and in crown glass [176]. Detailed characterisation of these coherent imaging fibres for interferometric imaging applications is

[‡]Critical angle refers to the angle of incidence, beyond which total internal reflection of light occurs. For core and cladding of refractive index of n_1 and n_2 respectively, where $n_1 > n_2$, the equation of critical angle θ_c is $\theta_c = \sin^{-1}(\frac{n2}{n1})$

provided in [177,178]. Two common types of coherent fibre bundles used with fluorescence microscopy applications are shown in Fig.2.11. Fused bundles, like those manufactured by Fujikura, are often multi-core bundles with high NA germanium-doped silica cores in common fluorine-doped silica cladding along the entire length. The core diameter and inter-core spacing is small and hence they can provide high resolution images. However, they are much less flexible with a bending radius of a few centimetres. A representative zoomed-in and cropped image of Fujikura fibre bundle (FIGH-30-800N) is shown in Fig.2.11(a). The inter-core spacing is about 4.5 μm and individual core-size is about 2.5 μm.

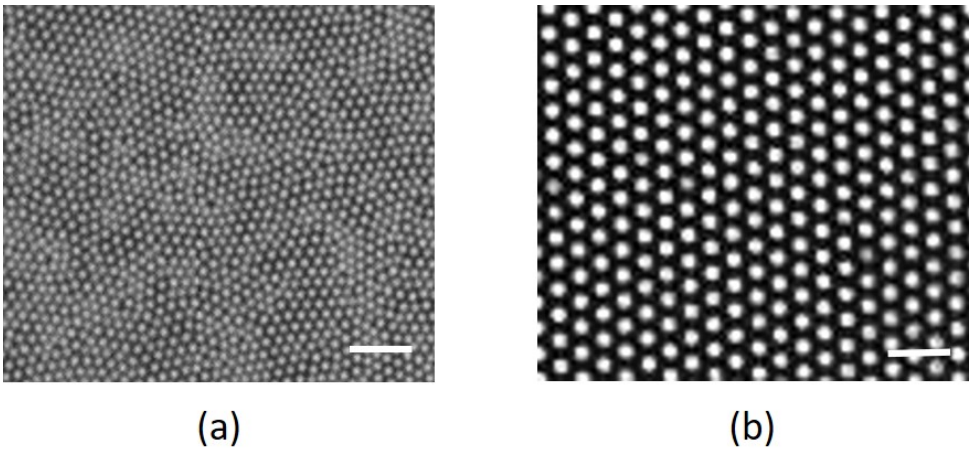

Figure 2.11: Cropped and zoomed-in image of (a) Fused Fujikura bundle, inter-core spacing of $\sim$4.5 μm and (b) Leeched Schott fibre bundle with inter-core spacing of $\sim$8 μm. The individual fibre cores are white and the cladding is black. Scale bar is 20 μm.

Leached bundles, like those from by Schott and Sumitomo, are manufactured by laying up rigid, double-clad core rods in a close packed array such that any particular core occupies the same position in the matrix at both ends of the bundle. The entire assembly is then fused and drawn to reduce the core diameter. Further, the outer layer of cladding is removed from each core by acid leaching which separates the fibres and renders the bundle extremely flexible. Leached bundles, with small inter-core spacing of 6-12 μm, are often used for endomicroscopy imaging applications due to their flexibility. An example cropped image of leeched bundle from Schott is shown in Fig.2.11(b). The number of individual fibres that can be packaged into the leeched bundle is about 13k as opposed to about 30k for typical fused bundles from Fujikura. Another type of fibre bundles are wound bundles made by winding sub-bundles of 5$\times$5 fibres into a single-layer ribbon on a cylindrical mandrel. These layers are assembled, ends are cut and polished for imaging applications [179].

A small distal objective is often used for focusing the excitation beam and for collection of the fluorescence light. High NA miniaturised compound objectives could be used, however, fabricating them at such small scale is challenging. Custom high-NA objective lenses ($\sim$ 0.4-1.0) can be designed with outer diameter as small as 3-7 mm [17, 180–183]. An economic solution of developing custom objectives made from injection-moulded plastic lenses has also been undertaken to reduce the manufacturing cost [184–186].

An attractive alternative is to use GRIN lenses, which are miniaturised lenses with radial index profiles. Such GRIN lenses can propagate the different electromagnetic spatial modes comprising an image at nearly the same velocity. As a result, they can serve as miniaturised distal objective lenses when cut to specific lengths. Usually GRIN microlenses of $\sim$3.5-1 mm outer diameter and high NA are used as distal objectives for single-photon, confocal and multi-photon microscopes [187–190]. These GRIN lenses exhibit refractive index that declines quadratically with radius. Such high-NA GRIN lens with up to 2.5$\times$ magnification are mounted on the distal fibre-bundle tip to enhance the spatial resolution, however the FOV is reduced by the same factor. A limitation of using GRIN lenses is that the optical aberrations often limits the resolving power to about twice the diffraction limit [190].

Recently, some custom miniaturised distal optics have been developed with an aim to minimise the trade-off between FOV and achievable resolution. Custom GRIN compound lens assemblies are designed by combining one or more GRIN lenses with different imaging characteristics. Custom microlens assemblies that are a combination of GRIN lens with conventional plano-spherical lens are commercially made available by GRINTech. (GRIN-Tech Gmbh). GRIN imaging probes have been demonstrated for *en-face* and side-viewing endomicroscopy imaging of tissue *in vivo* [173, 191–194]. However, these GRIN rod lens based endomicroscopes are rigid, and hence are mainly finding applications in small animal studies.

2.10.2 Wide-field fibre bundle endomicroscopes

high resolution microendoscopy (HRME) system, a combination of endoscopy and wide-field microscopy techniques, has emerged as an in-expensive and portable *in vivo* cellular-level imaging modality to detect malignancies in various clinical studies. A typical HRME system is composed of a light source, fibre bundle, dichroic mirror, emission and excitation filters, and CCD camera. Excitation light sources like bright LEDs are used to illuminate the stained sample. The distal tip of a coherent fibre-bundle, typically consisting of 30,000 fibres, is scanned over the stained tissue surface. The emitted fluorescence is collected by the fibre bundle and transmitted through the dichroic mirror to the CCD camera.

By optimising the choice of source illumination wavelength and fluorescent staining agent one can limit the out-of-focus light and make the system suitable for imaging several superficial tissue sites *in situ* [195]. Illumination sources like Blue LEDs with excitation wavelength centred at 455nm and topically applied contrast agents like acriflavine and proflavine with emission wavelength around 530 nm are typically used. HRME is not suitable to image intravenous fluorescein as out-of-focus light is significantly higher.

Owing to its low cost and simple optical configuration, HRME has found many pre-clinical and small clinical applications for high resolution imaging of oral mucosa, cervical cancer and GI tract malignancies [196–198]. Recently a dual wavelength HRME system has been developed for bacteria detection in *ex vivo* human lung tissue [199]. Optically sectioning wide-field endomicroscopes have also been developed by using a fibre-bundle to transport light to and from the specimen. These include adaptations like structured illumination endomicroscopy [184, 200, 201] and HiLo endomicroscopy [202] that enable optical sectioning under different conditions.

2.10.3 Confocal laser endomicroscopes

CLE can be implemented by distal scanning of the end of a single optical fibre or fibre-bundle with microelectromechanical system (MEMS) device, electromechanical elements or by scanning a laser beam across the proximal face of the fibre-bundle in 2D patterns. Typical point-scanning CLE is an application of Marvin Minsky's confocal microscope (1955) [134] that facilitates high resolution imaging by replacing the confocal pinhole and large objective lens with a flexible single-mode optical fibre. Initial work on single fibre confocal microscopy was performed by Giniunas et al. [203] and Juskaitis et al. [204] showing that the confocal pinhole could be replaced with an optical fibre, Fig.2.12(a). Since then different architectures involving distal optical scanning and distal fibre scanning have been developed by many research groups and companies using one or two optical fibres in single and dual axis configurations, Fig.2.12(b). Recent developments focus on using MEMS scanning mirrors that can fit in the imaging probe head for rapid scanning [205–210]. However much expertise is needed for MEMS fabrication.

First attempts to commercially develop endoscope based confocal laser endomicroscopy (eCLE) was by Optiscan (Optiscan, Australia) that integrated miniaturised confocal optics into the distal tip of conventional endoscope (EC-3870CIFK, Pentax Tokyo, Japan) [19, 211]. The eCLE system consisted of a single optical fibre which served as both the illumination and detection confocal pinholes. An electromagnetically driven distal scanning mechanism allowed it to perform raster scans of the fibre tip and generate 2D optically sectioned images.

A piezo actuator was also incorporated to provide a working of distance up to 250 μm. Images with lateral resolution of 0.7 μm and axial resolution of about 7 μm, for a FOV of 475×475 μm can be achieved. These endomicroscopes are, however, limited by the large diameter (>5 mm) of the distal tip and low scanning rates (∼1 fps) which greatly restricts their applicability for real-time clinical imaging of large tissue areas.

To circumvent the limitations of distal scanning, CLE probes with fibre bundle instead of single mode fibres have been developed and are widely used for clinical studies. In such a probe-based confocal laser endomicroscopy (pCLE) scheme, the scanning unit is located at the proximal end of the fibre bundle [17]. The most common mechanism used for proximal scanning is the combination of two cascaded galvanometer mirrors, one for horizontal scanning (resonant scanner - high speed up to 4 kHz) and one for vertical direction (lower speed), resulting in a raster scan pattern across the surface of the fibre bundle (Fig.2.12(c)). However, such point-by-point scanning mechanism limits the achievable frame rate of pCLE systems (∼12 frames/second).

Multi-point scanning pCLE system using Nipkow disks have been developed to improve the image acquisition rates by parallel illumination and detection [212]. Line-scanning systems using slit aperture or cylindrical lens have also become popular for high-speed CLE applications [180, 213–216]. Preliminary studies carried out by Sabharwal et al. used a single scan mirror, cylindrical lens and fixed width slit aperture in front of a 2D CCD camera to create 2D images [180]. Semi-confocal imaging at 30 fps was achieved. Hughes et al. accomplished a higher frame rate of 120 fps using a linear CCD detector [215] and later demonstrated similar performance using the rolling shutter of a complementary metal-oxide-semiconductor (CMOS) camera as a virtual slit [216].

Point-scanning pCLE endomicroscopes and a range of imaging probes with different diameters and specifications are commercially available by Mauna Kea technologies. For such systems, lateral and axial resolutions down to 0.5 and 3 μm, respectively, FOV of typically 240×240 μm, and objective lens and total probe outer diameters down to 0.35 and 1.25 mm, respectively, have been achieved for frame rates of ∼12 fps. Commercial and research based fibre bundle pCLE systems have found many applications for superficial and deep tissue imaging. With pre-clinical and small clinical studies on pCLE preliminary conducted on Upper GI tract for visualisation of Barrett's oesophagus, gastric neoplasia and celiac diseases and lower GI tract for screening colonoscopy, CLE has since then been explored in the imaging of breast, respiratory and urinary tract for *in situ* cancer diagnosis. A detailed review of CLE instrumentation and applications can be found in [3].

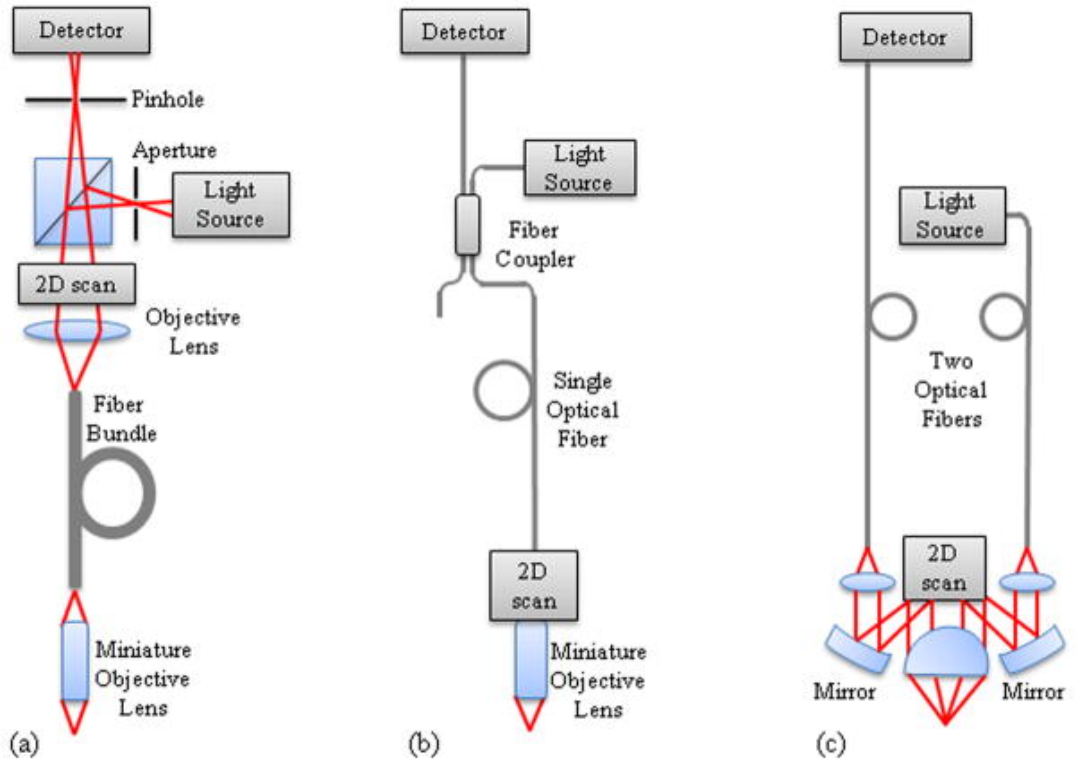

Figure 2.12: Different scanning configurations for CLE (a) Proximal scanning endomicroscope using optical fibre bundle for illumination and detection (b) Distal scanning endomicroscope using single optical fibre for illumination and detection and (c) Distal scanning endomicroscope in dual-axes confocal configuration using 2 optical fibres and a MEMS scanning mirror (Jabbour, Joey M., et al. "Confocal endomicroscopy: instrumentation and medical applications." Annals of biomedical engineering 40.2, 2012: Fig.2, p.380. Copyright © 2011, Biomedical Engineering Society, Used with permission of Springer [3])

2.10.4 Imaging challenges

Fibre-bundle endomicroscopy systems offer several challenges related to the spatial resolution and achievable FOV which greatly influence the quality of the acquired images.

Limited spatial resolution

Fibre-bundle endomicroscopes use individual fibres as image pixels such that each fibre of the bundle provides only one sampling point on the tissue. In order to minimise crosstalk between optical fibres, the spacing between cores of adjacent fibres is kept much larger than the mode field diameter of the fibre. The increase in size of non-imaging spaces between adjacent fibre cores however results in an enhanced fibre pixelation/sampling artefact. As the diameter of the fibre bundle is reduced the pixelation artefact becomes

more pronounced and is seen as a strong honeycomb pattern with reduced overall contrast and spatial resolution of the image. This inter-core spacing and sampling artefact limits the achievable spatial resolution of the imaging system.

In order to overcome the image-related artefacts, real-time or post-processing of the images is undertaken with additional image processing software. The artefacts due to fibre-optics manufacturing are mostly time-independent in nature and hence can be easily corrected computationally by image processing. Several imaging algorithms have been proposed that facilitate removal of the pixelation artefact by low-pass filtering and adaptive spectral masking in Fourier domain, and Gaussian filtering and spatial interpolation in spatial domain [183, 217–222]. Even-though such methods lead to removal of pixelation artefacts they do not result in improvement in spatial resolution caused due to under-sampling. Further discussion is presented in Chapter 7.

Limited field of view

Another limitation is that the FOV is limited by the size of the available fibre bundle. For commercial pCLE systems, the FOV is less than 1 mm^2. Such a small FOV makes it very difficult for the clinicians to interpret the endomicroscopy images correctly and acquire information about the tissue morphology and lesion sites particularly while imaging and surveying large tissues areas such as long segments of Barretts oesophagus. Further, a small FOV often results in sampling errors when imaging and modelling deformations of heterogeneous biological tissues, thus limiting its applicability in clinical use.

A popular solution to acquire images of a large-area of tissue without sacrificing resolution is to adopt video mosaicking technique (stitching of adjacent overlapping images in the direction of the probe motion). This approach has been extensively explored in literature as well as various on-line and off-line mosaicking algorithms for fibre bundle endomicroscopy imaging have been proposed. It is to be noted that the results of mosaicking are highly dependent on the ability of the operator to produce finely controlled motion of the probe tip. This is particularly challenging for point-scanning confocal endomicroscopes which typically have frame rates on the order of 10 fps. Other challenges with image mosaicking are in dealing with cumulative image registration errors and loss of image information due to various factors like probe motion, tissue deformation or lost probe-tissue contact. The best registration results are obtained from global alignment of image frames, but processing constraints limit real-time implementations to simple pair-wise image registration methods.

Image interpretation

Conventionally, histology images of biopsy samples are examined by trained pathologists for disease diagnosis and classification. Since FEM images closely resemble histology images, their interpretation is therefore a critical challenge for clinicians/surgeons who have little histopathology expertise. Further, as endomicroscopy imaging is a relatively new technique, it does not have a taxonomy of pathologies for various breast lesions types, thus making *in situ* diagnostics even more challenging.

2.11 Fluorescence microscopes for breast tissue imaging

Fluorescence microscopic imaging of fresh breast specimens has been predominantly demonstrated using multiphoton microscopy (MPM) [223–225]. Although the diagnostic accuracy of MPM is comparable to a histological assessment, a big hurdle towards large-scale clinical acceptance is its high cost due to use of femtosecond lasers. Single photon fluorescence microscopy systems like CFM are less expensive and widely demonstrated for imaging skin lesions [226–229]. However, studies for imaging breast cancer are very limited. Further, most of these studies are qualitative and provide feasibility results on a small cohort. A comparison of various single-photon fluorescence microscopy techniques on breast cancer imaging are presented in Table 2.1. The imaging modalities are categorised as bench-top and hand-held approaches and comparisons are made in terms of factors like resolution, acquisition rate, FOV and staining agent used. Choosing an appropriate technique for a particular breast IMA task must take such factors into consideration, which can affect diagnostic and imaging performance: instrument size, ease-of-use, cost, and impact on the clinical workflow.

Most of the literature on benchtop CFM for breast tissue imaging have been published using a commercial scanning confocal microscopy system (Vivascope 2500; Caliber Imaging and Diagnostics Inc., Rochester, New York). Vivascope2500 is designed for *ex vivo* tissue and provides microscopic resolution ($\sim$1 μm lateral resolution) confocal images of un-fixed breast tissue at 9 fps for a FOV of 750 μm [230–234]. Dobbs. et al. used the Vivascope system for imaging small surgical excisions and core biopsy specimens using 0.01% topical proflavine as a contrast agent [230–232]. Images are obtained at 488 nm excitation with a 550 nm$\pm$44 nm bandpass filter using a 30$\times$ water immersion objective lens with a numerical aperture of 0.8. Tissue experiments were performed on 70 breast specimens from 31 patients and sensitivity and specificity of 93% was achieved [230]. Feasibility studies have also been performed on using Vivascope2500 with acridine orange as a rapid nuclear-staining agent, to identify and distinguish different breast morphologies in small surgical excisions [233, 234].

Table 2.1: Comparison of single-photon fluorescence microscopy techniques for breast tissue characterization.

Imaging modalities	**Lateral resolution**	**Optical sectioning**	**Frame rate & image area**	**Staining agent**
Bench-top approaches				
Confocal fluorescence microscopy (Vivascope2500) [230–234]	1 μm	5 μm	9 fps 750×750 μm	Proflavine [230–232] Acridine orange [233, 234]
Confocal strip mosaicking microscopy [235]	1 μm	3 μm	20×20 mm in 10 minutes	Acridine orange
Structured illumination microscopy [236]	4.4 μm	∼128μm	3 fps 2.1×1.6 mm	Acridine orange
Light-sheet microscopy [237]	1.25 μm	∼7 μm	800 fps 0.32×2.56 mm	Acridine orange
Hand-held approaches				
Dual-axes confocal endomicroscopy [238]	4 μm	5 μm	5 fps 800×400 μm	IRDye800CW
Confocal laser endomicroscopy (Cellvizio) [239, 240]	1 μm	∼10 μm	12 fps 240×240 μm	Acriflavine [239] Fluorescein [240]
Confocal laser endomicroscopy [241]	4 μm	∼10 μm	20 fps 240×240 μm	Acriflavine
Wide-field fluorescence endomicroscopy [242]	4 μm	∼120 μm	11 fps 360×360 μm	Proflavine
Structured illumination endomicroscopy [185, 243]	4 μm	∼70 μm	3 fps 360×360 μm	Proflavine [185] Lugol's iodine [243]

Although these important findings using Vivascope have opened exploration into rapid histology of breast tissue, the low acquisition rate and small FOV limits its application for IMA of large specimens like whole breast margins. With an aim to overcome these limitations and provide large-area high-resolution imaging, bench-top set-ups for SIM [236], light-sheet microscopy with a solid-immersion lens [237], and a confocal strip-mosaicking microscope (CSM) integrated with custom designed tissue holder and levelling mechanism [235] have been demonstrated in the last 2 years. These systems have used acridine orange as a nuclear contrast agent and have demonstrated applications towards rapid imaging of whole core needle biopsies as well as breast margins with minimal tissue preparation. Abeytunge et al. conducted a study on 34 freshly excised specimens from 18 patients using CSM and demonstrated that imaging areas of 400 mm^2 could be imaged in 10 minutes with 1 μm lateral and 3 μm axial resolution [235].

Preliminary studies have shown application of optical fibre-bundle based wide-field techniques like HRME [184, 242] and structured illumination endomicroscopy (SI-HRME) [185,243] for freshly excised breast tissue specimens. Such studies have been demonstrated using topical application of proflavine and lugol's iodine. Chang et al. have demonstrated its capability in distinguishing normal from neoplastic breast tissue using a commercial Cellvizio CLE system integrated with a flexible fibre bundle and topical staining with 0.01% acriflavine [239, 244]. Cellular resolution confocal images with FOV of 240 μm were acquired at 12 fps. Imaging experiments were conducted on freshly excised breast tumour samples and adjacent non-diseased sections from 50 consenting patients and a 93% accuracy in detecting neoplasms by pathologists and surgeons was reported [244]. In the same year, Palma et al. reported the use of Cellvizio pCLE with intravenous fluoroscein as the contrast agent and demonstrated the feasibility of identifying different breast pathologies in surgically excised specimens from 13 patients [240]. While fluoroscein is attractive for *in vivo* applications, it did not highlight tissue morphology as effectively as acriflavine, causing difficulties in distinguishing between benign and malignant lesions.

While all the previous studies have been performed using non-specific dyes for imaging morphology of different breast pathologies, a recent study by Gao et al. demonstrated the molecular imaging capabilities of confocal endomicrosocpy [238]. A hand-held near-infrared dual axis confocal endomicroscope was developed to detect ErbB2 positive cells in breast tissue by using a specific targeting peptide labelled with IRDye800CW-malemide (LiCor Biosciences) fluorophore. Images were acquired at 5 fps and *in vivo* molecular imaging capabilities were demonstrated by assessing the uptake of specific peptide binding to human xenograft breast tumours expressing ErbB2.

2.12 Conclusion

Nationally, a significant proportion of cancer patients undergo re-operative intervention following attempted BCS (with average UK re-operation rates 30%). Positive margins during BCS have consistently been associated with a higher risk of local recurrence than negative margins. Achieving intra-operative management of breast margins is thus an important factor in reducing the morbidity, cost and inefficiency associated with re-operation for inadequate margins, or worse, with local recurrence.

Fluorescence microscopy techniques could be used for IMA of breast margins following BCS. An introduction to the principle of fluorescence is presented followed by overview of the current state-of-the-art of fluorescence microscopy systems (bench-top and fibre-coupled) describing their instrumentation, imaging principle, system specifications contrast mechanism and clinical applications within the context of breast tissue characterisation. To date only a few studies have been conducted on the investigation of breast tissue pathologies using CFM. Most of these studies have been suggested as feasibility experiments using slow point-scanning confocal laser microscopes (Vivascope2500 and Cellvizio pCLE system) and a single fluorescent dye. The role of CFM in the field of intra-operative imaging of breast cancer needs to be further investigated. It remains unclear whether endomicroscopy images obtained from *ex vivo* cut-outs (with specific tissue pathology) are representative of the margin features of whole wide local excision specimens. This thesis will focus on development of high-speed, portable fluorescence microscopy platforms with cellular resolution which can perform diagnostically relevant IMA, thereby reducing the number of invasive, time consuming, and expensive re-operations. This work will also serve as an important base for researchers considering this or similar problems which require surgical assessment surface of whole tissue specimens in a timely manner.

Chapter 3

Preliminary studies*

3.1 Introduction

Initial studies have described different morphologies of normal and neoplastic breast tissue by imaging small excised specimens using fibre-bundle based Cellvizio pCLE systems. Although these important findings open exploration into rapid digital pathology, using such systems for imaging circumferential margins during BCS and integrating it into a pathology reading setting warrants further examination. Much work needs to be carried out to standardise feature descriptions. Further, these imaging systems have some intrinsic limitations. The point-scanning pCLE provides high resolution images with better optically sectioning at the expense of reduced image acquisition rates $\sim$ 12 fps.

Recently, a high-speed LS-CLE has been developed by Hughes et al. [216] for rapid large-area tissue imaging at mosaicking. The system can achieve frame rates up to 120 fps, an order of magnitude improvement over commercially available pCLE systems. Initial work was carried out on topically stained *ex vivo* gastrointestinal tissues in a porcine model to demonstrate the feasibility of obtaining high quality real-time images with wider FOVs while still maintaining sufficient resolution and signal-to-noise ratio. The diagnostic performance of LS-CLE for breast tissue characterisation and its potential application as IMA tool for imaging breast margins has yet to be systematically evaluated.

This chapter presents a feasibility study for imaging *ex vivo* breast tissue specimens using the LS-CLE system. The goal is to assess if normal and neoplastic breast tissue pathologies can be distinguished using the LS-CLE system and whether LS-CLE is suitable for imaging margins of WLEs. 43 unfixed human breast tissue specimens used for

* The contents of this chapter were presented as:
Vyas, K., Hughes, M., Leff, D. R., & Yang, G. Z. (2016). Endomicroscopic Imaging Of Breast Cancer: Instrumentation And Applications. Poster presentation at Biophotonics and Imaging Graduate Summer School.

this study were stained with 0.02% acriflavine hydrochloride solution prior to imaging. The specimens belong to seven histopathological categories: IDC, DCIS, fibroadenoma, fibrocystic changes, normal glandular tissue, normal stroma and adipose tissue. A subset of 20 specimens were subsequently imaged using pCLE system. Various qualitative and quantitative image-based metrics were tested and side-by-side comparisons were made. Based on these metrics an image classification framework was developed to analyse the diagnostic content of images acquired using each system.

Such an evaluation is important to establish the potential of LS-CLE as an optimal imaging modality for the given breast IMA problem. Further, it will aid to understand the technical and clinical challenges in imaging breast tissues with these systems, which will lay the foundation for the research developments presented in the remaining chapters of the thesis.

3.2 Breast tissue samples

For this work, surgical breast resections were obtained through collaborators from Charing Cross Hospital London. The fresh tissue specimens were obtained from 10 patients undergoing mastectomy after written consent using the Imperial College tissue bank ethical protocol following the R-12047 project - 'Preliminary study on probe-based microconfocal for imaging breast diseases on freshly excised breast tissues'. Specimen cut-outs ($\sim$ 10×10 mm) were acquired from pathology following preliminary assessment and breadloafing. The frozen samples from 25 consented patients were obtained from Imperial College tissue bank database. The patients had undergone mastectomy (19 patients) and surgical excision of lump (6 patients). The frozen samples were stored at -80 °C, and thawed at room temperature while the freshly excised specimens were imaged straightaway.

3.3 Instrumentation

The high-speed LS-CLE system developed by Dr. Michael Hughes is utilised to acquire endomicroscopy images of breast tissue specimens [216]. Since this system and its adaptations are used for experimental investigations in other chapters of the thesis, a detailed description is presented here. Following this, a brief description of the commercial Cellvizio pCLE system is also presented and comparison of the specifications and performance is made.

3.3.1 Flexible fibre-bundle imaging probe

While the fluorescence imaging systems can be used with any fibre-bundle, for this work a high-resolution Coloflex UHD probe from Cellvizio was utilised. This consisted of a packaged fibre-bundle and distal GRIN micro-lens assembly. The fibre-bundle was a 30,000 core Fujikura fused bundle, with an inter-core spacing of 2.7 μm and an image circle diameter of 600 μm. The distal lens provided a 2.5$\times$ magnification, resulting in a field of view of 240 μm and an effective core spacing of 1.1 μm when projected onto the tissue. This suggests a sampling-limited spatial resolution of 2.2 μm when the Nyquist criterion is applied which is sufficient to resolve normal epithelial cell nuclei that range in diameter from 5 to 10 μm [245]. The working distance of the probes is about 60 μm making it suitable to image superficial cellular layers of the tissue under examination. A sterile plastic sheath with $\sim$50 μm thickness was kept between the probe tip and tissue surface to avoid any contamination.

3.3.2 Line-scan confocal laser endomicroscopy

Fig.3.1 shows the schematics and photograph of the LS-CLE system. The optical system consists of an illumination, sample arm and detection arm. The illumination consists of a compact laser diode delivering light at 488 nm (Vortran Stradus, 488) with a maximum output power of 50 mW. The output beam is expanded to about 4 mm by a 2$\times$ beam expander L1 (Thorlabs, GBE02-A). This is then reflected off a galvanometer scanning mirror M1 (Thorlabs, GVS001) and enters a telescope consisting of a plano-convex cylindrical lens L2 (Thorlabs, LJ1695RM, f = 50 mm) and an achromatic doublet L3 (Thorlabs, AC254-050-A-ML, f = 50 mm). The cylindrical lens shapes the laser beam into a line of illumination. A dichroic mirror (Thorlabs, MD498) reflects this beam towards the sample arm of the system.

The sample arm consists of the microscope objective, fibre-bundle and XY and Z translation mounts for the bundle. A dichroic mirror M2 (Thorlabs, MD498) reflects the illumination beam onto a 10$\times$ plan infinity-corrected microscope objective L4 (Thorlabs, RMS10X) which focuses it to a line across the proximal end of the fibre-bundle. A custom 3D printed holder is designed to mount the fibre-bundle in the lens mount. A manual XY actuator (Thorlabs, ST1XY-S) allows to adjust the lateral position and a manual high-precision Z-axis translation mount (Thorlabs, SM1ZM) allows to adjust the axial distance between the proximal end of the fibre-bundle and the microscope objective such that any beam translation and clipping by the objective can be avoided. The probe transfers the laser line to the tissue with some pixelation due to the fibre core pattern. During scanning, a time-averaged power of 1.6 mW is delivered to the tip of the probe. The average line

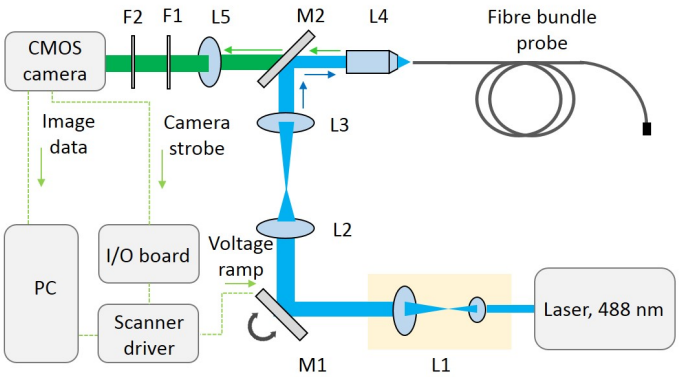

(a)

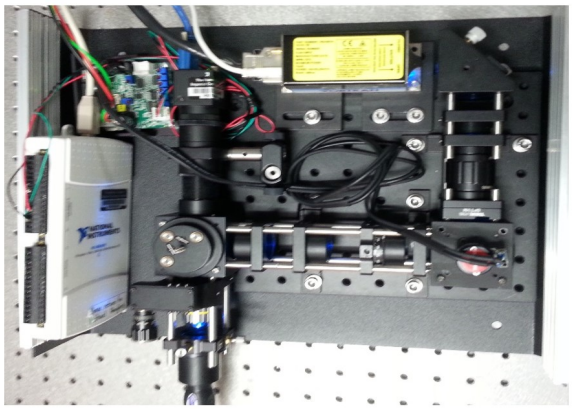

(b)

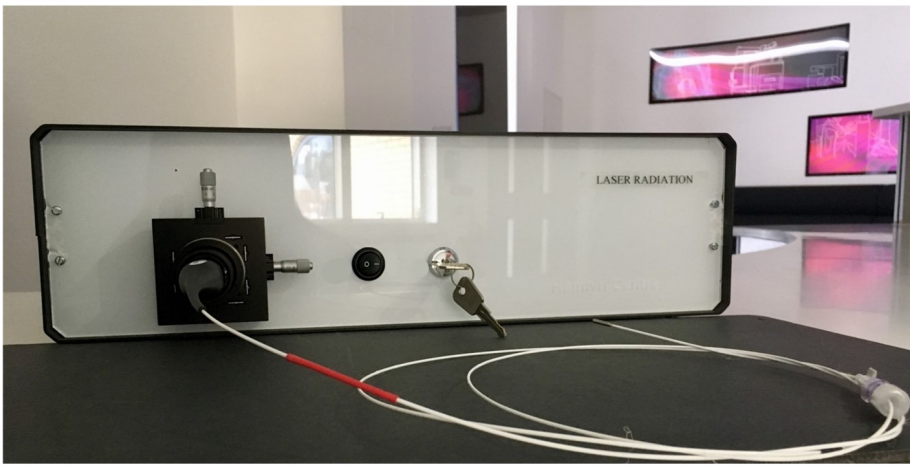

(c)

Figure 3.1: (a) Optical configuration of line-scan confocal laser endomicroscopy (LS-CLE) system and (b) Photograph of the LS-CLE system integrated with a Cellvizio fibre-bundle probe without and (c) with enclosure.

width at the tissue (measured by imaging the line onto a camera with a 20× objective) was 1.6 μm. The detector arm was designed to carry the fluorescence light from the tissue under examination and relay it to the camera through the same fibre-bundle and a series of lenses. Fluorescence emission returned along the bundle is transmitted by the dichroic mirror, fluorescence emission filter F1 (Thorlabs, FEL0500) and notch filter F2 (Thorlabs, NF488-15) to remove reflected 488 nm light.

The proximal face of the bundle is de-scanned and imaged onto a rolling-shutter CMOS camera (Point Grey Flea 3) using an air-spaced achromatic doublet L5 (Thorlabs, ACA254-075-A, f = 75 mm). The rolling shutter of the CMOS camera operates as a virtual detector slit that rejects most of the out-of-focus light, leading to optical sectioning. The magnification between the proximal face of the bundle and the camera was approximately 4.2, resulting in an image diameter of 2.5 mm on the camera. The camera had a 3.63 μm pixel pitch, providing 688 pixels across the fibre-bundle, or approximately 4.47 pixels per core spacing. This was sufficient sampling to allow individual cores to be visualised in the images.

Table 3.1 lists the specification of each optical element in the system. Thorlabs 30 mm cage system cubes, adapters and construction rods are used to align the lenses and mirrors to the optical axis and mounted on a portable optical breadboard for increased stability. The entire system is packaged in an aluminium enclosure box with dimensions of 367×300×134.5 mm (Farnell Metcase, M5505119) for easy transportation to the clinical imaging facilities. Fig.3.1(c) shows a picture of the enclosed LS-CLE system integrated with a fibre-bundle on an optical bench.

Table 3.1: Specifications of optical elements for LS-CLE imaging system

Element	**Specification**	**Purpose**	**Source**
L1	2X	Beam expander	Thorlabs, GBE02-A
L2	FL 50mm	Cylindrical lens	Thorlabs, LJ1695RM
L3	FL 50mm	Achromatic doublet	Thorlabs, AC254-050-A
L4	10X, 0.25 NA	Objective lens	Thorlabs, RMS10X
L5	FL 75mm	Camera lens	Thorlabs, ACA254-075-A
F1	>500nm	Emission filter	Thorlabs, FEL0500
F2	FWHM 15mm	Notch filter	Thorlabs, NF488-15
M1	12.5° scan angle	Galvo scanning mirror	Thorlabs, GVS001
M2	Long-pass, 498nm Cutoff	Dichroic mirror	Thorlabs, MD498

The camera is operated in free-run mode, which allows images to be acquired at the full frame rate of 120 fps by generating a trigger pulse on its strobe output pin at the start of each frame acquisition. The pulse triggers the analog output of a data acquisition card (NI-USB 6211) which has a 16-bit, 250 KS/s sampling rate to send a ramp voltage signal to the galvo-scanning mirror with some user-specified delay. Fine adjustment of the ramp slope and delay ensures that the virtual slit is aligned with the laser line throughout the acquisition of each frame. The Flea3 camera has line rate of 130.7506 kHz, pixel size of 3.63 μm, sensor size of 8.46 mm and minimum allowable exposure of 7.63 μs. This is equivalent to slit-width of 1 pixel on camera or about 0.86 μm on the proximal face of the bundle. For the experiments an exposure of 30μs, which corresponds to a slit-width of about 2.6 μm, was chosen.

3.3.3 Cellvizio confocal laser endomicroscopy

The Cellvizio is a commercial point-scanning pCLE system developed by Mauna-Kea Technologies, Fig.3.2. It has been widely demonstrated for high resolution imaging of oral cavity, GI tract and urinary system and has recently been applied for diagnosis of breast tissue morphology of freshly excised *ex vivo* specimens [240, 244]. The system consists of a laser-scanning unit with source wavelength of 488 nm. Real time imaging is achieved using a 4 kHz oscillating mirror for horizontal line scanning and a galvanometric mirror for vertical scanning, resulting in a 2D raster pattern that is scanned across the surface of the fibre-bundle. pCLE images are acquired in a point-by-point manner at 12 fps.

The system can be integrated with flexible fibre-bundle probes with diameters ranging from 0.3 to 2.3 μm, and lateral resolution of 1.0 to 3.3 μm, depending on the distal optics. Such imaging probes use a distal GRIN lens to increase the penetration depth and custom microlens assembly to improve the spatial resolution, depending on the application. There is also a built-in mechanism, using proprietary algorithms, to correct for image distortion from fibre-bundle artefacts as well as additional capabilities such as mosaicking of multiple microscopic images.

3.4 Specimen handling

The specimen collection and handling protocol is shown in Fig.3.3. Small cut-outs from freshly excised breast specimens following mastectomy were acquired from the histopathology laboratory in Charing Cross Hospital. The neoplastic tissue was obtained from macroscopically visible tumour site and the normal tissue was obtained from macroscopically visible normal region (~30 mm away from tumour site). The fresh tissue specimens were transported to St. Mary's Hospital on ice for endomicroscopic examination within 1 hour

Figure 3.2: Commercial Cellvizio probe-based confocal laser endomicroscopy imaging system (Cellvizio; Mauna Kea Technologies, Paris, France).

of excision and imaged straight-away. The frozen tissue specimen cut-outs of ∼10×10 mm were obtained from Imperial College tissue bank database and thawed at room temperature for 5 minutes before imaging.

A standard protocol was followed for the endomicroscopy measurements and maintained for all the samples in this study. Prior to image acquisition, the cut-outs (fresh and frozen) were first immersed in test tubes containing acriflavine hydrochloride solution at 0.02% concentration. The fluorescent agent was left to stain the tissues for 1 minute and then gently rinsed with water to wash off excess fluorescent agent. The tip of the microscope probe was gently navigated onto the tissue surface and images were obtained in real-time.

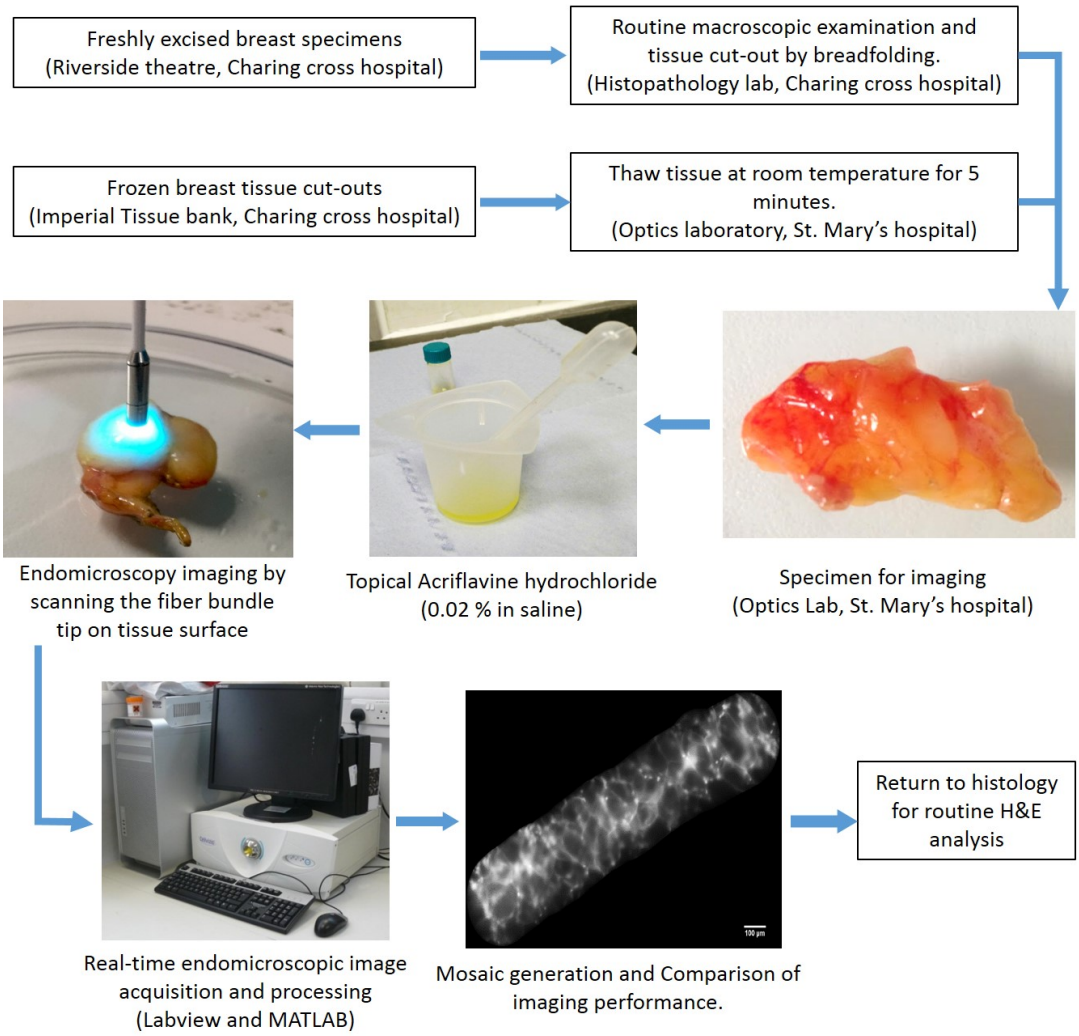

Figure 3.3: Specimen collection and handling protocol for examining un-fixed and acriflavine stained breast tissue specimen using LS-CLE system.

Endomicroscopy video loops were recorded for about 30 seconds from 2-6 sites depending on the size of each sample. The acquired LS-CLE images were stored digitally in a prospectively maintained database. Following this, pCLE images were also acquired from the same specimens for comparisons with LS-CLE images.

At the end of the imaging, excess fluorescent agents was gently wiped off the tissue surface. The tissue cut-outs were placed in labelled formalin pots and sent to Charing Cross Hospital for standard hematoxylin and eosin (H&E) staining and examination by an experienced pathologist blinded to the endomicroscopy imaging results. The histopathology report of each site was considered to be the gold standard.

3.5 Data processing

For both LS-CLE and Cellvizio systems, a post-processing step to remove the fibre-bundle pixelation artefacts followed by video mosaicking to create larger field of view images was implemented. For the Cellvizio system, ImageCell - Cellvizio's acquisition software was used to acquire images. The Cellvizio viewer's pixelation removal and video mosaicking functions were used to create automated mosaics. For the LS-CLE system, a Labview based GUI was used to acquire and record images in real-time. The acquired images were processed offline in Matlab. The image processing framework has been developed by Dr. Michael Hughes and Dr. Petros Giataganas and details are presented below.

3.5.1 Removal of fibre-pixelation artefacts

A Delaunay triangulation based approach similar to that described by Le Goualher et al., where a regional maxima algorithm was adopted to estimate the core centroids of all intact fibres [183]. To segment the individual cores, a mesh based on Delaunay triangulation was created around the fibre cores. For each pixel, the enclosed triangle was identified and corresponding barycentric coordinates ($b_1,\ b_2,\ b_3$) were stored in a look-up table. To reconstruct subsequent images each pixel was assigned a value I_p by interpolation of the scattered data on a uniformly spaced rectilinear grid:

$$I_p = b_1 I_{core,1} + b_2 I_{core,2} + b_3 I_{core,3} \tag{3.1}$$

where $I_{core,i}$ is the intensity value of the core at vertex i.

To account for variations in illumination intensity and coupling efficiency of the different fibres, an intensity correction method was implemented as a final step of pre-processing. Flat-field correction is a commonly used approach for this task. First, several images of a blank field (containing no cellular or fluorescent material) were collected using identical exposure times and acquisition settings as if one were collecting images of tissue. The average of these images was calculated which served as the dark-field frame 'I_D'. Next, a flat-field image frame 'I_F' is obtained similarly by shining light on a uniform fluorescent test target (Thorlabs, VRC2SM1). The intensity corrected image 'I_C' was obtained using the following formula:

$$I_C = \frac{(I_R - I_D)}{(I_F - I_D)} * M \tag{3.2}$$

where 'I_C' is the intensity-corrected image, 'I_R' is the raw acquired image, 'I_F' is the flat-field image, 'I_D' is the dark-field image and 'M' is the averaged intensity value of '$(I_F - I_D)$'.

3.5.2 Video mosaicking

A mosaicking algorithm was implemented, whereby overlapping frames were merged together into a single large-field image representing part of a 3D scene. For endomicroscopy interventions, the mosaicking algorithms are primarily used to stitch together endomicroscopy video frames and generate a wide FOV image while still maintaining microscopic resolution. This helps make a conclusive malignancy diagnosis from the acquired video sequences that could be compared to histological slides for cancer diagnosis.

For real-time applications, a fast normalised cross-correlation (NCC) algorithm was used for pair-wise image registration based on template matching. The primary intent behind using the fast NCC is to use fast fourier transform (FFT) to evaluate, in one pass, the correlation coefficient between consecutive image frames I_k and I_{k+1}. A 2D correlation map is generated using:

$$C_{NCC}(u,v) = \frac{\Sigma(I_k(x,y) - \bar{I}_k)(I_{k+1}(x-u, y-v) - \bar{I}_{k+1})}{\Sigma(I_k(x,y) - \bar{I}_k)^2 + \Sigma(I_{k+1}(x-u, y-v) - \bar{I}_{k+1})^2} \tag{3.3}$$

where $\bar{I}_k$ is the average pixel value of the image I_k, x, y are pixel co-ordinates and u, v is the translational shift.
Translational shift is obtained from the location of the maximum correlation peak in the 2D correlation map, and is given by:

$$\hat{C}(I_k, I_{k+1}) = arg\ max(C_{NCC}(u,v)) \tag{3.4}$$

To further optimise the estimation of translational shift and alleviate the lack of symmetry of the NCC algorithm, we adopt a scheme of averaging the forward and backward estimation of correlation coefficient proposed in [221] and given as:

$$\hat{C}^S(I_k, I_{k+1}) = \frac{\hat{C}(I_k, I_{k+1}) - \hat{C}(I_{k+1}, I_k)}{2} \tag{3.5}$$

While mosaicking, a threshold was set on the pair-wise NCC coefficient value $\hat{C}^S$ such that every time it would fall below 0.9, a new mosaic was reconstructed. This resulted in multiple high quality mosaics from each imaging site. Due to high NCC value, each mosaic consists of contiguous and partially-overlapping image frames.

As the final step, a weighted-average feathering function for image blending was implemented to reconstruct an output mosaic with minimum visible seams. Weighted-average feathering with distance map allows image blending by weighting the pixels near the centre of the overlapping region more heavily and down-weighting pixels at the edges. To further improve the quality of final mosaic and minimise the ghosting artefacts, distance map values raised to power of 8 were used to obtain seam-free mosaics.

3.6 Image analysis

3.6.1 Evaluation of mosaic quality

Since fibre-bundle endomicroscopy is a contact based imaging system, the image mosaicking quality is dependent on speed and consistency with which the fibre-bundle probe is scanned on the tissue surface. Especially for free-hand scanning, factors like probe motion, contact force as well as tissue deformation influence the quality of the acquired image. Further, the quality is also affected by the staining agent concentration. If the concentration is low, not enough photons are excited and the image has poor contrast whereas for high concentrations the images appear over-saturated. A noticeable degradation in image quality is evident when the probe loses contact from the tissue surface resulting in blank or partially-blurred images, with very few detectable features. Some representative poor quality image mosaics are shown in Fig.3.4. It is important to remove such degraded and sub-optimal images as that would affect the overall diagnostic performance of the system.

An image classification framework was developed to quantitatively measure the image quality and classify the mosaics as 'Good' and 'Bad' mosaics. The loss of sharpness/blur observed on the LS-CLE images due to sub-optimal probe-tissue contact was quantified by processing the images using multiple blur-based imaging criteria. Three image metrics namely Shannon's entropy (a measurement of amount of information/content present in an image), blur annoyance metric by Crété-Roffet et al. [246] (a nonreference perceptual blur metric obtained by blurring the image and comparing the variations between neighbouring pixels before and after low pass filtering) and speeded up robust features (SURF) descriptor [247] (using integral images for image convolutions and Fast-Hessian detector) were chosen on the basis of computational expense, the range of observed values, monotonicity, sensitivity to noise and ability to handle outliers.

Since no single metric satisfied all the requirements, a combined classifier was developed to define an overall metric for image quality assessment. The acquired data was first separated into training datset set (10 specimens, 320 mosaics) and study sets (33 specimens, 970 mosaics). All the image mosaics were manually classified as 'Good' and 'Bad' based on visual inspection and consensus between two people and then the three quality parameters were evaluated. Based on the training dataset, if either [SURF$<$ 130 OR blur $<$ 0.25 OR entropy$>$ 4.6], the mosaic was classified as 'Bad' mosaic. This initial classifier resulted in an accuracy of 78.3% for the entire dataset.

While this initial test was able to detect poor image mosaics due to lost tissue contact, over saturation or probe motion, it was not capable to identify images which were partially blurred due to inadequate probe-tissue contact, like Fig3.4(b). To improve the overall performance, the classifier was further optimised to detect sub-optimal images using a

second criteria: [SURF< 230 AND entropy> 3.8], yielding an improved accuracy of 97.4% over the entire dataset.

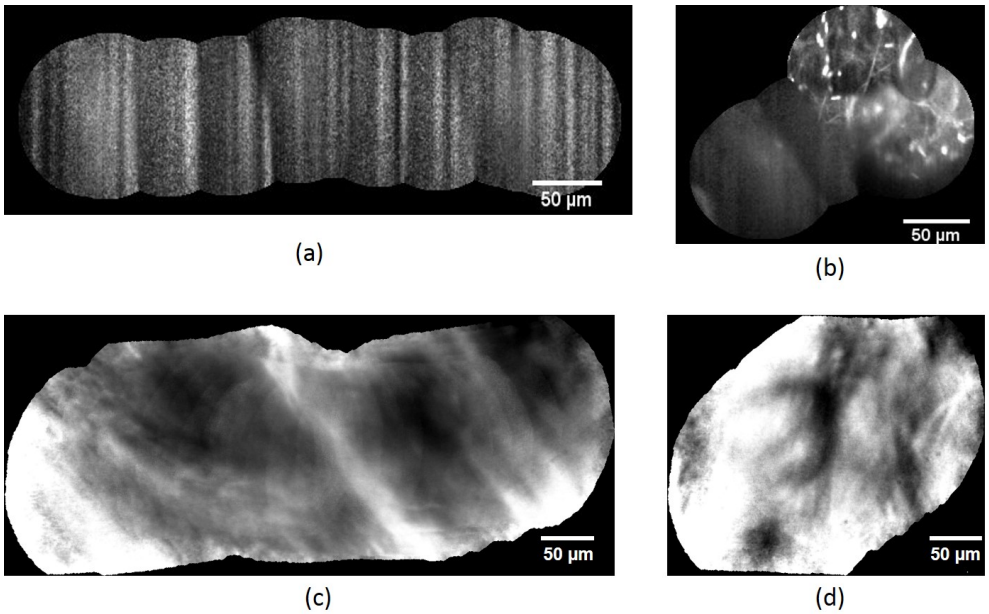

Figure 3.4: Representative poor quality image mosaics acquired using LS-CLE (top row) and Cellvizio pCLE (bottom row) due to (a) and (b) lost probe-tissue contact, (c) probe motion artefacts and (d) over saturation due to high concentration of staining agent.

3.6.2 Evaluation of mosaic length

The length of the mosaics that are classified as 'Good' using the image classifier framework are evaluated. The top three longest 'good' mosaics from each specimen are retrieved for comparison. The longest mosaic is defined as the maximum length extending along either horizontal or vertical axis of the image mosaic.

3.7 System characterisation

Before imaging breast tissue, the LS-CLE imaging system was tested on non-biological targets. The lateral resolution of the systems was measured by imaging a 1951 USAF resolution target back-illuminated by a green LED, see Fig.3.5(a). The smallest features the system could resolve were those of group 7, element 6, corresponding to a frequency of 228 lp/mm, or bar width of 2.19 μm. This closely resembles the sampling-limited spatial resolution of 2.2 μm due to inter-core spacing of the fibre-bundle as explained in Section 3.3.1.

The axial depth sectioning strength of LS-CLE was measured by removing the emission filter and measuring the reflectance signal from a mirror. Optically sectioned LS-CLE images were obtained by reducing the exposure to 30 μs which is equivalent to $\sim$2.5 μm slit width. The distal probe tip was initially placed in contact with the mirror and then driven away in the axial direction using a motorised translation stage. Images were acquired for every 0.1 μm axial shift. The average intensities from a 25 $\times$ 25 μm region in the centre of each image are plotted as a function of distance in Fig.3.5(b). Averaged across 10 experimental measurements, the half width half maximum (HWHM) of the LS-CLE was 5.1$\pm$0.1 μm.

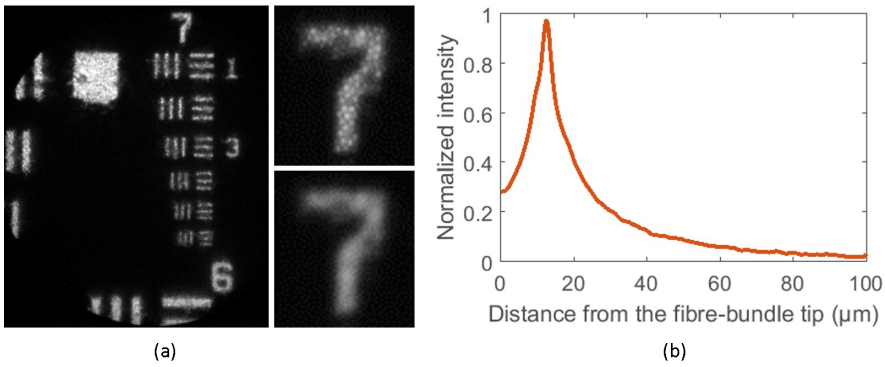

Figure 3.5: Image of high-resolution USAF resolution target showing group 7 elements 1-6 when back-illuminated with a red LED. Insets show zoomed in image of letter '7' before and after image processing to remove pixelation artefacts. (b) Axial sectioning profile for LS-CLE system with slit-width of 2.5 μm.

3.8 Results

3.8.1 Morphological classification of breast tissue using LS-CLE system

Multiple tissue types were imaged to provide images which are closer in quality to conventional histopathology examination. For this study 43 tissue specimens were collected from 35 patients, comprising of 25 non-neoplastic and 18 neoplastic tissue specimens, see Table 3.2. Out of the 43 specimens, 26 were frozen specimens (15 non-neoplastic and 11 neoplastic) and the remaining 17 were freshly excised following either mastectomy or BCS. The specimens belong to five histopathological categories: IDC (12 specimens), DCIS (6 specimens), fibroadenoma (8 specimens), normal stroma (6 specimens) and adipose tissue (9 specimens). For each specimen, imaging was performed three times at different imaging sites, and the mean duration of endomicroscopy imaging for each sample was about 5 minutes.

A total of 1290 endomicroscopy mosaics (average of 10 per each imaging site) were generated by slow and controlled hand-held manipulation of fibre-bundle tip on the tissue surface. After LS-CLE imaging, the samples were put in labelled formalin pots and corresponding histopathology images were obtained by thinly slicing it, staining with H&E and imaging using a conventional microscope. All the generated mosaics were assessed and their morphological features were visually compared with that on the corresponding histology slides, regardless of their image quality.

Table 3.2: Histological breakdown of fresh and frozen specimens used in this study.

Specimen pathology	**Number of patients**	**Number of specimens**	**Number of mosaics**
All specimens	35	43	1290
Non-Neoplastic	20	25	726
Neoplastic	15	18	564
Freshly excised specimens	10	17	495
Non-neoplastic	6	10	290
Neoplastic	4	7	205
Frozen specimens	25	26	795
Non-Neoplastic	14	15	475
Neoplastic	11	11	320

LS-CLE example mosaics of each non-neoplastic (normal and benign) and neoplastic tissue type in comparison to their histological counterparts are presented in Fig.3.6 and Fig.3.7 respectively. All of the 1290 acquired mosaics were analyzed to develop a list of essential descriptive morphological features to discern normal, benign and malignant LS-CLE images of breast tissue, as presented in Table 3.3. The analysis included 133 adipose, 118 normal stroma, 144 both normal adipose and stroma, 91 normal glandular tissue, 65 fibrocystic changes, 175 fibroadenoma, 155 DCIS, 322 IDC and 87 both DCIS and IDC mosaics. For each mosaic, correlations with histology slides was made based on visual inspection and morphological features were identified and described as follows.

On LS-CLE, the nuclei appear as bright hyperfluorescent dots. The adipose tissue appeared as well-defined and uniform black non-fluorescent oval or polygon shape with hyper-fluorescent borders and sparsely populated nuclei as bright spots along the borders, Fig.3.6(a). Normal glandular tissue appeared as small oval shape or floret like structures with a thin lining of bright epithelial cells and a well-defined dark lumen, Fig.3.6(b,c). The fibrous connective tissue appeared as well-defined hyper-fluorescent bundles of elastic wavy fibres, Fig.3.6(d). The collagen fibres appeared as grey fibres with parallel strands and were moderately stained, Fig.3.6(e). Normal tissue with sparse oval bright spots corresponding to fibroblast nuclei in the stroma is shown, Fig.3.6(f).

The fibroepithelial lesions are the most common benign breast tumours with uniform fibroblastic stroma surrounding well-defined, intact and sometimes compressed ductal spaces, Fig.3.6(g). In fibroadenomas, some form of hyperplasia is mostly found. On fluorescence endomicroscopy images, the increased nuclear density in the stroma and intact, oval and large ductal spaces with clear gland-stroma interface were visible, Fig.3.6(h). Another benign condition is fibrous scarring representing dense and compact fibrous connective tissue. Its corresponding LS-CLE image showing grey and dense fibre like structures in stroma is shown in Fig.3.6(i).

In-situ carcinomas like DCIS were observed to have a similar appearance to fibroadenoma on LS-CLE imaging. Both have a thickened epithelium with areas of increased nuclear density. However, for DCIS there is often a loss of distinction between glandular and stromal tissue as shown in Fig.3.7(a,b). LS-CLE images of invasive cancers are characterised by unorganised distribution of nuclei and unclear tissue architecture resulting in no identifiable features in the stroma and the glands. The structure and size of the adipose tissue remains unaltered, however, an increase in cellularity is observed at their borders, Fig.3.7(c). In IDC, hyper-fluorescent clusters of nuclei with no-defined shape are observed to completely obscure the distinction between the stroma and the glandular structures, Fig.3.7(d). Fig.3.7(e) demonstrates another invasive carcinoma type called spindle cell carcinoma, where the nuclei appear as bright spots having elongated shapes.

From Table 3.2 and representative images presented in Figs.3.6 - 3.7, it is observed that various normal and neoplastic breast tissue pathologies can be identified and visually distinguished qualitatively using LS-CLE. Further, the identified features qualitatively correlate well with standard histology images. The descriptive morphological features summarized in Table 3.3 will be used for the breast radial margin assessment study presented in Chapter 4.

3.8.2 Comparison with commercial system

This section presents comparative imaging results of 20 non-neoplastic and malignant breast specimens that are imaged using LS-CLE and commercial Cellvizio pCLE system. Overall, 352 mosaics were generated from both the systems and assessed for their diagnostic accuracy. The details of the histopathological distribution of the tissue sites are summarised below in Table 3.4.

Figs.3.8 - 3.11 contain three images that are acquired *via* different imaging modalities: Cellvizio pCLE systems, high-speed LS-CLE system and its corresponding histopathology image. The histopathology image is obtained by thinly slicing the sample, staining it with H&E and imaged using a conventional microscope. Each figure shows images that were obtained from the same tissue sample. It is to be noted that since the endomicroscopy imaging experiments are carried out using hand-held probes with different optical systems, imaging of the same region of interest is not guaranteed at all times.

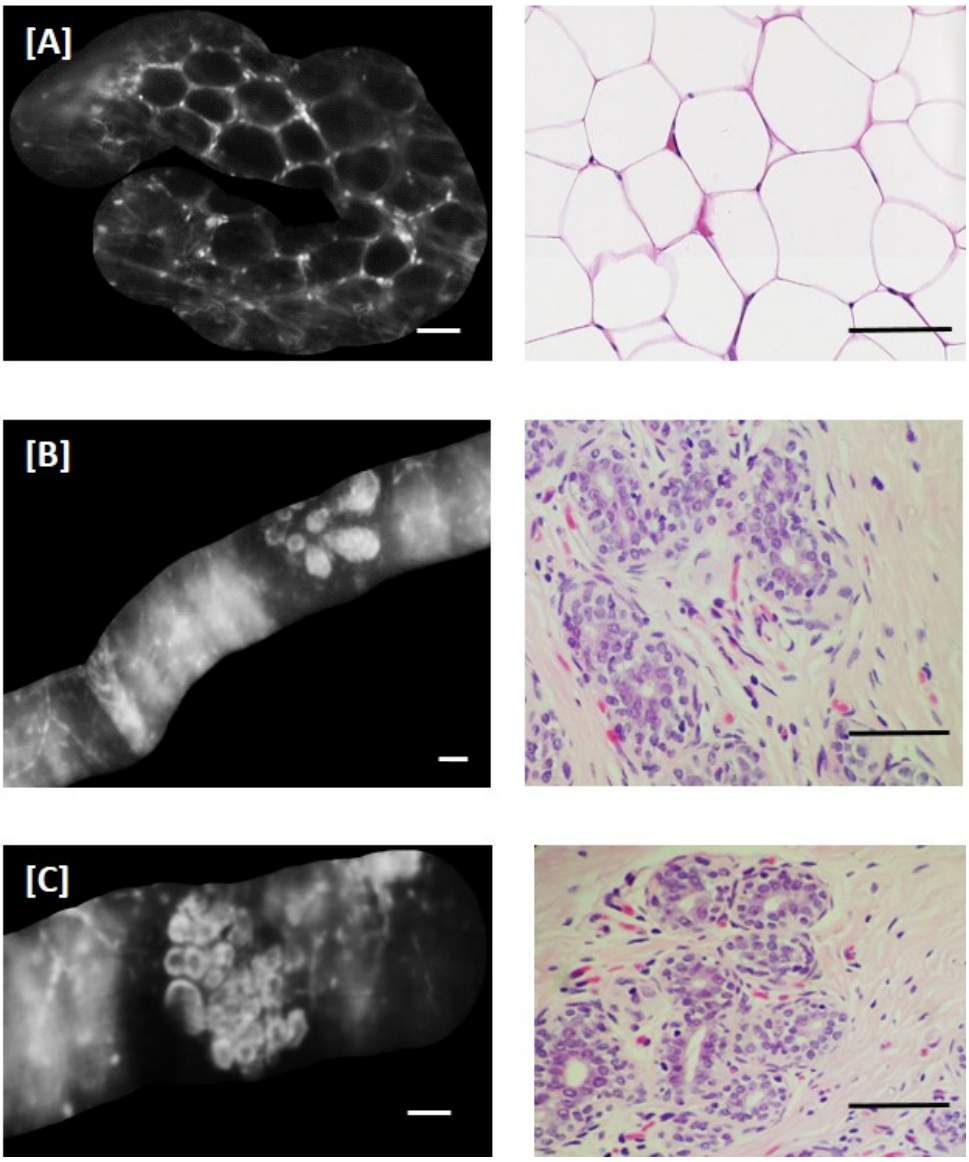
[A]
[B]
[C]

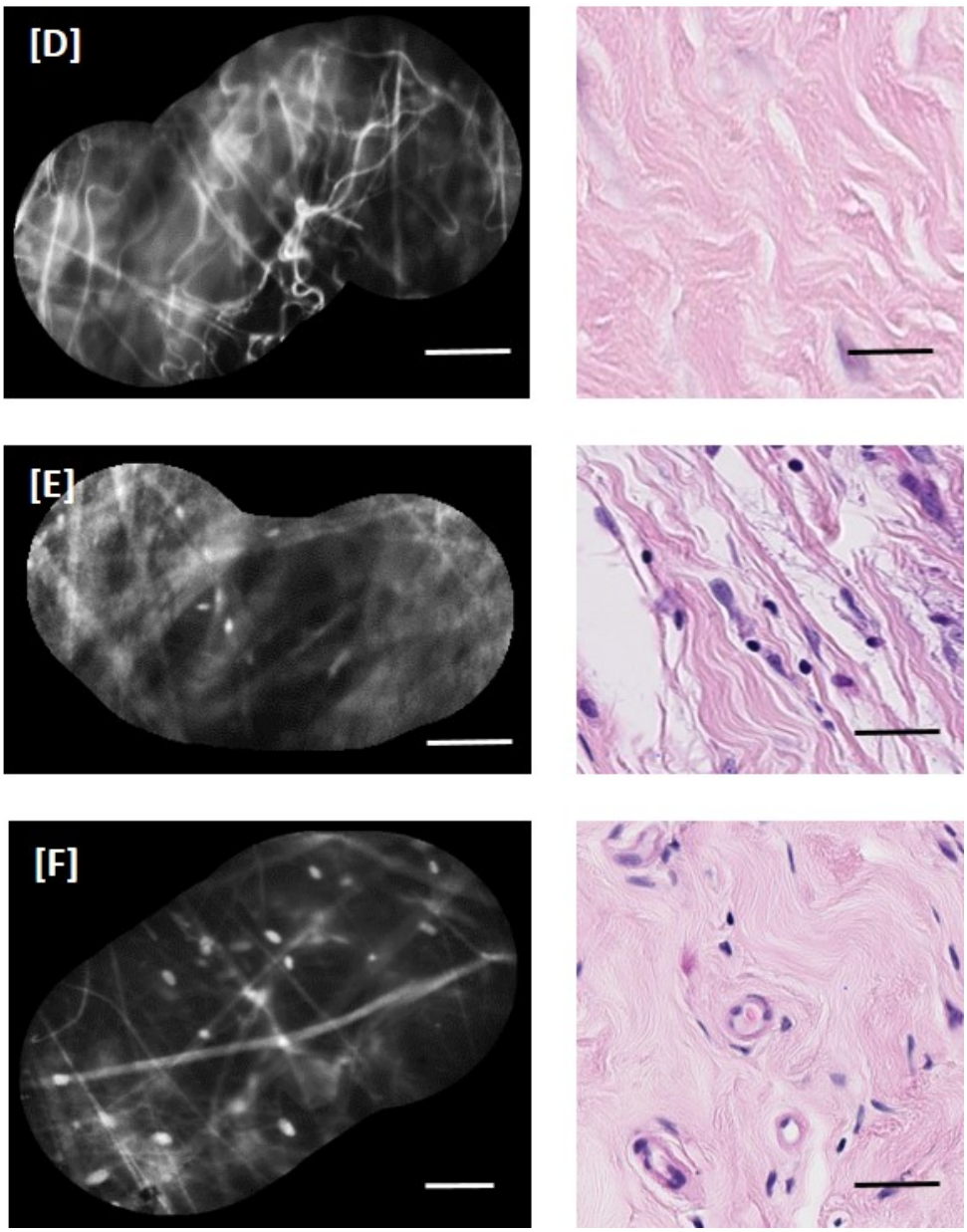
[D]
[E]
[F]

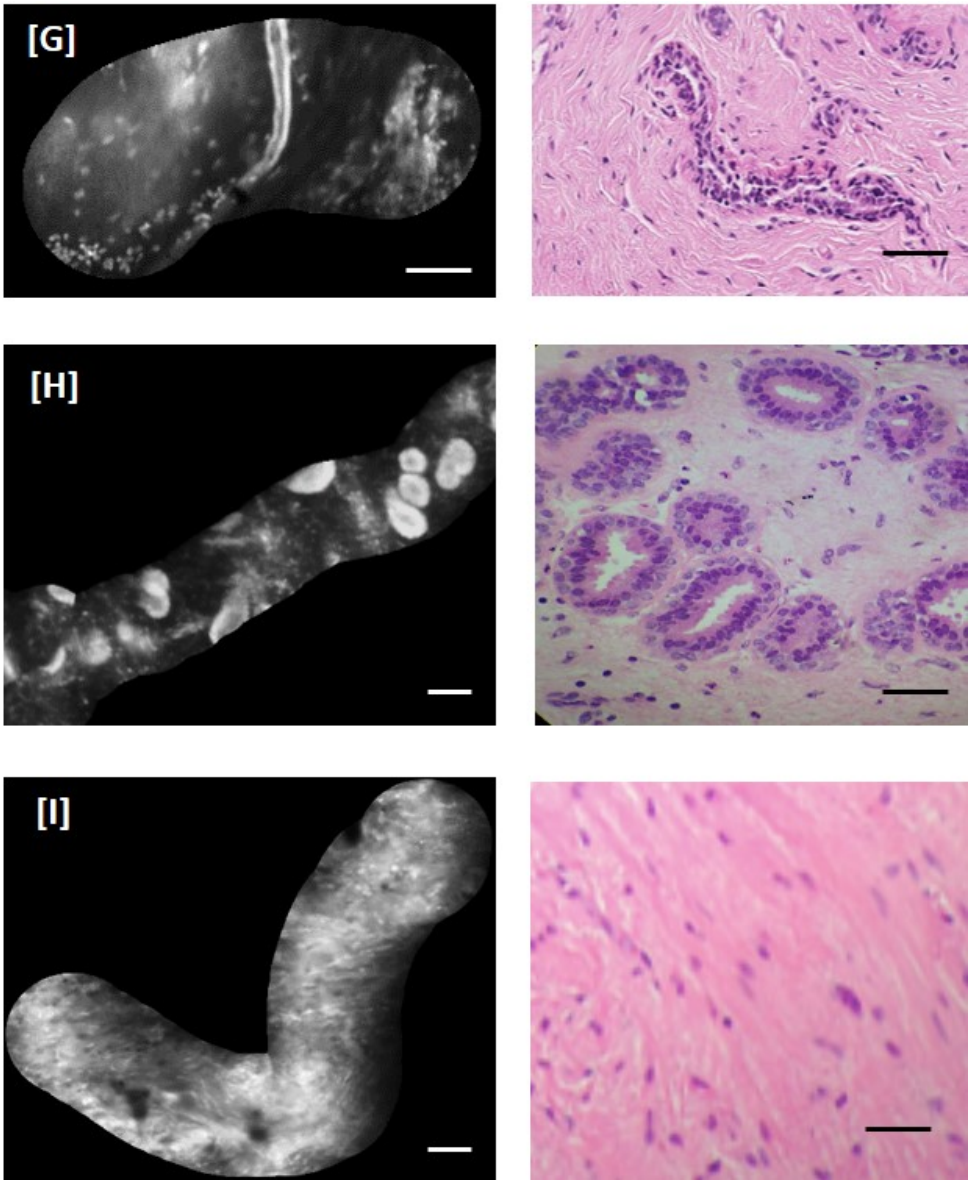

Figure 3.6: Each image depicts morphological appearance of non-neoplastic breast tissue on LS-CLE image (left) and histology image (right): [A] adipocytes. [B] ducts and [C] lobules having a floret-like appearance with well defined dark lumen, [D] Elastic fibres, [E] collagen fibres and [F] fibroblast nuclei in normal stroma. [G-H] depict benign breast conditions of [G] dilated and compressed ducts, [H] fibroadenoma and [I] fibrous scarring. Scale bar is 50 μm.

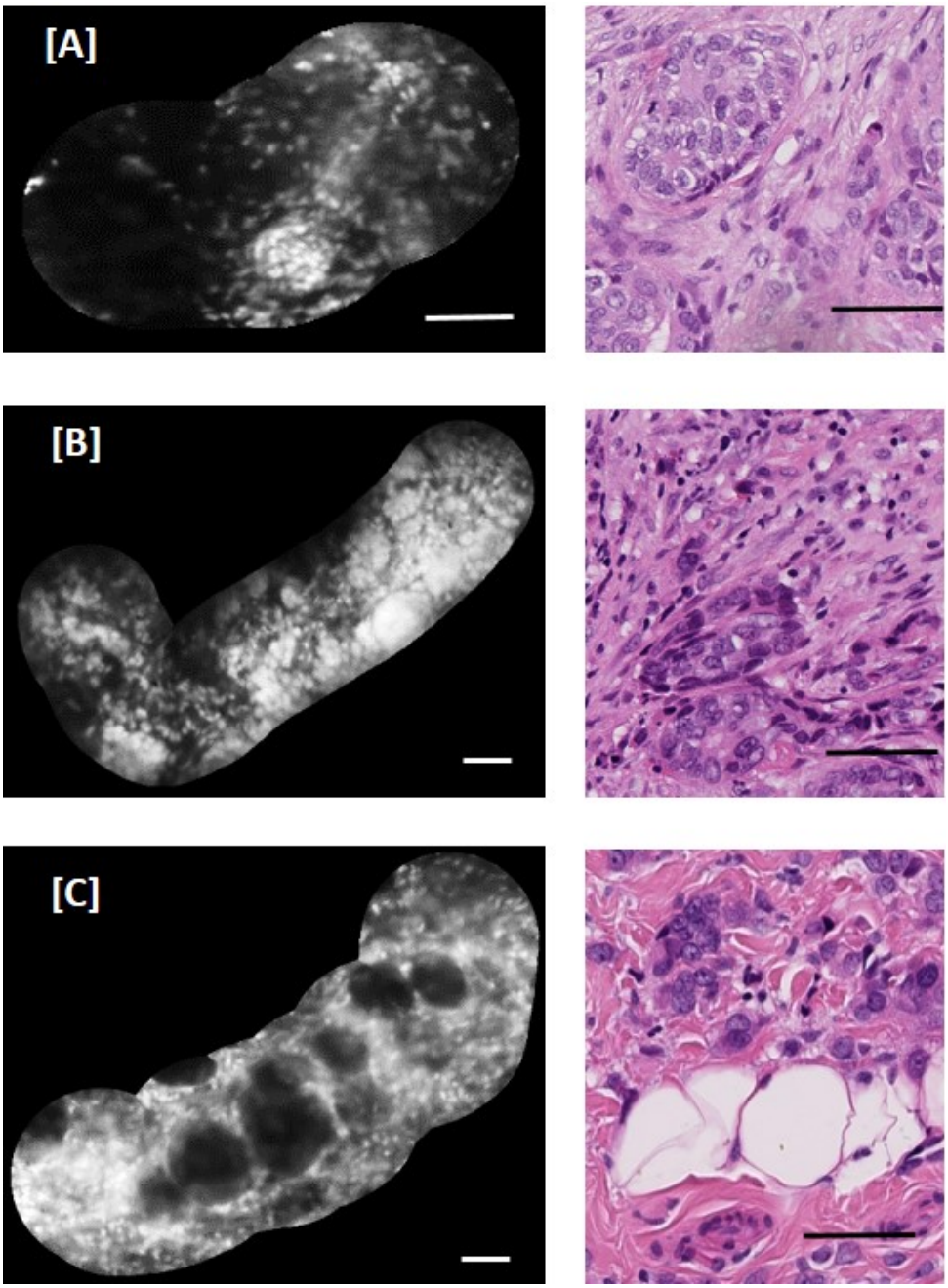
[A]
[B]
[C]

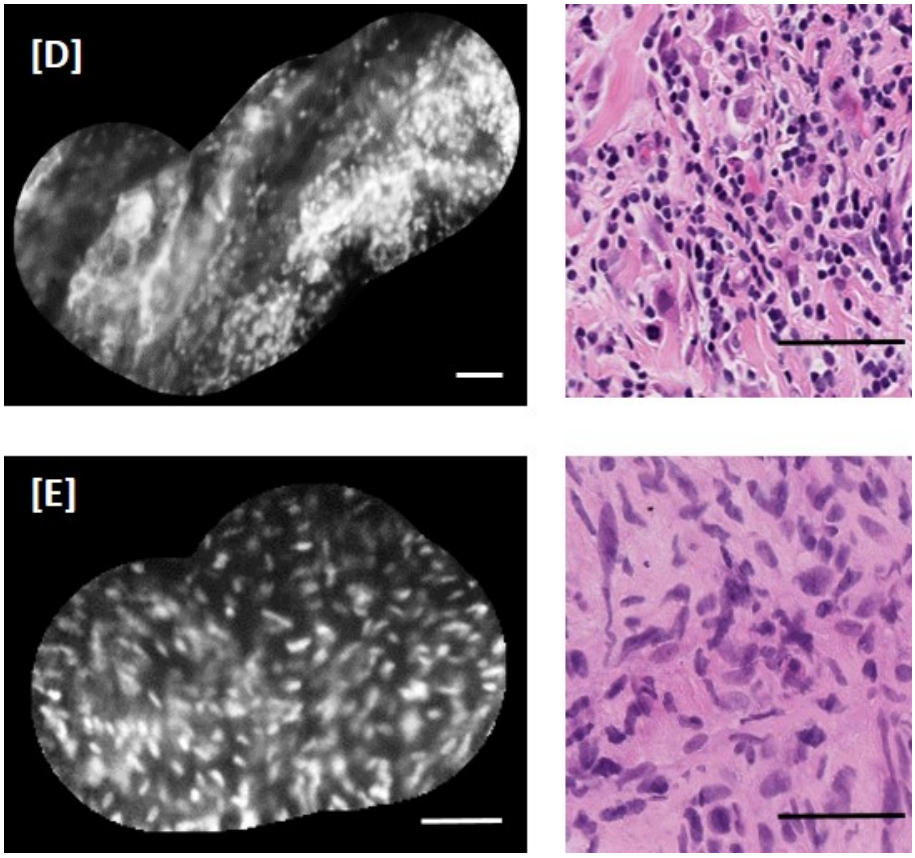

Figure 3.7: Each image depicts morphological appearance of neoplastic breast tissue on LS-CLE image (left) and histology image (right): [A] DCIS, [B] IDC with DCIS, [C] Invasive cancer infiltrating into fat cells, [D] IDC and [E] spindle cell carcinoma. Scale bar is 50 μm.

As a result, selection and identification of cellular features and tissue micro-architecture is made to provide a practicable means for system comparison. LS-CLE image mosaics are visually compared to pCLE mosaics using Cellvizio, demonstrating similar architectural features and image contrast for different non-neoplastic and neoplastic breast tissues.

3.8.3 Imaging performance assessment results

The image quality of 352 mosaics are assessed based on the image classification framework developed in Section 3.3. For the LS-CLE system, from a total of 165 image mosaics, 109 mosaics (66%) were classified as 'good' mosaics and 56 mosaics (34%) were classified as 'bad' mosaics. On taking a closer look it was identified that amongst the 56 bad LS-CLE mosaics, 22 mosaics were poor quality due to lost probe tissue contact where no imaging features were clearly visible and 34 mosaics were sub-optimal due to partially-blurred images in which some features were observed but not clearly discernible.

Table 3.3: Description of essential morphological features corresponding to non-neoplastic and neoplastic pathologies on LS-CLE images

Specimen pathology	Morphological features
NON-NEOPLASTIC	
Normal	
Adipose tissue	Dark polygonal structures with hyperfluorescent borders and spare peripheral nuclei.
Stromal tissue	Spare and uniformly distributed fibroblast nuclei that appear as bright dots in the stroma. Elastic and collagen fibres organised as fluorescence wavy bundles
Glandular tissue	Small floret like structures with a thin hyperfluorescent layer of epithelial and myoepithelial cells and a dark lumen.
Benign	
Fibrocystic changes	Size of ductal structures increases (>50 μm), however there is a clear distinction between glandular and stromal components. The population of fibroblast nuclei and fibrous connective tissue increases in the stroma, sometimes pushing the ducts into elongated slit-like shapes.
Fibroadenoma	Thickening of the epithelium of ductal structures however there is a clear distinction between glandular and stromal tissue.
NEOPLASTIC	
***In-situ* carcinoma**	Size of ductal structures increases (>50 μm) and the stromal-glandular interface is disrupted. The luminal intensity is greatly increased.
Invasive carcinoma	Distorted tissue architecture with no definable features. Little stroma dividing islands of cancerous cells. Increased nuclear density with haphazard orientation.

For Cellvizio pCLE, a total of 187 image mosaics were generated, out of which 125 mosaics (67%) were classified as 'good' mosaics and 62 mosaics (33%) as 'bad' mosaics. Amongst the 62 mosaics classified as 'bad', only 5 mosaics had no detectable features due to lost tissue contact. 57 mosaics had poor contrast and sub-optimal quality due to inadequate contact, resulting in blurred or fuzzy images or over-saturation due to excess stain. Following the image quality assessment, the mean length of image mosaics of three longest 'good' mosaics obtained using LS-CLE and Cellvizio were evaluated. Comparisons were also made between mosaic lengths of fresh and frozen tissue specimens, see Fig.3.12.

Table 3.4: Histological breakdown of tissue specimens used in this study, along with number of mosaics generated.

Specimen pathology	**Number of samples**	**Number of mosaics**
All specimens	20	352
Mastectomy	17	269
Excision of Breast mass	3	83
Non-neoplastic specimens	13	267
Normal	8	157
Benign breast disease (BBD)	5	110
Neoplastic specimens	7	85
Invasive ductal carcinoma (IDC)	7	85

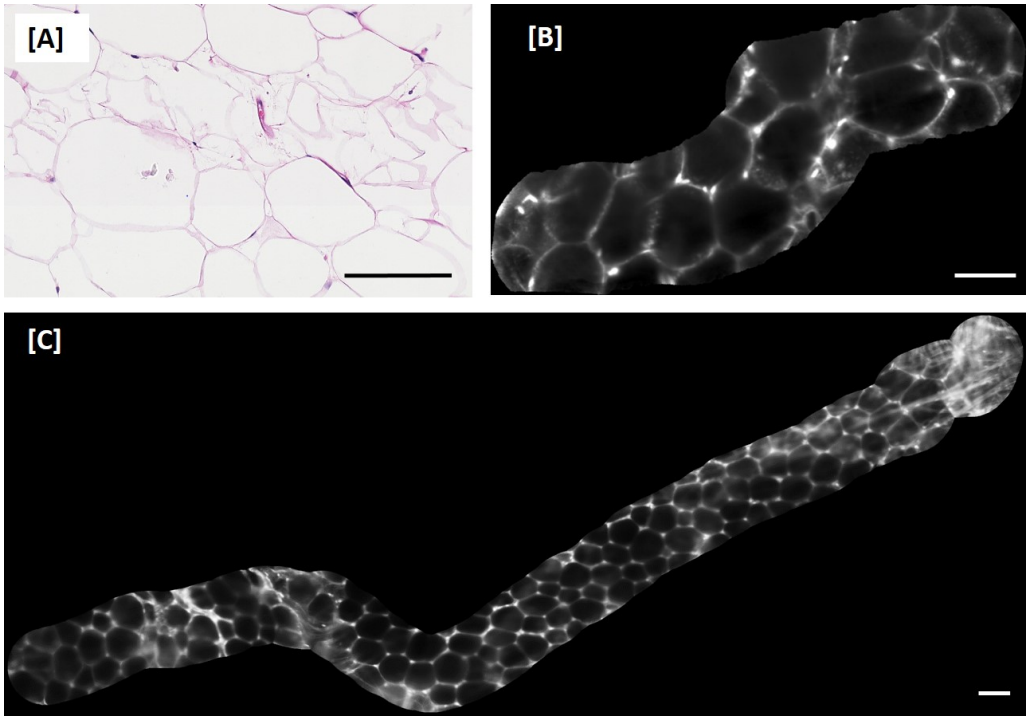

Figure 3.8: Normal adipose tissue from a breast tissue specimen imaged with (a) The conventional histopathology, (b) Commercial Cellvizio preclinical system and (c) High-speed line-scan confocal laser endomicroscope. Adipose cells appear as dark polygon shapes with bright and well defined borders. Scale bar is 100 μm.

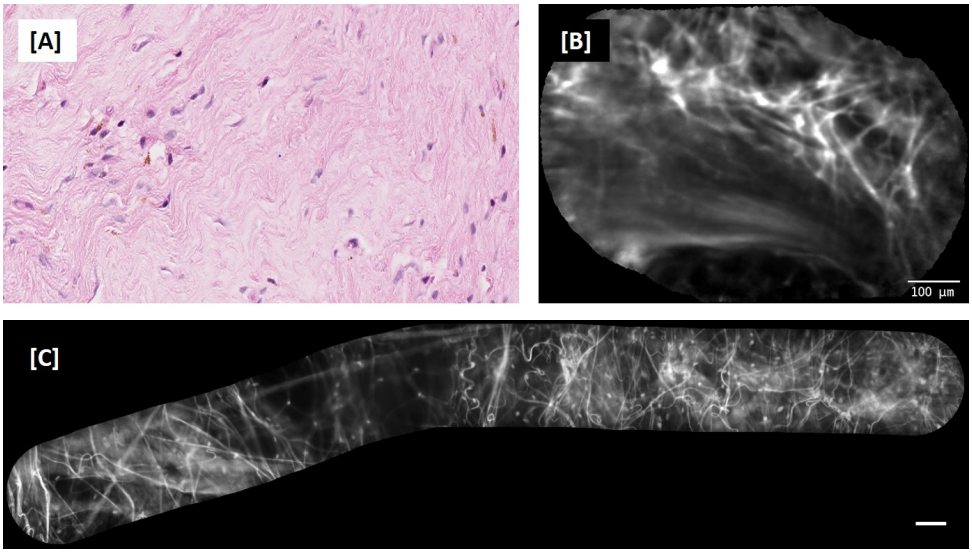

Figure 3.9: Hyper-fluorescent bundles of elastic wavy fibres in normal breast tissue specimen imaged with (a) The conventional histopathology, (b) Commercial Cellvizio preclinical system, (c) High-speed LS-CLE system. Scale bar is 100 μm.

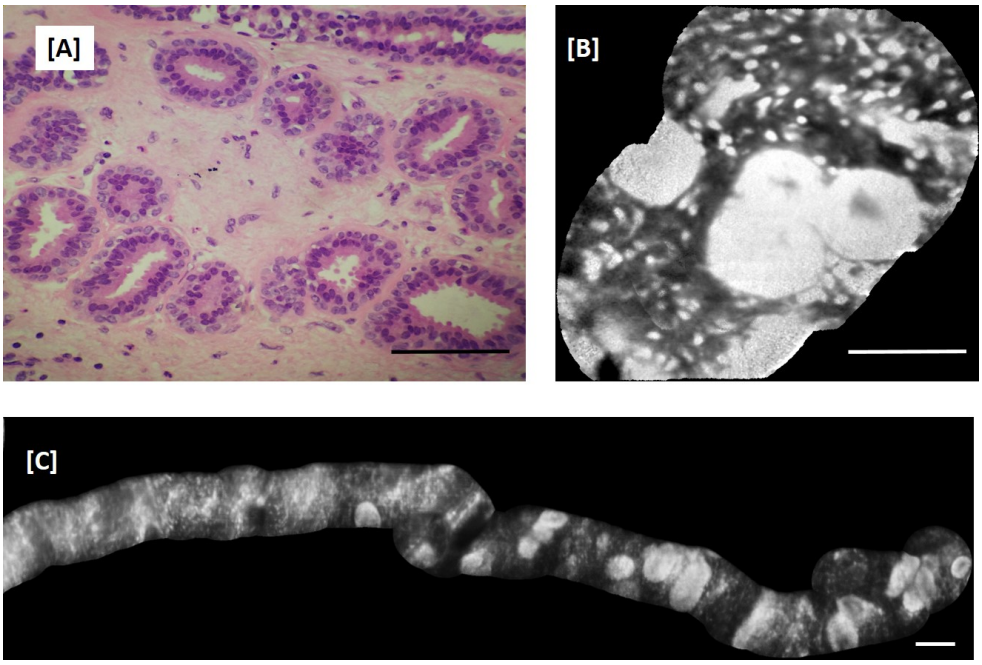

Figure 3.10: Fibroadenoma with large duct spaces marked by thick epithelium and dark lumen imaged with (a) The conventional histopathology, (b) Commercial Cellvizio preclinical system, (c) High-speed LS-CLE system. A good discrimination between glandular and stromal components is evident for both Cellvizio and LS-CLE images. Scale bar is 100 μm.

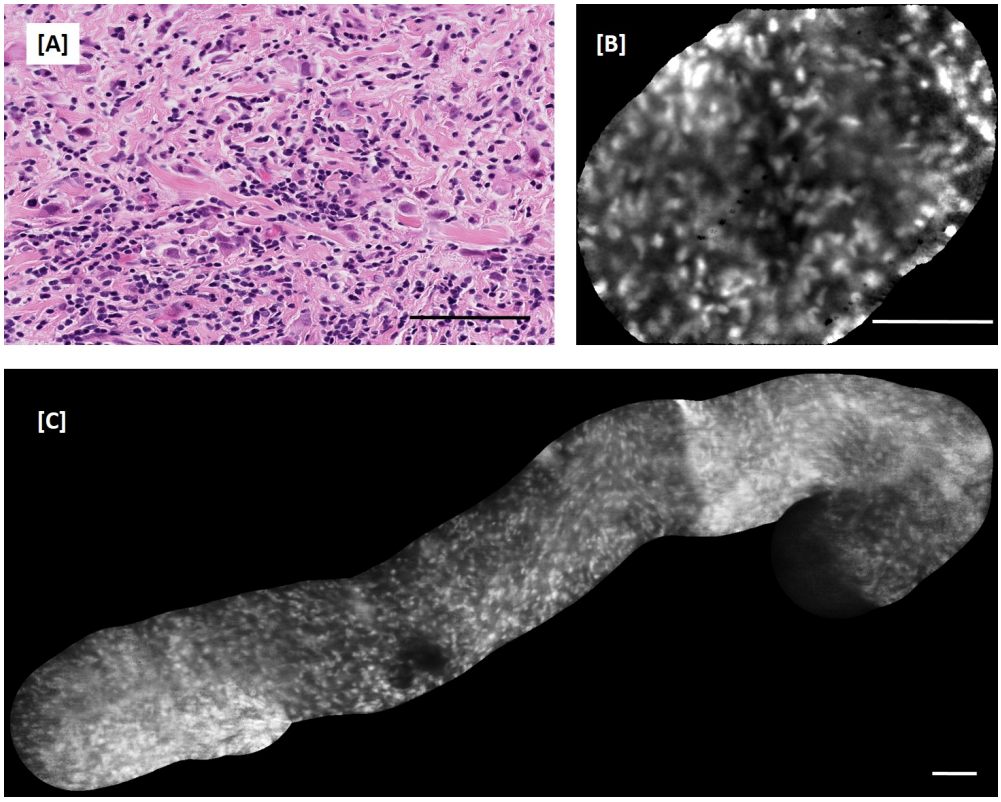

Figure 3.11: Invasive cancer represented by disorganised tissue structure with increased cellularity indicated by clusters of bright spots in breast tissue specimen. Images are obtained with (a) The conventional histopathology, (b) Commercial Cellvizio preclinical system, (c) LS-CLE system. Scale bar is 100 μm.

The reconstructed mosaic lengths were normally distributed for both LS-CLE and Cellvizio systems, as assessed by Shapiro-Wilk's test (p-value > 0.1, for chosen alpha level of 0.05). A two-sample t-test between each endomicroscopy modality was performed to assess for statistical difference between length of the generated mosaics. A p-value of < 0.05 was considered statistically significant. Statistical analysis was performed in SPSS (version 25, IBM). The mean length of LS-CLE image mosaics was found to be significantly longer than that of pCLE mosaics (1.72 mm + 0.4 *vs* 0.6 mm + 0.085; p = 0.0001). Further, the mosaic lengths of frozen samples were not significantly different to that of freshly excised specimens for both LS-CLE and Cellvizio systems (LS-CLE: 1.64 mm + 0.4 *vs* 1.7 mm + 0.5; p = 0.63) and (Cellvizio: 0.55 mm+ 0.09 *vs* 0.61 mm + 0.07; p = 0.24).

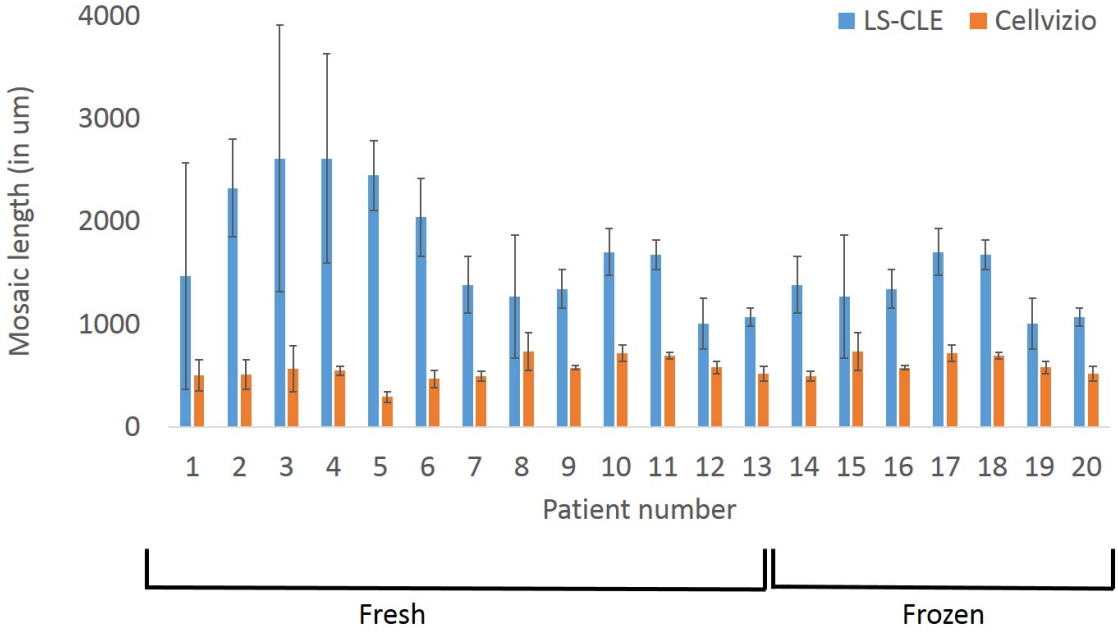

Figure 3.12: Comparison of the length of mosaics generated using LS-CLE system (blue bars) and Cellvizio pCLE (orange bars) for 20 patients. The mosaics generated using LS-CLE were significantly longer than those estimated using pCLE system for fresh as well as frozen specimens.

3.9 Discussion

LS-CLE has the potential to allow surgeons to image tissue morphologies at microscopic resolution and an image acquisition speed of 120 fps. In this chapter, the feasibility of using LS-CLE for breast tissue imaging is demonstrated using 488 nm laser source and topical acriflavine staining. For this study, 43 tissue specimens were collected from 35 consenting patients, comprising of 25 non-neoplastic and 18 neoplastic tissue specimens. A total of 1290 endomicroscopy mosaics were generated by slow and controlled hand-held manipulation of fibre-bundle tip on the tissue surface. This included 133 adipose, 118 normal stroma, 144 both normal adipose and stroma, 91 normal glandular tissue, 65 fibrocystic changes, 175 fibroadenoma, 155 DCIS, 322 IDC and 87 both DCIS and IDC mosaics. The acquired mosaics were used to develop a list of essential descriptive morphological features to discern normal, benign and malignant LS-CLE images of breast tissue. The findings indicated that a wide-range of normal, benign and neoplastic breast tissue pathologies could be identified using LS-CLE and qualitatively, the results visually correlate well with corresponding histology.

For a subset of 20 specimens, the LS-CLE imaging was compared with side-by-side point-scanning confocal imaging using commercial Cellvizio system. Imaging of freshly excised *ex vivo* specimens using Cellvizio pCLE was recently demonstrated by Chang et al. [244] and Palma et al. [240] using topical acriflavine and intravenous fluorescein staining agents respectively. The goal of this work was to evaluate whether images acquired using LS-CLE were comparable in terms of detectable features to that of Cellvizio.

With all 20 specimens imaged using both the endomicroscopy systems, when visually inspected, no significant discrepancies in the quality of images relating to different pathological states were observed. The spatial resolution, limited by the inter-core spacing of the fibre-bundle used, was also identical to be 2.2 μm. The axial resolution of LS-CLE was poorer than point-scanning confocal systems like Cellvizio [215], however, the semi-confocal optical sectioning was sufficient to image the tissue's epithelial surface where majority of the breast carcinomas originate.

The limited FOV due to the small size of the fibre-bundle reduced the amount of morphological features visualised. Image mosaicking techniques (stitching adjacent images next to each other as the probe moves) resulted in an increase in the effective image size, but required careful, slow and precise manipulation of the probe to ensure sufficient overlap between adjacent frames. For Cellvizio systems, which typically have image acquisition rates on the order of 10 fps, this was particularly found challenging. The high-speed LS-CLE system facilitated the acquisition of confocal images at frames rates up to 120 fps which is big improvement over the commercial Cellvizio systems. This allowed faster scanning of the tissue and generating large-area mosaics which otherwise was difficult to achieve. The mean length of LS-CLE image mosaics were significantly longer than that of pCLE mosaics (1.72 mm + 0.4 *vs* 0.6 mm + 0.085).

Factors like probe motion, contact force and stain concentration were found to affect the quality of reconstructed mosaics for both systems. By evaluating three image quality metrics, an image classification framework was developed to distinguish the 'good' mosaics with high contrast and detectable features from 'bad' sub-optimal mosaic reconstructions. The proposed image quality assessment framework resulted in an accuracy of 97.4% over the entire dataset, compared to manual visual assessment. About 34% of the reconstructed mosaics were found to be of sub-optimal quality for both systems.

3.10 Study limitations

There are several limitations to this study. Firstly, it is performed on small cut-outs of tissue specimens with *post-hoc* image evaluations performed in a controlled environment by a single user. It therefore does not take into account the challenges associated with intra-

operative probe deployment, probe scanning and tissue surface irregularity. Secondly, this is a feasibility study on small sample sizes which did not include invasive breast carcinomas such as ILC. To this end, efforts to include mastectomy specimens with these tumour types are currently underway.

3.11 Conclusion

The results demonstrate that LS-CLE offers a number of important potential advantages as an intra-operative imaging tool to evaluate breast tissue specimens. The system is portable and sample preparation is simple and rapid. High resolution images acquired using LS-CLE have microscopic resolution allowing evaluation of nuclear features and cell morphology which correlate to those observed in histology images. The high speed acquisition facilitates the reconstruction of large mosaics of the tissue surface which would be advantageous during scanning of large tissue specimens. The potential utility of LS-CLE platform for imaging radial margins of whole wide local excisions following BCS will be presented in the next chapter.

Chapter 4

Endomicroscopy for radial margin assessment during breast conserving surgery*

4.1 Introduction

BCS is often the treatment of choice for patients with early-stage breast cancer as it allows for complete tumour excision while still maintaining acceptable cosmesis. The goal of BCS is to remove tumour with a region of normal tissue surrounding it, such that the margins are tumour free. However, an unacceptably high number of BCS patients, 20-30%, require one or more re-operative interventions, mainly due to the presence of positive or close margins in post-operative histological analysis of the resected tissue [10, 29]. An imaging system that has sufficient imaging speed to scan the margins of whole WLE specimens and obtain high-resolution histology-like images of different breast pathologies, could substantially improve the detection of positive margins and subsequently reduce the BCS re-operation rates.

The potential of LS-CLE to image discernible changes between morphology of normal and neoplastic breast tissue has been demonstrated in Chapter 3. A striking advantage of LS-CLE systems over confocal endomicroscopes like Cellvizio and other microscopy platforms, is its ability to acquire semi-confocal images at high acquisition rates. This allows examination of large anatomical areas like the entire surface of surgically excised

* The contents of this chapter were presented as:
Vyas, K., Hughes, M., Leff, D. R., & Yang, G. Z. (2017). Microscale imaging of surgical margins in breast cancer using confocal laser endomicroscopy – a clinical study. (Conference Presentation-Oral), London Surgical Symposium.

specimens in a timely manner with microscopic resolution. While the preliminary results are promising, understanding whether endomicroscopy images obtained from *ex vivo* cut-outs (with specific tissue pathology) are representative of the margin features of whole WLE specimens is still to be explored and warrants further attention.

This chapter presents investigations on the use of LS-CLE for rapid *ex vivo* imaging and evaluation of margin status. Imaging is performed on freshly-excised whole surgical specimens stained with acriflavine, immediately following BCS. Selected areas on each margin are evaluated with overall imaging time restricted to 40 minutes from excision. The diagnostic accuracy of LS-CLE evaluation of margin status of freshly-excised specimens is assessed by comparing the endomicroscopic and corresponding histopathological features.

4.2 Methods

4.2.1 Imaging equipment and data acquisition

High resolution endomicroscopy images were acquired from multiple sites on each margin of the WLE specimen using the LS-CLE imaging system, operating at 488 nm. The LS-CLE system is compact and portable and can be easily used in the operating theatre and positioned close to the patient. A high resolution pre-clinical fibre-bundle imaging probe ColoFlex UHD from Cellvizio (Mauna Kea Technologies, France) with 2.5 mm outer diameter, FOV of 240 μm and Nyquist sampling resolution of 2.2 μm was integrated with the LS-CLE system and used for hand-held imaging. LS-CLE images were acquired at 120 fps by gently navigating the tip of the fibre-bundle on the tissue surface. The images were processed to remove the fibre pixelation artefacts and a video mosaicking algorithm was implemented to reconstruct large-area mosaics of the scanned margin surface. The description of the LS-CLE system and data processing and display steps are detailed in Chapter 3 of this thesis.

4.2.2 Patients and tissue preparation

This is a single-centre, prospective observational study performed at Charing Cross Hospital, London. Ethical approval was obtained from Imperial College London Institutional Review Board (Study number: R12047a). Tissue samples were obtained from 13 adult females undergoing BCS for confirmed or suspected breast cancer based on pre-operative radiology, biopsy or other relevant diagnostic information. All patients consented for their tissue to be used for research prior to surgery in the form of written informed consent.

Freshly excised whole WLE specimens, atypical lesions and margin excisions (n = 27, where n is the number of samples) were collected from the operating theatre and im-

mediately brought to the pathology department where the specimens were weighed and registered. The specimens were immediately taken for LS-CLE imaging, before any histological processing (like bread-loafing and sectioning) of the tissue. Real-time LS-CLE videos and images were acquired from the WLE specimen margins. The LS-CLE imaging time was restricted to 40 minutes from excision to prevent tissue degradation and potential interference with the histological diagnosis. Further, a sterile plastic sheath with $\sim$50 μm thickness was kept between the probe tip and tissue surface to avoid any contamination.

A system of sutures and clips was used to orient the WLE specimen and align the margins for the radial margin assessment task. For each specimen, the margins were divided into 6 regions: medial, lateral, superior, inferior, anterior and posterior. The superior margin is marked by a short suture with one clip and the lateral margin was marked with a long suture and two clips and often a guide wire was used to localise the tumour. The position of the LS-CLE imaging site in the breast was then represented as positions on a clock face coordinate system as depicted in Fig.4.1.

Once the specimen was oriented correctly, each margin (or the entire margin excision and atypical lesion) was topically stained with 0.02% of acriflavine solution for 1 minute. It was gently rinsed with saline and blotted dry to remove the excess stain and imaged immediately by manually making small linear scans of the fibre-bundle tip on the margin surface. On an average, three different regions were scanned for each margin surface and the co-ordinates on the clock face corresponding to the scanned region were manually recorded based on the measured position of the imaging probe around the clock face and distance (mm) to the centre from the margin. At the end of imaging, excess fluorescence agent was gently wiped off the tissue surface and the WLE specimen was returned immediately to Histopathology Department at Charing Cross Hospital for routine histopathology steps. The reconstructed mosaics (on an average 3 per scan) from each margin were later correlated with histology slides acquired from the same region and visual comparisons were made. The specimen acquisition and imaging protocol is presented in Fig.4.2.

4.2.3 Image analysis and histology correlation

The acquired LS-CLE images were visually analysed to evaluate tissue morphology and detectable features on breast WLE specimens. LS-CLE images were initially evaluated in real-time during acquisition to ensure that the images were of sufficient quality for evaluation and that they contained detectable diagnostic features. Following the image acquisition, mosaics (on an average 3 per scan, per margin) were reconstructed off-line using the video mosaicking framework presented in Section 3.5 and their image quality was assessed using the image classification framework presented in Section 3.6.1. All the image mosaics depicting cellular morphology of tumour samples and non-diseased

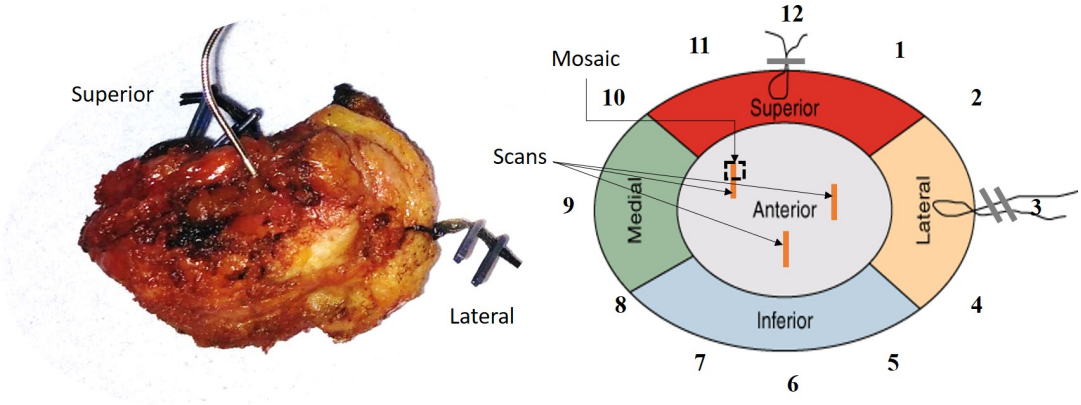

Figure 4.1: Schematic depicting the orientation of WLE specimens using a system of sutures and clips with the short suture and single clip marking the super margin and the long suture and double clip marking the lateral margin. Fibre tip positions were recorded based on their position around the clock face and distance in from the margin. LS-CLE mosaic, shown as black box, for each scan location on a margin was correlated with the corresponding histology image from the same region.

breast samples were stored digitally in specific folders into a prospectively maintained database. A senior breast histopathologist who was not involved in the data collection and I interpreted all the good quality LS-CLE mosaics and both were blinded to the margin status from conventional histology. The morphological features of the acquired mosaics were reviewed in accordance with the essential features of non-neoplastic and neoplastic tissue outlined in Table 3.3. Based on this, each mosaic was classified as non-neoplastic or neoplastic type. Any margin with at least one good quality mosaic classified as neoplastic was considered as a positive margin on LS-CLE system.

After all the image mosaics were assessed, the specimens were returned for routine histopathological analysis. Each WLE specimen was first oriented using system of sutures and clips and then multiple histology slides were obtained following medial to lateral sectioning. Any margin identified with neoplastic changes on the inked edge in the histological diagnosis report was considered as a positive margin on histology, and served as ground-truth for this study. Using the clock-face co-ordinate system, the detectable features in the reconstructed LS-CLE mosaics were correlated with the corresponding histology slides acquired from the exact region and visual comparisons were made.

4.2.4 Statistical analysis

All statistical analysis was performed in SPSS (version 25, IBM). Sensitivity, specificity, PPV, NPV and overall accuracy of LS-CLE images to detect margin status are presented using conventional histology analysis as gold standard.

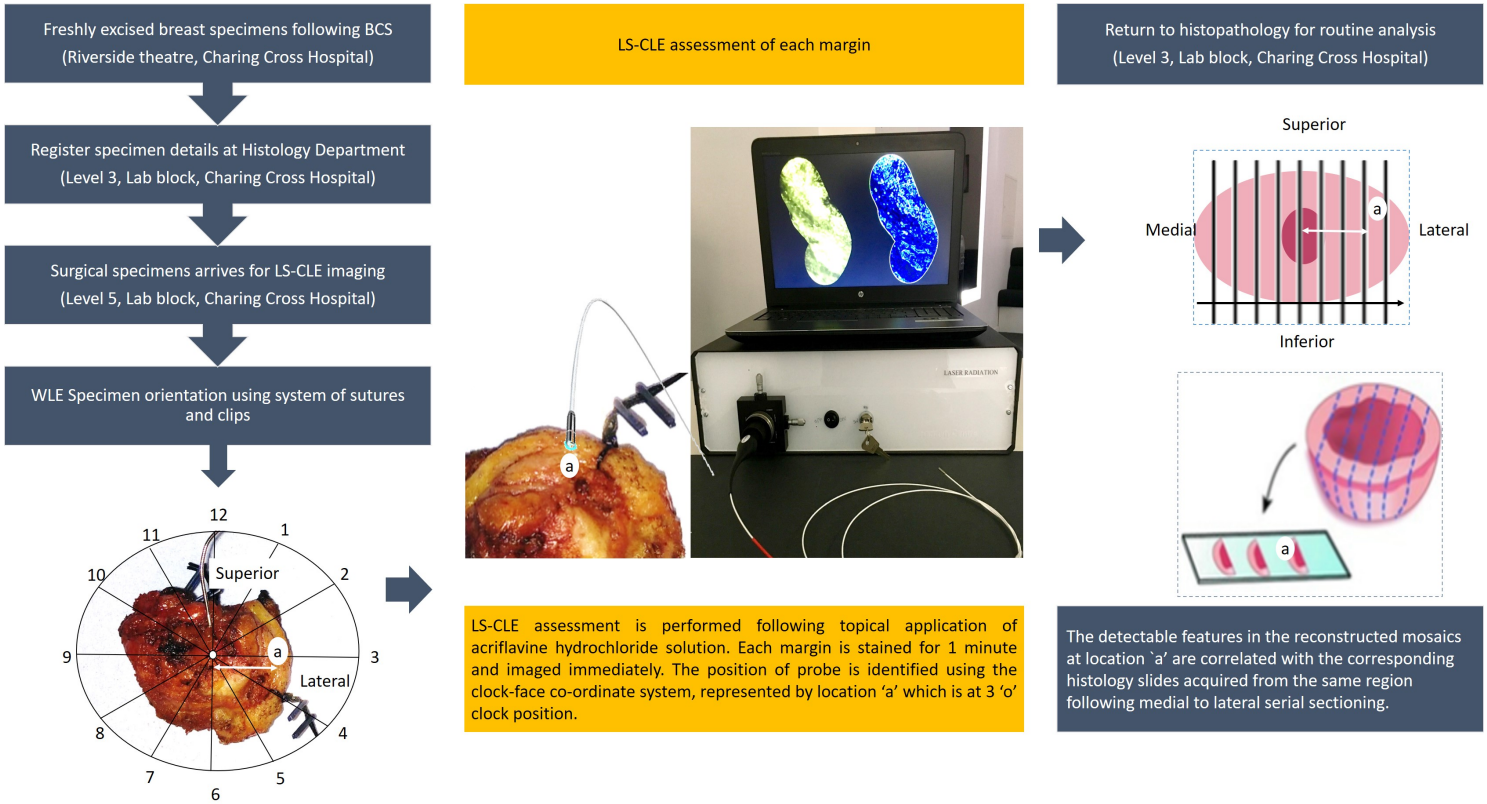

Figure 4.2: Whole surgical excisions imaging protocol, designed to image radial margins of whole wide local excisions freshly excised following BCS, using high-speed LS-CLE imaging system.

4.3 Results

4.3.1 Patient demographics and baseline characteristics

13 consented female patients with mean age of 54 years (range 30 to 79) who underwent BCS at Charing Cross Hospital were enrolled in this study. 27 specimens were collected which consisted of 11 WLEs, 2 excision biopsies of atypical lesions and 14 margin excisions. The final histological diagnosis confirmed 8 IDCs, 4 DCIS, 1 invasive mucinous carcinoma and 14 non-neoplastic tissue with some benign changes. The baseline demographic and disease states are given in Table 4.1. There were no findings of any adverse effects of acriflavine staining on histopathological assessment.

4.3.2 LS-CLE image mosaics

The scanning time was fixed at 30 minutes per patient. LS-CLE videos (mean 18 per specimen, range 16 to 20) were acquired by manually scanning the imaging probe on the tissue surface. For WLE lumpectomy specimens (Table 4.1, specimens 1 to 11), all 6/6 margins were scanned, except for Specimen 9, for which 5/6 margins were scanned due to the time constraint. For all other specimens (Table 4.1, specimens 12 to 27), images were acquired from multiple locations on the specimen surface (mean 5 sites per specimen, range 2 to 10) and data was recorded for post-processing and mosaicking. Fig.4.3 shows the flowchart of number of specimens imaged using LS-CLE for training and assessment.

An initial data set of 20 LS-CLE videos from 2 WLE specimens, (Table 4.1, specimens 1 and 2) was assessed to establish standard mosaic reconstruction strategies and image quality evaluation criteria. From discussions with breast pathologists it was found that, they first inspect the entire tissue section with low magnification objective, typically 4×, and then zoom in to the region of interest with higher magnifications to closely investigate suspected regions. The LS-CLE mosaic reconstruction was hence adapted, using a similar strategy, to accomplish examination of large specimens in a consistent and timely manner.

Long mosaics of the scanned area were constructed by acquiring the images at full frame rate of 120 fps and reducing the acceptable NCC coefficient value to 0.5 (as opposed to value of 0.9 used for imaging small cut-outs in Chapter 3). The advantages of doing so were two-fold: the sampling errors coming from the suboptimal regions missed during conventional mosaicking were greatly minimised, and secondly, the reconstructed mosaics were longer and fewer in number making it easier to assess them in a timely manner. Since breast is a very heterogeneous tissue, having long contiguous mosaics aided the assessment of features of both glandular and stromal components on the margins. Further, the size of each mosaic was constrained to 400-500 image frames to make the mosaics comparable in terms of detectable features and size. For a FOV of 240 μm at a frame rate of 120 fps, each mosaic corresponded to ∼3.8s of acquisition time.

Table 4.1: A summary of patients, specimens and invasive tumour cellularity estimated in histological examination.

Specimen number	Age (years)	Histological diagnosis	Tumour size(mm)	Grade	Distance to nearest margin
WLE lumpectomy specimens					
1	69	IDC	16	Grade 3	2 mm from lateral
2	66	IDC	25	Grade 2	4 mm from lateral
3	79	Invasive mucinous carcinoma	25	Grade 1	0.8 mm from posterior
4	50	IDC	7	Grade 1	DCIS at anterior and medial
5	71	IDC with DCIS	15	Grade 1	DCIS: 1 mm to lateral
		IDC	8	Grade 2	Invasive cancer: 1.5 mm to superior and posterior
6	54	Benign changes			
7	44	IDC	22	Grade 2	IDC at posterior and inferior
8	71	DCIS	6	Intermediate grade	2 mm from anterior
9	50	DCIS	50	High grade	1.5 mm from posterior
10	60	IDC	16	Grade 2	2 mm from lateral
11	50	Benign changes			
Atypical lesions					
12	34	Fibroadenoma		B2	
13	36	Fibroadenoma		B3	
Margin excisions					
14	59	Benign changes			
15	59	Benign changes			
16	59	Benign changes			
17	59	Benign changes			
18	59	IDC	2.3	Grade 1	0.5 mm from outer margin
19	59	Benign changes			
20	54	Benign changes			
21	71	Benign changes			
22	71	Benign changes			
23	71	Benign changes			
24	50	Benign changes			
25	50	DCIS	3.5	High grade	10 mm from outer margin
26	50	Benign changes			
27	50	Benign changes			

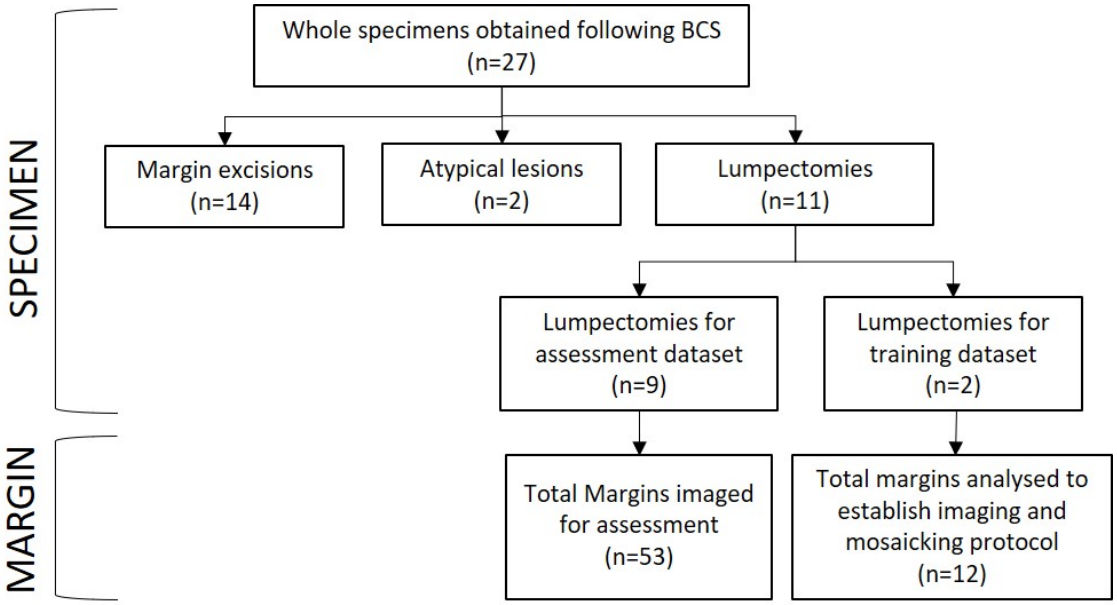

Figure 4.3: Flow chart of study population and the number of specimens imaged using LS-CLE for training and assessment.

Surgical artefacts of the tissue surface due to cauterisation procedures like diathermy were evident on the reconstructed mosaics. On LS-CLE images, the cauterisation artefacts appeared as cloud-like hyperfluorescent areas with rough edges scattered around dark regions with no detectable features in it. Another common reason for poor quality images was over-saturation and inadequate probe tissue contact while scanning on irregular tissue surfaces. In Fig.4.4(a), the disorganised and cloudy scattered structures represents a cauterised tissue surface. While in Fig.4.4(b), artefacts due to over saturation and in Fig.4.4(c-d), blurred images due to inadequate tissue contact are represented. After a gross visual inspection and histopathological findings, such un-interpretable images were excluded from further analysis. Table 4.2 summarises the total number of good quality and low quality images acquired from the study dataset images.

For WLE specimens, 79% of the reconstructed mosaics had satisfactory quality (at least 3 mosaics per margin), 13% had poor quality due to diathermy artefacts and 8% due to imaging artefacts like inadequate tissue contact. 71% of all margin excisions mosaics had high quality (at least 3 mosaics per specimen), whereas 17% were excluded due to cauterisation artefacts and 11% due imaging artefacts. For atypical lesions, the number of images excluded due to imaging artefacts was significantly high (38%). This was due to the poor images (77/80 were poor quality) acquired from Specimen 13, which was pre-stained with indocyanine green (ICG) prior to imaging with LS-CLE. Due to a low number of atypical lesion specimens, specimen 13 was not excluded from the study dataset.

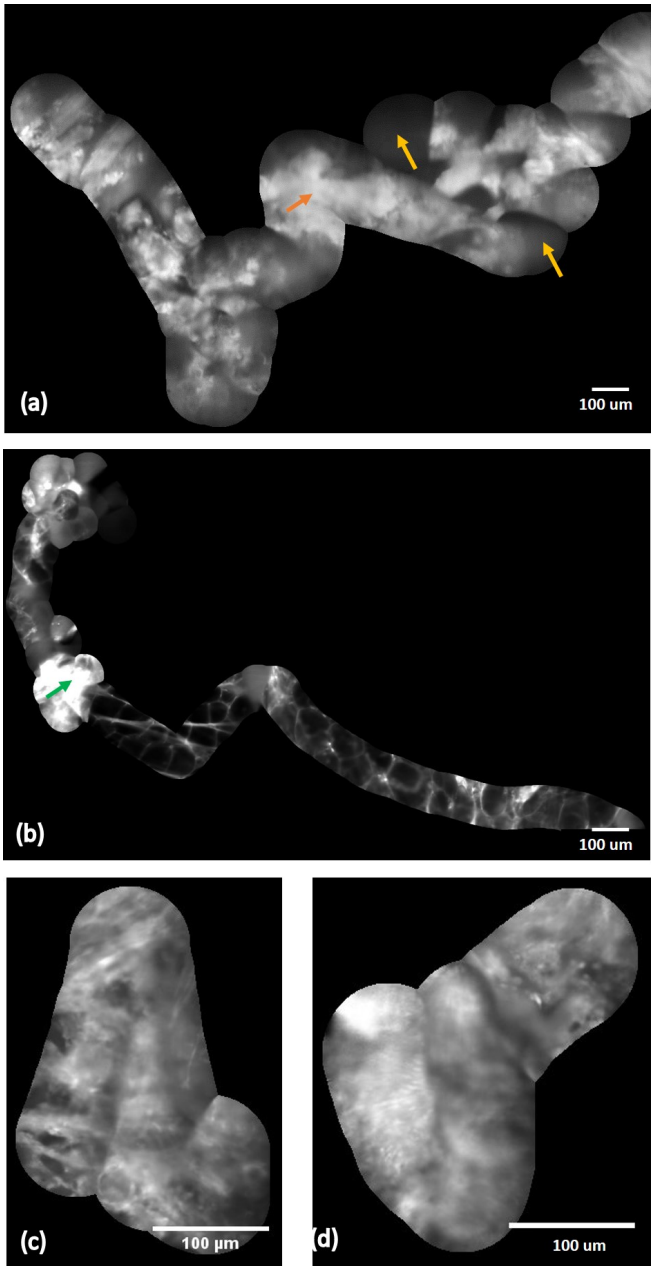

Figure 4.4: Representative sub-optimal quality LS-CLE images of surgical margins from WLE specimens with available artefacts. (a) shows surgical artefacts caused due to cauterisation of tissue surface represented by dark featureless areas (yellow arrow) and bright cloud-like irregular cauterised tissue scattered around it (orange arrow). (b) contains fibrofatty tissue which over-saturated (green arrow); (c) and (d) represent images of benign fibrocystic changes which are blurred due to inadequate probe-tissue contact. Scale bar is 100 μm.

Table 4.2: LS-CLE image quality analysis

	Total	High quality	Poor quality due to cauterisation artefacts	Poor quality due to imaging artefacts
		Included	Excluded	
WLE specimens	893	700	120	73
Atypical lesions	186	95	20	71
Margin excisions	262	185	43	31
Total	1341	980	183	175

The LS-CLE mosaic inclusion/exclusion results are shown in Table 4.2. From a total of 25 specimens (Table 4.1, specimens 3 to 27) used in the study dataset, 1341 mosaics were initially generated. After exclusion of un-interpretable images (n = 358, 26.7%), 980 mosaics (73.3%, at least 3 mosaics per margin) were deemed to be of satisfactory quality and used for the assessment for the diagnostic performance.

4.3.3 Assessment of diagnostic performance

Distinctive morphological features that were consistently observed across all 980 LS-CLE mosaics were described in three categories: glandular, fibrous and adipose tissue components according to the essential features for neoplastic and non-neoplastic tissue pathologies outlined in Table 3.3. During this analysis of glandular tissue component, careful attention was paid towards the size of ducts, epithelial thickness and visibility of lumen. The evaluation of fibrous stromal component comprised of assessments of stromal cellularity and uniformity of stromal architecture. The ability to distinguish stromal and glandular components was also assessed.

The adipose tissue component was focused on the recognition of individual fat cells and the stromal cellularity around them. The presence of any DCIS or invasive neoplastic cells on a margin were considered positive. Representative images of normal, benign and neoplastic pathologies imaged on margins are shown in Figs.4.5 - 4.7.

For LS-CLE system, any margin with at least one good quality mosaic classified as neoplastic was considered as a positive margin. Likewise, margin excision specimens and atypical lesions were considered neoplastic if at least one good quality mosaic was reviewed as neoplastic. A margin was considered to be a close margin if there was evidence of tumour on the histology findings within 1 mm from the nearest surface.

A comparison of the status of each margin of WLE specimen, atypical lesions and margin excisions as assessed by LS-CLE and histopathology is given in Table 4.3. Out of a total of 53 margins from 9 WLE specimens, six margins were identified as positive (11.3%) and 47 as negative (88.7%) with LS-CLE.

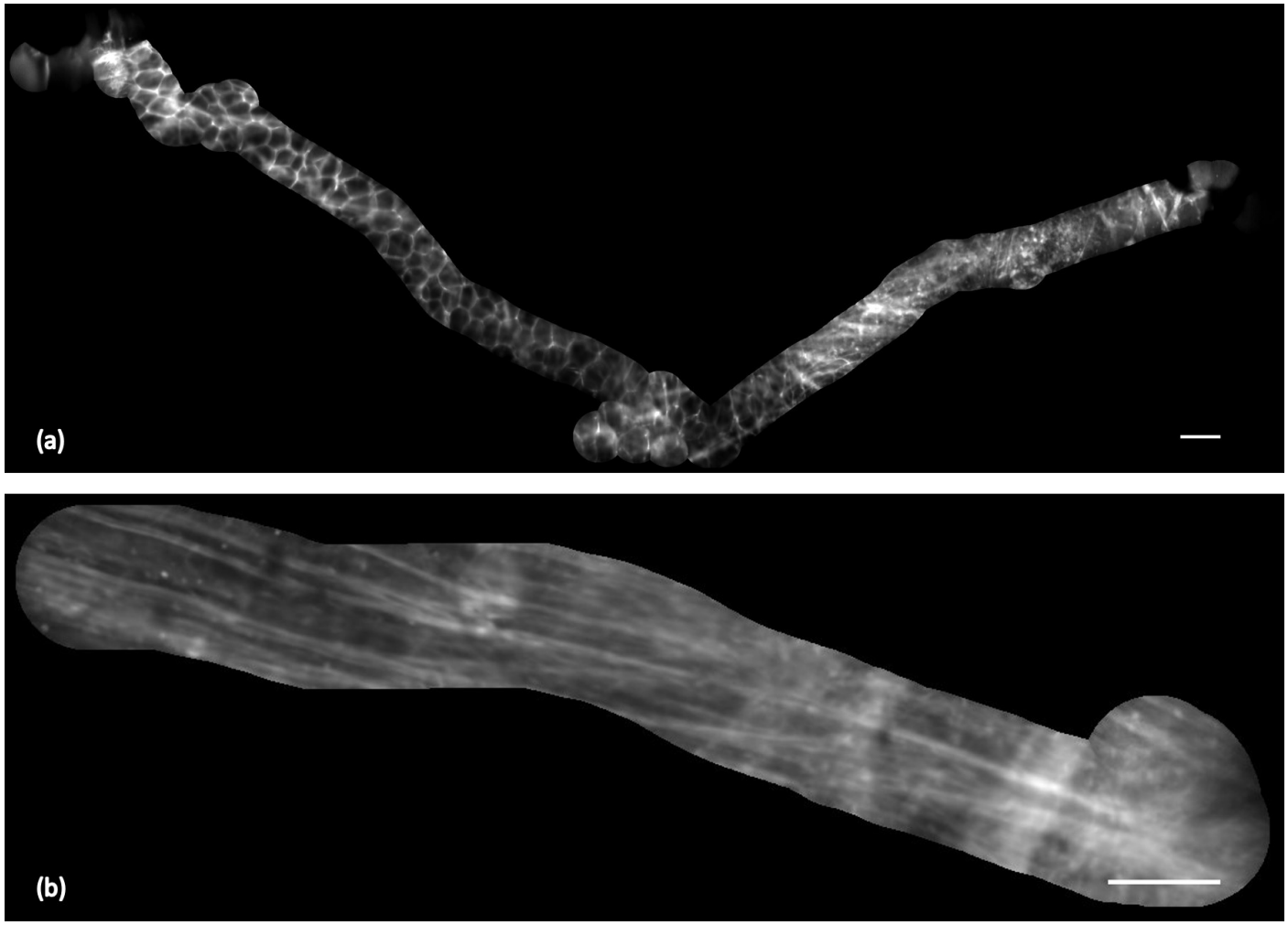

Figure 4.5: Non-neoplastic breast tissue showing (a) Adipose cells and fibrous tissue with sparse nuclei and (b) collagen fibres appearing as long strands of moderately stained fibres with sparse nuclei. Scale bar is 100 μm.

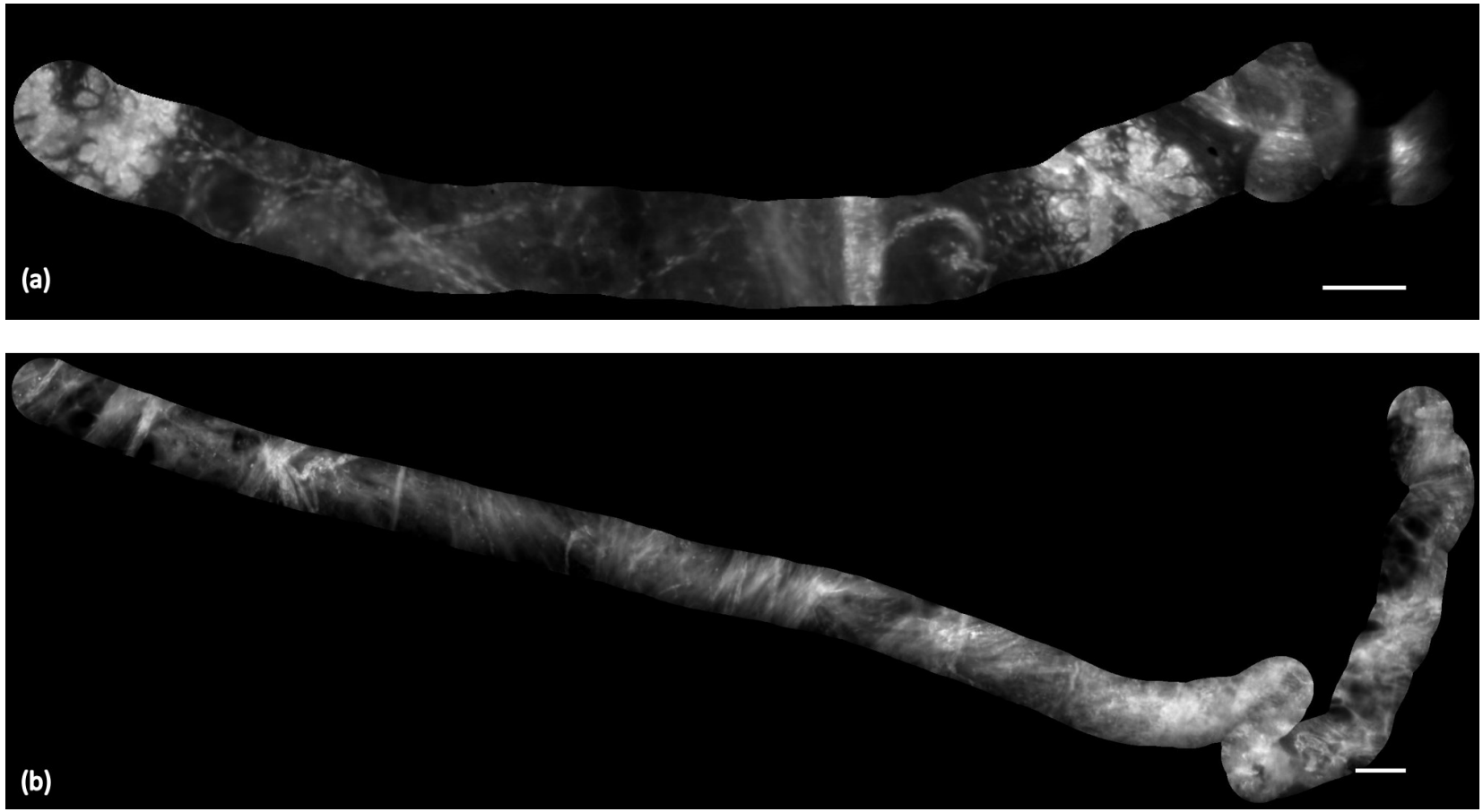

Figure 4.6: Breast tissue images showing benign changes. (a) The epithelium components show intracanalicular and paricanalicular patterns with mildly cellular stroma. The appearances are consistent with complex fibroadenoma. (b) Breast tissue showing fibrocystic changes and some fibrous scarring. Scale bar is 100 μm.

Figure 4.7: Neoplastic breast tissue showing (a) DCIS where ducts are seen to have high luminal density and thick epithelium and (b)IDC, representing increased cellularity and no-distinction between stromal and glandular components. Scale bar is 100 μm.

Table 4.3: Comparison of tumour status of mosaics reconstructed using LS-CLE system and corresponding histological assessment for WLE specimens, atypical lesions and margin excision specimens.

Specimen number	**Number of LS-CLE mosaics assessed (excluded)**	**LS-CLE assessment of tumour status**	**Histological assessment of tumour status**
WLE	**700 (193)**		
3	70 (8)	All negative	All negative
4	102 (16)	DCIS at anterior, inferior and medial margins	DCIS at anterior and medial margins
5	83 (19)	All negative	All negative
6	60 (15)	All negative	All negative
7	62 (30)	IDC at posterior margin	IDC at inferior and posterior margins
8	91 (33)	DCIS at inferior and medial margin	All negative
9	63 (18)	All negative	All negative
10	78 (24)	All negative	All negative
11	91 (30)	All negative	All negative
Atypical lesions	**95 (91)**		
12	92 (14)	All negative	All negative
13	3 (77)	All negative	All negative
Margin excisions	**185 (74)**		
14	18 (0)	IDC and DCIS at outer margin	All negative
15	19 (2)	IDC at outer margin	IDC at outer margin
16	13 (11)	IDC and DCIS at outer margin	All negative
17	21 (8)	All negative	All negative
18	21 (6)	DCIS at outer margin	All negative
19	20 (7)	DCIS at outer margin	All negative
20	14 (13)	All negative	All negative
21	10 (5)	All negative	All negative
22	4 (1)	All negative	All negative
23	6 (0)	IDC and DCIS at outer margin	All negative
24	9 (4)	All negative	All negative
25	15 (9)	All negative	All negative
26	5 (8)	All negative	All negative
27	10 (0)	All negative	All negative

Out of the 14 margin excisions, 6 were identified as positive (42.9%) and 8 as negative (57.1%), and both the atypical lesions were marked negative on LS-CLE images.

A detailed histology assessment report of each margin and specimen was obtained and considered as ground-truth for this study. Analysis of the corresponding histological diagnosis of each margin (or excision specimen) confirmed that 4 WLE margins (7.6%) and 1 margin excision (7.14%) were identified positive and 49 WLE margins (92.4%) and 13 margin excisions (92.8%) and both atypical lesions were identified negative for presence of abnormal cells.

On comparing the LS-CLE and histology findings (shown in Table 4.4), the WLE specimens demonstrated a sensitivity of 75%, specificity of 93.9%, PPV of 50%, NPV of 97.9% and accuracy of 92.45%. Based on Table 4.5, the excision specimens demonstrated higher sensitivity and NPV of 100%, however, the specificity and PPV were lower: 58.3% and 16.7% respectively, giving an accuracy of 61.5%. The atypical lesions were both detected negative and hence gave 100% sensitivity and specificity.

For a total of 25 specimens imaged with LS-CLE, an overall sensitivity of 80%, specificity 87.5% and accuracy of 87% is found. The PPV is 33.3% while the NPV is 98.2%.

Table 4.4: WLE lumpectomy specimens: Sensitivity and specificity of LS-CLE for distinguishing non-neoplastic and neo-plastic breast features on margins

	Histology margin assessment		
LS-CLE assessment	Neoplastic	Non-neoplastic	Total
Neoplastic	3	3	6
Non-neoplastic	1	46	47
Total	4	49	
Sensitivity, 75.0%; Specificity 93.9%; Accuracy 92.4%; PPV 50.0%; NPV 97.9%			

Table 4.5: Margin excisions: Sensitivity and specificity of LS-CLE for distinguishing non-neoplastic and neo-plastic breast features

	Histology assessment		
LS-CLE assessment	Neoplastic	Non-neoplastic	Total
Neoplastic	1	5	6
Non-neoplastic	0	8	8
Total	1	13	
Sensitivity, 100.0%; Specificity 61.5%; Accuracy 64.3%; PPV 16.7%; NPV 100.0%			

4.4 Discussion

This study presents the first application of LS-CLE as a portable, real-time and microscopic resolution technique to scan margins of whole freshly-excised specimens following BCS. By providing images with 1 μm spatial resolution and image acquisition rates of 120 fps, LS-CLE has the potential to provide surgeons with the ability to assess margin status intra-operatively. LS-CLE imaging with topical application of acriflavine, a rapid nuclear-staining fluorescence agent, allows visualisation of normal and neoplastic morphological features similar to that of routine histology. No interference is observed with conventional H&E staining, indicating that it would be possible to image tissue margins stained with acriflavine without affecting their oncopathological assessment and interpretation by histopathologists.

Several representative cases from the study set are presented in Fig.4.8 to Fig.4.11, and discussed below. The first patient (female, 71 years), diagnosed with Grade 1 IDC *via* core biopsy procedure had a 35 mm tumour removed by ultra-sound guided WLE surgery. LS-CLE images of the WLE specimen (Table 4.1, specimen 5) showed fibroadipose tissue along with some areas of inflammation and fibrosis appearing as thick and dense moderately stained fibres with spare bright nuclei. There was no evidence of malignancy in the LS-CLE images. The histological evaluation of the WLE specimen (Table 4.1, specimen 5) indicated the presence of two foci of IDC in the breast tissue. Tumour1 was Grade 1, 15 mm with DCIS which was located 1 mm from the lateral margin and Tumour2 was Grade 2, 8 mm and was located 1.4 mm from the posterior margin. The histological diagnosis confirmed the LS-CLE findings of a negative margin. The LS-CLE and histology images for this case of negative tumour margins are shown in Fig.4.8.

The second patient (female, 79 years) had a 25 mm Grade 1 invasive mucinous carcinoma (Table 4.1, specimen 3) surgically removed by BCS. The tumour was located 0.8 mm from the posterior margin and more than 10 mm from all other margins. This case demonstrates LS-CLE imaging of a close margin, Fig.4.9. LS-CLE images of the posterior margin indicated benign fibrocystic changes and fibroadipose tissue. Some dilated ducts with dark enlarged lumen lined by 2-3 layers of inflammatory cells appearing as bright spots surrounding the lumen were also observed. In corroboration with LS-CLE results, the histological findings also revealed widespread fibrocystic changes with ductal ectasia (dilated ducts) and ductal hyperplasia, with no evidence of malignancy on margins.

A third patient (female, 50 years) was diagnosed with Grade 1 IDC with a 7 mm tumour. LS-CLE images revealed suspicious sites with well-circumscribed ductal regions of high luminal density on the anterior, inferior and medial margins of the WLE specimen (Table 4.1, specimen 4). The corresponding histology findings indicated low-grade DCIS

at the anterior and medial margins and more than 5 mm from all other margins. The LS-CLE and histology images for this case of positive *in situ* tumour on margins are shown in Fig.4.10.

When the inferior margin was reviewed again, it was noted that large circumscribed ducts with thickened epithelium were present with partial disruption of stromal-glandular interface. This margin was falsely classified as positive with DCIS on LS-CLE system, however, it might be indicative of benign fibrocystic changes like ADH and fibroadenoma which have similar appearance to DCIS on LS-CLE imaging.

A fourth patient (female, 44 years) was diagnosed with IDC *via* core biopsy procedure and had a 22 mm Garde 2 IDC tumour removed with wire-guide WLE surgery (Table 4.1, specimen 7). The histological findings indicated tumour reaching the posterior and inferior margins and more than 2 mm away from all other margins. For LS-CLE images, only the posterior margin indicated an increase in cellularity resulting in a 'blizzard' effect due to nuclei depicted as bright dots, with loss of stromal-glandular interface. Surrounding regions of invasive cancer infiltrating in the fat cells was also evident in some mosaics from the posterior margin. The LS-CLE and histology images for this case of positive IDC on margins are shown in Fig.4.11.

On examining the LS-CLE images of the inferior margin, it was observed that 13/16 reconstructed mosaics from this margin scan were of poor quality and rejected due to cauterisation artefacts. Due to cloudy and hazy stroma, it was difficult to image the nuclear density and cellular organisation in these images, misclassifying them as benign changes. This single false negative case could be attributed to the degraded quality of the acquired images due to cauterisation artefacts.

Of the eight false positive results (three from WLE and five from margin excisions), three were from a very dense, fibrous tissue which fibrocystic changes. The histological findings also indicated fibrocystic changes and ductal hyperplasia. It is possible that due to increased cellularity, these lesions were misidentified as positive. Five false positives came from two tissue specimens with a positive finding at a different margin, and here as well the benign changes were misconstrued as neoplastic changes. The differentiation of malignant from benign tumours is an ongoing research effort, as with many other biomedical imaging techniques.

To reduce the re-operation rates during BCS procedures, it is paramount for the surgeon to be confident that no tumour cells are left behind and that diagnosis of non-neoplastic margins is accurate. For IMA applications, a significant statistic that aids to evaluate this is NPV which indicates a percentage of patients with a negative diagnosis who do not have any malignancy. From the study dataset, the overall NPV of 98.2% was achieved. High PPV values are also desirable to avoid unnecessary excision of non-neoplastic tissue

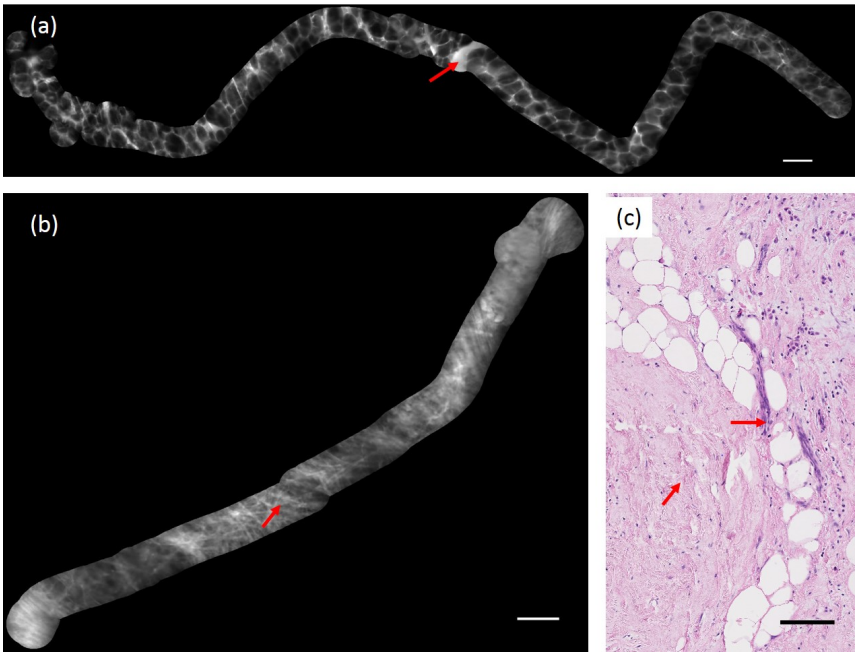

Figure 4.8: Representative negative margin. (a,b) LS-CLE images and (c) corresponding H&E stained histology of normal fibrofatty breast tissue imaged at the margin of WLE specimen. Well defined large adipose cells, with sparse nuclei as bright spots are thin fibres of connective tissue are predominant in the LS-CLE images. These features correspond well with those identified in histology section. Scale bar is 100 μm.

during BCS. The overall PPV of LS-CLE was found to be low: 33.3%. The difficulty in distinguishing between benign fibrocystic changes and neoplastic conditions, which has resulted in poor PPV of this work. This suggests that the image classification criteria may need to be refined to better differentiate benign and neoplastic conditions.

There were several limitations to this study. The diagnostic accuracy was tested by comparing the LS-CLE images with corresponding histological findings on a small dataset. While this gives preliminary understanding about the capabilities of LS-CLE in imaging breast margins, the intraoperative feasibility needs to be further investigated by assessing the learning curve for surgeons and pathologists to acquire and interpret the images.

From this study, it was observed that 13% of the reconstructed mosaics were un-interpretable due to excessive diathermy artefacts, indicating that superficial tissue imaging systems like LS-CLE may lead to sampling errors while investigating tissue areas highly affected or charred due to cauterization. The corresponding histology images from these regions were also found to be un-interpretable and not used for diagnosis. Further investigations need to be carried out to assess the thermal depth and tissue damage on margins of whole WLE specimens caused due diathermy tools, and its corresponding effect on LS-CLE image quality.

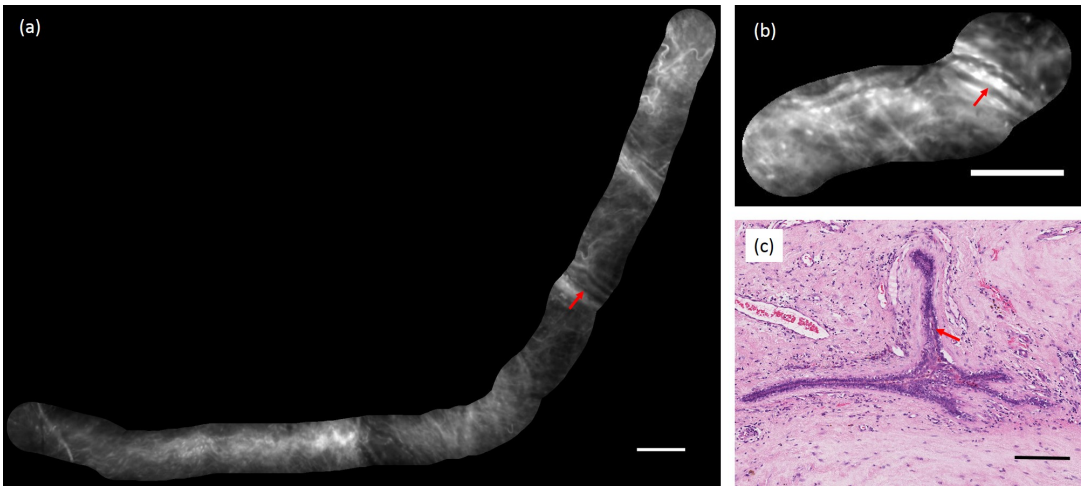

Figure 4.9: Representative negative margin with benign changes. (a,b) LS-CLE images and (c) corresponding H&E stained histology showing distinct fibrocystic changes in the imaged margin of WLE specimen. LS-CLE images represent dilated ducts with dark enlarged lumen lined by 2-3 layers of inflammatory cells appearing as bright spots surrounding the lumen were also observed. Both LS-CLE and histology images show corresponding features. Scale bar is 100 μm.

4.5 Conclusion

This study has provided useful insights into the advantages and challenges in using LS-CLE for IMA breast margin assessment. A total of 1341 mosaics were generated from a test dataset, consisting of 25 WLE and surgical excision specimens, by freehand scanning of the imaging probe on the tissue surface. After correlation with histopathology findings, an overall sensitivity of 80%, specificity of 87.5% and accuracy of 87% was achieved. The positive predictive value (PPV) was 33.3% while the negative predictive value (NPV) was 98.2%. With these preliminary results, LS-CLE could be a valuable tool for examining the superficial margin status of excised breast tumour specimens.

53/54 margins of whole WLE specimens were successfully imaged in 9 patients within 40 minutes of excision. While the high image acquisition speed of LS-CLE aided to scan large-areas of the tissue surface, it must be noted that the current scope of LS-CLE with acriflavine staining is not to perform *in vivo* imaging of the whole margin/cavity, but to give the surgeons a miniaturized intra-operative tool to rapidly scan over suspicious regions of excised specimens and determine whether additional margins need to be taken-out or not. This could help to achieve better cosmesis by preventing unnecessary removal of healthy breast tissue. It could also minimise the number of repeat BCS by identifying occult lesions that may otherwise have been left behind.

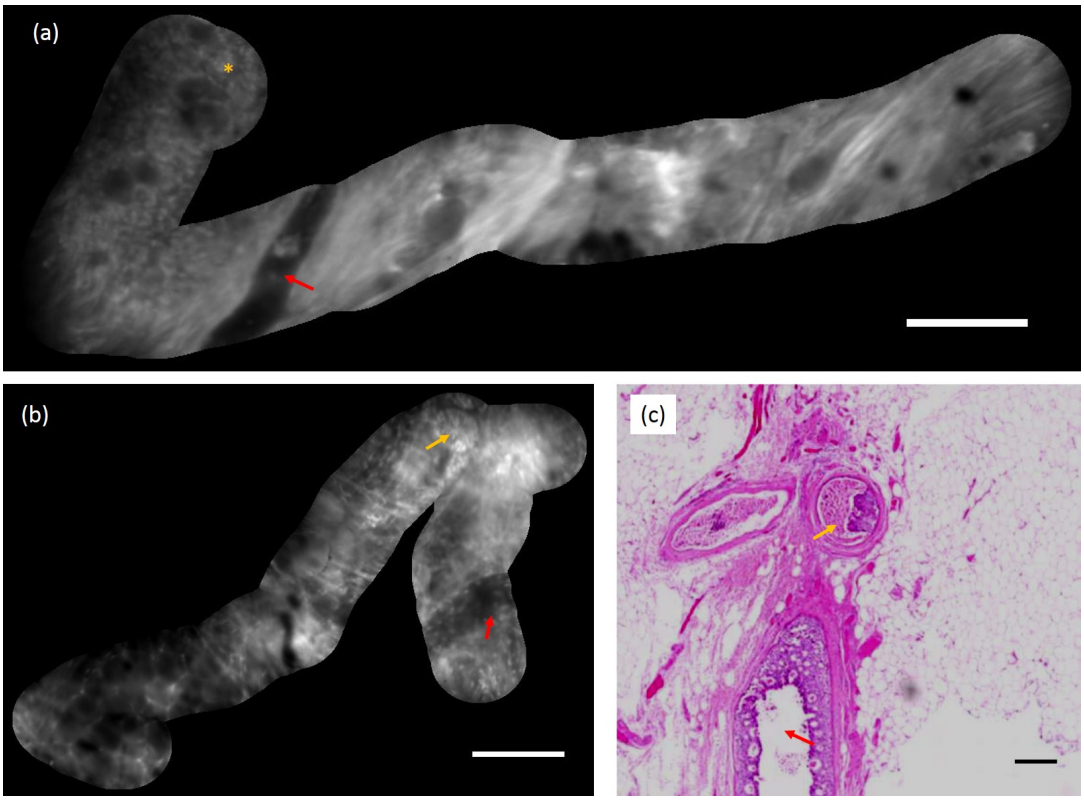

Figure 4.10: Representative positive tumour margin detected with *in situ* changes. (a,b) LS-CLE images and (c) corresponding H&E stained histology showing DCIS in the imaged margin of WLE specimen. In (a), the epithelial lining of ducts appear markedly thickened and the luminal border of the epithelium is seen to be encroaching into the lumen. There is also loss of stromal-glandular interface. (b) The duct is enlarged, well circumscribed and its lumen is completely filled with nuclei appearing as islands of hyperfluorescent dots. Some dilated ducts are also evident in all three images. Both LS-CLE and histology images show corresponding features. Scale bar is 100 μm.

Whilst preliminary results are promising, LS-CLE still needs some technical developments to provide adequate resolution and magnification for accurate differentiation of neoplastic from non-neoplastic tissues. The current LS-CLE system, as well as most of the existing fluorescence endomicroscopy systems, are limited to single excitation and single fluorescence spectral band. Typically a fast-acting non-specific fluorescence agent, which is not safe for *in vivo* use, is applied to generate grayscale confocal images of tissue morphology. While normal and neoplastic morphologies can be more easily distinguished, benign and malignant disease types and subtypes might be difficult to differentiate. There exists a need to explore the effectiveness of other rapid staining agents for both *ex vivo* and *in vivo* imaging of different breast disease types and subtypes.

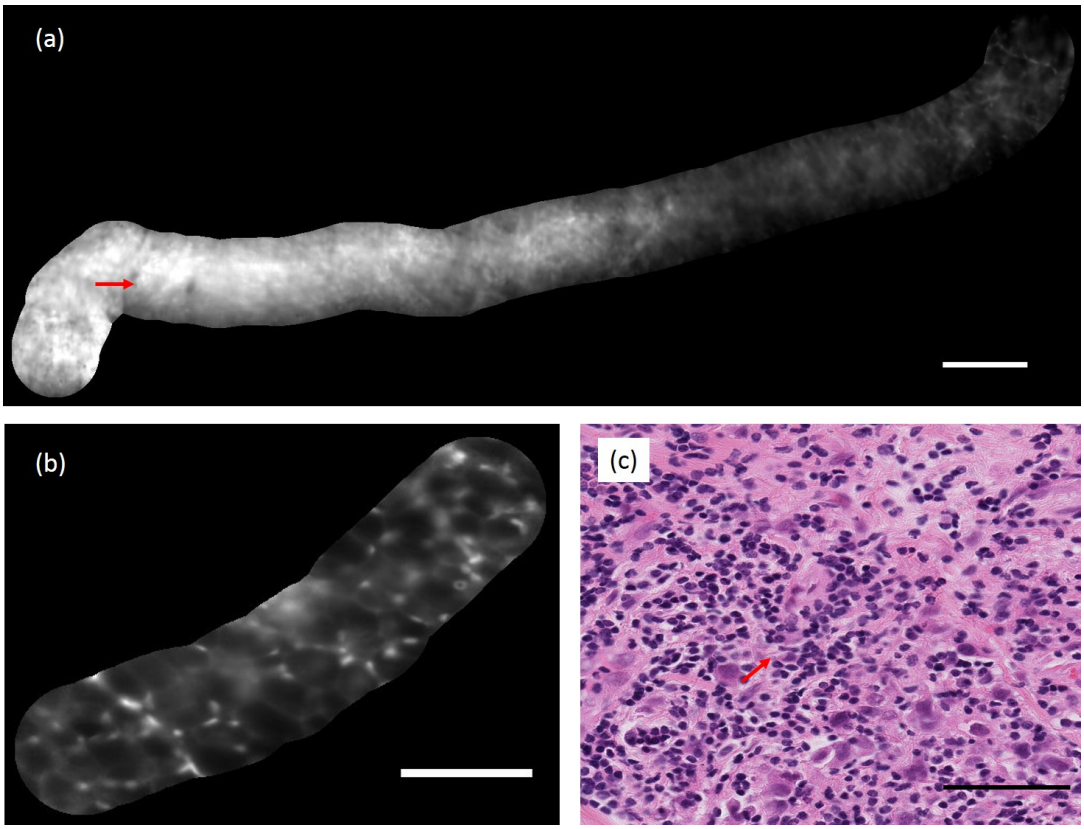

Figure 4.11: Representative positive tumour margin detected with *invasive* carcinoma. (a,b) LS-CLE images and (c) corresponding H&E stained histology showing (a) IDC and (b) cancer infiltrating in fat on WLE margins. On LS-CLE the invasive carcinoma appears as broad sheet of densely packed tumour cells, with completely disrupted stromal-glandular interface. On histology, increase of cellularity and haphazard organisation are evident as well. Both LS-CLE and histology images show corresponding features, confirming the presence of positive margin. Scale bar is 100 μm.

Due to the limited FOV of fibre-bundle based LS-CLE system, in some cases tumour cells may be missed during imaging, especially due to free-hand scanning operation. A high-speed automated scanning platform or robotic probe might be able to acquire contiguous large FOV images on the entire margin without sacrificing resolution or imaging speed.

Currently, the spatial resolution of LS-CLE images is limited by fibre-pixelation artefacts. While this provides sufficient clarity to visualise common glandular and stromal characteristics of both neoplastic and non-neoplastic morphology, it might be inadequate to image sub cellular features.

The following three chapters of this thesis will aim to address these technical limitations.

Chapter 5

Methylene-blue aided line-scan confocal endomicroscopy of breast cancer*

5.1 Introduction

The diagnostic capability of fluorescence-based fibre-bundle endomicroscopy (FEM) systems, operating on confocal and wide-field principles, has been demonstrated by *ex vivo* breast tissue experiments [185, 196, 240, 243, 244, 248]. The images acquired in these studies provide cellular resolution morphology information similar to that obtained using conventional excision biopsy. Clinically relevant morphological features of neoplastic and non-neoplastic breast tissues can be readily visualised and distinguished for rapid tissue diagnosis. However, new techniques must be developed to enable rapid *in vivo* imaging applications like scanning the breast cavity during BCS.

* The contents of this chapter were published and presented as:
Vyas, K., Hughes, M., Leff, D. R., & Yang, G. Z. (2017). Methylene-blue aided rapid confocal laser endomicroscopy of breast cancer. Journal of Biomedical Optics, 22(2), 020501.
Vyas, K., Hughes, M., Leff, D. R., & Yang, G. Z. (2018) Robot-assisted Endomicroscopic Imaging Of Breast Cancer: Instrumentation And Applications. Poster presentation at Advanced Biophotonics workshop, Hamlyn Symposium on Medical Robotics.
Vyas, K., Hughes, M., & Yang, G. Z. (2018) A dual-wavelength line-scan confocal endomicroscopy system for rapid molecular imaging (Conference Presentation-Oral). Proc. SPIE 10470, Endoscopic Microscopy XIII, 104700V.
Wisanuvej, P., Vyas, K., Giataganas, P., Leibrandt K., Liu, J., Hughes, M., & Yang, G. Z. (2017). Three-dimensional Robotic-assisted Endomicroscopy with a Force Adaptive Robotic Arm. Robotic challenge at Hamlyn Symposium on Medical Robotics.
Vyas, K., Hughes, M., Leff, D. R., & Yang, G. Z. (2016) Establishing imaging protocol for evaluation of breast cancer margins using high-speed confocal endomicroscopy and methylene blue. Poster presentation at Hamlyn Symposium on Medical Robotics.

Until recently, the state-of-the-art FEM systems have been limited in their capabilities of imaging *in vivo* tissue for the following three reasons: (1) lack of suitable non-toxic fluorophores for rapid visualisation of different tissue morphologies (2) insufficient image acquisition rates and (3) lack of robotic catheter or scanning probe that enables FEM imaging and mosaicking over large tissue areas and (4) restriction to use single fluorescent agent due to low speed of existing CLE systems.

This chapter serves to address these issues and their potential solutions. A detailed description of bespoke LS-CLE technology with MB, an US food and drug administration (FDA) approved fluorescent agent, and integration with robotic scanner is presented to enable *in vivo* imaging of breast cancer. A further modification of this system for dual-wavelength imaging is also presented to suggest potential molecular imaging applications.

5.1.1 Overview

The ability of LS-CLE to provide cellular-level imaging of tissue morphology with acquisition rates ∼10× greater than commercial Cellvizio pCLE system (Mauna Kea Technologies) has motivated the design and construction of a bespoke LS-CLE system suitable for *in vivo* imaging. A previous study on 71 *ex vivo* breast tissue samples imaged with the Cellvizio pCLE system demonstrated that cancerous and normal tissue could be differentiated by histopathologists with an accuracy of 94% [244]. This study used topically applied acriflavine hydrochloride (AH), excited at 488 nm, which stains cell nuclei and enables high contrast imaging of tissue morphology.

The findings from the previous chapter demonstrated that LS-CLE system with 488 nm laser source have provided many promising results on cellular imaging of freshly excised breast tissue specimens using AH as a staining agent. The image quality is comparable to that of Cellvizio pCLE. However, this is not currently an attractive option for *in vivo* imaging due to the lack of regulatory approval and suggested risks of mutagenicity [240].

To avoid these safety concerns, a subsequent *in-vivo* human study used intravenous fluorescein as the contrast agent. Fluorescein is well-established as being safe for *in vivo* human use [240] and is commonly employed for other clinical applications of pCLE [249, 250]. However, since fluorescein staining is non-specific, it did not effectively highlight tissue morphology which made it difficult to distinguish between benign and malignant lesions [240]. Other studies have demonstrated effectiveness of proflavine with HRME, with and without structured illumination, to detect breast cancer [185,196,243,248]. These studies are investigational as proflavine is not FDA approved or commercially available for *in vivo* human use.

For *in vivo* imaging in routine clinical practice, it is desirable to use endomicroscopes with approved fluorescent dyes which are both safe for human use and provide suffi-

cient contrast to distinguish between different tissue morphologies. MB is one of the few FDA approved dyes for *in vivo* human application. It has been demonstrated previously for the treatment of methemoglobinemia and is an alternative to isosulphan blue for *in vivo* localisation of non-palpable lesions and sentinel lymph node mapping during breast surgeries [130–132]. Topical MB has also been demonstrated to image precancerous and neoplastic lesions of central airways using Cellvizio pCLE system [251, 252]. Understanding how MB concentration, uptake and staining time affects the image quality specific for breast tissue assessment is still to be explored.

Further, a major limitation of FEM systems is that their FOV is limited by the size of the fibre-bundle, typically 0.25 to 0.8 mm, depending on the selection of the distal optics. This makes it difficult for surgeons to maintain adequate probe-tissue contact and dexterity while scanning inside large-areas like breast cavities, especially during manual scanning. An attractive option to overcome this limitation is to develop systems for mechanical and robotic scanning of FEM probes. Latt et. al developed a hand-held one degree-of-freedom active force controlled robotic probe to maintain optimum probe-tissue contact during scanning. Rosa et al. used a large industrial robotic manipulator to scan the FEM probe and enlarge the FOV. Visual servoing was used to optimise the scan trajectory [220]. Zhang et al. integrated FEM and OCT probes with the da Vinci surgical robot, demonstrating large-area closed-loop scanning using information from both imaging channels [253]. Zuo et al. demonstrated prototypes of several surface scanning systems specifically designed for whole-breast cavity scanning [254, 255]. Recently, Giagaganas et al. have developed a portable robot-assisted scanning probe with micrometer-scale accuracy that can achieve mosaicking work-space up to 14 mm^2 [256]. Such a probe could be used hand-held or with an articulated or passive arm for large-area scanning applications. The operation of such systems have indicated the potential for large-area scanning using FEM system. The application of these robotic-assisted FEM systems for breast cavity scanning warrants further investigation.

5.1.2 Aim and hypothesis

The hypothesis is that MB aided LS-CLE in breast cavity scanning can provide rapid decision-making during BCS, allowing oncological status of resection margins to be determined *in vivo*. It is critical to first establish the morphological appearances of neoplastic and non-neoplastic breast tissues using histology as the gold standard for comparison prior to assessing its potential to guide intra-operative decision-making. The morphological features are further compared to AH-stained tissue imaged with Cellvizio pCLE system and it is hypothesised that the quality in imaging glandular and stromal components is comparable.

This study, performed on freshly excised breast tissues, demonstrates the feasibility of LS-CLE imaging towards intra-operative *in situ* margin assessment. Proof-of-concept experiments on the integration of MB aided LS-CLE system with the robotic scanning probe developed by Giagaganas et al. [256] are carried out and effectiveness of such a system for breast cavity scanning is discussed. It is hypothesised that by using MB aided LS-CLE system operating at 120 fps, long and high quality mosaics could be generated both by hand-held and robotic scanning, which otherwise would be challenging. This would allow the surgeon to accomplish more accurate and complete surgical resections, thus reducing the re-operation rates and improving outcomes of BCS.

5.2 Materials and methods

5.2.1 Imaging system

The system configuration is illustrated in Fig.5.1. The system set-up is similar to a previously developed virtual-slit LS-CLE at 488 nm [216], but is adapted and optimised for MB imaging. A full description of LS-CLE operating principles can be found in Chapter 3, Section 3.3.2. In brief, a cylindrical lens L2 (Thorlabs, LJ1695RM) with focal length of 50 mm is used to create a focused line from a 100 mW, 660 nm laser (Vortran Stradus, 660). A galvo-mirror M1 (Thorlabs, GVS001) sweeps the line across the proximal end of the fibre-bundle probe (Cellvizio Gastroflex UHD, Mauna Kea Technologies) in a direction perpendicular to the line. The fibre-bundle probe relays the line to the tissue *via* a distal objective L4 with 10× magnification. The tissue is illuminated with a time-averaged power of 2.5 mW when placed in contact with the distal tip of the probe.

The same fibre-bundle returns the collected fluorescence from all the points along the line. The emitted fluorescence is then imaged onto a monochrome rolling-shutter CMOS camera (Point grey Flea 3, FL3-U3-13S2M-CS) which acts as a virtual detector slit leading to optical sectioning at frame rates of up to 120 Hz. The average laser line-width at the distal tip (measured by imaging the line onto a camera with a 10× objective) is equal to about 3.5 pixels in the vertical direction. Projected onto the proximal face of the bundle, this provides a detector slit width of about 2.6 μm which is approximately equal to the core spacing. A comparison of images of laser line-width obtained using LS-CLE at 488 nm and 660 nm, showing background autofluorescence from the fibre-bundle cores, is presented in Fig.5.2. The slit width obtained using LS-CLE at 660 nm is comparable to line-width of 2.4 μm obtained using 488 nm LS-CLE system. To accommodate the 660 nm excitation wavelength, the dichroic and emission filters from the system reported previously are replaced with a longpass dichroic mirror M2 (Thorlabs, DMLP650R) with cut-off wavelength of 650 nm and a longpass emission filter F1 (Semrock, BLP01-664R-25) respectively. A complete list of the specification of each optical element in the system is

given in Table 5.1.

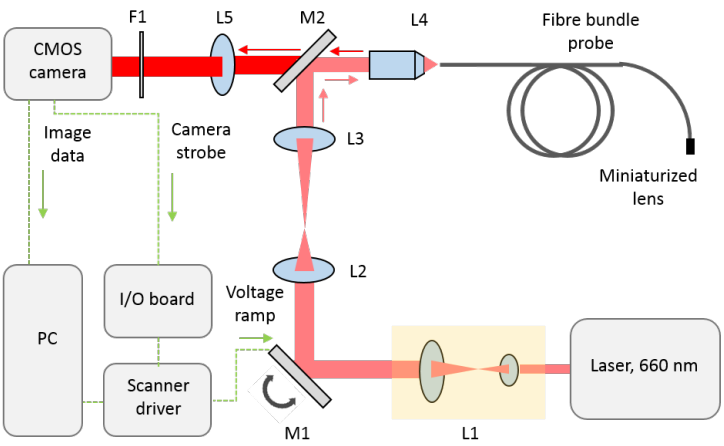

Figure 5.1: (a) Optical configuration of 660 nm line-scan confocal laser endomicroscopy (LS-CLE) system

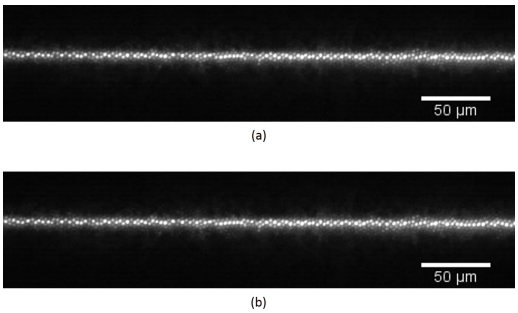

Figure 5.2: Background autofluorescence in imaging fibre-bundles. Laser line-width at the distal tip measuring using (a) 488 nm and (b) 660 nm LS-CLE system. Projected onto the proximal face of the bundle, this corresponds to a detector slit width of (a) 2.4 μm and (b) 2.6 μm.

5.2.2 System characterisation

The spatial resolution of the system is measured by back-illuminating a 1951 United States air force (USAF) resolution target with a red LED, Fig.5.3(a) shows an image of G7, E1-6 of the USAF target. For real-time visualisation, pixelation artefacts due to the fibre cores are removed by convolution with a 2D Gaussian filter (σ = 1.6 pixels, 1.4 μm on the bundle). Fig.5.3(b) shows an image of the numeral '7' of the resolution target before (top) and after (bottom) removal of pixelation artefacts and Fig.5.3(c) shows the intensity profile along the line segment (orange line) passing through horizontal line pairs of all elements of G7.

Table 5.1: Specifications of optical elements for MB aided LS-CLE imaging system

Element	Specification	Purpose	Source
L1	2X	Beam expander	Thorlabs, GBE02-A
L2	FL 50 mm	Cylindrical lens	Thorlabs, LJ1695RM
L3	FL 50 mm	Achromatic doublet	Thorlabs, AC254-050-A
L4	10X, 0.25 NA	Objective lens	Thorlabs, RMS10X
L5	FL 75 mm	Camera lens	Thorlabs, ACA254-075-A
F1	>664 nm	Emission filter	Semrock, BLP01-664R-25
M1	12.5° scan angle	Galvo scanning mirror	Thorlabs, GVS001
M2	longpass, 650 nm Cutoff	Dichroic mirror	Thorlabs,DMLP650R

The axial sectioning strength is measured by removing the emission filter and measuring the reflectance signal from a mirror as previously described in Chapter 3, Section 3.7. The distal probe tip is initially placed in contact with the mirror and then driven away using a motorised translation stage. Images are acquired for every 0.1 μm step. The average intensities from a 25×25 μm region in the centre of each image are plotted as a function of distance in Fig.5.3(d). For this study a slit width of 4 μm is used to give a HWHM of approximately 5.5 μm.

While point-scanning pCLE would probably be needed for intravenous fluorescein imaging, this partially sectioning system is sufficient for imaging tissue sites topically stained with MB and also provides the advantage of a much higher frame-rate. The high frame-rate enables image mosaics to be assembled more readily which as discussed in [215] is important for allowing features to be identified with confidence.

5.2.3 Patients and tissue preparation

The study comprises of 24 non-neoplastic and neoplastic human breast tissue specimens from 13 patients who underwent breast surgery at Imperial Breast Unit, Charing Cross Hospital (London, United Kingdom). Written informed consent was obtained from the patients using the Imperial College tissue bank ethical protocol (R-12047). Small cut-outs (∼10 mm×10 mm) are acquired following preliminary assessment and bread-folding by senior breast pathologists and imaged approximately 30-45 minutes after excision.

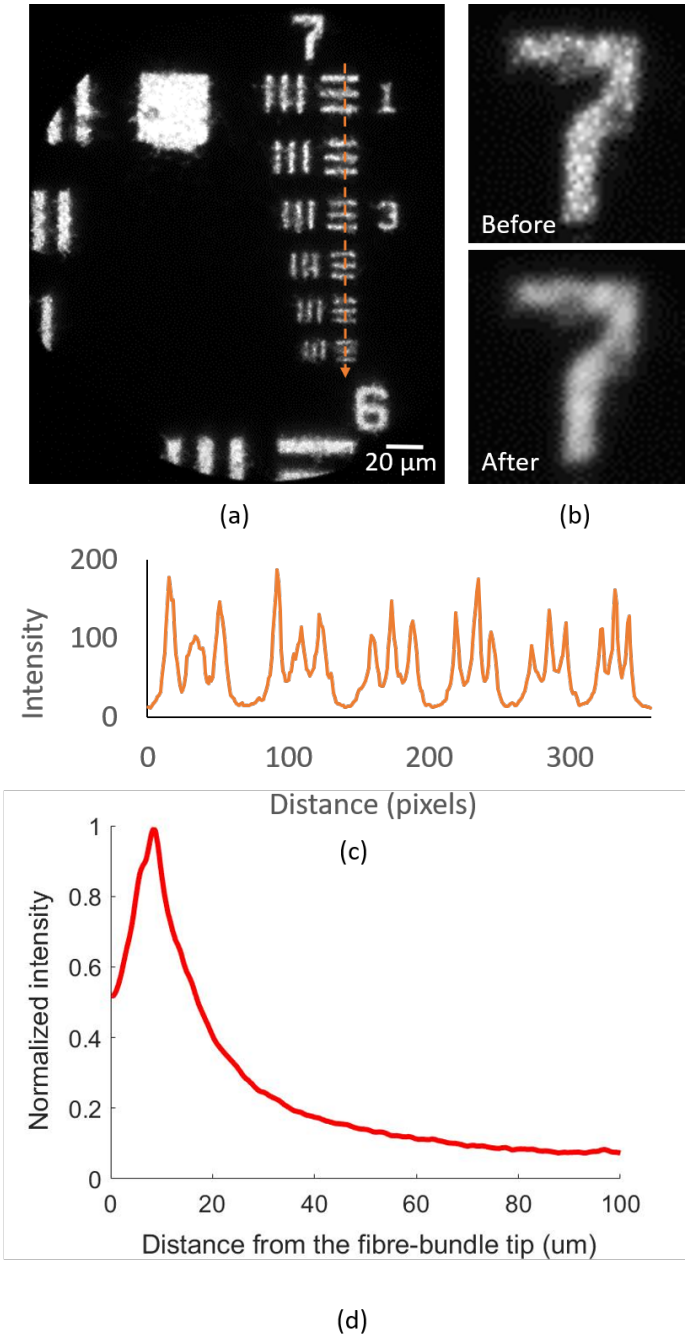

Figure 5.3: (a) Image of high-resolution USAF resolution target showing G7,E1-6 when back-illuminated with a red LED. (b) Zoomed images show numeral '7' of the resolution target before (top) and after (bottom) removal of pixelation artefacts (c) 2-D plot of the intensities of pixels along the line segment shown by an orange line on G7,E1-6. (d) Axial sectioning profile for the 660 nm LS-CLE system at a slit width of 4 μm.

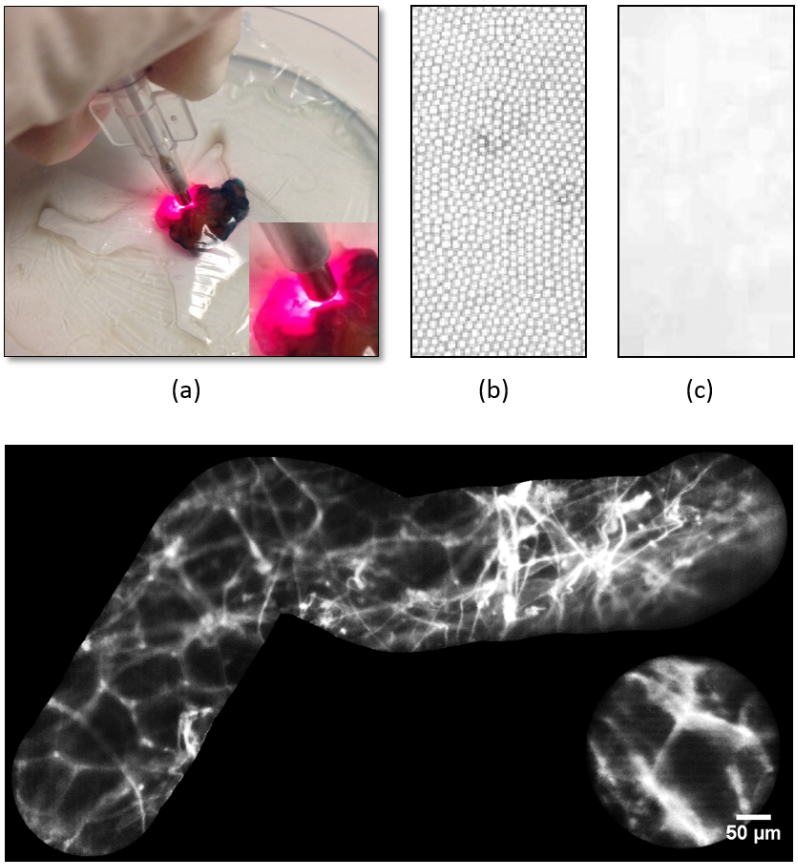

Figure 5.4: (a) Photograph of the fiber-bundle probe examining MB stained breast tissue. (b-c) Image of background autofluorescence before (b) and after (c) the removal of fibre-bundle pixelation artefacts. (d) Shows reconstructed mosaic from 550 image frames of breast stroma stained with MB. The inset shows a single acquired image frame, scale bar is 50 μm.

The cut-outs are first immersed in test tubes containing MB solution (Sigma Aldrich, UK) for 30s followed by a gentle wash with water to remove excess stain. For manual scanning, the tip of the endomicroscope probe is gently applied to the tissue as shown in Fig.5.4(a) and scanned over the tissue surface. Images are acquired at 120 fps. At the end of the imaging, excess MB dye is gently wiped off the surface of the tissue and the specimen is returned to histology for routine analysis.

5.2.4 Data acquisition and processing

Images are processed by removal of the pixelation artefacts produced due to the fibre cores by convolution with 2D Gaussian filter (σ = 1.6 pixels, 1.4 μm on the bundle). To

assist with probe scanning during image acquisition, a real-time preview of the mosaics is displayed to the operator using one-way NCC and dead-leaf blending. This was accomplished by using a custom Labview program developed by Dr. Michael Hughes. Fig.5.4(b) and Fig.5.4(c) show an image of background light before and after removal of pixelation artefacts respectively. One such mosaic generated by free-hand scanning of the tip of fibre-bundle on the tissue surface reconstructed from 550 image frames is shown in Fig.5.4(d). The inset shows a single acquired image frame, scale bar is 50 μm.

In post-processing, a mosaicking algorithm is used to stitch overlapping frames to produce a larger image that is more comparable to histology slides. This algorithm, described fully in Chapter3, Section 3.5.2, is based on an established procedure that uses two-way fast normalised cross-correlation (NCC) for pair-wise image registration [221]. The images are combined using distance-weighted alpha-blending and referred to as 'processed' mosaics.

5.2.5 Image enhancement

Although the high-speed of LS-CLE helped to minimise probe motion artefacts to a great extent, it was difficult to maintain optimum probe-tissue contact for small tissue samples with non-smooth surface. This caused a blurring effect in some frames. Furthermore, since MB is a non-specific staining dye, the image features like nuclei were sometimes not clearly distinguishable from the surrounding components. It is important to acquire high contrast images and preserve the edges of such micro-structures for further detection, localisation and computer-aided classification applications.

To overcome these challenges and improve the contrast of detectable features, an algorithm for endomicroscopy image enhancement is developed. The processed mosaics generated in Section 5.2.4 are used as input images. The image enhancement is a two-step process: the first step is histogram equalisation (HE) for adjusting contrast and the second step consists of applying an edge operator to improve the local image details. Image enhancement is performed offline using ImageJ, however, all the process steps are computationally inexpensive and could be done in real-time. The brightness and contrast of the mosaic are optimised based on HE using ImageJ's 'enhance contrast tool'. Following this a Sobel edge detector is applied to highlight sharp changes in intensity using ImageJ's 'Find edges tool'. Two 3×3 convolution kernels are used to generate vertical and horizontal derivatives.

$$\begin{bmatrix} 1 & 2 & 1 \\ 0 & 0 & 0 \\ -1 & -2 & -1 \end{bmatrix} \qquad \begin{bmatrix} 1 & 0 & -1 \\ 2 & 0 & -2 \\ 1 & 0 & -1 \end{bmatrix}$$

The final 'enhanced' mosaic is produced by combining the two derivatives using the square root of the sum of the squares and pseudo-coloured (ImageJ, LUT Green-fire-blue) to display the enhancements. The 'processed' and 'enhanced' mosaics are stored digitally in a prospectively maintained database.

5.3 Results

5.3.1 Methylene blue dosage

Prior to the start of this study, a preliminary assessment is carried out on 2 cut-outs (∼30×30 mm) of non-neoplastic breast tissue obtained from 2 patients. Each tissue specimen is further cut in 4 smaller samples and stained with MB concentrations of 0.1%, 0.2%, 0.5% and 1%. On an average, 3 imaging tests are performed on each smaller sample and a total of 120 image mosaics are generated. For each concentration, the fluorescent agent is left to stain the tissue for 30s. After staining, the cut-outs are gently rinsed with water to wash off excess stain for 1 minute and imaged immediately.

A photograph of 4 samples stained with different MB concentrations is shown in Fig.5.5. From visual inspection it is evident that for all samples, the uptake of MB in the stroma is much higher than the adipose tissue, and it increases with increase in concentration. Further for 0.5% and 1% MB, the stroma appear heavily and uniformly stained indicating that it might be difficult to distinguish between different glandular and stromal components.

Endomicroscopy images of normal samples at different staining concentrations are shown in Fig.5.5. Morphological features are identified following the taxonomy of breast pathologies developed previously and the image quality is assessed from the visibility of those features in the reconstructed mosaics. In LS-CLE images, the adipose tissue appeared as uniform dark polygon shapes with hyper-fluorescent borders and sparsely populated nuclei as bright spots along the borders. The fibrous connective tissue appeared as well-defined hyper-fluorescent bundles of elastic wavy fibres with sparse bright spots corresponding to fibroblast nuclei in the stroma. Fig.5.5(c-d) had excessive fluorescence retained despite repeated washouts with water and the underlying morphological architecture could not be discerned.

The mosaics are scored '1', '2' or '3' based on the clarity with which the tissue structure is visualised (where '1'- almost invisible structure, '2'- partly visible and '3'– clear classification of tissue morphology). The rationale for this categorisation is that if the tissue is stained non-specifically, different tissue structures such as fat cells, nuclei and connecting fibres would all be stained uniformly, thus making it difficult to distinguish them. Fig.5.7 shows the overall scores from the assessment of tissue structure visibility in LS-CLE mosaics stained at different concentrations.

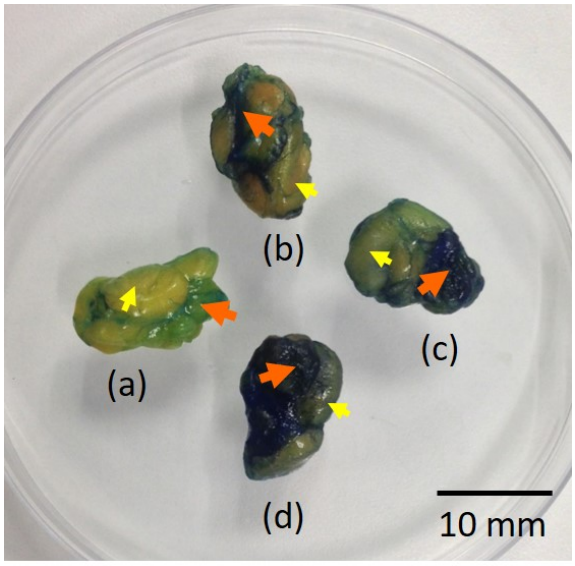

Figure 5.5: Photograph of four non-neoplastic breast tissue specimens, acquired from a single patient, and stained with MB at (a) 0.1%, (b) 0.2%, (c) 0.5% and (d) 1.0% concentration. Orange arrows indicate the stroma and yellow arrows indicate the adipose tissue sites.

From Figs.5.5 - 5.7 it is evident that for non-neoplastic tissue, for 0.1% and 0.2% of MB, tissue structure is clearly visible and nuclei are visible as bright spots. For higher concentrations of 0.5% and 1%, even though adipose tissue is partially visible, the hyper-fluorescent, thread-like connective fibres are not identified and the stoma appears uniformly bright thus reducing overall contrast and making it difficult to distinguish different morphologies. The results corroborate with existing literature on endomicroscopy imaging of lung nodules suggesting a MB concentration of 0.1% [251]. Based on the above, all tissue cut-outs are stained using 0.1% concentration solution.

5.3.2 Comparison with AH staining and histology

The main purpose of this pilot study is to determine that the 660 nm LS-CLE system with MB can identify features following the taxonomy of pathologies developed using AH and Cellvizio pCLE [244]. A total of 720 image mosaics (mean 30 per sample; range 20-40) are generated from 24 specimens. Since a limited number of tissue samples are used, many more mosaics are acquired than necessary for detailed performance assessment. With slow and controlled hand-held manipulation of the imaging probe, it is possible to generate high quality mosaics to expand the FOV by up to eight times ($\sim$ 2 mm) to create more representative and interpretable LS-CLE images. The final histopathology diagnosis from these samples showed 7 neoplastic, 6 benign and 11 non-neoplastic tissue pathologies.

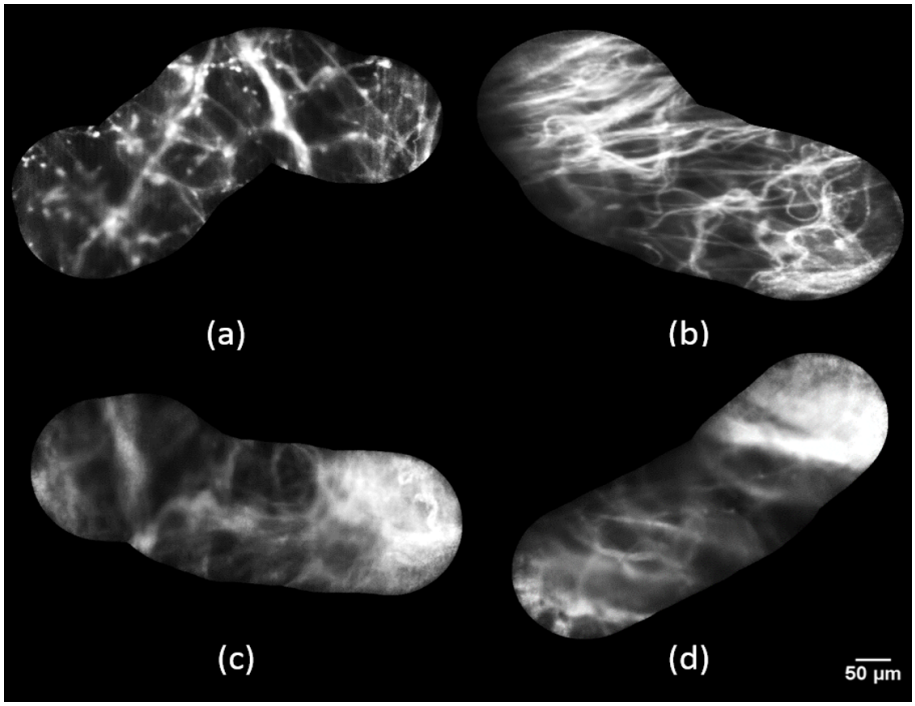

Figure 5.6: Representative endomicroscopy mosaics of non-neoplastic breast tissue stained with MB at (a) 0.1%, (b) 0.2%, (c) 0.5% and (d) 1.0% concentration. Scale bar is 50 μm.

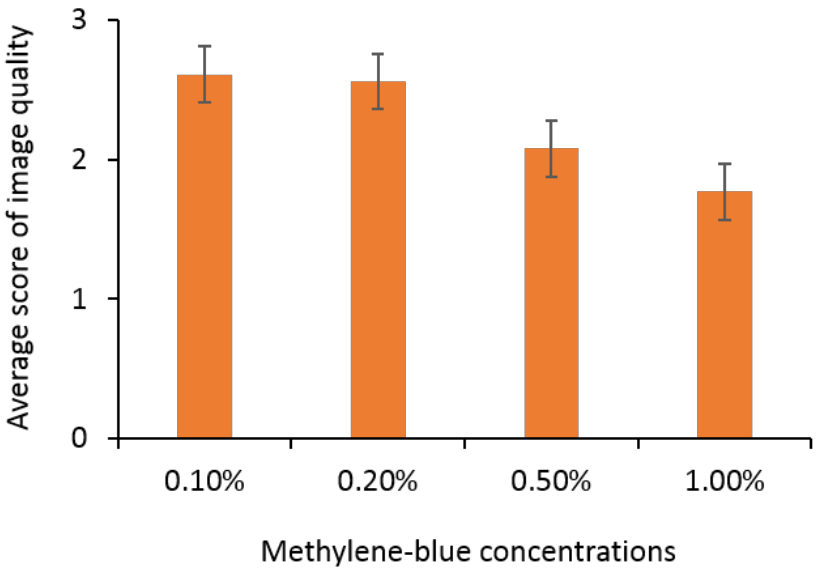

Figure 5.7: Overall scores from the assessment of tissue structure visibility at different MB concentrations.

LS-CLE 'processed' mosaics obtained with MB staining were visually compared to pCLE mosaics collected by Dr. Tou Pin Chang with AH demonstrating similar architectural features. Two features typifying normal breast tissue are identified: adipose tissue and the presence of collagen and elastic fibres in the stroma. As shown in Fig.5.8(A) the fluorescence images obtained from MB (top) and AH stained adipose tissue (middle) depict similar morphological features: the well-defined and uniform dark polygon shape of the adipose tissue with hyper-fluorescent borders can clearly be observed in both cases with sparsely populated nuclei as bright spots on the borders. Further the structure of adipose tissue corroborates well with H&E stained histology images. In Fig.5.8(B) the fibrous connective tissue appears as hyper-fluorescent bundles of elastic wavy fibres with spare fibroblast nuclei appearing as hyper-fluorescent dots.

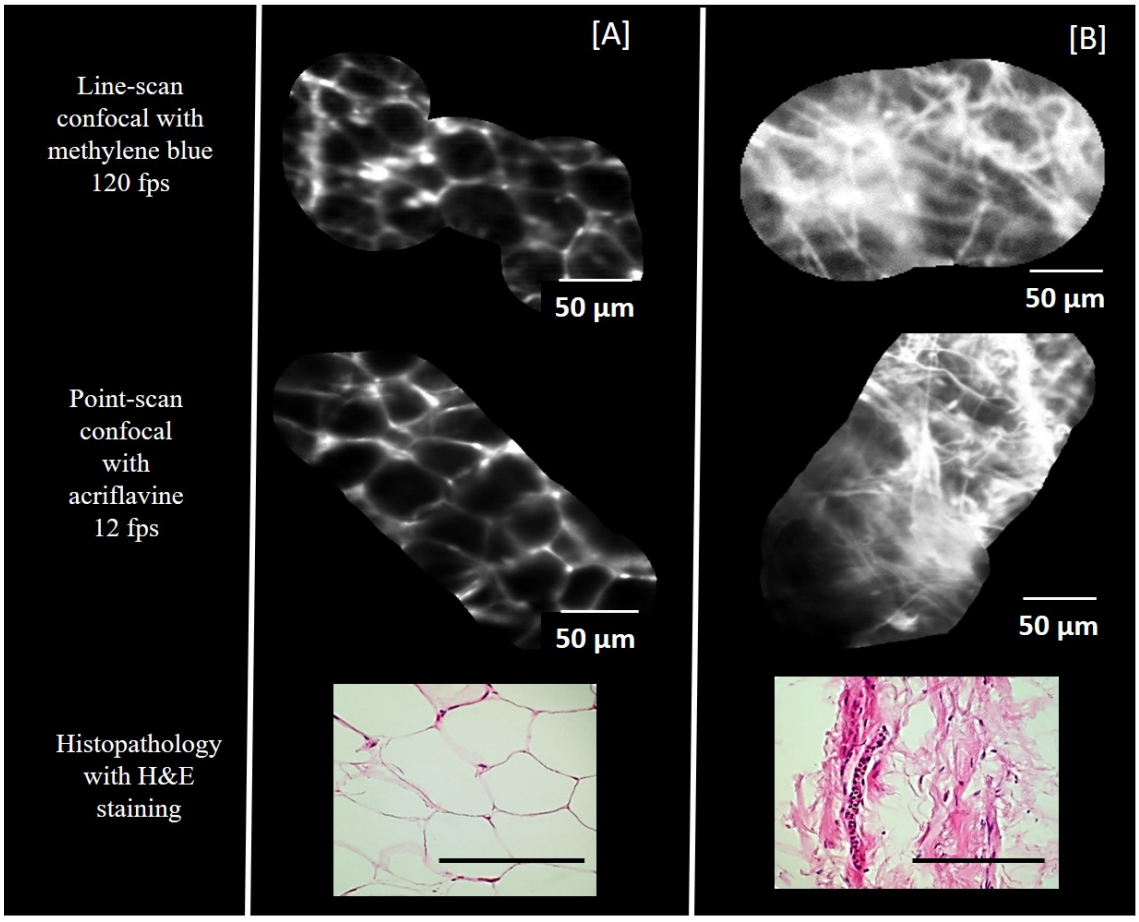

Figure 5.8: Normal breast tissue imaged with LS-CLE with MB (first row), point-scan pCLE with AH (middle row) and conventional histology with H&E staining (bottom row). Non-neoplastic features shown are adipose tissue [A] and fibrous connective tissue [B]. Scale bar is 50 μm.

Fig.5.9(A) represent fibrocystic changes where compressed bright slit-like glandular spaces are surrounded by loose fibrous stroma. The lumen is enlarged and remained dark grey-coloured due to presence of calcification. Fig.5.9(B) represents fibrous scarring in the stroma due by increase in dense connective tissue. The dense connective tissue appears as grey fibrous mass on MB and AH stained tissue images. In Fig.5.9(C) stroma composed of spindle-shaped myofibroblasts appear as small hyperfluorescent oval shapes surrounded by weakly stained grey collagen fibres.

The MB aided LS-CLE system also enable comparable visualisation of distinctive neoplastic changes characterised by increased cellularity in the stroma as depicted in Fig.5.10(A) and (B). Consistent with findings from the previous chapter, the disorganised distribution of cell nuclei and the unclear tissue architecture is clearly visible as large clusters of hyper-fluorescent spots. Similar features are observed in AH stained tissue (middle row) and matched histology images (bottom row).

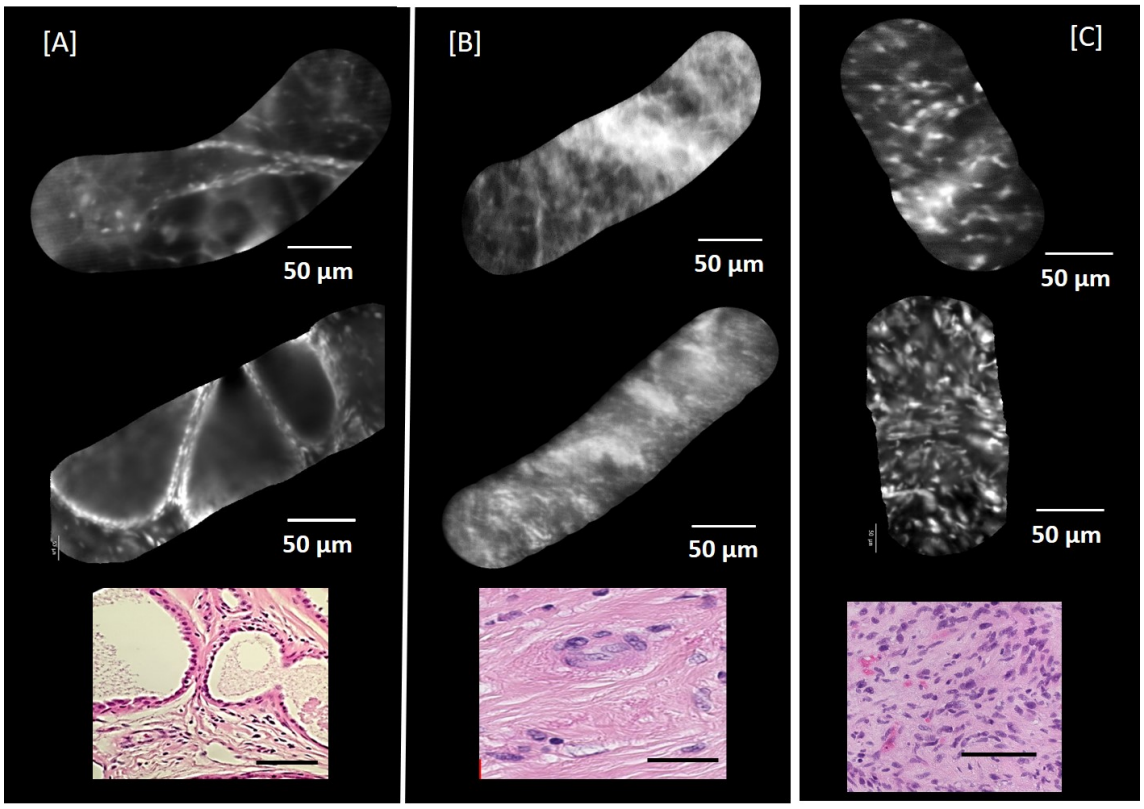

Figure 5.9: Benign breast tissue imaged with LS-CLE with MB (first row), pCLE with AH (middle row) and histology with H&E staining (bottom row). Benign features shown are fibrocyctic changes [A], fibrous scarring [B] and Spindle cell myofibroblasts [C]. Scale bar is 50 μm.

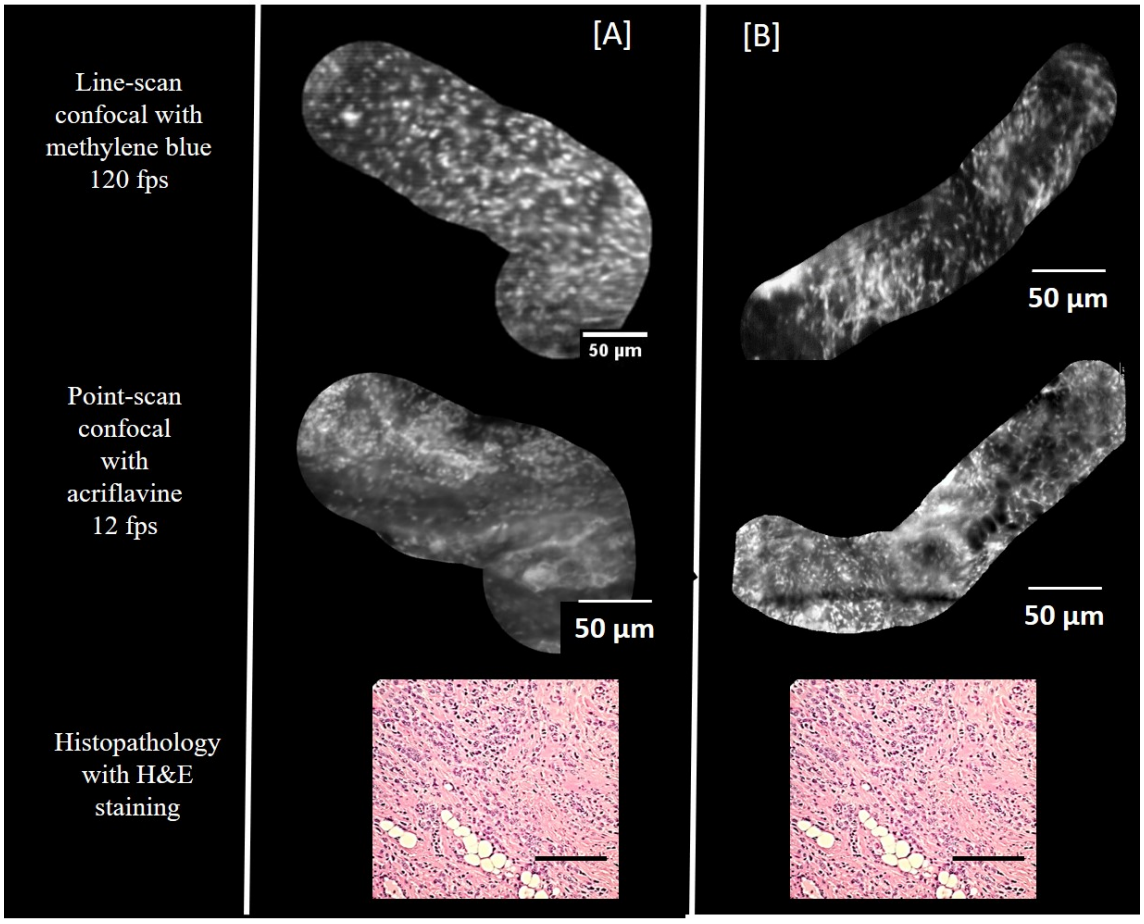

Figure 5.10: Neoplastic breast tissue imaged with LS-CLE with MB (first row), point-scan pCLE with AH (middle row) and conventional histology with H&E staining (bottom row). Neoplastic features shown are [A] invasive ductal carcinoma (IDC) where a broad area of densely packed nuclei which appear as hyper-fluorescent dots with disorganised appearance. [B] represents invasive cancer infiltrating into fat. Scale bar is 50 μm.

5.3.3 SNR comparison

In addition to visual comparison, a signal-to-noise (SNR) based evaluation is carried out to quantitatively evaluate the imaging capabilities of AH and MB staining using pCLE and LS-CLE respectively. For both the systems, the SNR is obtained by the ratio of the mean intensity of a homogeneous stained area of 10×10 pixels of the tissue (signal) to the standard deviation of an unstained region of 10×10 pixels (noise). Averaged across 100 images, the measured SNR is (185±13) for the AH stained images and (176±18) for the MB stained images. Despite the differences in stain, imaging system and processing, the noise in the final processed images are broadly comparable.

5.3.4 Image enhancement results

The results of LS-CLE images before and after the application of the image enhancement algorithm are presented here. Some representative images of normal breast tissue features like adipose cells (A,D) blood vessels (B,E) and elastic fibres (C,F) and are shown in Fig.5.11. Benign conditions like fibrocystic changes (A,C) and fibrosis (B,D) are shown in Fig.5.12 and neoplastic conditions like DCIS (A,C) and IDC (B,D) are highlighted in Fig.5.13.

From Figs.5.11-5.13, it can be seen that structural details of the fibres, ducts and adipocytes are more visible with higher contrast on the enhanced images as compared to grey-scale 'processed' images. Further, contours of nuclei are highlighted, making it possible to distinguish nuclei from the surrounding structures. Additionally, Fig.5.12(D) shows an increase in visibility of moderately-stained thread-like wavy fibres as opposed to a dense cloud like cluster of fibrous tissue seen in Fig.5.12(B). A noticeable enhancement in visibility and contour detection of nuclei is also seen in the images of DCIS Fig.5.13. Such an enhancement could to used to further identify, highlight and segment individual nuclei and calculate parameters such as nuclear density and size.

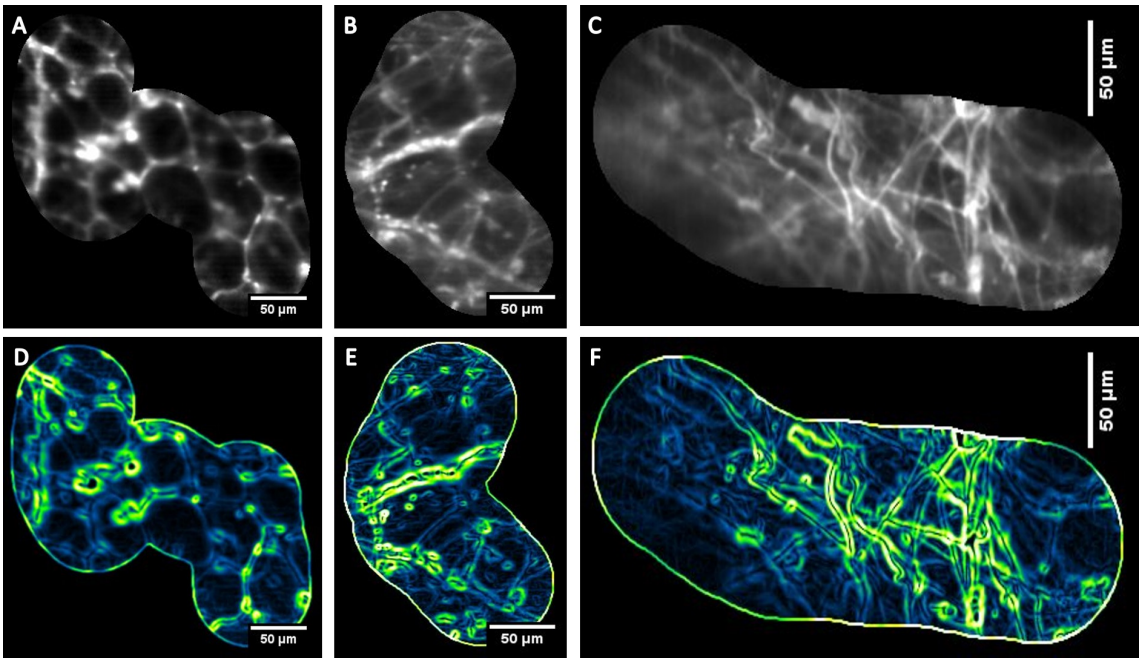

Figure 5.11: Input 'processed' grey-scale LS-CLE images of normal breast tissue obtained after MB staining (A-C, top row) and corresponding pseudo-coloured 'enhanced' mosaics obtained using proposed 2-step image enhancement method (D-F, bottom row). Scale bar is 50 μm.

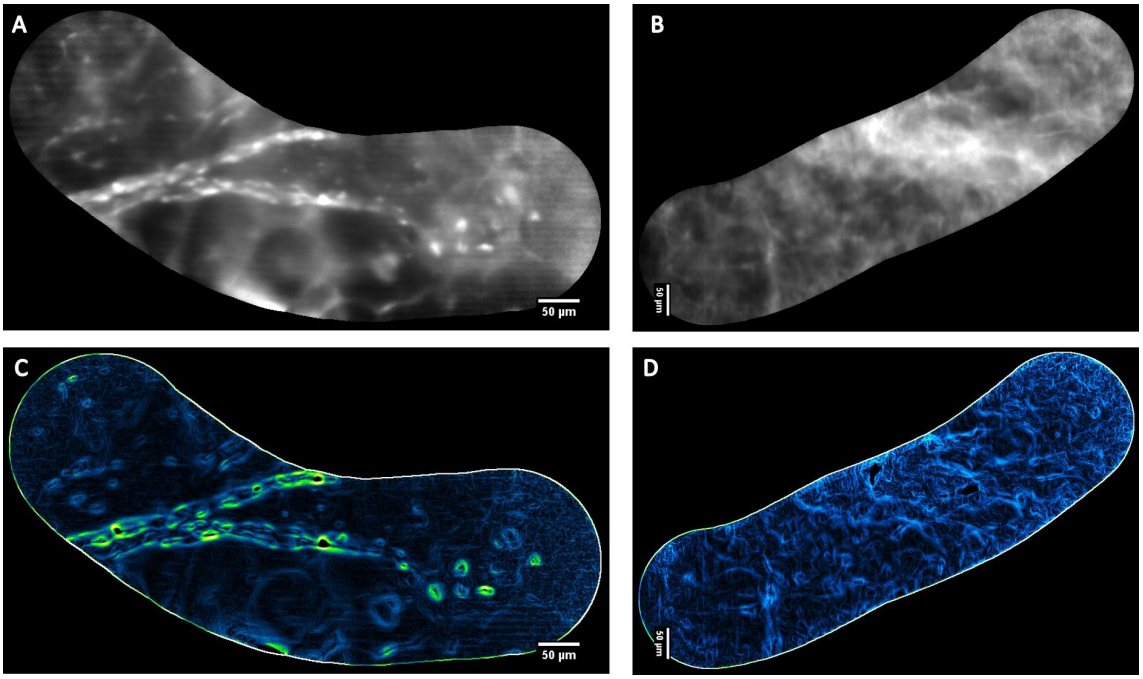

Figure 5.12: Benign breast tissue imaged with LS-CLE with MB staining, each image comprises of a grey-scale confocal (A-B, top row) and corresponding pseudo-coloured enhanced mosaics (C-D, bottom row). Scale bar is 50 μm.

5.4 Discussion

The objective of this work is to determine if assessment of breast architecture using MB as a staining agent has comparable performance to AH staining and conventional histology. The findings of this study show that LS-CLE images of unfixed breast tissue stained topically with MB provides adequate information to visually and qualitatively assess different non-neoplastic and neoplastic breast features. The portable size of the LS-CLE system together with rapid staining capabilities of MB, makes it an attractive tool for intra-operative cavity scanning in a routine clinical scanning. This could allow the surgeon to accomplish more accurate and complete surgical resections, thus reducing the re-operation rates and improve surgical outcomes. To the best of our knowledge, this is the first study to describe use of MB and LS-CLE to visualise breast tissue morphology.

The specimen staining and imaging protocol is very fast and simple. Freshly excised unfixed tissue samples are stained topically with 0.1% MB solution for 30 s and washed to remove excess stain. The stained sample is immediately imaged without any further preparation or processing. Using the LS-CLE system, cellular level images of the tissue surface are acquired at 120 fps with 2.2 μm lateral resolution and displayed in real-time.

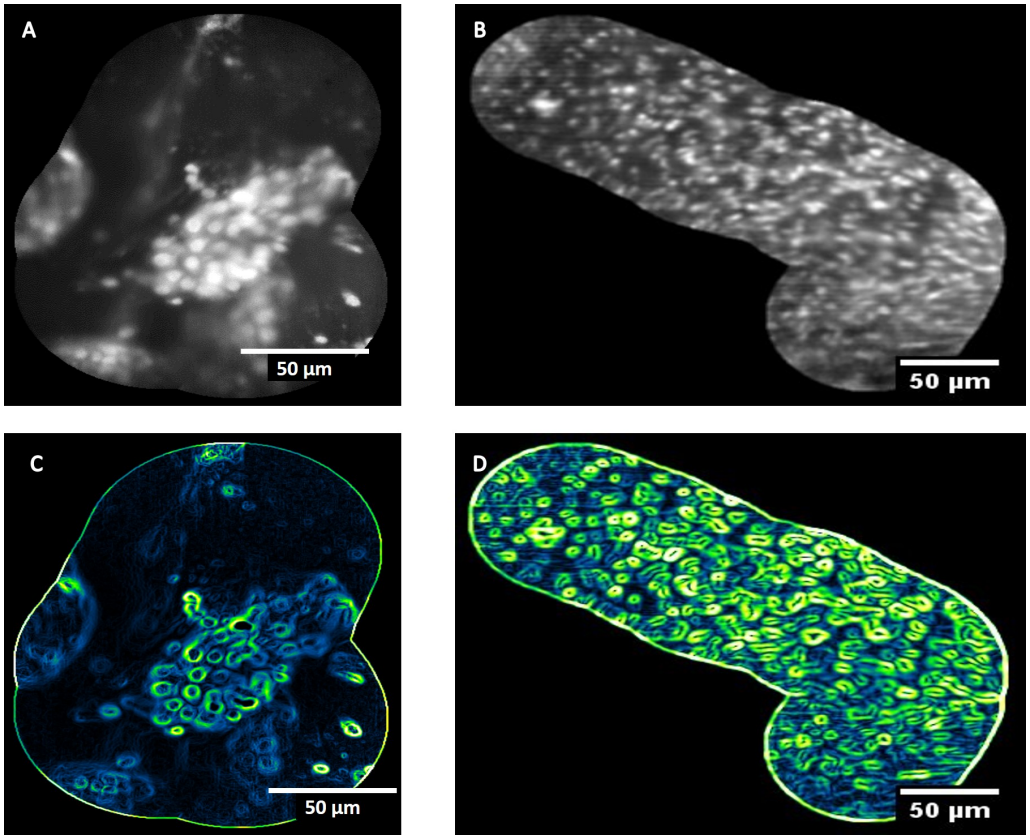

Figure 5.13: Neoplastic breast tissue imaged with LS-CLE with MB staining, each image comprises of a grey-scale confocal (A-B, top row) and corresponding pseudo-coloured enhanced mosaics (C-D, bottom row). Scale bar is 50 μm.

In all patients a non-specific staining of both glandular and stromal components is found on using MB. The MB aided LS-CLE produced images with comparable contrast to point-scanning pCLE with AH staining for both neoplastic and non-neoplastic tissues, but with the advantage of a higher frame rate and use of a safe and regulatory-approved (off-label) stain. It is also observed that visually, the contrast of invasive cancer tissue stained with MB is slightly poorer as compared to that from AH. Since acriflavine has nuclear-staining capabilities, it is observed that tissue specimens with increased cellularity are visualised with higher contrast. On the other hand, MB binds to negatively charged particles in the cells such as DNA in the fibroblast nucleus as well as RNA in the cytoplasm with low affinity. As a result it may not only stain the nuclei but also the surrounding stroma and connective fibres to some extent. Nevertheless from the undertaken experiments, the uptake of MB by neoplastic tissue is visually observed to be remarkably higher than non-neoplastic tissue.

5.5 New developments

In this section, two novel applications for the developed LS-CLE system are presented. The first application discusses the integration and testing of the LS-CLE system with a robotic scanner to aid large-area mosaicking without sacrificing resolution. In the second advancement, the LS-CLE system at 660 nm is extended to achieve high speed dual-wavelength imaging (at 488 nm and 660 nm) of fresh tissue specimens stained with multiple contrast agents. The robotic integration and multi-wavelength aspects of this study are still in early stages. The imaging results presented here are intended to give an idea of incorporating single and dual wavelength LS-CLE system with a portable robotic scanning device and demonstrate large-area imaging, which potentially could be beneficial for *in vivo* cavity scanning.

5.5.1 Integration with robotic scanner

This section demonstrates the integration of LS-CLE with robotic scanning probe for large-area imaging applications. For this work, robot-assisted endomicroscopy is achieved by the use of a high-speed, rigid robotic scanning device designed for CLE and laser ablation into which the LS-CLE imaging fibre-bundle is introduced. The robotic device developed by Giataganas et al. enables large-area forward viewing LS-CLE imaging by scanning the fibre-bundle tip in 2D on the tissue surface, without any axial position control [256]. In post-processing, a mosaicking algorithm as presented in Section 5.2.4 is used to stitch the acquired images obtained during scanning. The reconstructed mosaics are enhanced using the algorithm presented in Section 5.2.5. Full details can be found in [256]. In summary, it consists of a 58 mm long hollow steel tube, with outer diameter 3.3 mm, through which imaging probes can be passed. This tube is mounted inside a 3D printed case and fixed in place at the back of the case. At the distal end, the tube is fixed to a cam-roller assembly which allows it to be deflected in two dimensions by the rotation of two brush-less DC servomotors. This allows the tip of the tube to be moved over a 2D work-space of up to 14 mm^2 with an absolute positioning accuracy of better than 30 μm. The tube is offset within the assembly so that it is always under load throughout the entire work-space, minimising backlash and hysteresis effects.

The robotic scanner is driven *via* two analog input signals applied to the motor controllers. At the tip of the tube, a holder with an outer diameter of about 3.7 mm is fixed. The holder is custom designed to hold a Mauna Kea Cellvizio Gastroflex UHD endomicroscopy probe (diameter of 2.6 mm) and a laser ablation fibre (diameter of approximately 0.7 mm). The axial positions of the probes were fixed at the rear end of the device case. Fig.5.14 shows a photograph of the robotic scanner mounted on a passive arm.

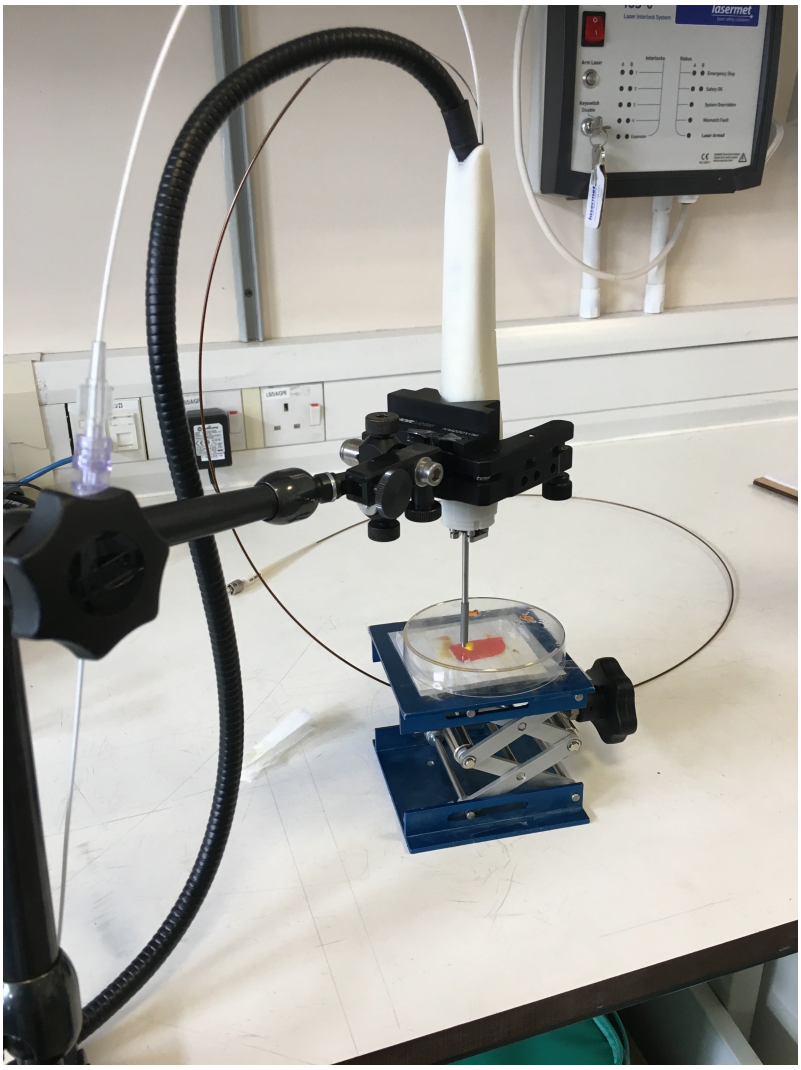

Figure 5.14: Photograph of rigid scanner clamped on a passive arm

The performance of robot-assisted LS-CLE system with MB staining is assessed by conducting *ex vivo* tissue experiments. Representative images of normal and neoplastic breast tissue obtained using the robotic scanner are shown in Fig.5.15. For these experiments, the robotic scanner is mounted on a passive arm. The tissue was stained with 0.1% MB solution based on the protocol described earlier and imaged immediately. The tip of the fibre-bundle inside the scanner was manually brought in contact with the tissue surface such that the scanner was perpendicular to the tissue. Once positioned, the surface of the tissue was scanned in a spiral pattern by the robotic probe and large mosaics areas up to 3 mm^2 were obtained.

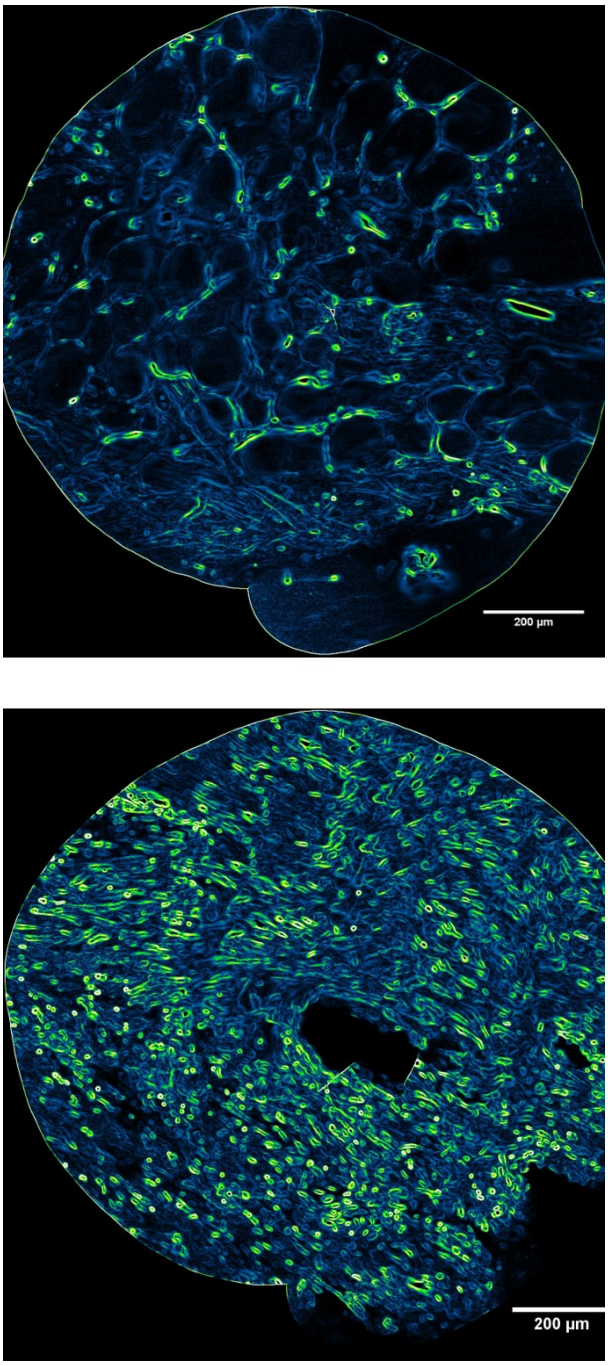

Figure 5.15: Representative enhanced MB-aided LS-CLE mosaics of (a) normal adipose tissue and (b) IDC acquired using a robotic scanning device. Large-area mosaics covering 1.3×1.3 mm of the tissue surface are reconstructed using a spiral scanning pattern. Scale bar corresponds to 200 μm.

In the acquired mosaics, consistent with the earlier findings, the morphological features corresponding to adipose tissue appear as dark hexagons and hyperfluorescent borders with spare nuclei as bright dots on the borders, as shown in Fig.5.15(a). The neoplastic changes are represented by increased cellularity as bright dots and non clear distinction between stromal and glandular components, as shown in Fig.5.15(b). These preliminary results demonstrate that feasibility of obtaining histology-like images over a large-area of 3 mm^2 in less than 10s without the removal or destruction of any tissue structure.

5.5.2 Dual-wavelength line-scan confocal endomicroscopy

This section will provide details of the architecture and preliminary tests of a dual-wavelength LS-CLE system that is suitable for high-resolution and rapid multiplexed imaging. There are two ways of reconstructing a dual-wavelength LS-CLE image from a set of images acquire under different illumination or detection spectral conditions: through simultaneous imaging or by sequential imaging. Imaging of two or more fluorescent probes at the same time is referred to as simultaneous image collection. Usually both the illumination lasers are kept on and two separate and synchronised detectors are used to collect the dual excitations. Such simultaneous imaging is advantageous for rapid multi-spectral imaging with no temporal displacement between the acquired images - this is especially useful to image organisms and cellular processes in live tissues. However, for broad emission and excitation spectra, cross talk due to spectral bleed-through makes it very challenging to separate different fluorophores.

A better approach is to take sequential images using filters matching the excitations/emission spectra of each dye. Sequential imaging involves exciting fluorophores on a sample with only one laser wavelength at a time and collecting fluorescent light emitted by the excited fluorophores. By switching the source wavelength and detecting photons emitted from another fluorophore, spectrally separate signals can be detected with minimal bleed-through. As a result, motion and synchronisation artefacts can be greatly reduced but at the expense of reducing the image acquisition rates. This makes it difficult to image moving objects. Conventional multi-wavelength CFM systems sequentially modulate the illumination or detection wavelength by using filter wheels or tunable filters. The slow transition times of such mechanical filters, however, reduces the overall image acquisition speed. In the proposed design, rapidly modulated laser diodes digitally triggered using a DAQ card are used to produce wavelength modulation. A multiband filter set is used to rapidly multiplex fluorescent and absorption spectra for multicolour imaging. Cross talk is minimised by using fluorophores that have spectrally separated emission spectra.

A prototype dual-wavelength LS-CLE is built by extending the design of single wavelength LS-CLE system described in Chapter 5, Section 5.2.1. The schematics of the optical system is shown in Fig.5.16. A full list of components is presented in Table 5.2. The prototype consists of three subsystems: illumination arm, sample arm and detector arm. The illumination arm consists of two continuous wave laser sources: a laser diode at 488 nm (Vortran Stradus 488 nm, 50mW) and a laser diode at 660 nm (Vortran Stradus 660 nm, 100mW). A longpass dichroic beamsplitter (Thorlabs, DMLP605) with reflection band of 470-590 nm and transmission band of 620-700 nm is used to co-align the two laser sources. The combined laser beams then pass on to the scanning mirror *via* a 2× beam expander. The other illumination optics are same as the single wavelength LS-CLE system. The fibre-bundle transmits the scanned line profiles to the tissue surface via 10× microscope objective. The induced sample fluorescence is relayed back to the optical system via the same fibre-bundle.

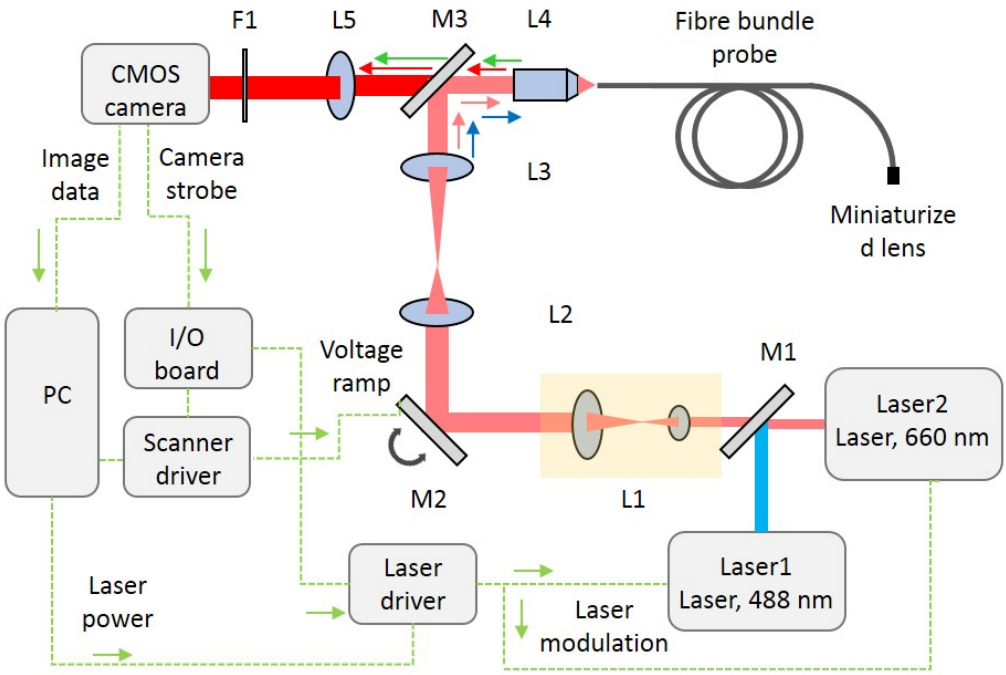

Figure 5.16: Optical configuration of dual-wavelength LS-CLE system operating at 488 nm and 660 nm wavelength.

A monochrome rolling shutter CMOS camera (Point Grey Flea3, FL3-U3-13S2M-CS) used in conjunction with an appropriate multi-band filter set (Semrock, DA/FI/TR/Cy5-A-000) is chosen to simplify the optical design for application in a clinical environment. A multiband beam splitter (Semrock, FF410/504/582/669), that transmits multiple narrow

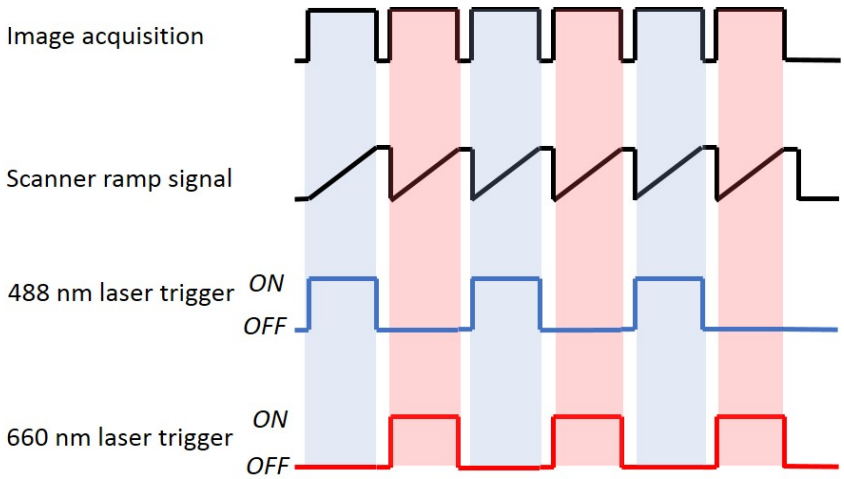

Figure 5.17: The control signals for the galvanometer scanning mirror, CMOS camera and laser source modulation.

spectral bands and reflects desired wavelength ranges is used to direct the emission into the detector arm. In the current configuration, the beam splitter transmits 510-531 nm and 677-722 nm wavelengths and reflects 475-495 nm and 643-656 nm wavelengths. In the detector arm, a multiband emission filter (Semrock, FF01-440/521/607/700-25) is used to allow desired narrow spectral bands to pass through to the CMOS camera detector. Further, each dichroic beam splitter is mounted on a gimble optical mount on a locking baseplate so that they could be easily interchanged to use additional lasers and excite multiple fluorophores. As a result, multicolor imaging with additional laser sources could be achieved with minor hardware and software modification.

Image formation is accomplished by synchronising the operations of the scanning mirror, laser modulation and camera strobe using an input/output DAQ board (National Instruments USB-6343), as shown in Fig.5.17. During imaging, the camera generates a pulse on its strobe output pin at the start of each frame acquisition. The pulse triggers the analog output of a DAQ which is programmed to send a ramp-shaped voltage signal to the galvo mirror on each trigger, with a user-specified delay. Simultaneously, the pulse also triggers the analog output of the DAQ board to sequentially switch the lasers ON and OFF such that alternate image frames are acquired at each laser wavelength. This allows the camera to operate in free-run mode, with which the full frame-rate of 120 fps and effective frame rate of 60 fps can be obtained with 512×512 pixels. Complementing the high speed performance, such a system also allows to individually tune the power of each laser such that optimum SNR and dynamic range can be achieved.

Table 5.2: Specifications of optical elements for dual-wavelength LS-CLE imaging system

Element	Specification	Purpose	Source
Laser1	488nm, 50mW	Laser source	Vortran, 488nm
Laser2	660nm, 100mW	Laser source	Vortran, 660nm
L1	2X	Beam expander	Thorlabs, GBE02-A
L2	FL 50mm	Cylindrical lens	Thorlabs, LJ1695RM
L3	FL 50mm	Achromatic doublet	Thorlabs, AC254-050-A
L4	10X, 0.25 NA	Objective lens	Thorlabs, RMS10X
L5	FL 75mm	Camera lens	Thorlabs, ACA254-075-A
F1	Quad-band	Emission filter	Semrock, FF01-440/521/607/700-25
M1	Long-pass, 605nm Cutoff	Dichroic mirror	Thorlabs, DMLP605
M2	12.5° scan angle	Galvo scanning mirror	Thorlabs, GVS001
M3	Quad-band	Dichroic mirror	Semrock, FF410/504/582/669

The performance of dual-wavelength LS-CLE system for multiplexed imaging is assessed by conducting experiments on phantoms and *ex vivo* breast tissue specimens. The 488 nm excitation is used with Acriflavine, a non specific dye to stain epithelial cells and NucGreen® Dead 488 ReadyProbes® Reagent, a cell-impermanent stain that emits green fluorescence when bound to DNA for more targeted staining of nuclei. The 660 nm excitation is used with methylene blue for general staining of tissue morphology and staining nuclei to some extent.

Fig.5.18 shows image of lens tissue paper stained with AH and MB, using dual wavelength LS-CLE system. The imaging was performed using the robotic probe to scan a region of tissue paper where both dyes meet. The results reveal the intricate thread structure of the lens paper and how the scanning and mosaic preserves the continuity of threads through the image. The red fibres indicate the region stained with MB, green with AH and yellow is where both the dyes interfere. A similar effect is seen in images of normal adipose cells of human breast tissue which were stained with AH followed by a staining with MB as shown in Fig.5.19. Since both the dyes are non-specific, they tend to highlight similar tissue morphology.

Fig.5.20 shows image of benign human breast tissue imaged in dual-wavelength imaging mode stained using non-specific and specific dye. The tissue specimen is stained with 0.01% of MB for 1 minute, washed with PBS saline and re-stained with NucGreen Dead 488 for 5 minutes. While MB stains the tissue morphology, nuclei-green highlights individual cells. The figure demonstrates that fibrocystic tissues can also be effectively examined by selectively highlighting dense fibrous tissue in red and fibroblasts in green. These preliminary results indicate the capability of imaging tissue stained with multiple dyes using LS-CLE. The results demonstrate the capability of imaging tissue stained with multiple dyes using LS-CLE, however investigations are preliminary. The specific combination of fast-acting staining agents, staining protocols and applications of this system are currently being explored. Studies to explore additional stain combinations and demonstrate the clinical feasibility of the technique are currently underway.

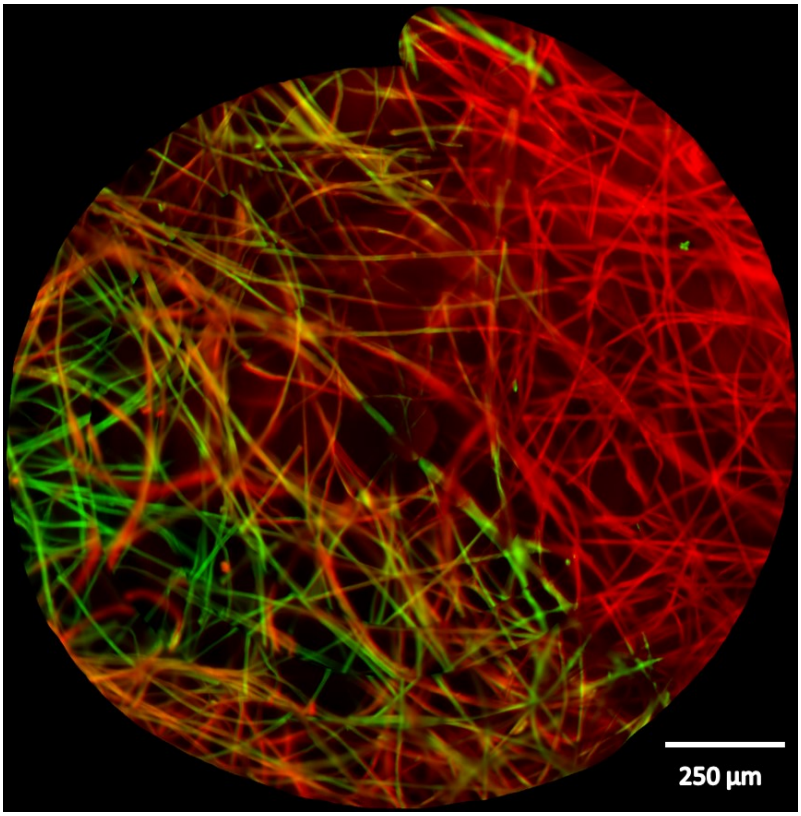

Figure 5.18: Dual-colour LS-CLE image mosaic of lens cleaning tissue paper stained with acriflavine (green) and methylene blue (red) acquired by robotic scanning in spiral scanning pattern. The scale bar is 250 μm.

.

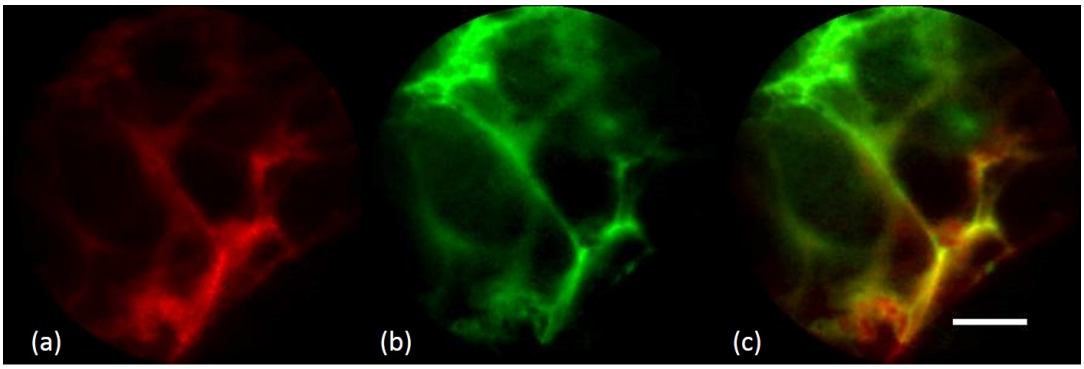

Figure 5.19: Dual-colour single LS-CLE image frame of adipose cells of normal human breast tissue stained with acriflavine and methylene blue. (a) Red channel showing methylene blue, (b) Green channel showing acriflavine and (c) Merged image. The scale bar is 50 μm.

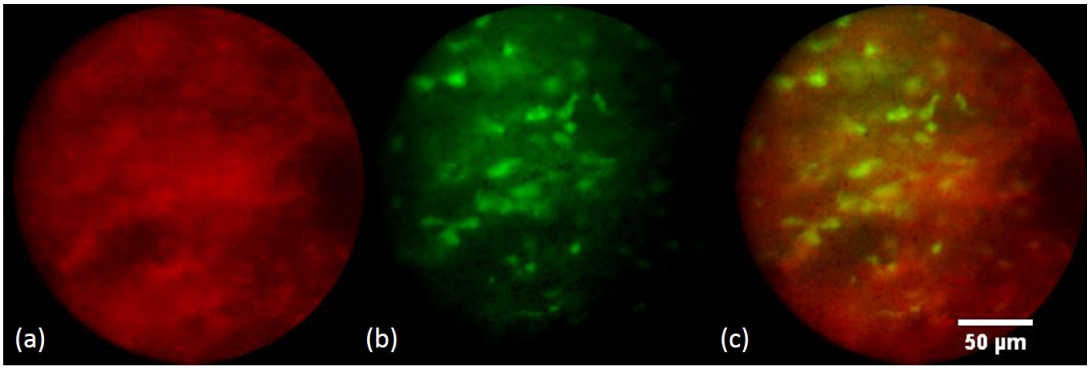

Figure 5.20: Dual-colour single LS-CLE image frame of adipose cells of benign human breast tissue stained with NucGreen 488 Dead and methylene blue.(a) Red channel showing tissue morphology highlighted by methylene blue, (b) Green channel shows nuclei stained with NucGreen 488 Dead and (c) Merged image. The scale bar is 50 μm.

5.6 Conclusion

In summary, a high-speed 660 nm LS-CLE system has been used with topical application of 0.1% MB to demonstrate rapid morphological assessment of *ex-vivo* breast cancer tissues. Images and mosaics of normal and neoplastic breast tissue, acquired with a lateral resolution of 2.2 μm at 120 Hz, showed distinctive morphological features. The MB aided LS-CLE produced images with comparable contrast to point-scanning CLE with AH staining, but with the advantage of a higher frame rate and use of a safe and regulatory-approved (off-label) stain.

In the last section of this chapter, novel advancements on LS-CLE system are presented. The high-speed of LS-CLE is found to be very beneficial in creating long and continuous mosaics using a robotic scanning device. The creation of long mosaics in envisaged to provide a distinct advantage in breast cavity wall scanning. Using low frame rate systems like Cellvizio pCLE, there exists a risk of introducing sampling errors while scanning large and non-smooth areas like that of breast cavity and as a result miss tumour cells that may be present in the gap between two short mosaic acquisitions. Robot-assisted LS-CLE with MB staining provides large coverage of the tissue surface in a timely manner and hence suspicious tumour sites could potentially be detected more effectively.

Dual-wavelength LS-CLE imaging is demonstrated by sequentially switching between 488 nm and 660 nm laser sources for alternate frames, avoiding spectral bleed-through, and providing an effective frame rate of 60 Hz. The two channels are pseudo-coloured and combined, and large-area dual-wavelength mosaics are created by registering and stitching the image frames as the probe moves across the tissue. By staining the tissue specimen with complementary non-specific and molecular fast-acting dye, dual colour images are generated providing morphological and function information about the sample. Preliminary images with a calculated resolution of 2.2 μm are presented from fluorescent stained *ex vivo* tissue, demonstrating the potential clinical feasibility of the technique. These current results suggest a clinical application for MB aided single and dual-wavelength LS-CLE in breast cavity scanning for rapid decision-making during BCS, allowing oncological status of resection margins to be determined intra-operatively.

5.7 Study limitations

In this chapter, preliminary results on hand-held and robotic manipulation of fibre-bundle based LS-CLE system are presented using MB as a staining agent. Although the initial results are promising, there are several limitations to this study. This is a small cohort study that did not include conditions like ILC and only one specimen with DCIS was examined. Further, imaging was performed on small cut-outs ($\sim$ 10×10 mm) of freshly excised non-neoplastic and neoplastic tissues. The specimens were collected from one centre and imaging experiments were conducted on smooth tissue specimens in a controlled environment by a single user. This work did not take into account challenges associated with intra-operative administration of MB (topical or intravenous), potential complications involved like skin and parenchymal necrosis [252, 257] and artefacts due to tissue irregularity during hand-held or robotic scanning. Further studies are currently underway to confirm that the quantitative accuracy when using MB staining is similar to that when using AH and to establish whether similar images can be obtained *in vivo*.

Chapter 6

Pixel super-resolution fibre-bundle endomicroscopy*

The previous chapters demonstrate the potential of fibre-bundle based fluorescence endomicroscopes for rapid imaging of breast tissue without the need of slicing and fixing. However, under-sampling of artefacts due to inter-core spacing of the fibre-bundle limit the achievable spatial resolution of the imaging system. The aim of this chapter is to show that the use of fibre-shifting and computational approaches will overcome this limitation.

A brief review of computational methods for alleviating under-sampling artefacts is presented in Section 6.1. Alternative strategies for increasing the spatial-sampling by which a high resolution (HR) image is restored from multiple pixelation-limited low resolution (LR) images whilst causing fibre-bundle movement are discussed. Given the small inter-core spacing distance of fibre-bundles ($\sim$ 4-8 μm), precise movements of the fibre tip at the micrometer scale are required to improve the sampling.

The development of a new prototype endomicroscope that incorporates a miniaturised piezoelectric tube scanner and a GRIN lens to induce precise micro-shifts of the fibre-bundle is presented. A fast Delaunay triangulation-based super-resolution algorithm is developed to restore an HR image from multiple pixelation-limited LR images. Various scanning patterns are examined and a criteria to select optimal shift pattern is derived. The resolution enhancement is demonstrated on high resolution video-rate imaging of lens paper and *ex-vivo* human breast tissue.

* The contents of this chapter were published as:
K. Vyas, M. Hughes, and G. Yang, "Fiber-shifting endomicroscopy for enhanced resolution imaging", in Frontiers in Optics 2017, OSA Technical Digest (online) (Optical Society of America, 2017), paper JTu2A.79.
K. Vyas, M. Hughes, B. Rosa, and G. Yang, "Fiber bundle shifting endomicroscopy for high-resolution imaging", Biomed. Opt. Express 9, 4649-4664 (2018).

6.1 Background

A significant problem with using fibre-bundle endomicroscopes for point-of-care diagnostics is the trade-off between the resolution and achievable FOV. This is because the quantity of fibres that can be packed into a single bundle (typically up to 30,000 fibres) limits the number of effective pixels of information in the image. Further, the inter-core spacing results in pronounced fibre-pixelation and under-sampling artefacts. This is seen as a strong honeycomb pattern and which reduces the overall contrast and spatial resolution of the image [18]. For such systems the achievable resolution is not limited by diffraction but by the inter-core spacing, making it difficult to resolve sub-cellular features when imaging biological samples.

Previously reported fibre-bundle endomicroscopy systems often utilised computational approaches such as Gaussian smoothing or linear interpolation between the cores to eliminate the pixelation artefacts [183, 217–219]. Even though such methods lead to removal of pixelation artefacts they do not result in an improvement in spatial resolution caused due to under-sampling.

An alternate approach is to begin with an LR endomicroscopy image and attempt to increase the resolution using multi-frame pixel super resolution (p-SR) techniques. p-SR, a well explored topic in the machine vision community, utilises sub-pixel source/image sensor shifting to create multiple under-sampled LR images and combines them to reconstruct an HR image [258]. For fibre-bundle endomicroscopes, if the imaging probe shifts a small distance between the acquisition of two image frames, and this shift is not an integer multiple of the fibre core spacing along the direction of motion, then if the two images are registered and appropriately combined an enhancement in resolution can be obtained. Indeed, this tends to occur naturally during video mosaicking [221] or can be induced deliberately by causing random vibrations [259] or dithering [260, 261] of the fibre-bundle. However, as these motions are essentially uncontrolled, any improvement in resolution is variable and may only occur along one direction. Further, for multi-frame p-SR methods, the enhancement is highly dependent on the performance of the registration algorithm, and hence on the signal-to-noise ratio of the images.

An alternative is to mechanically induce controlled micro-shifts of the fibre-bundle. This concept is first suggested, although not demonstrated, for confocal endomicroscopy in [261, 262] and later shown in principle using a translation stage for epi-fluorescence endomicroscopy in [263, 264]. In [263], a fibre-bundle is placed in direct contact with the sample and shifted laterally, using a bulky stage, in various patterns. Higher resolution images are obtained by a reconstruction technique based on mean threshold bitmapping and a 2-fold resolution improvement is achieved. In [264], a maximum *a posteriori* es-

timate of the HR image is calculated using conjugate gradient descent and a 2.8 times enhancement is achieved when imaging a USAF target using 16 LR images. Furthermore, an abstract from Cheng et al. suggested using a piezoelectric tube for inducing the shift, and their work aimed at enhancing the resolution of two-photon endomicroscopy [265].

To date, these handful of studies have been initial proof-of-concept experiments only. Approaches relying on random motion may be too inconsistent for clinical use, while for induced motion, high-speed scanning systems are difficult to miniaturise and the system sacrifices image acquisition rate and probe size for improved image quality. Even if the current approaches were successfully miniaturised, when the moving fibre-bundle is placed in direct contact with the tissue, friction and tissue deformation will tend to make them unreliable for clinical practice.

This provides the motivation for the development of a new computational method for fibre-bundle shifting endomicroscopy system that can increase the spatial resolution, and a novel distal fibre-shifting probe design that can provide resistance to friction and tissue deformation whilst keeping the entire assembly miniaturised. In the proposed design, precise micro-shifts of the fibre-bundle tip are achieved using miniaturised piezoelectric tube scanners. A brief overview of piezoelectric theory and a mathematical model for the actuated deflection for a piezoelectric tube are presented in the following section.

6.2 Piezoelectric tube scanner

The piezoelectric effect is a well-known phenomenon in which certain materials are able to generate an electric charge in response to applied mechanical stress. The reverse is also possible and is known as 'inverse piezoelectric effect' which causes the material to change length or generate mechanical stress when an electric voltage is applied. There are many materials (both natural and man-made) that exhibit a range of piezoelectric effects. The piezoelectric effect of naturally occurring materials like quartz, tourmaline, topaz, and sugar is relatively small. Commercially available piezoelectric materials are mostly based on barium titanate or lead-zirconate titanate as they exhibit larger displacements or induce higher electric voltages. By special doping of the piezoelectric ceramics with Ni, Bi, Sb or Nb ions, it is possible to specifically optimise piezoelectric and dielectric parameters and use them for different actuator or sensor applications [266].

A piezoelectric tube scanner is a thin-walled cylinder of radially polarised piezoelectric material originally invented by Binnig and Smith in 1986 [267]. Electrodes are applied to the internal and external faces of the tube. A typical setup for lateral deflection of a piezoelectric tube, with the outer electrode quartered parallel to the axis is shown in Fig.6.1.

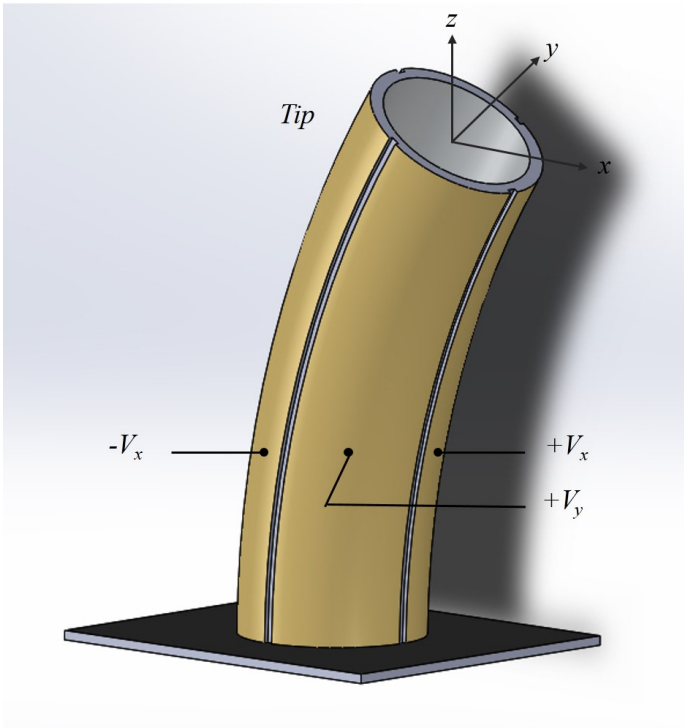

Figure 6.1: Diagram of lateral deflection of a quartered piezoelectric tube.

The lower end of the tube is generally clamped, while the upper one (denoted as 'tip') can freely move in all three dimensions. By applying a bias between the inner electrode and all the outer electrodes, the tube will extend or contract causing axial displacement. Alternately, if the bias is applied only to one of the outer quarters the tube will bend causing lateral displacement. These types of tube scanners are often used in applications that require precise positioning such as scanning tunnelling microscopy [267,268], scanning force microscopy (SFM), nano-fabrication systems as well as for rapid large-area imaging in various fibre-optic scanning endomicroscopy systems based on *en face* OCT and two-photon microscopy [269–271].

6.2.1 Mathematical model for piezoelectric tube deflection

Several physically-based and experimentally derived models for the tube scanner are available in the literature [268, 272]. The expression for the actuated deflection for a piezoelectric tube using the standard methods in the theory of elasticity is presented below.

Equations governing piezoelectricity are usually expressed as tensors. For a piezoelectric tube scanner under the influence of electric field E', the induced strain S_{piezo} is expressed as:

$$S_{piezo} = sT_{piezo} + dE' \tag{6.1}$$

where T_{piezo} is the stress tensor, S_{piezo} is the strain tensor and E' is the electric field tensor. The anisotropic material properties of the radially polarised piezoceramic are described by the elastic tensor s and piezoelectric tensor d. For piezoelectric material, PZT, the d matrix is given by:

$$d = \begin{pmatrix} 0 & 0 & 0 & 0 & d_{31} & 0 \\ 0 & 0 & 0 & d_{15} & 0 & 0 \\ d_{31} & d_{31} & d_{33} & 0 & 0 & 0 \end{pmatrix}$$

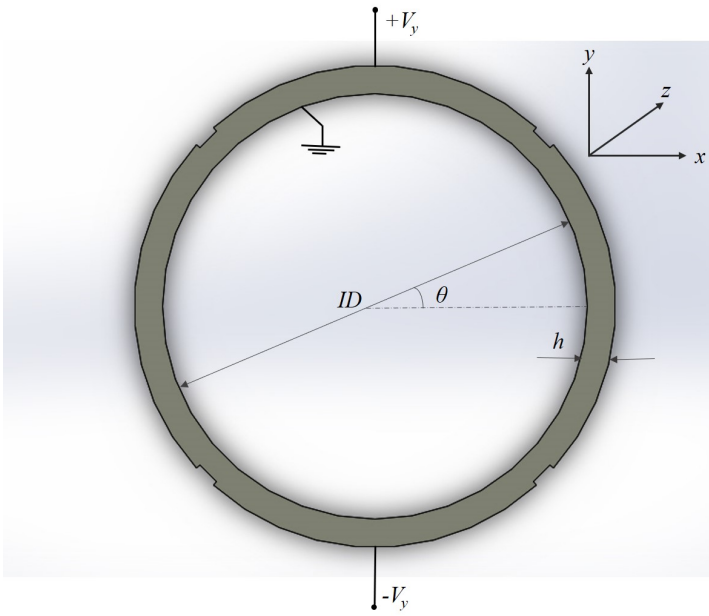

Figure 6.2: Diagram of a cross section of piezoelectric tube scanner in twin-electrode excitation configuration for lateral deflection in the 'y' direction.

The deflection of a PZT tube with quartered electrodes in the twin-electrode configuration shown in Fig.6.2. In the figure, two voltages equal in magnitude and opposite in sign are applied to two quadrants of Y. The inner metal coating and two X quadrant electrodes are grounded. For simplicity, it is assumed that the wall thickness is much smaller than the tube diameter. Additionally, variations in strain and stress over all but the axial direction are neglected.

When the voltage is applied, strain/stress is generated in the z direction given by:

$$S_{piezo} = d_{31}\frac{V_y}{h} \tag{6.2}$$

$$T_{piezo} = ES_{piezo} \tag{6.3}$$

where E is the Young's modulus of elasticity, h is the thickness of the tube, V_y is the applied voltage and d_{31} is the PZT strain constant. The torque of this pair of forces causes the tube to bend. Equilibrium requires this strain/stress to be resisted by a bending moment in the opposite direction that occurs in all four quadrants.

From basic mechanics and Fig.6.2, bending strain S_{bend} is proportional to the distance from the neutral axis, given by:

$$S_{bend} = \frac{Dsin\theta}{2R} \tag{6.4}$$

where R is the radius of curvature of the tube and D is the tube diameter. In voltage supplied quadrants, that is along y axis, the total strain 'S' is expressed as:

$$S = S_{piezo} - S_{bend} \tag{6.5}$$

And in grounded quadrants:

$$S = -S_{bend} \tag{6.6}$$

Assuming that the stress generated by bending is linear with respect to V_y, the total stress 'T' in the pair of adjacent quadrants can be expressed as a function of θ as:

$$\begin{aligned} 0 < \theta < \frac{\pi}{4} \qquad & T(\theta) = -T_{bend} = -\alpha sin(\theta) \\ \frac{\pi}{4} < \theta < \frac{\pi}{2} \qquad & T(\theta) = T_{piezo} - T_{bend} = T_{piezo} - \alpha sin(\theta) \end{aligned} \tag{6.7}$$

where α is a constant of proportionality and can be determined by solving for the condition of zero torque (by integrating over the angle θ) as:

$$\alpha = \frac{2\sqrt{2}}{\pi}T_{piezo} \tag{6.8}$$

The radius of curvature R can be written as:

$$\frac{1}{R} = \frac{\frac{d^2y}{dz^2}}{[1 + (\frac{dy}{dz})^2]^{\frac{3}{2}}} \tag{6.9}$$

Since the deflection of tube is small as compared to the tube length, $(\frac{dy}{dz}) \rightarrow 0$, thus:

$$\frac{1}{R} \approx \frac{d^2y}{dz^2} \tag{6.10}$$

Integrating, the deflection Δy can be obtained as a function of curvature R and tube length Z as:

$$\Delta y \approx \frac{Z^2}{2R} \tag{6.11}$$

Combining the above equations, the equation of deflection of a PZT tube in twin electrode configuration is:

$$\Delta y \approx \frac{2\sqrt{2}d_{31}V_y Z^2}{\pi D h} \tag{6.12}$$

6.3 Instrumentation

6.3.1 Optical system

A schematic of the fibre-shifting p-SR endomicroscopy system for fluorescence imaging is illustrated in Fig.6.3. The proximal face of the fibre-bundle is coupled to the optical imaging system which, for the purposes of this study, is a custom and high-speed LS-CLE unit. The bundle used is a fused Fujikura imaging fibre-bundle (FIGH-30-850N, Fujikura) with approximately 30,000 cores. However, the proposed approach can be implemented using any endomicroscopy system and fibre-bundle without major modification.

A full description of the LS-CLE system's operating principles can be found in Chapter 3, Section 3.3.2. In brief, a cylindrical lens (f = 50 mm) is used to create a focused line from a 50 mW, 488 nm laser (Vortran Stradus, 488). A galvo-mirror (Thorlabs, GVS001) sweeps the line across the proximal end of the fibre-bundle in a direction perpendicular to the line. The bundle relays the line to the tissue *via* the distal GRIN objective and returns the collected fluorescence from all the points along the line. The fluorescence is then imaged onto a monochrome rolling-shutter CMOS camera (Flea 3, FL3-U3-13S2M-CS). The rolling shutter of the CMOS camera operates as a virtual detector slit that rejects most of the out-of-focus light leading to optical sectioning at frame rates of up to 120 Hz.

6.3.2 Imaging probe design

The optical system of the distal probe assembly is designed to achieve a high magnification imaging regime in close proximity to the tissue surface. A single GRIN lens is used for simplicity of assembly and adequate level of aberrations. A prototype fibre-shifting probe is assembled for testing purposes and employed in *ex-vivo* feasibility studies. The schematics of the probe which consists of the fibre-bundle, a miniaturised quadruple PZT tube (PI Ceramics, PT230.94) and a high-NA (0.8) GRIN microlens is shown in Fig.6.4(a).

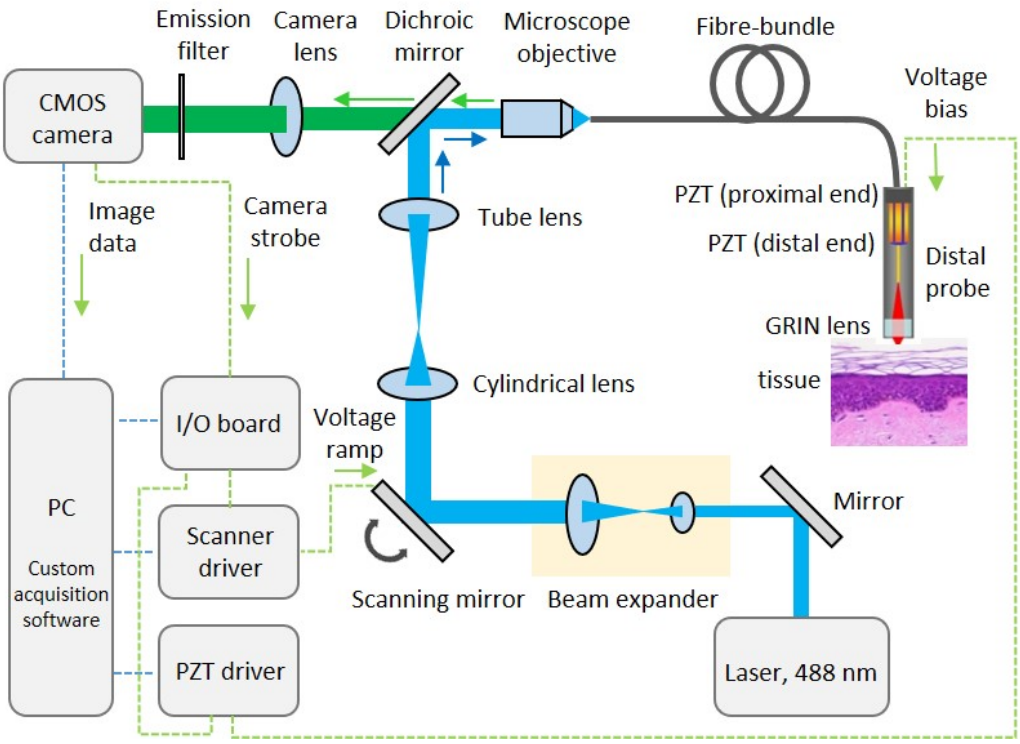

Figure 6.3: Optical setup for fibre-shifting line-scan confocal laser endomicroscope. The proximal face of the fibre-bundle is placed at the focal plane of the LS-CLE and the distal end is actuated by a PZT tube behind a GRIN lens with 1.92× magnification.

In this design, the proximal end of the PZT tube is mounted on a custom printed base, while the distal end can freely move in all three dimensions. The PZT tube is encased in a custom 3D printed plastic tube which accepts detachable mounts that contain an optical system such as a GRIN lens. The fibre-bundle is passed through the centre of the PZT tube and rigidly secured to the distal end of the tube tip by a custom designed 3D printed holder and epoxy. For applications where the PZT tube is used for resonant scanning, the free-length of the fibre determines its resonance. However, here we make use of small displacements only by operating the PZT tube for non-resonant scanning and keeping the free-length of the fibre-bundle to be 10 mm.

The distance between the fibre tip and the lens surface is carefully controlled by adjusting the position of detachable lens holder. A stock 1.4 mm diameter GRIN micro-lens assembly (GRINTech, GT-MO-080-0415-488) is fixed in front of the fibre-bundle such that the distal tip of the fibre is imaged onto a plane approximately 80 μm deep in the tissue with a 1.92× magnification factor. As the GRIN lens does not move, this avoids friction between the moving fibre and the tissue which would otherwise make the scanning less

reproducible due to tissue deformation. The entire probe assembly is encased in a custom 3D printed plastic tube with a 45 mm rigid length including the GRIN lens and 5 mm outer diameter. A photograph of the prototype probe is shown in Fig.6.4(b).

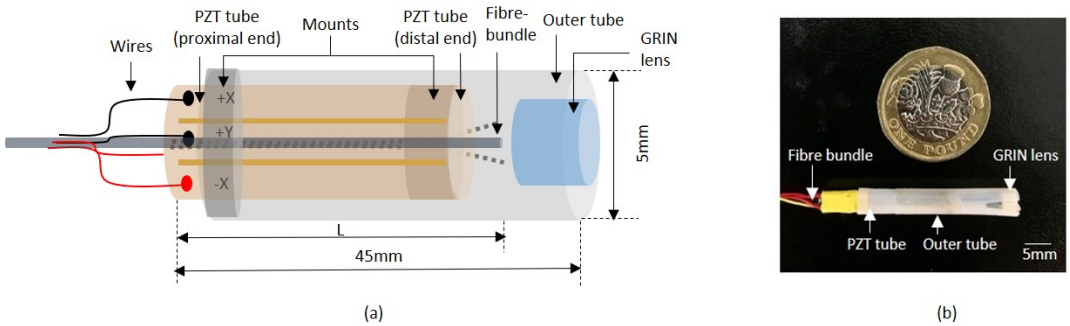

Figure 6.4: (a) Illustrative schematic of a PZT tube actuated fibre-shifting distal probe with 1.92× GRIN lens. (b) A photograph of the assembled 3D printed probe holder tube with 5 mm outer diameter. A UK one pound coin is shown for scale.

In standard-resolution operation the camera is operated in free-run mode which allows LR images to be acquired at the full frame rate of 120 fps by generating a trigger pulse on its strobe output pin at the start of each frame acquisition. The pulse triggers the analog output of a 16-bit data acquisition card with a 250 KS/s sampling rate (National instruments, NI-USB 6211) to send a ramp voltage signal to the galvo-scanning mirror with a user-specified delay. Fine adjustment of the ramp slope and delay ensures that the virtual slit is aligned with the laser line throughout the acquisition of each frame.

In super-resolution mode, activated by the click of a button on the custom control software, the trigger pulse also triggers the delivery of a series of drive signals to the PZT tube (explained in the next section). This results in the fibre-bundle being shifted to a series of different positions and synchronised such that one image frame is acquired for each position. An experimentally determined delay is provided such that the data acquisition starts once the fibre-bundle reaches each stationary position and an image frame is acquired for each position of the PZT tube at 120 fps.

6.3.3 Electronic circuit for PZT tube actuation

The PZT tube used for the prototype probe has a lateral range of ± 35 μm and a vertical range of 3.5 μm at room temperature for a given voltage of ± 250 V range. Pre-amplifiers and driver amplifiers create the voltage necessary for precise shifting of the fibre-bundle and maintaining the probe-GRIN lens distance. The piezo driver circuit was designed and assembled by Dr. Bruno Gil Rosa.

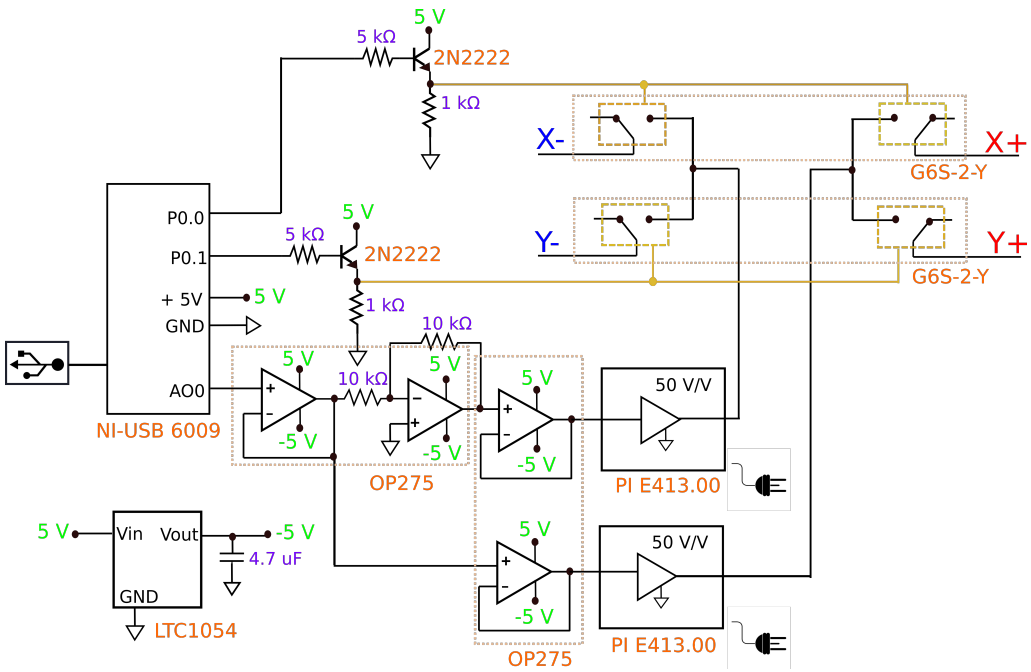

Figure 6.5: Schematics of PZT tube driver circuit

The schematic diagram is shown in Fig.6.5. The amplifier setup consists of a two stage system. The first stage has two pre-amplifiers that provide unitary gain. A data acquisition card (National instruments, NI-USB 6009) is used to produce a DC voltage (in the range from 0 V to 5 V) from one of the analog outputs of the card (AO0). This voltage is split into two different signals with equal magnitude and opposite sign through an inverting amplifier (Analog Devices, OP275) with unitary gain. This is followed by signal buffering *via* two voltage-followers (Analog Devices, OP275) mounted on a printed circuit board.

In the second stage, both the channels are amplified by a high voltage amplifier (PI, E413.00) specially designed for driving PZT transducers with gain of 50 V/V and output span between -250 V and 250 V. One amplifier is used for each pre-amplifier to drive the inner scanning PZT tube. Both the amplifiers are inverting and identical in design.

The routing of these amplified signals or drive voltages to the corresponding PZT tube electrode pair is achieved by two solid state relays (Omron, G6S-2-Y) that, when triggered, excite the electrodes independently. The trigger signals are generated by two digital outputs from the acquisition card with 5 V magnitude. Since the electronic current provided by the card is not enough to activate the relays, due to the low impedance of their coils, an additional transistor (Multicomp, 2N2222) in a common-collector configuration is employed to supply a larger current to the relays and activate the switching mechanism. A charge pump device (Linear Technology, LTC1054) is used to produce a negative 5 V

supply for all the electronic components except the piezo amplifiers. This is done as the acquisition card could only generate the positive 5 V. Symmetric supply levels are required to accommodate the bipolar signals leading to the piezo amplifiers.

6.4 p-SR image reconstruction

The p-SR image reconstruction task is divided into two stages: a one-time calibration and then subsequent reconstruction of each SR image as depicted in Fig.6.6. The calibration stage involves identifying the core-centre positions of the bundle and determining the geometric transformation matrix for each step of the fibre-bundle shifting pattern driven by the PZT tube. In the second stage, a fast Delaunay triangulation (DT) based interpolation algorithm is used to reconstruct the p-SR image from the multiple LR images acquired at each position.

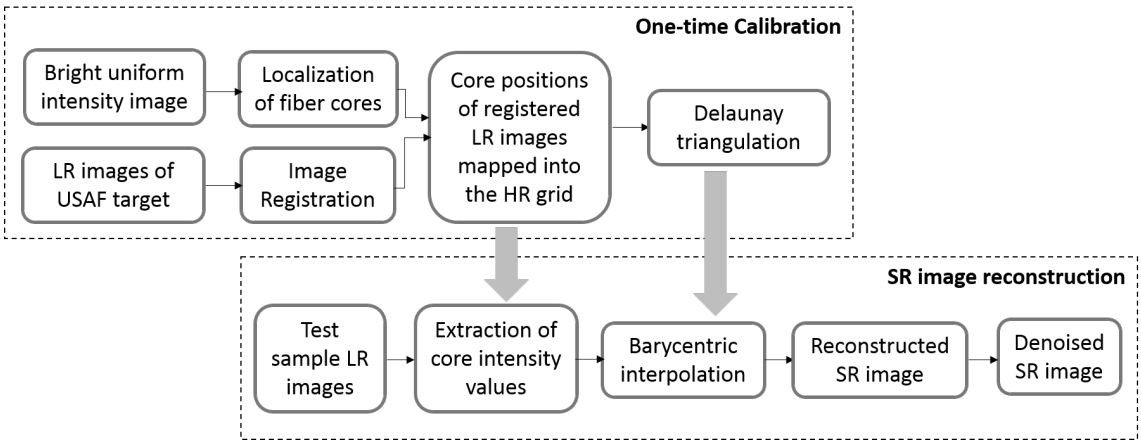

Figure 6.6: Sequence of steps illustrating Delaunay triangulation based reconstruction of p-SR image from a set of fibre-bundle pixelation limited LR image frames.

6.4.1 Core-centre estimation

Prior to imaging, a dark background calibration is performed by recording 50 frames with the tip of the probe covered. Such an image suffers from fibre-pixelation artefacts, and may also show specular reflections, non-uniform intensity distribution, and artefacts due to broken fibres. A circular area of interest is taken using convex hull algorithm to remove artefacts from the edges of the fibre-bundle, leading to final image diameter of 350 μm.

The next step is to detect the core-centre positions. The probe is pointed at a bright uniform target and the core-centre positions are detected using a Hough transform implemented in Matlab® (Mathworks, Massachusetts). Cores with saturated or low intensity values are assumed broken and removed from the record.

6.4.2 Image registration

The probe is pointed at an object with high resolution detail (such as a USAF resolution target). The chosen pattern of fibre-bundle shifts is run, LR images are acquired from each shifted position and the background image is subtracted from each LR image. A sub-pixel frequency domain-based phase correlation technique presented in [273] is then used to estimate the geometric transformation between the consecutive LR image frames. The geometric transformation is made in one step using a discrete Fourier transform to make it high-speed. Given two LR images, 'f_1' and 'f_2', shifted horizontally and vertically by $(\triangle x, \triangle y)$, in the spatial domain their relationship can be expressed as:

$$f_2(x, y) = f_2(x, y)(x + \triangle x, y + \triangle y) \tag{6.13}$$

In the Fourier domain this can be expressed as:

$$F_2(u, v) = e^{2\pi i(u^T \triangle x + v^T \triangle y)} F_1(u, v) \tag{6.14}$$

where $F_1(u, v)$ and $F_2(u, v)$ are 2D Fourier transforms, at frequencies (u,v), of $f_1(x, y)$ and $f_2(x, y)$ respectively. For N image frames, the shift parameters $(\triangle x_k)$ and $(\triangle y_k)$ between every image frame $f_k(x, y)$ and the first image $f_1(x, y)$ are computed from Eq.6.14 as the least-squares solution of the slope of the phase difference.

Once the translation shift parameters $(\triangle x_k, \triangle y_k)$ are calculated, the core-centre positions are shifted accordingly and assembled irregularly on the initial HR image grid. This array of core positions is used as input to a Delaunay- based interpolation algorithm to create a triangulation mesh between neighbour points.

6.4.3 Delaunay triangulation based p-SR image reconstruction

In this section a Delaunay triangulation-based approach, similar to that proposed by [274], is adapted to improve the resolution of fibre-bundle endomicroscopy images. If there are N cores in the bundle, and p fibre-bundle positions are used, this results in a total of Np core positions. A DT is then formed over these Np core positions by first computing the Voronoi diagram that decomposes the HR reconstruction grid into regions around each core position such that all the points in the region around each core c_i, are closer to c_i than any other core. A DT mesh is then constructed by connecting points with which the Voronoi cells have common boundaries such that every pixel is enclosed in one triangle with vertices corresponding to the closest three core-centre positions. A representation of the different steps of the DT based p-SR reconstruction process of LS-CLE images of a USAF target is presented in Fig.6.7.

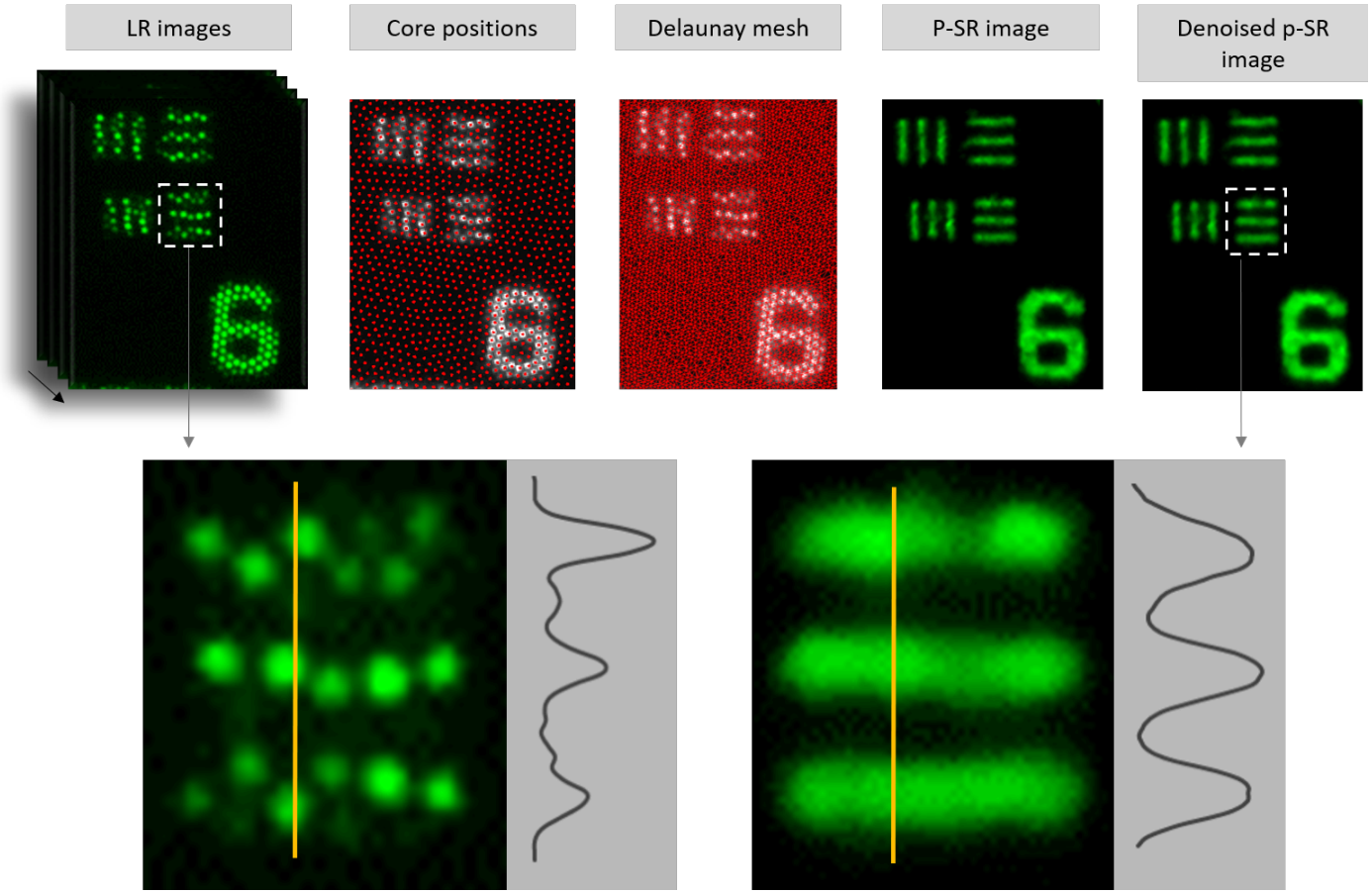

Figure 6.7: The observation model of the p-SR endomicroscopy imaging system relating a HR image to the LR observation frames. The cropped region corresponds to letter 6 of group(G) 6, and Element(E) 5 and 6 of group(G) 7. The zoomed inset corresponds to G7,E6.

First, a DT mesh is constructed over the scattered core positions in the irregularly sampled raster formed from the set of LR frames. Once the reconstruction grid is chosen, the enclosing DT is identified by converting the pixel location to triangular barycentric co-ordinates (a measure of its distance from each vertex of the enclosing triangle). In particular, barycentric coordinates define the weights that each pixel inside the triangle should be assigned depending on the triangular areas calculated between the pixel and the vertices of the triangle. For cores c_i at vertex i, for $i = 1, 2, 3$, p as the pixel location and A_1, A_2 and A_3 to be the area of three triangles c_2c_3p, c_1c_3p and c_1c_2p, the barycentric co-ordinate b_i is calculated as:

$$b_i = \frac{A_i}{A_1 + A_2 + A_3} \qquad where\ i = 1, 2, 3 \tag{6.15}$$

During imaging, following acquisition of the set of LR images from each shifted position, the core intensity is extracted from each core position in each image. The resulting SR image is reconstructed by assigning each pixel an intensity value, I_p , obtained by triangular linear interpolation between the intensity values of the three nearest cores of the enclosing Delaunay triangle. This is expressed as:

$$I_p = b_1 I_{C,1} + b_2 I_{C,2} + b_3 I_{C,3} \tag{6.16}$$

where $I_{C,i}$ is the intensity values of the core at vertex i and b_i is the corresponding pre-calculated barycentric co-ordinate for that reconstruction pixel p.

In the last step, a median filter is used to remove salt-and-pepper impulse noise from the reconstructed p-SR image. For the prototype system reported here, LR images are recorded at 120 fps and then processed offline, but the reconstruction step is computationally inexpensive and could be implemented in real-time.

6.5 Results

The experimental investigations presented in this chapter are based on a fused Fujikura fibre-bundle (FIGH-30-850N) with approximately 30,000 cores. The Fujikura bundles are commonly used for endomicroscopy imaging due to their smaller core spacing and hence better intrinsic resolution. The core diameter and inter-core spacing are estimated by acquiring SEM images of the fibre-bundle tip, one such representative image is shown in Fig.6.8. It is observed that the bundle has some cores arranged irregularly rather than a strict hexagonal pattern and the shape of the individual fibres is also not observed to be perfectly circular for some cases.

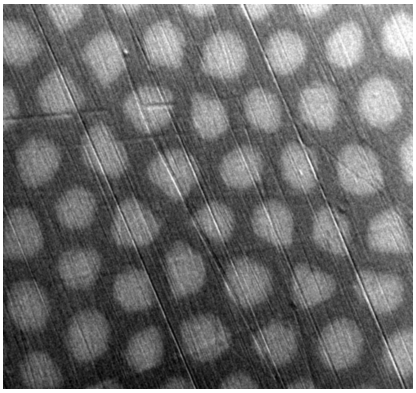

Figure 6.8: SEM image of a Fujikura fibre-bundle with the core diameter and inter-core spacing as 2.45 μm and 4.48 μm respectively.

From the SEM image, the measured core-to-core spacing is about 4.48 μm and core diameter is about 2.45 μm which closely matches the original fibre-bundle manufacturing specifications. The excitation and illumination is transferred coherently from the proximal to the distal end of the same fibre-bundle. When imaged onto the microscope CMOS camera in our system, there are approximately 6.2 pixels per core spacing for the Fujikura bundle and so the sampling limitation on resolution is dominated by the fibre-bundle core spacing and not by the pixel size of the camera.

6.5.1 PZT tube characterisation

Following the probe assembly, the dependence of the fibre-bundle tip deflection on the voltage applied to the PZT tube electrodes is experimentally measured using the optical set-up shown in Fig.6.9(a). The output of a laser diode (Vortran, 488) is focused onto the fibre-bundle *via* Objective1 with 40X magnification. The transmitted light is imaged onto a CCD camera (Thorlabs, DCU224C) *via* a 20× microscope Objective2. The NA of the focusing objective is matched with the NA of the imaging fibre, such that the spot size is approximately the size of an individual core or pixel.

When a single core of the image fibre is illuminated, the output showed some distribution of power among neighbouring cores, indicating inter-core coupling. An intensity thresholding algorithm is applied to eliminate the low-intensity neighbouring pixels and a centroid estimation algorithm is used to find the centre of individual cores as shown in Fig.6.9(b).

Input voltages in the range of 0 to 125 V with a step-size of 5 V are provided to the x and y axis of the PZT tube using the electronic circuit described in Section 6.3.3. For each axis, the lateral displacement of the fibre-bundle tip is estimated by tracking the position of the centroid of the focused spot on the CCD camera, averaged over 5 runs.

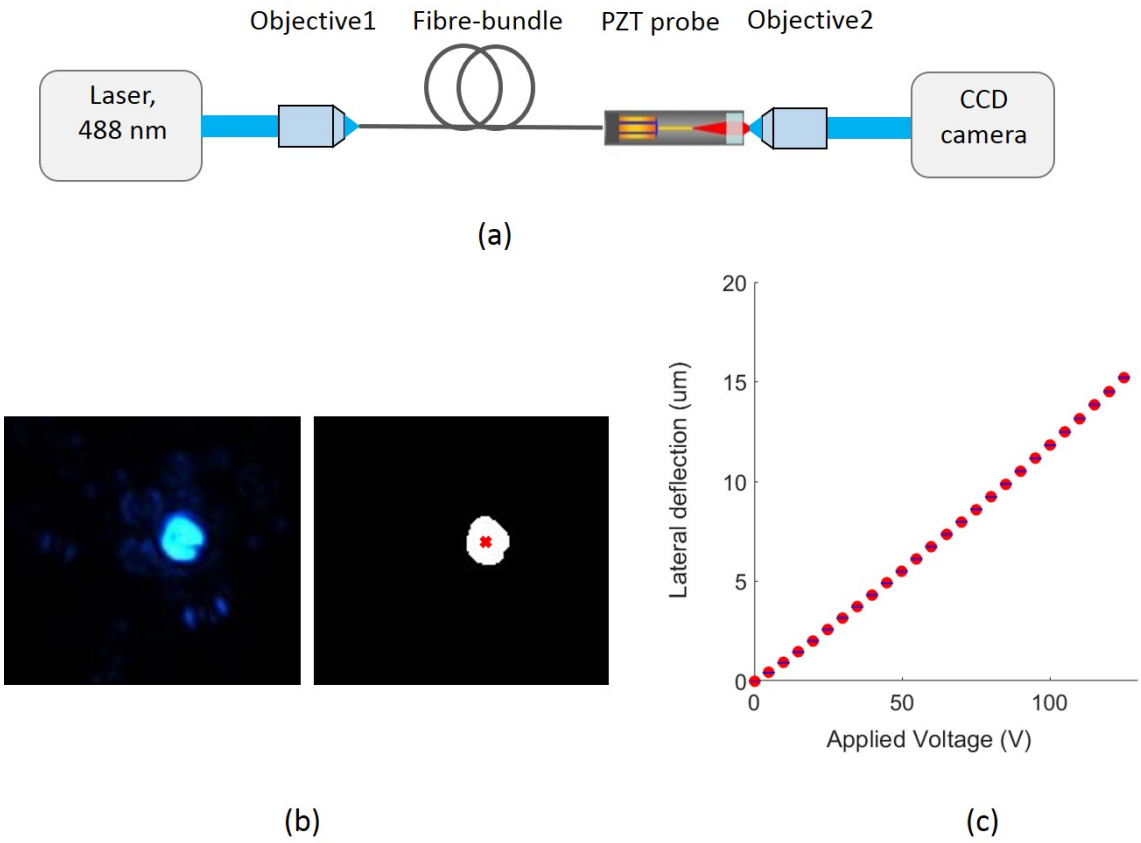

Figure 6.9: (a) Experimental setup to estimate the deflection of piezo tube with respect to applied voltage. (b) Image acquired when a single core of the fibre-bundle is illuminated and processed binary image obtained after applying the centroid estimation algorithm (The centroid is marked as red asterisk. (c) 2D plot of fibre-bundle deflection *versus* applied voltage on the PZT electrode pair.

A representative plot of deflection versus applied voltage along the x axis is shown in Fig.6.9(c). As the input voltage is increased, the displacement of the fibre-bundle tip gradually increases. From these direct measurements, a voltage shift of 5 V is determined to correspond to a fibre tip deflection of 0.61 $\pm$ 0.03 μm. For the Fujikura fibre-bundle with an inter-core spacing of 4.48 μm, the experimentally measured desired shift equal to half the core spacing of 2.24 μm, corresponds to a drive voltage of about 19 V.

Using Eq.6.12, for the stock PZT tube from PI Ceramics (PT230.94) with quoted dimensions 30(Z) $\times$ 3.2(OD) $\times$ 2.2(ID) mm, h of 0.5 mm and d_{31} of -180×10^{-12} m/V, a drive voltage of 19 V should result in a lateral deflection of about 2.52 μm. A stiff fibre-bundle inside the PZT tube, with fibre free-length L of 10 mm, would experience lateral deflections proportional to its length by considering only small deformations in the elastic regime and without torsion occurring along the fibre length.

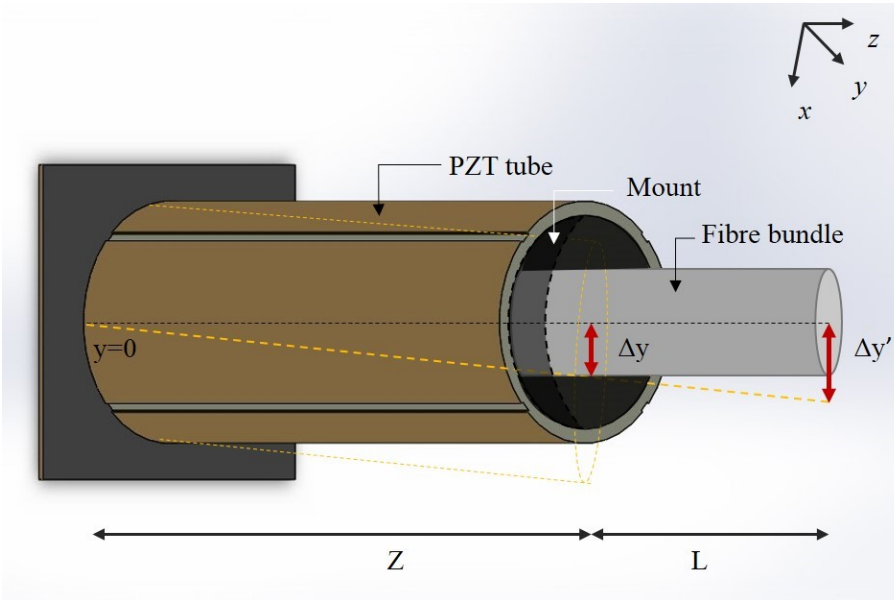

Figure 6.10: Diagram of deflection of PZT tube scanner with fibre-bundle rigidly mounted inside the tube. The base of the PZT tube is mounted to a fixed support and the tip is allowed to deflect freely.

Using simple trigonometric relations, as shown in Fig.6.10, the estimated deflection $\triangle y'$ experienced by the tip of the fibre-bundle is obtained to be 3.35 μm. In practice, a smaller deflection is experimentally measured which could be due to the stiffness of the fibre-bundle. It could also be attributed to the discrepancy in the way in which D is defined in the theoretical formulation of piezo tube deflection presented in Eq.6.12.

For D equal to ID of 2.2 mm, the calculated fibre tip deflection is 3.35 μm (as stated above). Using the piezo deflection formula quoted from PI Ceramics website, D is defined as $(ID + h)$ equal to $2.7mm$ which gives the fibre tip deflection to be 2.73 μm. Whereas by choosing D as OD of $3.2mm$, according to Chen's paper on small deflections [272], the theoretical deflection of the fibre tip is found to be about 2.31 μm, which closely matches the experimental value. Further investigations need to be carried out to confirm this dependence - which are beyond the scope of this thesis.

6.5.2 Evaluation of scanning patterns

The distribution of energy within each fibre core and hence the area of the sample that each core integrates over, follows an approximate Gaussian profile with a mode field diameter (MFD) smaller than the spacing between adjacent cores. Knowledge of the core-spacing and MFD is therefore necessary to determine the scanning pattern with the optimal num-

ber and magnitude of fibre shifts in order to enhance resolution while maintaining an acceptable frame rate.

The experimental set-up to estimate the MFD is shown in Fig.6.11. The output of the LS-CLE system is focused onto the fibre-bundle via a 10× microscope objective. The light transmitted through the fibre-bundle is imaged onto a monochrome CCD camera (Thorlabs, DCU224C) via a 20× microscope objective. For the Fujikura fibre-bundle the core diameter and inter-core spacing are estimated as 2.45 μm and 4.48 μm respectively. The MFD is experimentally measured to be about 4.23 ± 0.14 μm, and FWHM to be 2.49 ± 0.08 μm. Applying the Rayleigh criterion for an Airy disc with the same FWHM (i.e. with a first minimum at 1.19 times the FWHM), the minimum fibre-bundle shift necessary to obtain two resolved peaks would be approximately 2.96 μm. Using the Sparrow criterion the required shift is about 2.12 μm. On comparing these values to the core spacing of 4.48 μm, it is clear that there is significant under-sampling occurring in the conventional fibre-bundle system with a potential for up to a 2-fold resolution improvement by fibre-shifting.

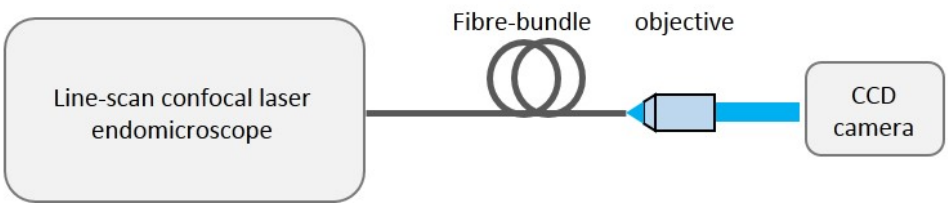

Figure 6.11: Experimental set-up for estimation of mode field diameter of the fibre-bundle imager. Objective is 20× microscope objective.

To determine the desired scanning pattern, independently from the performance of the PZT scanner, 1D linear and 2D square scanning patterns using a motorised translation stage (Standa Ltd., 8MT173) are tested and the results are further compared with several existing pixelation removal algorithms. A simple test involving imaging of a high resolution 1951 USAF target consisting of 9 groups of horizontal and vertical line pairs with various spacing is carried out. As the target is not fluorescent, it is back-illuminated by a green LED and imaged in transmission. Fig.6.11(a) shows the image acquired with the LS-CLE system and 1.92× GRIN lens (no fibre-bundle). This represents the fundamental limit on resolution from diffraction and aberrations in the optics.

Fig.6.11(b) shows a single un-cropped image representing all elements of groups 6-9 of USAF target acquired using a fibre-bundle and 1.92× GRIN lens. Full FOV (in white circle) is 350 μm without any processing. The reduced resolution and honeycomb pattern due to fibre pixelation artefacts are clearly evident in the image. Fig.6.11(c) shows a zoomed and cropped image corresponding to region of interest (marked in red) in Fig.6.11(b).

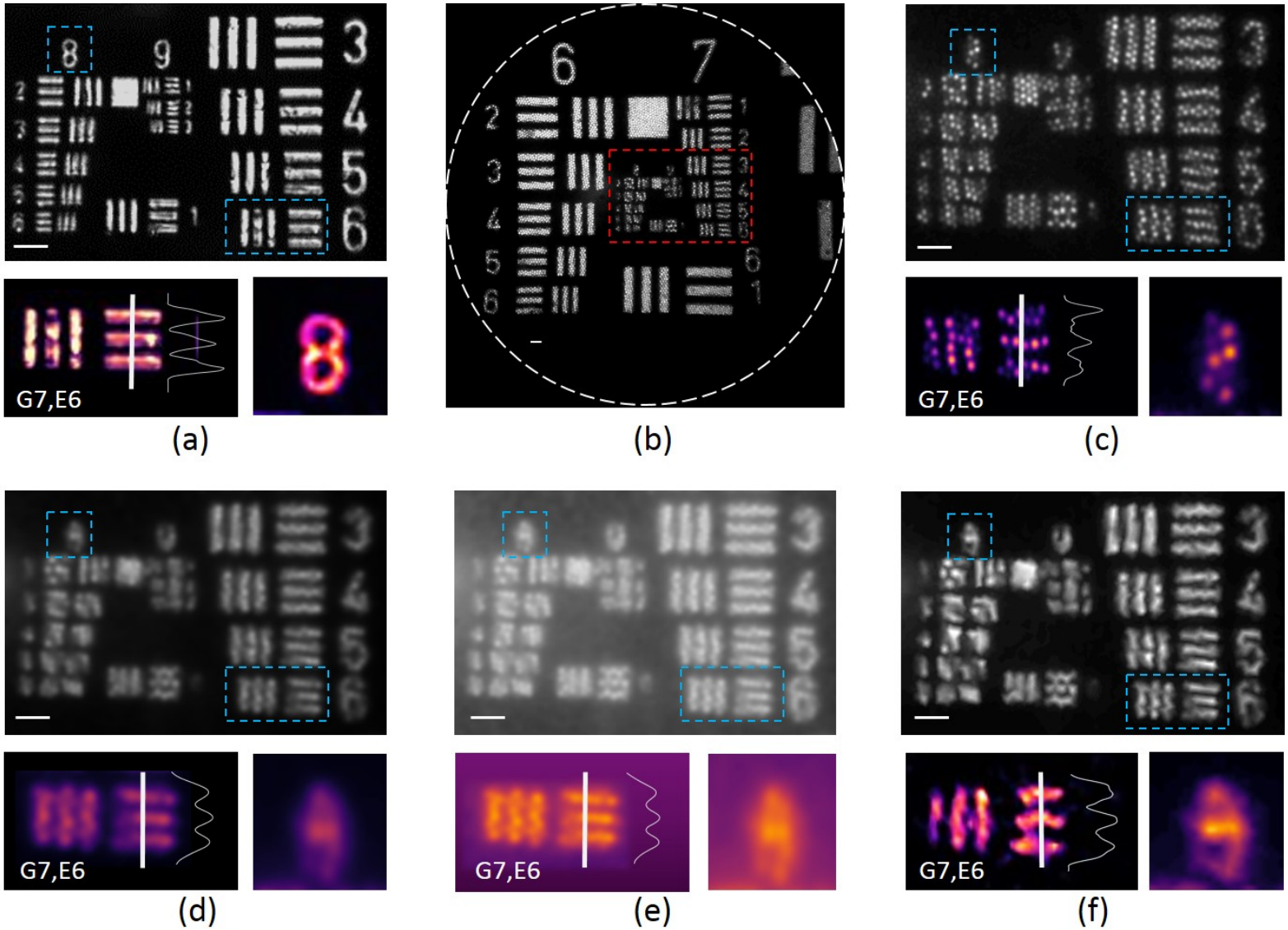
G7,E6
(a)
(b)
G7,E6
(c)
G7,E6
(d)
G7,E6
(e)
G7,E6
(f)

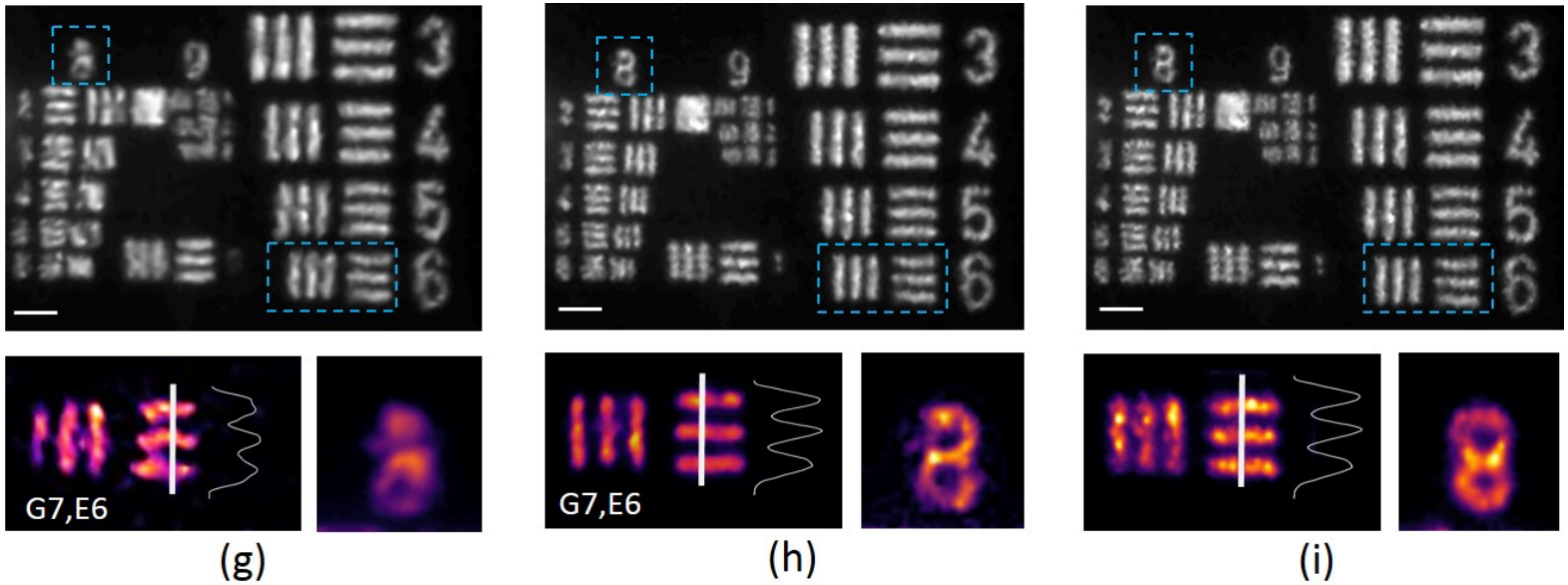

Figure 6.11: Cropped images of USAF resolution target with fibre-shifting motion performed using a translation stage. Large images show Group(G) 7, Elements(E) 3-6, and all elements of Group 8 and 9. Smaller zoomed images show G7,E6, a 2D plot of the pixel intensities along the line segment shown by a white line on G7,E6, and the numerical '8'. (a) Image acquired with the LS-CLE system and 1.92 times GRIN lens (no fibre-bundle). (b) Single un-cropped image representing all elements of groups 6-9 of USAF target acquired using a fibre-bundle and 1.92 times GRIN lens. Full field of view (in white circle) is 350 μm. Region of interest (in red) corresponds to zoomed inset in (c). (d-f) Image reconstructed by (d) Gaussian smoothing ($\sigma = 1.7 pixels$), (e) Gaussian smoothing with pre histogram equalisation and (f) DT algorithm on a single LR image. (g) a 1D shift pattern along the horizontal direction where 2 images are acquired with shift of 2.24 μm, (h) a 2D shift pattern where 4 images are acquired in a square pattern with a shift of 2.24 μm, and (i) a 2D shift pattern where 16 images are acquired with a 1.12 μm inter-image shift. The scale bar corresponds to 10 μm.

This and subsequent images are cropped from the full FOV which is 350 μm for better visualisation of high resolution features consisting of Group 7, Elements 3-6, and all Elements of Group 8 and 9. The zoomed insets correspond to Group 7, Element 6 (G7,E6) and the numeral '8'. Fig.6.11(d) shows an image reconstructed by the Gaussian smoothing ($\sigma = 1.7$ pixels) and Fig.6.11(e) by Gaussian smoothing with a pre-histogram equalisation as proposed in [217] on a single LR image. Fig.6.11(f) shows an image reconstructed by the DT algorithm on a single LR image.

The Nyquist frequency of the fibre-bundle corresponds to approximately 112 lp/mm. Due to the 1.92× magnification of the GRIN lens, the Nyquist frequency of the fibre-bundle with lens corresponds to approximately 215 lp/mm. The smallest line pairs on the USAF target that can be completely resolved for a single LR image are of Group 7, Element 6, as shown in Fig.6.11(b). This corresponds to 228.1 lp/mm and a bar width of 2.19 μm.

For the image reconstructed using only Gaussian smoothing, Gaussian smoothing with a pre-histogram equalisation and DT algorithm to a single LR image, the pixelation artefacts are reduced, due to which line pairs from Group 8, Element 1, with a spatial frequency of 256 lp/mm can be resolved. However, no significant improvements in spatial resolution are observed.

Next, the spatial resolution improvements when the fibre-bundle is shifted in 1D and 2D by half the inter-core spacing are compared. This corresponds to combining 2 images in Fig.6.11(g) and 4 images in Fig.6.11(h) with 2.24 μm inter-image shift. For the reconstructed image using a 1D shift only, although the image quality is enhanced, the resolution enhancement is somewhat directionally dependent. The smallest resolvable line pairs correspond to Group 8, Element 2, with a spatial frequency of 287.4 lp/mm as shown in Fig.6.11(g). When LR images shifted in a 2D square pattern are combined using the proposed p-SR algorithm the smallest resolvable lines are of Group 8, Element 6, Fig.6.11(h). This corresponds to a spatial frequency of 456.1 lp/mm and a bar width of 1.1 μm, resulting in $\sim 1.8\times$ resolution improvement compared with reconstruction from a single image.

Lastly, comparisons are made in spatial resolution improvement from the 2D square pattern when the fibre-bundle is shifted by steps of half and one-fourth of the inter-core spacing, corresponding to 4 images with 2.24 μm and 16 images with 1.12 μm inter-image shift, shown in Fig.6.11(h) and (i) respectively. It is observed that the 2D square pattern provides about 2-fold resolution improvement whether 4 or 16 images are used, broadly as expected from the measurement of the core spot size.

Using the LS-CLE system with an image acquisition rate of 120 fps, for a p-SR image reconstructed from 4 LR images, an overall acquisition rate of 30 fps can be achieved

which makes it suitable for real-time imaging. Given the significant frame rate penalty of using 16 images without any noticeable further resolution improvement, the 2×2 pattern is selected for use with the prototype probe as the optimised fibre-shifting pattern for biological tissue imaging experiments.

6.5.3 Probe spatial resolution estimation

Two methods are used to evaluate the spatial resolution of the fibre-bundle endomicroscopy system before and after the application of the proposed fibre-shifting method. A simple first test involved imaging a standard 1951 USAF resolution target consisting of groups of horizontal and vertical line pairs with various spacing. The highest resolved spatial frequency roughly indicated the resolving power of the optical system. As the target is not fluorescent, it is back-illuminated by a green LED and imaged in transmission.

Qualitatively, the PZT tube-based fibre-shifting probe can resolve Group 8, Element 6 of the USAF target, which corresponds to 456.1 lp/mm or a bar width of 1.1 μm, as shown in Fig.6.12(a). The measured contrast using the proposed p-SR algorithm at 456.1 lp/mm is 29.7% while that for the averaged LR images is 2.6%. Fig.6.12(b) shows an image of Group 8 and 9 of USAF target obtained when a translation stage is used for fibre-shifting. By comparing the pixel intensities along a line-segment on G8, E2-6 of Fig.6.12(a) and (b) it can be seen that the resolution enhancement obtained using the PZT based prototype probe is comparable to that using the translation stage, as shown Fig.6.12(c).

To determine the spatial resolution quantitatively, the square wave transfer function, which is a similar concept to the modulation transfer function, is determined by finding the observed modulation depth across all elements of USAF target Groups 6-9, averaged over 3 runs. Four image frames are acquired by scanning the imaging probe in a 2D square pattern, with the fibre-bundle shifted by half the inter-core spacing, and the contrast is measured for the p-SR image reconstructed using the p-SR algorithm described above. This is compared with the contrast of an image reconstructed using the same DT algorithm applied to a simple average of four frames and to an image acquired directly through the 1.92× GRIN lens with no fibre-bundle.

The observed modulation depth (square wave contrast) of the USAF bar patterns is plotted against their spatial frequencies in Fig.6.12(d). The contrast of Group 7, Element 6 on the USAF target (228.1 lp/mm) is chosen for comparison as it is closest to the Nyquist frequency of the fibre-bundle with the GRIN lens. Calculating the average modulation depth of the USAF pattern, returned a contrast of 55.9% using the proposed method, showing a 2.15× improvement from 28% for the average of four LR images.

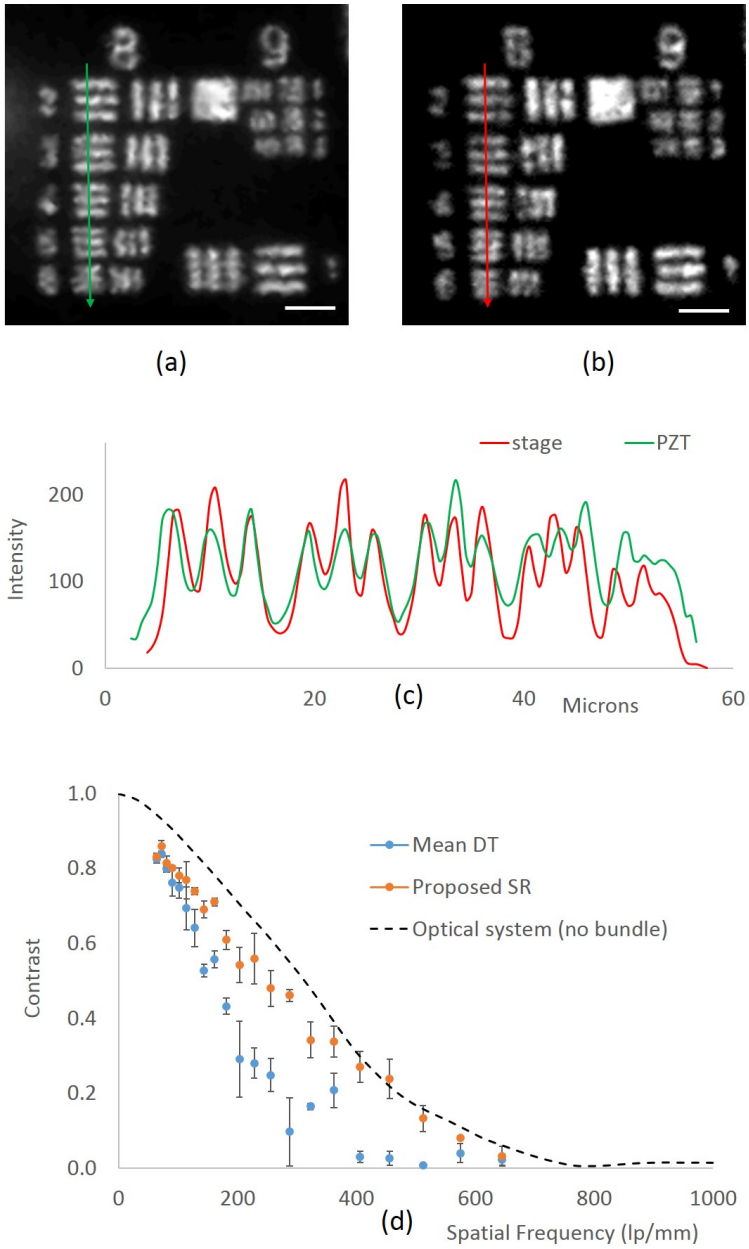

Figure 6.12: Image of USAF target showing all elements of Groups 8 and 9, reconstructed using the proposed method where fibre shifts are generated using (a) PZT scanner and (b) motorised translation stage. (c) shows 2D graph of the intensities of pixels along a line segment on G8, E2-6. (d) shows the plot of square wave modulation contrast obtained by applying the DT algorithm on the average of 4 frames and the proposed p-SR method. This is compared with imaging through the 1.92× GRIN lens optical system with no imaging bundle. Scale bar is 10 μm.

6.5.4 Imaging results

The performance of the prototype probe and p-SR reconstruction algorithm is tested by video-rate imaging of lens tissue cleaning paper and *ex vivo* human breast tissue. In standard resolution mode, images are acquired at 120 fps and in p-SR mode four images are acquired in a 2D square pattern at 30 fps. The deflection voltage applied to each electrode-pair of the PZT tube is ± 19V, corresponding to a 2.24 μm shift.

The one-time calibration step to determine the core-centre positions and shift parameters is performed by repeating the 2D square scanning pattern multiple times on a USAF resolution target. For each axis, the standard deviation of the shift, averaged over 5 runs, is about 0.12 μm. The estimated shift values are then used as the input for p-SR image reconstruction for all the test samples. All processing is performed offline in MATLAB, although the system is suitable for real-time applications.

Lens-paper imaging

Fig.6.13 shows cropped images, with zooms in the insets, of lens tissue paper stained with 0.02% AH solution. Four image frames are acquired by scanning the imaging probe in the 2D square pattern with 2.24 μm inter-image shifts. For comparison a single acquired LR image, labelled as 'Raw Image', is shown in Fig.6.13(a), additionally the Gaussian smoothing (σ = 1.7 pixels) and the DT algorithm reconstruction of this single LR raw image, labelled 'Single Gauss' and 'Single DT' is shown in Fig.6.13(b) and (c) respectively.

An image reconstructed using the DT algorithm on an average of four acquired frames, labelled 'Mean DT', is shown in Fig.6.13(d), and an image reconstructed using the proposed p-SR algorithm, labelled 'Proposed SR', is in Fig.6.13(e). Full FOV images of a single LR frame and p-SR image reconstructed using the PZT based fibre-shifting probe and proposed p-SR algorithm are shown in Fig.6.13(f).

For Fig.6.13(a)-(e), a small area where two lens paper fibres overlap is chosen and magnified 3.1 times for visualisation purposes. The intensity values along a yellow line are plotted in Fig.6.16. Michelson image contrast (or visibility) is calculated from measuring the local maxima (at peaks 1 and 2) corresponding to the centre of each lens paper fibre and the local minima corresponding to the low intensity space between them. For the 'Raw image', the fibre pixelation artefacts lead to significant intensity modulations making it difficult to distinguish fibre strands of the lens tissue paper. For the 'Single Gauss', Single DT' and 'Mean DT' reconstruction, although the fibre cores are no longer visible, the edges appear fuzzy and the local image contrast is found to be low: 5%, 8.2% and 10.8% for peak-1 and 21.3%, 28.0% and 27.8% for peak-2 respectively. Using the proposed p-SR method, the two fibres of lens paper are clearly distinguishable, resulting in narrower and well-defined peaks with image contrast values of 24.6% for peak-1 and 40.0% for peak-2.

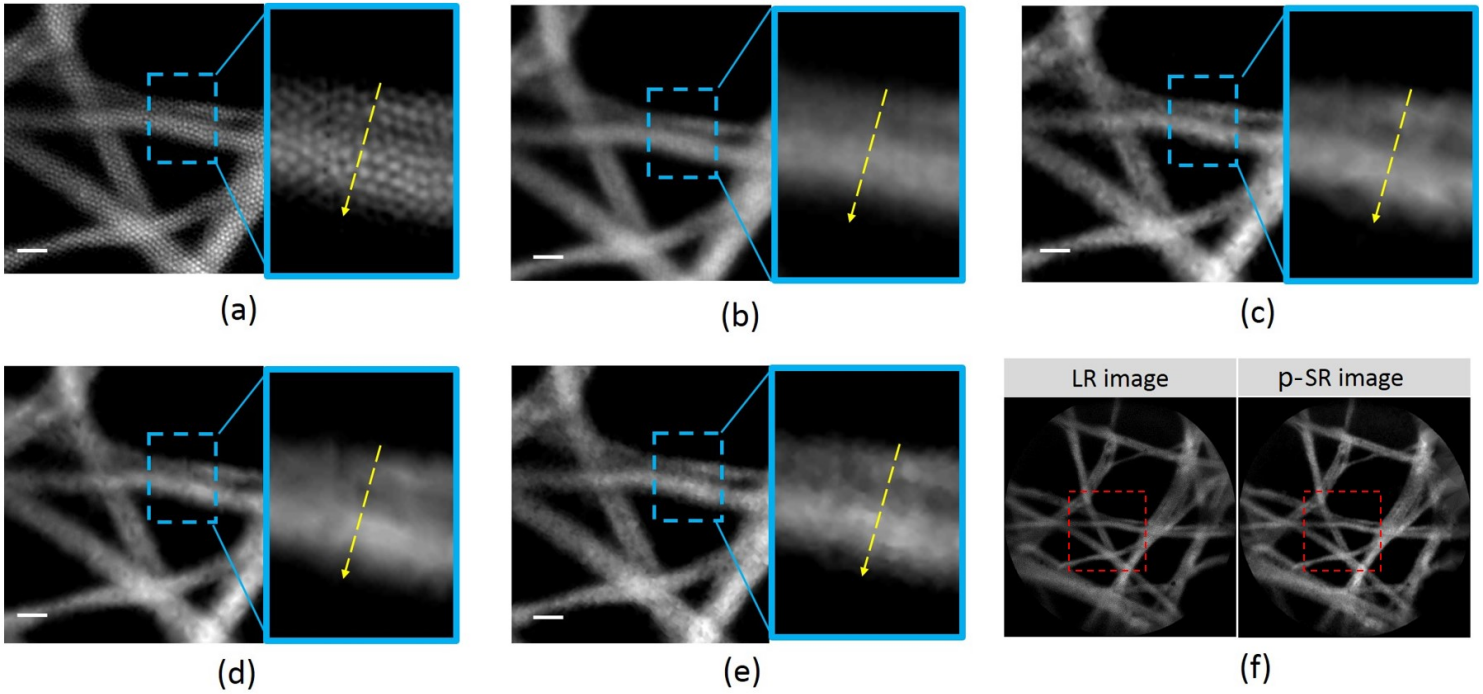

Figure 6.13: Results from imaging lens tissue paper using four images with a 2x2 square shift pattern, showing (a) single raw acquired LR image, (b) reconstruction by Gaussian smoothing on a single LR image, (c) reconstruction by DT algorithm on a single LR image, (d) reconstruction by DT algorithm on the average of 4 shifted LR images, (e) reconstruction using the proposed p-SR method and (f) un-cropped images of single LR frame and p-SR image reconstructed using the proposed method. For (a)-(e), images are cropped to 233x233 pixels for better visualisation and shown as red box in (f). Zoomed insets (3.1X magnification) correspond to a small area where two lens paper fibres overlap. The scale bar is 10 μm.

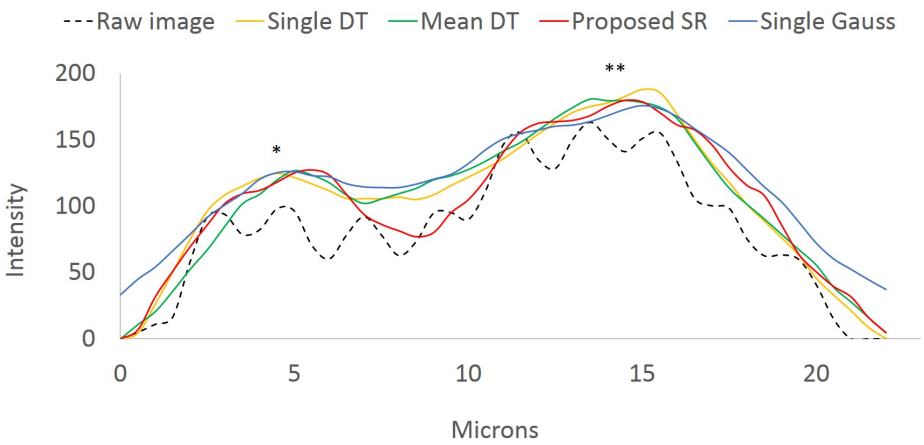

Figure 6.14: Plot of pixel intensity along a line segment shown on the insets in Fig.6.13. Image contrast values are calculated at *peak-1 and **peak-2.

Ex-vivo breast tissue imaging

The performance of the proposed system is further demonstrated by using it to image normal adipose cells of human breast tissue. Small cut-outs (2 mm × 2 mm) are sectioned from the tissue specimen and stained using AH 0.02% in saline solution. The specimen is immersed in a test tube containing the staining solution for 1 minute and then rinsed with water to remove excess stain before being imaged immediately. Fluorescence fibre-bundle endomicroscopy imaging of normal adipose cells of human breast tissue are acquired. Fig.6.15 shows images and zoomed insets of stained adipose cells of normal breast tissue. The adipose cells appear as dark hexagons with bright borders. There are sparse nuclei on the borders which are positively stained by the dye and can be clearly distinguished as hyper-fluorescent dots [244]. LR and p-SR images are reconstructed as for the lens tissue paper as in the previous section.

A small area where two nuclei are close to each other is chosen and magnified 3.1 times, as shown in the insets, for visualisation purposes. The intensity values along a yellow line are plotted as a function of distance in Fig.6.15(e). From the intensity plot, it is evident that for the raw image, the fibre-pixelation artefacts lead to significant intensity modulations making it difficult to identify any underlying structures. For 'single DT' and 'mean DT', the profile appears as a single broad band with some modulations in intensity but the contrast for them is significantly low, less than 1.3%. As a result, the two nuclei cannot be resolved. Using the proposed p-SR algorithm, two peaks corresponding to the two nuclei are observed with image contrast values of 14.0% for peak-1 and 12.2% for peak-2, making it possible to resolve the two neighbouring nuclei, which otherwise is not possible.

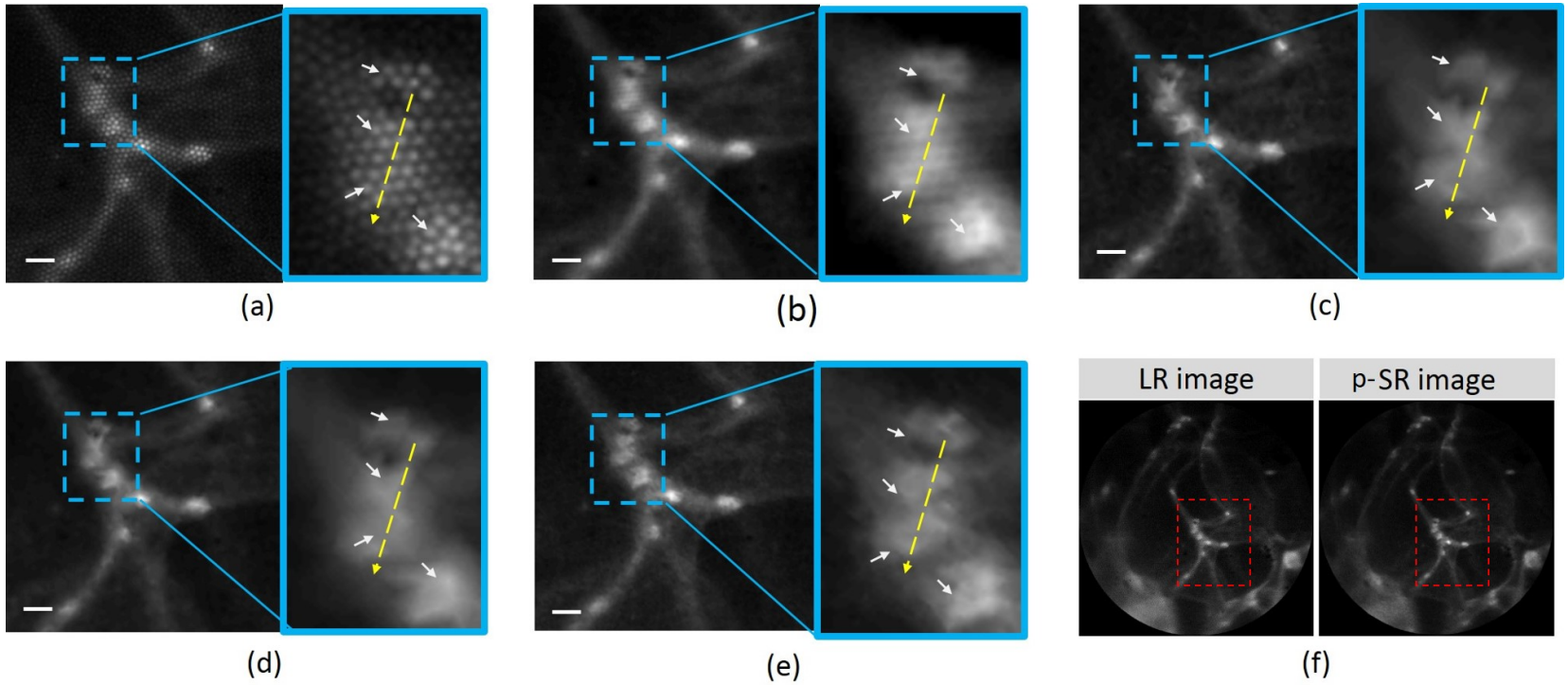

Figure 6.15: Results from imaging adipose cells of human breast tissue using four images with a 2x2 square shift pattern, showing (a) raw single acquired LR image, (b) reconstruction by Gaussian smoothing on a single LR image, (c) reconstruction by DT algorithm on a single LR image, (d) reconstruction by DT algorithm on the average of 4 images, (e) reconstruction using the proposed p-SR method and (f) un-cropped images of single LR frame and p-SR image reconstructed using the proposed method with field of view of 350μm. For (a)-(e), images are cropped to 233x233 pixels for better visualisation and shown as red box in (f). Zoomed insets (3.1X magnification) correspond to a small area containing adjacent nuclei on the borders of adipose cells. The scale bar is 10μm.

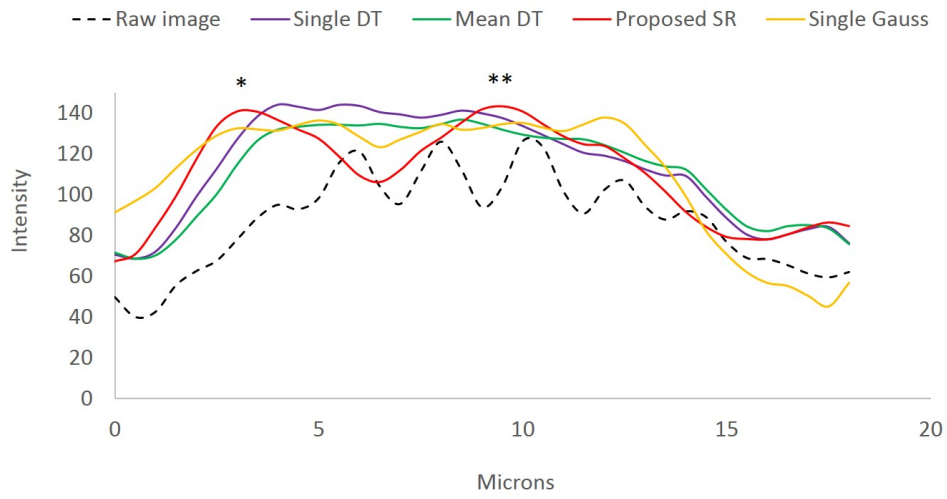

Figure 6.16: Plot of pixel intensity along a line segment shown on the insets in Fig.6.15. Image contrast values are calculated at *peak-1 and **peak-2.

6.6 Discussion

The imaging results demonstrate that the proposed PZT based fibre-shifting system allows for an enhancement of the resolution compared to reconstructions based on single images. These experiments are conducted using a line-scan confocal laser endomicroscopy system because of the high image acquisition rate of 120 fps. With the proposed system, p-SR images can be acquired at 30 fps making it suitable for real-time imaging applications. In principle, the proposed system can be implemented with any microscope and fibre-bundle without major hardware modification. The reconstructed images demonstrate higher contrast and the details such as nuclear shape are more readily visualised in the zoomed-in sections.

In the literature, several nuclear morphometric metrics such size, shape and number in a given area, as well as nucleus/cytoplasm ratio, have been shown to help distinguish between normal, benign and neoplastic breast conditions, making it important to resolve each nuclei accurately [245]. The preliminary experiments reported here demonstrate that the system has sufficient resolution to resolve features separated by less than 2.2 μm (on the USAF target) and nuclei with a diameter of about 2.5 μm. Considering that the neoplastic tissue exhibits an increase in size for the population of nuclei, these *ex vivo* imaging results suggest a potential benefit of this system for cancer diagnosis by real-time assessment of epithelial structures with sub-cellular resolution. However, further work will be required to determine the applicability of this work to nucleic imaging more generally and to establish whether there is a significant benefit over lower-resolution approaches.

The prototype probe is constructed using a stock GRIN lens and PZT tube. A drive voltage of 19 V is applied to each electrode-pair of the PZT tube to achieve the required lateral deflection of 2.24 μm, which is equal to half the inter-core spacing of Fujikura fibre-bundle. This is below the stipulated limit of 42.4 V peak AC as per the IEC 60601-1 standard which makes the approach suitable for clinical *in vivo* imaging.

However, size limitations prevent the probe assembly to be used through most endoscopic working channels due to its rigid length of 45 mm and an outer diameter of 5 mm (including the GRIN lens). The larger size of the design is driven by the PZT tube (30(L) $\times$ 3.2(OD) $\times$ 2.2(ID) mm) and the 3D printed outer tube. This limitation could potentially be overcome by using custom-made smaller PZT scanning tubes and thin-walled outer packaging making the probe assembly more compact. Once the size limitation is overcome, the assembly can be deployed through the conventional endoscopes' working channels resulting in improved diagnostic performance of optical biopsy systems. The improved performance will increase the ability to identify and differentiate features of neoplastic and non-neoplastic cells at a sub-cellular scale.

For this approach to function as desired, the probe assembly needs to be held steady against the tissue and cannot be used with video mosaicking techniques. This is because this method employs a multi-frame technique which enforces minimal motion between large frames. In instances where motion is present, the algorithm could be adapted to use the motion of the probe in-place of the controlled PZT motion for super-resolution. This would, however, be at the expense of losing the repeatability benefit of the approach.

The two-fold improvement in resolution is achieved using a DT based p-SR construction algorithm and a 2$\times$2 scanning pattern. Using this algorithm, no benefit is found by the use of a more dense scanning pattern. However, it is possible that a further resolution enhancement could be obtained by using different reconstruction algorithms and scanning patterns. A large number of pixel-super-resolution algorithms have been developed for other applications, with a comparison of the performance and computation time of some such approaches available in [264], [275]. It may be possible to adapt these algorithms to this application and develop customised scanning patterns to exceed the gains demonstrated here.

6.7 Conclusion

This chapter demonstrates the development of a miniaturised, high-speed PZT-based fibre-shifting endomicroscope to enhance the resolution over conventional fibre-bundle based imaging systems. The fibre-shifting endomicroscope provides almost a two-fold improvement in resolution, and coupled to a high-speed scanning system could provide real-time

imaging of biological samples at 30 fps. The approach can be used for other fibre-bundle based imaging systems, providing that a four-fold reduction in net frame rate is acceptable. By improving the resolution while maintaining a large FOV, this technique could potentially provide the basis for improving the diagnostic abilities of LS-CLE in clinical settings. The resolution enhancement could allow the surgeon to accomplish more accurate and complete tumour resections, thus reducing the re-operation rates and improving surgical outcomes.

Chapter 7

Conclusions and future work

Breast conserving surgery (BCS), in the form of wide local excision, is the recommended treatment for a large number of patients with early stage disease, or in more advanced cases following neoadjuvant chemotherapy, as it allows complete tumour resection while maintaining acceptable cosmesis. However, on average approximately 20-30% of BCS patients require one or more re-operative interventions, mainly due to the presence of positive or close margins. The standard of care for surgical margin assessment is post-operative examination of histopathological tissue sections, however, this process is invasive, introduces sampling errors and does not provide real-time assessment of the local tumour status of radial margins. As the literature review presented in Chapter 2 demonstrates, there is an unmet clinical need to develop safe and rapid intra-operative margin assessment tool to ensure the completeness of tumour excisions and minimise re-operation rates.

This dissertation focused on the development and testing of novel fluorescence microscopy systems as intra-operative tools for (i) *ex vivo* application: by performing rapid digital histology of freshly excised specimens using acriflavine staining and (ii) *in vivo* application for intra-operative cavity scanning using methylene blue staining. Miniaturised fibre-bundle based confocal fluorescence microscopes were demonstrated to perform *in vivo* and high-resolution optical biopsies of unfixed breast specimens. The undertaken research was presented in two categories - clinical investigations and technical novelties.

Chapter 3 presented a feasibility study on 43 *ex vivo* breast tissue specimens to assess different normal and neoplastic breast pathologies using virtual-slit LS-CLE system. A subset of 20 specimens were subsequently imaged using commercial Cellvizo pCLE system and comparisons were made. Quantitative analysis using three image quality parameters namely blur, entropy and SURF features demonstrated that similar quality of reconstructed mosaics was obtained with the LS-CLE system and commercial point-scanning CLE system. Further, the morphological features in the acquired images visually and qual-

itatively correlated well with histology. The high-speed of LS-CLE facilitated to acquire long contiguous mosaics at frames rates up to 120 fps which was an order of magnitude improvement over the commercial system. This allowed faster scanning of the tissue and generating large-area mosaics which otherwise was difficult to achieve.

Based on the morphological classification of breast tissue from the feasibility study, a clinical study to assess the radial margin status of whole *ex vivo* WLE specimens stained with acriflavine was presented in Chapter 4. A clock-face co-ordinate system was developed to correlate the LS-CLE findings on the margins with corresponding histology. Once the WLE specimen was correctly oriented, mosaics of images from all the 6 margins were assessed within 40 minutes from excision. A total of 1341 mosaics were generated from a test dataset consisting of 25 WLE and surgical excision specimens and an overall classification accuracy of 87.0% and NPV of 98.2% was achieved. The 80% sensitivity and 87.5% specificity was found to be comparable with FSA (Sensitivity of 65%-90% and specificity of 85% to 100% [97, 98, 276, 277] but lower than existing OCT [119, 120] and multiphoton [223] techniques. Further work in this area with larger cohort may be required to compare the results with other optical techniques for imaging margins. Only then a comprehensive assessment of the usefulness of LS-CLE for intra-operative margin assessment can be made.

Various technical limitations were also identified during these clinical studies. The second half of this thesis focused on the development of solutions to these problems. One limitation was the restriction of suitable non-toxic fluorophores for rapid *in vivo* visualisation of different tissue morphologies as acriflavine is not suitable for *in vivo* use. In Chapter 5, a custom high-speed LS-CLE system at 660 nm was developed with topical application of 0.1% MB and demonstrated for rapid morphological assessment of freshly excised breast cancer tissues. Images and mosaics of normal, benign and neoplastic breast tissue, acquired with a lateral resolution of 2.2 μm at 120 Hz, showed distinctive morphological features. Results were comparable in contrast to commercial pCLE with acriflavine staining but with the advantage of a higher frame-rate and use of a safe and regulatory-approved (off-label) stain. An image enhancement algorithm based on histogram equalisation and edge filtering was also developed that improved the image quality of the reconstructed mosaics. Following this, proof-of-concept experiments on the integration of MB aided LS-CLE system with an existing robotic scanning probe were carried out and effectiveness of such a system for imaging large-areas of breast tissue without sacrificing resolution was demonstrated.

The chapter also highlighted the details of design and development of a high-speed dual-wavelength LS-CLE system suitable for multiplexed imaging. Dual-wavelength imaging was achieved by sequentially switching between 488 nm and 660 nm laser sources for

alternate frames, avoiding spectral bleed-through and providing an effective frame rate of 60 Hz. By staining the tissue specimen with complementary non-specific and molecular fast-acting dye, morphological and function information about the sample can be imaged. The two channels were pseudo-coloured and combined, and large-area dual-wavelength mosaics were created by registering and stitching the image frames as the probe moves across the tissue.

The final limitation discussed was the low spatial resolution of current FEM systems due fibre inter-core spacing. A miniaturised, high-speed PZT-based fibre-shifting endomicroscope, capable of enhancing the spatial resolution was demonstrated in Chapter 6. The fibre-shifting endomicroscope provided almost a two-fold improvement in resolution, and coupled to a high-speed scanning system could provide real-time imaging of breast tissue specimens at 30 fps. The higher resolution offered the surgeon with much more comprehensive information about the tissue architecture and improve the prospects for CLE for intraoperative margin evaluation.

As presented in Chapter 3-5, we had the opportunity to perform endomicroscopy imaging on several freshly excised breast cancer cut-outs as well as whole wide local specimens. Significant further development and clinical translation of LS-CLE depends not only on the technical capabilities of the imaging system, but also on the ability of surgeons to interprete and use the information to make a diagnosis. In order for LS-CLE or similar imaging platforms to be useful in a clinical setting, the performance and learning curve for expert pathologists and surgeons for interpretation of the acquired information must be assessed. The future work in this area would focus on expanding the margin assessment study to a larger cohort across multiple centres with the goal to create an Atlas of breast endomicroscopy images and define a taxonomy of pathologies for discrimination of various normal, benign and malignant states. In order to improve the clinical relevance of the work, a computer-based system for autonomous diagnosis and classification of breast lesions will also need to be developed.

The future work would also focus on establishing a staining protocol suitable for clinical implementation of the LS-CLE systems by examining the ability of different topical fluorescent agents to provide additional morphologically useful information of *ex vivo* breast tissues (such as improved delineation of cell membrane and nucleus). The results presented in Chapter 5 demonstrated the capability of imaging tissue stained with multiple dyes using LS-CLE, however investigations were preliminary. The specific combination of fast-acting staining agents, staining protocols and applications of this system are currently being explored. An important application of dual-wavelength LS-CLE for breast margin assessment would be for intra-operative staging and grading of cancer types and subtypes. Advanced pathology practice often utilises IHC techniques with a number of fluorescent

stains and molecular probes to guide treatment decisions, estimate prognosis, to classify cancer into stages and subtypes as well as for individualised, systemic therapy. The most common IHC breast cancer prognostic and diagnostic markers used include: estrogen receptor, human epidermal growth factor receptor-2, Ki-67, progesterone receptor, and p53. Further studies to assess fluorescence probes for quantifying these receptor expressions as well as other rapid staining molecular dyes with LS-CLE, are currently underway.

Bibliography

[1] W. H. Hindle, *Breast care: a clinical guidebook for women's primary health care providers.* Springer Science & Business Media, 1998.

[2] R. Tomer, K. Khairy, and P. J. Keller, "Light sheet microscopy in cell biology," in *Cell Imaging Techniques*, pp. 123–137, Springer, 2012.

[3] J. M. Jabbour, M. A. Saldua, J. N. Bixler, and K. C. Maitland, "Confocal endomicroscopy: instrumentation and medical applications," *Annals of Biomedical Engineering*, vol. 40, no. 2, pp. 378–397, 2012.

[4] W. J. Croft, *Under the microscope: a brief history of microscopy.* World Scientific Hackensack, NJ, 2006.

[5] D. B. Schmolze, K. E. Fogarty, and A. H. Fischer, "Advances in microscopy techniques," *Archives of Pathology & Laboratory Msedicine*, vol. 135, no. 2, p. 255, 2011.

[6] X. Chen, B. Zheng, and H. Liu, "Optical and digital microscopic imaging techniques and applications in pathology," *Analytical Cellular Pathology*, vol. 34, no. 1-2, pp. 5–18, 2011.

[7] A. R. Kherlopian, T. Song, Q. Duan, M. A. Neimark, M. J. Po, J. K. Gohagan, and A. F. Laine, "A review of imaging techniques for systems biology," *BioMed Central Systems Biology*, vol. 2, no. 1, p. 74, 2008.

[8] D. J. Stephens and V. J. Allan, "Light microscopy techniques for live cell imaging," *Science*, vol. 300, no. 5616, pp. 82–86, 2003.

[9] S. Boppart, T. Deutsch, and D. Rattner, "Optical imaging technology in minimally invasive surgery," *Surgical Endoscopy*, vol. 13, no. 7, pp. 718–722, 1999.

[10] R. Jeevan, D. Cromwell, M. Trivella, G. Lawrence, O. Kearins, J. Pereira, C. Sheppard, C. Caddy, J. van der Meulen, *et al.*, "Reoperation rates after breast conserving

surgery for breast cancer among women in england: retrospective study of hospital episode statistics," *British Medical Journal*, vol. 345, p. e4505, 2012.

[11] N. Houssami, P. Macaskill, M. L. Marinovich, and M. Morrow, "The association of surgical margins and local recurrence in women with early-stage invasive breast cancer treated with breast-conserving therapy: a meta-analysis," *Annals of Surgical Oncology*, vol. 21, no. 3, pp. 717–730, 2014.

[12] M. Singh, G. Singh, K. T. Hogan, K. A. Atkins, and A. T. Schroen, "The effect of intraoperative specimen inking on lumpectomy re-excision rates," *World Journal of Surgical Oncology*, vol. 8, no. 1, p. 4, 2010.

[13] G. C. Balch, S. K. Mithani, J. F. Simpson, and M. C. Kelley, "Accuracy of intraoperative gross examination of surgical margin status in women undergoing partial mastectomy for breast malignancy," *The American Surgeon*, vol. 71, no. 1, pp. 22–28, 2005.

[14] G. Oh, E. Chung, and S. H. Yun, "Optical fibers for high-resolution in vivo microendoscopic fluorescence imaging," *Optical Fiber Technology*, vol. 19, no. 6, pp. 760–771, 2013.

[15] T. J. Muldoon, M. C. Pierce, D. L. Nida, M. D. Williams, A. Gillenwater, and R. Richards-Kortum, "Subcellular-resolution molecular imaging within living tissue by fiber microendoscopy," *Optics Express*, vol. 15, no. 25, pp. 16413–16423, 2007.

[16] M. C. Pierce, Y. Guan, M. K. Quinn, X. Zhang, W.-H. Zhang, Y.-L. Qiao, P. Castle, and R. Richards-Kortum, "A pilot study of low-cost, high-resolution microendoscopy as a tool for identifying women with cervical precancer," *Cancer Prevention Research*, vol. 5, no. 11, pp. 1273–1279, 2012.

[17] A. F. Gmitro and D. Aziz, "Confocal microscopy through a fiber-optic imaging bundle," *Optics Letters*, vol. 18, no. 8, pp. 565–567, 1993.

[18] E. Laemmel, M. Genet, G. Le Goualher, A. Perchant, J.-F. Le Gargasson, and E. Vicaut, "Fibered confocal fluorescence microscopy (cell-vizio^{TM}) facilitates extended imaging in the field of microcirculation," *Journal of Vascular Research*, vol. 41, no. 5, pp. 400–411, 2004.

[19] A. L. Polglase, W. J. McLaren, S. A. Skinner, R. Kiesslich, M. F. Neurath, and P. M. Delaney, "A fluorescence confocal endomicroscope for in vivo microscopy of the upper-and the lower-gi tract," *Gastrointestinal Endoscopy*, vol. 62, no. 5, pp. 686–695, 2005.

[20] G. J. Tearney, M. E. Brezinski, B. E. Bouma, S. A. Boppart, C. Pitris, J. F. Southern, and J. G. Fujimoto, "In vivo endoscopic optical biopsy with optical coherence tomography," *Science*, vol. 276, no. 5321, pp. 2037–2039, 1997.

[21] D. C. Adler, Y. Chen, R. Huber, J. Schmitt, J. Connolly, and J. G. Fujimoto, "Three-dimensional endomicroscopy using optical coherence tomography," *Nature Photonics*, vol. 1, no. 12, pp. 709–716, 2007.

[22] K. Murari, Y. Zhang, S. Li, Y. Chen, M.-J. Li, and X. Li, "Compensation-free, all-fiber-optic, two-photon endomicroscopy at 1.55 μm," *Optics Letters*, vol. 36, no. 7, pp. 1299–1301, 2011.

[23] M. Goetz and R. Kiesslich, "Confocal endomicroscopy: in vivo diagnosis of neoplastic lesions of the gastrointestinal tract," *Anticancer Research*, vol. 28, no. 1B, pp. 353–360, 2008.

[24] A. Hoffman, M. Goetz, M. Vieth, P. Galle, M. Neurath, and R. Kiesslich, "Confocal laser endomicroscopy: technical status and current indications," *Endoscopy*, vol. 38, no. 12, pp. 1275–1283, 2006.

[25] A. Meining, "Confocal endomicroscopy," *Gastrointestinal Endoscopy Clinics*, vol. 19, no. 4, pp. 629–635, 2009.

[26] K. Wu, J.-J. Liu, W. Adams, G. A. Sonn, K. E. Mach, Y. Pan, A. H. Beck, K. C. Jensen, and J. C. Liao, "Dynamic real-time microscopy of the urinary tract using confocal laser endomicroscopy," *Urology*, vol. 78, no. 1, pp. 225–231, 2011.

[27] R. C. Newton, S. V. Kemp, G.-Z. Yang, D. S. Elson, A. Darzi, and P. L. Shah, "Imaging parenchymal lung diseases with confocal endomicroscopy," *Respiratory Medicine*, vol. 106, no. 1, pp. 127–137, 2012.

[28] A. Fugazza, F. Gaiani, M. C. Carra, F. Brunetti, M. Lévy, I. Sobhani, D. Azoulay, F. Catena, G. L. de'Angelis, and N. de'Angelis, "Confocal laser endomicroscopy in gastrointestinal and pancreatobiliary diseases: a systematic review and meta-analysis," *BioMed Research International*, vol. 2016, 2016.

[29] S. E. Singletary, "Surgical margins in patients with early-stage breast cancer treated with breast conservation therapy," *The American Journal of Surgery*, vol. 184, no. 5, pp. 383–393, 2002.

[30] S. Standring, *Gray's anatomy e-book: the anatomical basis of clinical practice*. Elsevier Health Sciences, 2015.

[31] P. P. Rosen, *Rosen's breast pathology.* Lippincott Williams & Wilkins, 2001.

[32] D. Ramsay, J. Kent, R. Hartmann, and P. Hartmann, "Anatomy of the lactating human breast redefined with ultrasound imaging," *Journal of Anatomy*, vol. 206, no. 6, pp. 525–534, 2005.

[33] S. M. Love and S. H. Barsky, "Anatomy of the nipple and breast ducts revisited," *Cancer*, vol. 101, no. 9, pp. 1947–1957, 2004.

[34] J. M. Tanner, *Growth at Adolescence: With a General Consideration of the Effects of Hereditary and Environmental Factors Upon Growth and Maturation from Birth to Maturity. 2d Ed.* Blackwell Scientific Publications, 1973.

[35] J. Stines and H. Tristant, "The normal breast and its variations in mammography," *European Journal of Radiology*, vol. 54, no. 1, pp. 26–36, 2005.

[36] R. G. Abramson, A. Mavi, T. Cermik, S. Basu, N. E. Wehrli, M. Houseni, S. Mishra, J. Udupa, P. Lakhani, A. D. Maidment, *et al.*, "Age-related structural and functional changes in the breast: multimodality correlation with digital mammography, computed tomography, magnetic resonance imaging, and positron emission tomography," in *Seminars in nuclear medicine*, vol. 37, pp. 146–153, Elsevier, 2007.

[37] G. Söderqvist, E. Isaksson, B. von Schoultz, K. Carlström, E. Tani, and L. Skoog, "Proliferation of breast epithelial cells in healthy women during the menstrual cycle," *American Journal of Obstetrics and Gynaecology*, vol. 176, no. 1, pp. 123–128, 1997.

[38] J. Russo, R. Moral, G. A. Balogh, D. Mailo, and I. H. Russo, "The protective role of pregnancy in breast cancer," *Breast Cancer Research*, vol. 7, no. 3, p. 131, 2005.

[39] J. Russo and I. H. Russo, "Development of the human breast," *Maturitas*, vol. 49, no. 1, pp. 2–15, 2004.

[40] A. Jemal, F. Bray, M. M. Center, J. Ferlay, E. Ward, and D. Forman, "Global cancer statistics," *CA: A Cancer Journal for Clinicians*, vol. 61, no. 2, pp. 69–90, 2011.

[41] J. Ferlay, E. Steliarova-Foucher, J. Lortet-Tieulent, S. Rosso, J.-W. W. Coebergh, H. Comber, D. Forman, and F. Bray, "Cancer incidence and mortality patterns in europe: estimates for 40 countries in 2012," *European Journal of Cancer*, vol. 49, no. 6, pp. 1374–1403, 2013.

[42] B. W. Stewart and C. Wild, "World cancer report 2014. lyon, france: International agency for research on cancer," *World Health Organization*, p. 630, 2014.

[43] *Census 2001: General Report for England and Wales.* Office for National Statistics, Palgrave Macmillan, 2005.

[44] R. Blanks, S. Moss, C. McGahan, M. Quinn, and P. Babb, "Effect of nhs breast screening programme on mortality from breast cancer in england and wales, 1990-8: comparison of observed with predicted mortality," *British Medical Journal*, vol. 321, no. 7262, pp. 665–669, 2000.

[45] K. I. Bland, J. B. Mccraw, E. M. Copeland, and L. O. Vasconez, *Breast: Comprehensive Management of Benign and Malignant Diseases, Fifth Edition.* Elsevier, 2009.

[46] J. R. Harris, M. E. Lippman, C. K. Osborne, and M. Morrow, *Diseases of the Breast.* Lippincott Williams & Wilkins, 2012.

[47] S. Wellings and H. Jensen, "On the origin and progression of ductal carcinoma in the human breast," *Journal of the National Cancer Institute*, vol. 50, no. 5, pp. 1111–1118, 1973.

[48] P. Cole, J. M. Elwood, and S. D. Kaplan, "Incidence rates and risk factors of benign breast neoplasms," *American Journal of Epidemiology*, vol. 108, no. 2, pp. 112–120, 1978.

[49] S. J. London, J. L. Connolly, S. J. Schnitt, and G. A. Colditz, "A prospective study of benign breast disease and the risk of breast cancer," *The journal of the American Medical Association*, vol. 267, no. 7, pp. 941–944, 1992.

[50] C. L. Carter, D. K. Corle, M. S. Micozzi, A. Schatzkin, and P. R. Taylor, "A prospective study of the development of breast cancer in 16,692 women with benign breast disease," *American Journal of Epidemiology*, vol. 128, no. 3, pp. 467–477, 1988.

[51] W. B. Hutchinson, D. B. Thomas, W. B. Hamlin, G. J. Roth, A. V. Peterson, and B. Williams, "Risk of breast cancer in women with benign breast disease," *Journal of the National Cancer Institute*, vol. 65, no. 1, pp. 13–20, 1980.

[52] S. Wellings, H. Jensen, and R. Marcum, "An atlas of subgross pathology of the human breast with special reference to possible precancerous lesions," *Journal of the National Cancer Institute*, vol. 55, no. 2, pp. 231–273, 1975.

[53] P. P. Rosen, "The pathological classification of human mammary carcinoma: past, present and future," *Annals of Clinical & Laboratory Science*, vol. 9, no. 2, pp. 144–156, 1979.

[54] C. Haagensen, N. Lane, R. Lattes, and C. Bodian, "Lobular neoplasia (so-called lobular carcinoma in situ) of the breast," *Cancer*, vol. 42, no. 2, pp. 737–769, 1978.

[55] R. Ashikari, A. G. Huvos, J. A. Urban, and G. F. Robbins, "Infiltrating lobular carcinoma of the breast," *Cancer*, vol. 31, no. 1, pp. 110–116, 1973.

[56] R. L. Ridolfi, P. P. Rosen, A. Port, D. Kinne, and V. Miké, "Medullary carcinoma of the breast. a clinicopathologic study with 10 year follow-up," *Cancer*, vol. 40, no. 4, pp. 1365–1385, 1977.

[57] E. Avisar, M. A. Khan, D. Axelrod, and K. Oza, "Pure mucinous carcinoma of the breast: a clinicopathologic correlation study," *Annals of Surgical Oncology*, vol. 5, no. 5, pp. 447–451, 1998.

[58] R. W. McDivitt, W. Boyce, and D. Gersell, "Tubular carcinoma of the breast. clinical and pathological observations concerning 135 cases.," *The American Journal of Surgical Pathology*, vol. 6, no. 5, pp. 401–411, 1982.

[59] I. Ahmed, R. Nazir, M. Chaudhary, and S. Kundi, "Triple assessment of breast lump.," *Journal of the College of Physicians and Surgeons–Pakistan: JCPSP*, vol. 17, no. 9, pp. 535–538, 2007.

[60] C. Borrelli, S. Cohen, A. Duncan, *et al.*, *NHS breast screening programme: clinical guidance for breast cancer screening assessment.* Public Health England, London, 2016.

[61] S. A. Feig, "Decreased breast cancer mortality through mammographic screening: results of clinical trials.," *Radiology*, vol. 167, no. 3, pp. 659–665, 1988.

[62] D. D. Dershaw, "Mammographic screening of the high-risk woman," *The American Journal of Surgery*, vol. 180, no. 4, pp. 288–289, 2000.

[63] H. D. Nelson, K. Tyne, A. Naik, C. Bougatsos, B. K. Chan, and L. Humphrey, "Screening for breast cancer: an update for the us preventive services task force," *Annals of Internal Medicine*, vol. 151, no. 10, pp. 727–737, 2009.

[64] P. A. Carney, D. L. Miglioretti, B. C. Yankaskas, K. Kerlikowske, R. Rosenberg, C. M. Rutter, B. M. Geller, L. A. Abraham, S. H. Taplin, M. Dignan, *et al.*, "Individual and combined effects of age, breast density, and hormone replacement therapy use on the accuracy of screening mammography," *Annals of Internal Medicine*, vol. 138, no. 3, pp. 168–175, 2003.

[65] T. M. Kolb, J. Lichy, and J. H. Newhouse, "Comparison of the performance of screening mammography, physical examination, and breast us and evaluation of factors that influence them: an analysis of 27,825 patient evaluations," *Radiology*, vol. 225, no. 1, pp. 165–175, 2002.

[66] M. Wallis, M. Walsh, and J. Lee, "A review of false negative mammography in a symptomatic population," *Clinical Radiology*, vol. 44, no. 1, pp. 13–15, 1991.

[67] R. F. Brem, M. J. Lenihan, J. Lieberman, and J. Torrente, "Screening breast ultrasound: Past, present, and future," *American Journal of Roentgenology*, vol. 204, no. 2, pp. 234–240, 2015.

[68] W. Teh and A. Wilson, "The role of ultrasound in breast cancer screening. a consensus statement by the european group for breast cancer screening," *European Journal of Cancer*, vol. 34, no. 4, pp. 449–450, 1998.

[69] C. K. Kuhl, S. Schrading, C. C. Leutner, N. Morakkabati-Spitz, E. Wardelmann, R. Fimmers, W. Kuhn, and H. H. Schild, "Mammography, breast ultrasound, and magnetic resonance imaging for surveillance of women at high familial risk for breast cancer," *Journal of Clinical Oncology*, vol. 23, no. 33, pp. 8469–8476, 2005.

[70] D. Thigpen, A. Kappler, and R. Brem, "The role of ultrasound in screening dense breasts—a review of the literature and practical solutions for implementation," *Diagnostics*, vol. 8, no. 1, p. 20, 2018.

[71] D. Saslow, C. Boetes, W. Burke, S. Harms, M. O. Leach, C. D. Lehman, E. Morris, E. Pisano, M. Schnall, S. Sener, *et al.*, "American cancer society guidelines for breast screening with mri as an adjunct to mammography," *CA- A Cancer Journal For Clinicians*, vol. 57, no. 2, pp. 75–89, 2007.

[72] M. Kriege, C. T. Brekelmans, C. Boetes, P. E. Besnard, H. M. Zonderland, I. M. Obdeijn, R. A. Manoliu, T. Kok, H. Peterse, M. M. Tilanus-Linthorst, *et al.*, "Efficacy of mri and mammography for breast-cancer screening in women with a familial or genetic predisposition," *New England Journal of Medicine*, vol. 351, no. 5, pp. 427–437, 2004.

[73] M. Morrow, J. Waters, and E. Morris, "Mri for breast cancer screening, diagnosis, and treatment," *The Lancet*, vol. 378, no. 9805, pp. 1804–1811, 2011.

[74] T. S. Kline, L. P. Joshi, and H. S. Neal, "Fine-needle aspiration of the breast: Diagnoses and pitfalls. a review of 3545 cases," *Cancer*, vol. 44, no. 4, pp. 1458–1464, 1979.

[75] J. Dixon, T. Anderson, J. Lamb, S. Nixon, and A. Forrest, "Fine needle aspiration cytology, in relationships to clinical examination and mammography in the diagnosis of a solid breast mass," *British Journal of Surgery*, vol. 71, no. 8, pp. 593–596, 1984.

[76] E.-K. Kim, C. S. Park, W. Y. Chung, K. K. Oh, D. I. Kim, J. T. Lee, and H. S. Yoo, "New sonographic criteria for recommending fine-needle aspiration biopsy of non-palpable solid nodules of the thyroid," *American Journal of Roentgenology*, vol. 178, no. 3, pp. 687–691, 2002.

[77] J. E. Meyer, D. N. Smith, S. C. Lester, C. Kaelin, P. J. DiPiro, C. M. Denison, R. L. Christian, S. C. Harvey, D.-L. G. Selland, and S. M. Durfee, "Large-core needle biopsy of nonpalpable breast lesions," *Jama*, vol. 281, no. 17, pp. 1638–1641, 1999.

[78] M. S. Ballo and N. Sneige, "Can core needle biopsy replace fine-needle aspiration cytology in the diagnosis of palpable breast carcinoma: A comparative study of 124 women," *Cancer: Interdisciplinary International Journal of the American Cancer Society*, vol. 78, no. 4, pp. 773–777, 1996.

[79] S. Mitra and P. Dey, "Fine-needle aspiration and core biopsy in the diagnosis of breast lesions: A comparison and review of the literature," *Cyto Journal*, vol. 13, 2016.

[80] K. D. Miller, R. L. Siegel, C. C. Lin, A. B. Mariotto, J. L. Kramer, J. H. Rowland, K. D. Stein, R. Alteri, and A. Jemal, "Cancer treatment and survivorship statistics, 2016," *CA: A Cancer Journal for Clinicians*, vol. 66, no. 4, pp. 271–289, 2016.

[81] U. Veronesi, E. Marubini, L. Mariani, V. Galimberti, A. Luini, P. Veronesi, B. Salvadori, and R. Zucali, "Radiotherapy after breast-conserving surgery in small breast carcinoma: long-term results of a randomized trial," *Annals of Oncology*, vol. 12, no. 7, pp. 997–1003, 2001.

[82] U. Veronesi, N. Cascinelli, L. Mariani, M. Greco, R. Saccozzi, A. Luini, M. Aguilar, and E. Marubini, "Twenty-year follow-up of a randomized study comparing breast-conserving surgery with radical mastectomy for early breast cancer," *New England Journal of Medicine*, vol. 347, no. 16, pp. 1227–1232, 2002.

[83] J. A. Jacobson, D. N. Danforth, K. H. Cowan, T. d'Angelo, S. M. Steinberg, L. Pierce, M. E. Lippman, A. S. Lichter, E. Glatstein, and P. Okunieff, "Ten-year results of a comparison of conservation with mastectomy in the treatment of stage i and ii breast cancer," *New England Journal of Medicine*, vol. 332, no. 14, pp. 907–911, 1995.

[84] B. Fisher, S. Anderson, J. Bryant, R. G. Margolese, M. Deutsch, E. R. Fisher, J.-H. Jeong, and N. Wolmark, "Twenty-year follow-up of a randomized trial comparing total mastectomy, lumpectomy, and lumpectomy plus irradiation for the treatment of invasive breast cancer," *New England Journal of Medicine*, vol. 347, no. 16, pp. 1233–1241, 2002.

[85] R. Arriagada, M. G. Lê, F. Rochard, and G. Contesso, "Conservative treatment versus mastectomy in early breast cancer: patterns of failure with 15 years of follow-up data. institut gustave-roussy breast cancer group.," *Journal of Clinical Oncology*, vol. 14, no. 5, pp. 1558–1564, 1996.

[86] J. Landercasper, E. Whitacre, A. C. Degnim, and M. Al-Hamadani, "Reasons for re-excision after lumpectomy for breast cancer: insight from the american society of breast surgeons masterysm database," *Annals of Surgical Oncology*, vol. 21, no. 10, pp. 3185–3191, 2014.

[87] J. J. Jobsen, J. van der Palen, F. Ong, and J. H. Meerwaldt, "The value of a positive margin for invasive carcinoma in breast-conservative treatment in relation to local recurrence is limited to young women only," *International Journal of Radiation Oncology* Biology* Physics*, vol. 57, no. 3, pp. 724–731, 2003.

[88] N. B. Kouzminova, S. Aggarwal, A. Aggarwal, M. D. Allo, and A. Y. Lin, "Impact of initial surgical margins and residual cancer upon re-excision on outcome of patients with localized breast cancer," *The American Journal of Surgery*, vol. 198, no. 6, pp. 771–780, 2009.

[89] D. Aziz, E. Rawlinson, S. A. Narod, P. Sun, H. L. A. Lickley, D. R. McCready, and C. M. Holloway, "The role of reexcision for positive margins in optimizing local disease control after breast-conserving surgery for cancer," *The Breast Journal*, vol. 12, no. 4, pp. 331–337, 2006.

[90] R. Wolters, A. Regierer, L. Schwentner, V. Geyer, K. Possinger, R. Kreienberg, M. Wischnewsky, and A. Wöckel, "A comparison of international breast cancer guidelines–do the national guidelines differ in treatment recommendations?," *European Journal of Cancer*, vol. 48, no. 1, pp. 1–11, 2012.

[91] M. S. Moran, S. J. Schnitt, A. E. Giuliano, J. R. Harris, S. A. Khan, J. Horton, S. Klimberg, M. Chavez-MacGregor, G. Freedman, N. Houssami, *et al.*, "Society of surgical oncology–american society for radiation oncology consensus guideline on margins for breast-conserving surgery with whole-breast irradiation in stages i and

ii invasive breast cancer," *Annals of Surgical Oncology*, vol. 21, no. 3, pp. 704–716, 2014.

[92] *Early and locally advanced breast cancer: diagnosis and treatment.* National Collaborating Centre for Cancer (UK), 2009.

[93] M. Muttalib, C. Tai, T. Briant-Evans, I. Maheswaran, N. Livni, S. Shousha, and H. Sinnett, "Intra-operative assessment of excision margins using breast imprint and scrape cytology," *The Breast*, vol. 14, no. 1, pp. 42–50, 2005.

[94] K. Esbona, Z. Li, and L. G. Wilke, "Intraoperative imprint cytology and frozen section pathology for margin assessment in breast conservation surgery: a systematic review," *Annals of Surgical Oncology*, vol. 19, no. 10, pp. 3236–3245, 2012.

[95] A. J. Creager, J. A. Shaw, P. R. Young, and K. R. Geisinger, "Intraoperative evaluation of lumpectomy margins by imprint cytology with histologic correlation: a community hospital experience," *Archives of Pathology & Laboratory Medicine*, vol. 126, no. 7, pp. 846–848, 2002.

[96] M. Bakhshandeh, S. O. Tutuncuoglu, G. Fischer, and S. Masood, "Use of imprint cytology for assessment of surgical margins in lumpectomy specimens of breast cancer patients," *Diagnostic Cytopathology*, vol. 35, no. 10, pp. 656–659, 2007.

[97] T. Olson, J. Harter, A. Munoz, D. Mahvi, and T. Breslin, "Frozen section analysis for intraoperative margin assessment during breast-conserving surgery results in low rates of re-excision and local recurrence," *Annals of Surgical Oncology*, vol. 14, no. 10, p. 2953, 2007.

[98] W. P. Weber, S. Engelberger, C. T. Viehl, R. Zanetti-Dallenbach, S. Kuster, S. Dirnhofer, D. Wruk, D. Oertli, and W. R. Marti, "Accuracy of frozen section analysis versus specimen radiography during breast-conserving surgery for nonpalpable lesions," *World Journal of Surgery*, vol. 32, no. 12, p. 2599, 2008.

[99] J. M. Jorns, D. Visscher, M. Sabel, T. Breslin, P. Healy, S. Daignaut, J. L. Myers, and A. J. Wu, "Intraoperative frozen section analysis of margins in breast conserving surgery significantly decreases reoperative rates: one-year experience at an ambulatory surgical center," *American Journal of Clinical Pathology*, vol. 138, no. 5, pp. 657–669, 2012.

[100] G. Abbas, K. S. Heller, A. Khoynezhad, S. Dubner, and L. A. Sznyter, "The incidence of carcinoma in cytologically benign thyroid cysts," *Surgery*, vol. 130, no. 6, pp. 1035–1038, 2001.

[101] B. Erguvan-Dogan, G. J. Whitman, V. A. Nguyen, M. J. Dryden, R. J. Stafford, J. Hazle, K. R. McAlee, M. J. Phelps, M. F. Ice, H. M. Kuerer, *et al.*, "Specimen radiography in confirmation of mri-guided needle localization and surgical excision of breast lesions," *American Journal of Roentgenology*, vol. 187, no. 2, pp. 339–344, 2006.

[102] J. T. McCormick, A. J. Keleher, V. B. Tikhomirov, R. J. Budway, and P. F. Caushaj, "Analysis of the use of specimen mammography in breast conservation therapy," *The American Journal of Surgery*, vol. 188, no. 4, pp. 433–436, 2004.

[103] D. Layfield, D. May, R. Cutress, C. Richardson, A. Agrawal, M. Wise, and C. Yiangou, "The effect of introducing an in-theatre intra-operative specimen radiography (iosr) system on the management of palpable breast cancer within a single unit," *The Breast*, vol. 21, no. 4, pp. 459–463, 2012.

[104] S. P. Harlow, D. N. Krag, S. E. Ames, and D. L. Weaver, "Intraoperative ultrasound localization to guide surgical excision of nonpalpable breast carcinoma1," *Journal of the American College of Surgeons*, vol. 189, no. 3, pp. 241–246, 1999.

[105] L. F. Smith, I. T. Rubio, R. Henry-Tillman, S. Korourian, and V. S. Klimberg, "Intraoperative ultrasound-guided breast biopsy," *The American Journal of Surgery*, vol. 180, no. 6, pp. 419–423, 2000.

[106] N. M. Krekel, M. H. Haloua, A. M. L. Cardozo, R. H. de Wit, A. M. Bosch, L. M. de Widt-Levert, S. Muller, H. van der Veen, E. Bergers, E. S. d. L. de Klerk, *et al.*, "Intraoperative ultrasound guidance for palpable breast cancer excision (cobalt trial): a multicentre, randomised controlled trial," *The Lancet Oncology*, vol. 14, no. 1, pp. 48–54, 2013.

[107] C. Ngô, A. G. Pollet, J. Laperrelle, G. Ackerman, S. Gomme, F. Thibault, V. Fourchotte, and R. J. Salmon, "Intraoperative ultrasound localization of nonpalpable breast cancers," *Annals of Surgical Oncology*, vol. 14, no. 9, p. 2485, 2007.

[108] T. Karni, I. Pappo, J. Sandbank, O. Lavon, V. Kent, R. Spector, S. Morgenstern, and S. Lelcuk, "A device for real-time, intraoperative margin assessment in breast-conservation surgery," *The American Journal of Surgery*, vol. 194, no. 4, pp. 467–473, 2007.

[109] T. M. Allweis, Z. Kaufman, S. Lelcuk, I. Pappo, T. Karni, S. Schneebaum, R. Spector, A. Schindel, D. Hershko, M. Zilberman, *et al.*, "A prospective, randomized, controlled, multicenter study of a real-time, intraoperative probe for positive margin

detection in breast-conserving surgery," *The American Journal of Surgery*, vol. 196, no. 4, pp. 483–489, 2008.

[110] F. Schnabel, S. K. Boolbol, M. Gittleman, T. Karni, L. Tafra, S. Feldman, A. Police, N. B. Friedman, S. Karlan, D. Holmes, *et al.*, "A randomized prospective study of lumpectomy margin assessment with use of marginprobe in patients with nonpalpable breast malignancies," *Annals of Surgical Oncology*, vol. 21, no. 5, pp. 1589–1595, 2014.

[111] J. M. Dixon, L. Renshaw, O. Young, D. Kulkarni, T. Saleem, M. Sarfaty, R. Sreenivasan, C. Kusnick, J. Thomas, and L. Williams, "Intra-operative assessment of excised breast tumour margins using clearedge imaging device," *European Journal of Surgical Oncology (EJSO)*, vol. 42, no. 12, pp. 1834–1840, 2016.

[112] J. Balog, L. Sasi-Szabó, J. Kinross, M. R. Lewis, L. J. Muirhead, K. Veselkov, R. Mirnezami, B. Dezső, L. Damjanovich, A. Darzi, *et al.*, "Intraoperative tissue identification using rapid evaporative ionization mass spectrometry," *Science Translational Medicine*, vol. 5, no. 194, pp. 194ra93–194ra93, 2013.

[113] E. R. St John, J. Balog, J. S. McKenzie, M. Rossi, A. Covington, L. Muirhead, Z. Bodai, F. Rosini, A. V. Speller, S. Shousha, *et al.*, "Rapid evaporative ionisation mass spectrometry of electrosurgical vapours for the identification of breast pathology: towards an intelligent knife for breast cancer surgery," *Breast Cancer Research*, vol. 19, no. 1, p. 59, 2017.

[114] D. Calligaris, D. Caragacianu, X. Liu, I. Norton, C. J. Thompson, A. L. Richardson, M. Golshan, M. L. Easterling, S. Santagata, D. A. Dillon, *et al.*, "Application of desorption electrospray ionization mass spectrometry imaging in breast cancer margin analysis," *Proceedings of the National Academy of Sciences*, vol. 111, no. 42, pp. 15184–15189, 2014.

[115] I. J. Bigio, S. G. Bown, G. M. Briggs, C. Kelley, S. Lakhani, D. C. O. Pickard, P. M. Ripley, I. Rose, and C. Saunders, "Diagnosis of breast cancer using elastic-scattering spectroscopy: preliminary clinical results," *Journal of Biomedical Optics*, vol. 5, no. 2, pp. 221–229, 2000.

[116] M. D. Keller, S. K. Majumder, M. C. Kelley, I. M. Meszoely, F. I. Boulos, G. M. Olivares, and A. Mahadevan-Jansen, "Autofluorescence and diffuse reflectance spectroscopy and spectral imaging for breast surgical margin analysis," *Lasers in Surgery and Medicine: The Official Journal of the American Society for Laser Medicine and Surgery*, vol. 42, no. 1, pp. 15–23, 2010.

[117] A. S. Haka, Z. Volynskaya, J. A. Gardecki, J. Nazemi, J. Lyons, D. Hicks, M. Fitzmaurice, R. R. Dasari, J. P. Crowe, and M. S. Feld, "In vivo margin assessment during partial mastectomy breast surgery using raman spectroscopy," *Cancer Research*, vol. 66, no. 6, pp. 3317–3322, 2006.

[118] K. Kong, F. Zaabar, E. Rakha, I. Ellis, A. Koloydenko, and I. Notingher, "Towards intra-operative diagnosis of tumours during breast conserving surgery by selective-sampling raman micro-spectroscopy," *Physics in Medicine & Biology*, vol. 59, no. 20, p. 6141, 2014.

[119] R. A. McLaughlin, B. C. Quirk, A. Curatolo, R. W. Kirk, L. Scolaro, D. Lorenser, P. D. Robbins, B. A. Wood, C. M. Saunders, and D. D. Sampson, "Imaging of breast cancer with optical coherence tomography needle probes: feasibility and initial results," *IEEE journal of Selected Topics in Quantum Electronics*, vol. 18, no. 3, pp. 1184–1191, 2012.

[120] F. T. Nguyen, A. M. Zysk, E. J. Chaney, J. G. Kotynek, U. J. Oliphant, F. J. Bellafiore, K. M. Rowland, P. A. Johnson, and S. A. Boppart, "Intraoperative evaluation of breast tumor margins with optical coherence tomography," *Cancer Research*, vol. 69, no. 22, pp. 8790–8796, 2009.

[121] M. Jain, N. Shukla, M. Manzoor, S. Nadolny, and S. Mukherjee, "Modified full-field optical coherence tomography: A novel tool for rapid histology of tissues," *Journal of Pathology Informatics*, vol. 2, 2011.

[122] F. T. Nguyen, A. M. Zysk, E. J. Chaney, S. G. Adie, J. G. Kotynek, U. J. Oliphant, F. J. Bellafiore, K. M. Rowland, P. A. Johnson, and S. A. Boppart, "Optical coherence tomography: the intraoperative assessment of lymph nodes in breast cancer," *IEEE Engineering in Medicine and Biology Magazine*, vol. 29, no. 2, pp. 63–70, 2010.

[123] A. M. Zysk, K. Chen, E. Gabrielson, L. Tafra, E. A. M. Gonzalez, J. K. Canner, E. B. Schneider, A. J. Cittadine, P. S. Carney, S. A. Boppart, *et al.*, "Intraoperative assessment of final margins with a handheld optical imaging probe during breast-conserving surgery may reduce the reoperation rate: Results of a multicenter study," *Annals of Surgical Oncology*, vol. 22, no. 10, pp. 3356–3362, 2015.

[124] R. A. McLaughlin, L. Scolaro, P. Robbins, S. Hamza, C. Saunders, and D. D. Sampson, "Imaging of human lymph nodes using optical coherence tomography: potential for staging cancer," *Cancer Research*, pp. 0008–5472, 2010.

[125] M. Chalfie, Y. Tu, G. Euskirchen, W. W. Ward, and D. C. Prasher, "Green fluorescent protein as a marker for gene expression," *Science*, vol. 263, no. 5148, pp. 802–805, 1994.

[126] D. B. Murphy, *Fundamentals of light microscopy and electronic imaging.* John Wiley & Sons, 2002.

[127] A. Kohler, "A new method of illumination for photomicrographical purposes," *Journal of Royal Microscopy Society*, vol. 10, pp. 433–440, 1893.

[128] M. Born and E. Wolf, *Principles of optics: electromagnetic theory of propagation, interference and diffraction of light.* Elsevier, 2013.

[129] E. Abbe, "Beiträge zur theorie des mikroskops und der mikroskopischen wahrnehmung," *Archiv für mikroskopische Anatomie*, vol. 9, no. 1, pp. 413–418, 1873.

[130] J. M. East, C. S. Valentine, E. Kanchev, and G. O. Blake, "Sentinel lymph node biopsy for breast cancer using methylene blue dye manifests a short learning curve among experienced surgeons: a prospective tabular cumulative sum (cusum) analysis," *BioMed Central Surgery*, vol. 9, no. 1, p. 1, 2009.

[131] A. Nasrinossadat, F. Ladan, E. Fereshte, O. Asieh, C. Reza, S. Akramossadat, and M. Golshan, "Marking non-palpable breast masses with injected methylene blue dye, an easy, safe and low cost method for developing countries and resource-limited areas," *Asian Pacific Journal of Cancer Pathology*, vol. 12, pp. 1189–1192, 2011.

[132] J. Tang, X. Wang, Y.-P. Wu, X. Wang, Z.-Q. Lian, J.-H. Fu, and M.-T. Yang, "Significance of methylene blue dye for localization biopsy of nonpalpable breast lesions," *Chinese Journal of Cancer*, vol. 28, pp. 79–81, 2009.

[133] R. Kiesslich, J. Burg, M. Vieth, J. Gnaendiger, M. Enders, P. Delaney, A. Polglase, W. McLaren, D. Janell, S. Thomas, *et al.*, "Confocal laser endoscopy for diagnosing intraepithelial neoplasias and colorectal cancer in vivo," *Gastroenterology*, vol. 127, no. 3, pp. 706–713, 2004.

[134] M. Minsky, "Confocal scanning microscope," *Rapport Technique, Patent*, vol. 3, 1955.

[135] J.-A. Conchello and J. W. Lichtman, "Optical sectioning microscopy," *Nature Methods*, vol. 2, no. 12, p. 920, 2005.

[136] J. Pawley, *Handbook of biological confocal microscopy.* Springer Science & Business Media, 2010.

[137] T. Wilson, "Resolution and optical sectioning in the confocal microscope," *Journal of Microscopy*, vol. 244, no. 2, pp. 113–121, 2011.

[138] C. Sheppard, D. Shotton, and C. Sheppard, *Confocal Laser Scanning Microscopy. Microscopy Handbook.* New York: BIOS Scientific Publishers Ltd, 1997.

[139] T. Wilson and C. Sheppard, *Theory and practice of scanning optical microscopy*, vol. 180. Academic Press London, 1984.

[140] C. Sheppard and X. Mao, "Confocal microscopes with slit apertures," *Journal of Modern Optics*, vol. 35, no. 7, pp. 1169–1185, 1988.

[141] S. Kimura and C. Munakata, "Three-dimensional optical transfer function for the fluorescent scanning optical microscope with a slit," *Applied Optics*, vol. 29, no. 7, pp. 1004–1007, 1990.

[142] D. R. Sandison and W. W. Webb, "Background rejection and signal-to-noise optimization in confocal and alternative fluorescence microscopes," *Applied Optics*, vol. 33, no. 4, pp. 603–615, 1994.

[143] K.-B. Im, S. Han, H. Park, D. Kim, and B.-M. Kim, "Simple high-speed confocal line-scanning microscope," *Optics Express*, vol. 13, no. 13, pp. 5151–5156, 2005.

[144] R. Wolleschensky, B. Zimmermann, and M. Kempe, "High-speed confocal fluorescence imaging with a novel line scanning microscope," *Journal of Biomedical Optics*, vol. 11, no. 6, p. 064011, 2006.

[145] V. Poher, G. T. Kennedy, H. B. Manning, D. M. Owen, H. X. Zhang, E. Gu, M. D. Dawson, P. M. French, and M. A. Neil, "Improved sectioning in a slit scanning confocal microscope," *Optics Letters*, vol. 33, no. 16, pp. 1813–1815, 2008.

[146] E. Mei, P. Fomitchov, R. Graves, and M. Campion, "A line scanning confocal fluorescent microscope using a cmos rolling shutter as an adjustable aperture," *Journal of Microscopy*, vol. 247, no. 3, pp. 269–276, 2012.

[147] M. Petráň, M. Hadravskỳ, M. D. Egger, and R. Galambos, "Tandem-scanning reflected-light microscope," *Journal of the Optical Society of America*, vol. 58, no. 5, pp. 661–664, 1968.

[148] R. Juskaitis, T. Wilson, M. Neil, and M. Kozubek, "Efficient real-time confocal microscopy with white light sources," *Nature*, vol. 383, no. 6603, p. 804, 1996.

[149] J. Huisken, J. Swoger, F. Del Bene, J. Wittbrodt, and E. H. Stelzer, "Optical sectioning deep inside live embryos by selective plane illumination microscopy," *Science*, vol. 305, no. 5686, pp. 1007–1009, 2004.

[150] A. H. Voie, D. Burns, and F. Spelman, "Orthogonal-plane fluorescence optical sectioning: three-dimensional imaging of macroscopic biological specimens," *Journal of Microscopy*, vol. 170, no. 3, pp. 229–236, 1993.

[151] K. Greger, J. Swoger, and E. H. Stelzer, "Basic building units and properties of a fluorescence single plane illumination microscope," *Review of Scientific Instruments*, vol. 78, no. 2, p. 023705, 2007.

[152] P. J. Keller, A. D. Schmidt, J. Wittbrodt, and E. H. Stelzer, "Reconstruction of zebrafish early embryonic development by scanned light sheet microscopy," *Science*, vol. 322, no. 5904, pp. 1065–1069, 2008.

[153] M. B. Ahrens, M. B. Orger, D. N. Robson, J. M. Li, and P. J. Keller, "Whole-brain functional imaging at cellular resolution using light-sheet microscopy," *Nature Methods*, vol. 10, no. 5, p. 413, 2013.

[154] P. J. Keller and E. H. Stelzer, "Digital scanned laser light sheet fluorescence microscopy," *Cold Spring Harbor Protocols*, vol. 2010, no. 5, pp. pdb–top78, 2010.

[155] T. Vettenburg, H. I. Dalgarno, J. Nylk, C. Coll-Lladó, D. E. Ferrier, T. Čižmár, F. J. Gunn-Moore, and K. Dholakia, "Light-sheet microscopy using an airy beam," *Nature Methods*, vol. 11, no. 5, p. 541, 2014.

[156] B.-C. Chen, W. R. Legant, K. Wang, L. Shao, D. E. Milkie, M. W. Davidson, C. Janetopoulos, X. S. Wu, J. A. Hammer, Z. Liu, *et al.*, "Lattice light-sheet microscopy: imaging molecules to embryos at high spatiotemporal resolution," *Science*, vol. 346, no. 6208, p. 1257998, 2014.

[157] C. Dunsby, "Optically sectioned imaging by oblique plane microscopy," *Optics Express*, vol. 16, no. 25, pp. 20306–20316, 2008.

[158] P. J. Verveer, M. J. Gemkow, and T. M. Jovin, "A comparison of image restoration approaches applied to three-dimensional confocal and wide-field fluorescence microscopy," *Journal of Microscopy*, vol. 193, no. 1, pp. 50–61, 1999.

[159] J. G. McNally, T. Karpova, J. Cooper, and J. A. Conchello, "Three-dimensional imaging by deconvolution microscopy," *Methods*, vol. 19, no. 3, pp. 373–385, 1999.

[160] T. J. Holmes, "Blind deconvolution of quantum-limited incoherent imagery: maximum-likelihood approach," *Journal of the Optical Society of America A*, vol. 9, no. 7, pp. 1052–1061, 1992.

[161] P. Sarder and A. Nehorai, "Deconvolution methods for 3-d fluorescence microscopy images," *IEEE Signal Processing Magazine*, vol. 23, no. 3, pp. 32–45, 2006.

[162] J.-B. Sibarita, "Deconvolution microscopy," in *Microscopy Techniques*, pp. 201–243, Springer, 2005.

[163] M. A. Neil, R. Juškaitis, and T. Wilson, "Method of obtaining optical sectioning by using structured light in a conventional microscope," *Optics Letters*, vol. 22, no. 24, pp. 1905–1907, 1997.

[164] B. Bailey, D. L. Farkas, D. L. Taylor, and F. Lanni, "Enhancement of axial resolution in fluorescence microscopy by standing-wave excitation," *Nature*, vol. 366, no. 6450, p. 44, 1993.

[165] M. G. Gustafsson, "Surpassing the lateral resolution limit by a factor of two using structured illumination microscopy," *Journal of Microscopy*, vol. 198, no. 2, pp. 82–87, 2000.

[166] V. Poher, H. Zhang, G. Kennedy, C. Griffin, S. Oddos, E. Gu, D. Elson, J. Girkin, P. French, M. Dawson, *et al.*, "Optical sectioning microscopes with no moving parts using a micro-stripe array light emitting diode," *Optics Express*, vol. 15, no. 18, pp. 11196–11206, 2007.

[167] P. Kner, B. B. Chhun, E. R. Griffis, L. Winoto, and M. G. Gustafsson, "Super-resolution video microscopy of live cells by structured illumination," *Nature Methods*, vol. 6, no. 5, p. 339, 2009.

[168] L. Shao, P. Kner, E. H. Rego, and M. G. Gustafsson, "Super-resolution 3d microscopy of live whole cells using structured illumination," *Nature Methods*, vol. 8, no. 12, p. 1044, 2011.

[169] D. Dan, M. Lei, B. Yao, W. Wang, M. Winterhalder, A. Zumbusch, Y. Qi, L. Xia, S. Yan, Y. Yang, *et al.*, "Dmd-based led-illumination super-resolution and optical sectioning microscopy," *Scientific Reports*, vol. 3, p. 1116, 2013.

[170] A. G. York, S. H. Parekh, D. Dalle Nogare, R. S. Fischer, K. Temprine, M. Mione, A. B. Chitnis, C. A. Combs, and H. Shroff, "Resolution doubling in live, multicellular organisms via multifocal structured illumination microscopy," *Nature Methods*, vol. 9, no. 7, p. 749, 2012.

[171] O. Schulz, C. Pieper, M. Clever, J. Pfaff, A. Ruhlandt, R. H. Kehlenbach, F. S. Wouters, J. Großhans, G. Bunt, and J. Enderlein, "Resolution doubling in fluorescence microscopy with confocal spinning-disk image scanning microscopy," *Proceedings of the National Academy of Sciences*, vol. 110, no. 52, pp. 21000–21005, 2013.

[172] M. Epstein, "Fiber optics in medicine.," *Critical Reviews in Biomedical Engineering*, vol. 7, no. 2, pp. 79–120, 1982.

[173] B. A. Flusberg, E. D. Cocker, W. Piyawattanametha, J. C. Jung, E. L. Cheung, and M. J. Schnitzer, "Fiber-optic fluorescence imaging," *Nature Methods*, vol. 2, no. 12, pp. 941–950, 2005.

[174] S. Kimura and T. Wilson, "Confocal scanning optical microscope using single-mode fiber for signal detection," *Applied Optics*, vol. 30, no. 16, pp. 2143–2150, 1991.

[175] G. J. Tearney, R. Webb, and B. Bouma, "Spectrally encoded confocal microscopy," *Optics Letters*, vol. 23, no. 15, pp. 1152–1154, 1998.

[176] J. A. Udovich, N. D. Kirkpatrick, A. Kano, A. Tanbakuchi, U. Utzinger, and A. F. Gmitro, "Spectral background and transmission characteristics of fiber optic imaging bundles," *Applied Optics*, vol. 47, no. 25, pp. 4560–4568, 2008.

[177] Z. A. Steelman, S. Kim, E. T. Jelly, M. Crose, K. K. Chu, and A. Wax, "Comparison of imaging fiber bundles for coherence-domain imaging," *Applied Optics*, vol. 57, no. 6, pp. 1455–1462, 2018.

[178] H. D. Ford and R. P. Tatam, "Characterization of optical fiber imaging bundles for swept-source optical coherence tomography," *Applied Optics*, vol. 50, no. 5, pp. 627–640, 2011.

[179] H. D. Ford and R. P. Tatam, "Coherent fibre bundles in full-field swept-source oct," in *Optical Coherence Tomography and Coherence Domain Optical Methods in Biomedicine XIII*, vol. 7168, p. 71682P, International Society for Optics and Photonics, 2009.

[180] Y. S. Sabharwal, A. R. Rouse, L. Donaldson, M. F. Hopkins, and A. F. Gmitro, "Slit-scanning confocal microendoscope for high-resolution in vivo imaging," *Applied Optics*, vol. 38, no. 34, pp. 7133–7144, 1999.

[181] A. R. Rouse, A. Kano, J. A. Udovich, S. M. Kroto, and A. F. Gmitro, "Design and demonstration of a miniature catheter for a confocal microendoscope," *Applied Optics*, vol. 43, no. 31, pp. 5763–5771, 2004.

[182] C. Liang, K.-B. Sung, R. R. Richards-Kortum, and M. R. Descour, "Design of a high-numerical-aperture miniature microscope objective for an endoscopic fiber confocal reflectance microscope," *Applied Optics*, vol. 41, no. 22, pp. 4603–4610, 2002.

[183] G. Le Goualher, A. Perchant, M. Genet, C. Cavé, B. Viellerobe, F. Berier, B. Abrat, and N. Ayache, "Towards optical biopsies with an integrated fibered confocal fluorescence microscope," in *Medical Image Computing and Computer-Assisted Intervention–MICCAI 2004*, pp. 761–768, Springer, 2004.

[184] M. Kyrish and T. S. Tkaczyk, "Achromatized endomicroscope objective for optical biopsy," *Biomedical Optics Express*, vol. 4, no. 2, pp. 287–297, 2013.

[185] M. R. Kyrish, J. L. Dobbs, S. Jain, X. Wang, D. Yu, R. R. Richards-Kortum, and T. S. Tkaczyk, "Needle-based fluorescence endomicroscopy via structured illumination with a plastic, achromatic objective," *Journal of Biomedical Optics*, vol. 18, no. 9, p. 096003, 2013.

[186] K. Carlson, M. Chidley, K.-B. Sung, M. Descour, A. Gillenwater, M. Follen, and R. Richards-Kortum, "In vivo fiber-optic confocal reflectance microscope with an injection-molded plastic miniature objective lens," *Applied Optics*, vol. 44, no. 10, pp. 1792–1797, 2005.

[187] L. Fu and M. Gu, "Fibre-optic nonlinear optical microscopy and endoscopy," *Journal of Microscopy*, vol. 226, no. 3, pp. 195–206, 2007.

[188] D. Bird and M. Gu, "Two-photon fluorescence endoscopy with a micro-optic scanning head," *Optics Letters*, vol. 28, no. 17, pp. 1552–1554, 2003.

[189] J. Knittel, L. Schnieder, G. Buess, B. Messerschmidt, and T. Possner, "Endoscope-compatible confocal microscope using a gradient index-lens system," *Optics Communications*, vol. 188, no. 5-6, pp. 267–273, 2001.

[190] J. C. Jung, A. D. Mehta, E. Aksay, R. Stepnoski, and M. J. Schnitzer, "In vivo mammalian brain imaging using one-and two-photon fluorescence microendoscopy," *Journal of Neurophysiology*, vol. 92, no. 5, pp. 3121–3133, 2004.

[191] W. Lee and S. Yun, "Adaptive aberration correction of grin lenses for confocal endomicroscopy," *Optics Letters*, vol. 36, no. 23, pp. 4608–4610, 2011.

[192] P. Kim, E. Chung, H. Yamashita, K. E. Hung, A. Mizoguchi, R. Kucherlapati, D. Fukumura, R. K. Jain, and S. H. Yun, "In vivo wide-area cellular imaging by side-view endomicroscopy," *Nature Methods*, vol. 7, no. 4, p. 303, 2010.

[193] R. P. Barretto, T. H. Ko, J. C. Jung, T. J. Wang, G. Capps, A. C. Waters, Y. Ziv, A. Attardo, L. Recht, and M. J. Schnitzer, "Time-lapse imaging of disease progression in deep brain areas using fluorescence microendoscopy," *Nature Medicine*, vol. 17, no. 2, p. 223, 2011.

[194] J. K. Kim, W. M. Lee, P. Kim, M. Choi, K. Jung, S. Kim, and S. H. Yun, "Fabrication and operation of grin probes for in vivo fluorescence cellular imaging of internal organs in small animals," *Nature Protocols*, vol. 7, no. 8, pp. 1456–1469, 2012.

[195] M. H. Koucky and M. C. Pierce, "Axial response of high-resolution microendoscopy in scattering media," *Biomedical Optics Express*, vol. 4, no. 10, pp. 2247–2256, 2013.

[196] M. Pierce, D. Yu, and R. Richards-Kortum, "High-resolution fiber-optic microendoscopy for in situ cellular imaging," *Journal of Visualized Experiments: JoVE*, no. 47, 2011.

[197] M. C. Pierce, P. M. Vila, A. D. Polydorides, R. Richards-Kortum, and S. Anandasabapathy, "Low-cost endomicroscopy in the esophagus and colon," *The American Journal of Gastroenterology*, vol. 106, no. 9, p. 1722, 2011.

[198] P. M. Vila, C. W. Park, M. C. Pierce, G. H. Goldstein, L. Levy, V. V. Gurudutt, A. D. Polydorides, J. H. Godbold, M. S. Teng, E. M. Genden, *et al.*, "Discrimination of benign and neoplastic mucosa with a high-resolution microendoscope (hrme) in head and neck cancer," *Annals of Surgical Oncology*, vol. 19, no. 11, pp. 3534–3539, 2012.

[199] N. Krstajić, A. R. Akram, T. R. Choudhary, N. McDonald, M. G. Tanner, E. Pedretti, P. A. Dalgarno, E. Scholefield, J. M. Girkin, A. Moore, *et al.*, "Two-color widefield fluorescence microendoscopy enables multiplexed molecular imaging in the alveolar space of human lung tissue," *Journal of Biomedical Optics*, vol. 21, no. 4, p. 046009, 2016.

[200] N. Bozinovic, C. Ventalon, T. Ford, and J. Mertz, "Fluorescence endomicroscopy with structured illumination," *Optics Express*, vol. 16, no. 11, pp. 8016–8025, 2008.

[201] P. Keahey, T. Tkaczyk, K. Schmeler, and R. Richards-Kortum, "Optimizing modulation frequency for structured illumination in a fiber-optic microendoscope to image nuclear morphometry in columnar epithelium," *Biomedical Optics Express*, vol. 6, no. 3, pp. 870–880, 2015.

[202] T. N. Ford, D. Lim, and J. Mertz, "Fast optically sectioned fluorescence hilo endomicroscopy," *Journal of Biomedical Optics*, vol. 17, no. 2, pp. 0211051–0211057, 2012.

[203] L. Giniunas, R. Juskaitis, and S. Shatalin, "Scanning fibre-optic microscope," *Electronics Letters*, vol. 27, no. 9, pp. 724–726, 1991.

[204] R. Juškaitis and T. Wilson, "Direct-view fiber-optic confocal microscope," *Optics Letters*, vol. 19, no. 22, pp. 1906–1908, 1994.

[205] D. Dickensheets and G. Kino, "Micromachined scanning confocal optical microscope," *Optics Letters*, vol. 21, no. 10, pp. 764–766, 1996.

[206] D. L. Dickensheets and G. S. Kino, "Silicon-micromachined scanning confocal optical microscope," *Journal of Microelectromechanical Systems*, vol. 7, no. 1, pp. 38–47, 1998.

[207] K. C. Maitland, H. J. Shin, H. Ra, D. Lee, O. Solgaard, and R. Richards-Kortum, "Single fiber confocal microscope with a two-axis gimbaled mems scanner for cellular imaging," *Optics Express*, vol. 14, no. 19, pp. 8604–8612, 2006.

[208] U. Hofmann, S. Muehlmann, M. Witt, K. Doerschel, R. Schuetz, and B. Wagner, "Electrostatically driven micromirrors for a miniaturized confocal laser scanning microscope," in *Miniaturized Systems with Micro-Optics and MEMS*, vol. 3878, pp. 29–39, International Society for Optics and Photonics, 1999.

[209] K. Murakami, A. Murata, T. Suga, H. Kitagawa, Y. Kamiya, M. Kubo, K. Matsumoto, H. Miyajima, and M. Katashiro, "A miniature confocal optical microscope with mems gimbal scanner," in *TRANSDUCERS, Solid-State Sensors, Actuators and Microsystems, 12th International Conference on, 2003*, vol. 1, pp. 587–590, IEEE, 2003.

[210] W. Piyawattanametha, H. Ra, K. E. Loewke, M. J. Mandella, C. H. Contag, Z. Qiu, T. D. Wang, S. Friedland, J. T. Liu, G. S. Kino, *et al.*, "In vivo near-infrared dual-axis confocal microendoscopy in the human lower gastrointestinal tract," *Journal of Biomedical Optics*, vol. 17, no. 2, p. 021102, 2012.

[211] H.-J. Shin, M. C. Pierce, D. Lee, H. Ra, O. Solgaard, and R. Richards-Kortum, "Fiber-optic confocal microscope using a mems scanner and miniature objective lens," *Optics Express*, vol. 15, no. 15, pp. 9113–9122, 2007.

[212] M. D. Risi, H. Makhlouf, A. R. Rouse, A. A. Tanbakuchi, and A. F. Gmitro, "Design and performance of a multi-point scan confocal microendoscope," in *Photonics*, vol. 1, pp. 421–431, Multidisciplinary Digital Publishing Institute, 2014.

[213] A. A. Tanbakuchi, A. R. Rouse, J. A. Udovich, K. D. Hatch, and A. F. Gmitro, "Clinical confocal microlaparoscope for real-time in vivo optical biopsies," *Journal of Biomedical Optics*, vol. 14, no. 4, p. 044030, 2009.

[214] H. Makhlouf, A. F. Gmitro, A. A. Tanbakuchi, J. A. Udovich, and A. R. Rouse, "Multispectral confocal microendoscope for in vivo and in situ imaging," *Journal of Biomedical Optics*, vol. 13, no. 4, p. 044016, 2008.

[215] M. Hughes and G.-Z. Yang, "High speed, line-scanning, fiber bundle fluorescence confocal endomicroscopy for improved mosaicking," *Biomedical Optics Express*, vol. 6, no. 4, pp. 1241–1252, 2015.

[216] M. Hughes and G.-Z. Yang, "Line-scanning fiber bundle endomicroscopy with a virtual detector slit," *Biomedical Optics Express*, vol. 7, no. 6, pp. 2257–2268, 2016.

[217] J.-H. Han, J. Lee, and J. U. Kang, "Pixelation effect removal from fiber bundle probe based optical coherence tomography imaging," *Optics Express*, vol. 18, no. 7, pp. 7427–7439, 2010.

[218] M. Dumripatanachod and W. Piyawattanametha, "A fast depixelation method of fiber bundle image for an embedded system," in *Biomedical Engineering International Conference (BMEiCON), 2015 8th*, pp. 1–4, IEEE, 2015.

[219] A. Shinde and M. V. Matham, "Pixelate removal in an image fiber probe endoscope incorporating comb structure removal methods," *Journal of Medical Imaging and Health Informatics*, vol. 4, no. 2, pp. 203–211, 2014.

[220] B. Rosa, M. S. Erden, T. Vercauteren, B. Herman, J. Szewczyk, and G. Morel, "Building large mosaics of confocal edomicroscopic images using visual servoing," *IEEE Transactions on Biomedical Engineering*, vol. 60, no. 4, pp. 1041–1049, 2013.

[221] T. Vercauteren, A. Meining, F. Lacombe, and A. Perchant, "Real time autonomous video image registration for endomicroscopy: fighting the compromises," in *Biomedical Optics (BiOS) 2008*, pp. 68610C–68610C, International Society for Optics and Photonics, 2008.

[222] J. Westwood *et al.*, "Real-time image mosaicing for medical applications," *Medicine Meets Virtual Reality 15: In Vivo, in Vitro, in Silico: Designing the Next in Medicine*, vol. 125, p. 304, 2007.

[223] Y. K. Tao, D. Shen, Y. Sheikine, O. O. Ahsen, H. H. Wang, D. B. Schmolze, N. B. Johnson, J. S. Brooker, A. E. Cable, J. L. Connolly, *et al.*, "Assessment of breast pathologies using nonlinear microscopy," *Proceedings of the National Academy of Sciences*, vol. 111, no. 43, pp. 15304–15309, 2014.

[224] F. Helmchen and W. Denk, "Deep tissue two-photon microscopy," *Nature Methods*, vol. 2, no. 12, p. 932, 2005.

[225] X. Wu, G. Chen, J. Lu, W. Zhu, J. Qiu, J. Chen, S. Xie, S. Zhuo, and J. Yan, "Label-free detection of breast masses using multiphoton microscopy," *PloS One*, vol. 8, no. 6, p. e65933, 2013.

[226] M. Rajadhyaksha, M. Grossman, D. Esterowitz, R. H. Webb, and R. R. Anderson, "In vivo confocal scanning laser microscopy of human skin: melanin provides strong contrast," *Journal of Investigative Dermatology*, vol. 104, no. 6, pp. 946–952, 1995.

[227] J. M. Bini, J. Spain, K. S. Nehal, M. Rajadhyaksha, V. Hazelwood, and C. A. DiMarzio, "Confocal mosaicing microscopy of human skin ex vivo: spectral analysis for digital staining to simulate histology-like appearance," *Journal of Biomedical Optics*, vol. 16, no. 7, p. 076008, 2011.

[228] D. S. Gareau, Y. Li, B. Huang, Z. Eastman, K. S. Nehal, and M. Rajadhyaksha, "Confocal mosaicing microscopy in mohs skin excisions: feasibility of rapid surgical pathology," *Journal of Biomedical Optics*, vol. 13, no. 5, p. 054001, 2008.

[229] D. S. Gareau, J. K. Karen, S. W. Dusza, M. Tudisco, K. S. Nehal, and M. Rajadhyaksha, "Sensitivity and specificity for detecting basal cell carcinomas in mohs excisions with confocal fluorescence mosaicing microscopy," *Journal of Biomedical Optics*, vol. 14, no. 3, p. 034012, 2009.

[230] J. L. Dobbs, H. Ding, A. P. Benveniste, H. M. Kuerer, S. Krishnamurthy, W. T. Yang, and R. R. Richards-Kortum, "Feasibility of confocal fluorescence microscopy for real-time evaluation of neoplasia in fresh human breast tissue," *Journal of Biomedical Optics*, vol. 18, no. 10, p. 106016, 2013.

[231] J. Dobbs, S. Krishnamurthy, M. Kyrish, A. P. Benveniste, W. Yang, and R. Richards-Kortum, "Confocal fluorescence microscopy for rapid evaluation of invasive tumor cellularity of inflammatory breast carcinoma core needle biopsies," *Breast Cancer Research and Treatment*, vol. 149, no. 1, pp. 303–310, 2015.

[232] J. L. Dobbs, D. Shin, S. Krishnamurthy, H. Kuerer, W. Yang, and R. Richards-Kortum, "Confocal fluorescence microscopy to evaluate changes in adipocytes in

the tumor microenvironment associated with invasive ductal carcinoma and ductal carcinoma in situ," *International Journal of Cancer*, vol. 139, no. 5, pp. 1140–1149, 2016.

[233] S. Krishnamurthy, A. Cortes, M. Lopez, M. Wallace, S. Sabir, K. Shaw, and G. Mills, "Ex vivo confocal fluorescence microscopy for rapid evaluation of tissues in surgical pathology practice," *Archives of Pathology & Laboratory Medicine*, vol. 142, no. 3, pp. 396–401, 2017.

[234] M. Ragazzi, S. Piana, C. Longo, F. Castagnetti, M. Foroni, G. Ferrari, G. Gardini, and G. Pellacani, "Fluorescence confocal microscopy for pathologists," *Modern Pathology*, vol. 27, no. 3, p. 460, 2014.

[235] S. Abeytunge, B. A. Larson, G. Peterson, M. Morrow, M. Rajadhyaksha, and M. P. Murray, "Evaluation of breast tissue with confocal strip-mosaicking microscopy: a test approach emulating pathology-like examination," *Journal of Biomedical Optics*, vol. 22, no. 3, p. 034002, 2017.

[236] H. L. Fu, J. L. Mueller, M. J. Whitley, D. M. Cardona, R. M. Willett, D. G. Kirsch, J. Q. Brown, and N. Ramanujam, "Structured illumination microscopy and a quantitative image analysis for the detection of positive margins in a pre-clinical genetically engineered mouse model of sarcoma," *PloS One*, vol. 11, no. 1, p. e0147006, 2016.

[237] A. K. Glaser, N. P. Reder, Y. Chen, E. F. McCarty, C. Yin, L. Wei, Y. Wang, L. D. True, and J. T. Liu, "Light-sheet microscopy for slide-free non-destructive pathology of large clinical specimens," *Nature Biomedical Engineering*, vol. 1, no. 7, p. 0084, 2017.

[238] Z. Gao, G. Li, X. Li, J. Zhou, X. Duan, J. Chen, B. P. Joshi, R. Kuick, B. Khoury, D. G. Thomas, *et al.*, "In vivo near-infrared imaging of erbb2 expressing breast tumors with dual-axes confocal endomicroscopy using a targeted peptide," *Scientific Reports*, vol. 7, no. 1, p. 14404, 2017.

[239] T. P. Chang, D. R. Leff, S. Shousha, D. J. Hadjiminas, R. Ramakrishnan, M. Gudi, R. Al Mufti, R. C. Newton, A. Darzi, and G. Z. Yang, "Imaging of breast cancer morphology using probe-based confocal laser endomicroscopy: Towards a novel imaging tool for real-time intra-operative cavity scanning," *European Journal of Surgical Oncology*, vol. 11, no. 39, p. S80, 2013.

[240] G. D. De Palma, D. Esposito, G. Luglio, G. Limite, A. Accurso, V. Sollazzo, F. Maione, G. Cassese, S. Siciliano, N. Gennarelli, *et al.*, "Confocal laser endomi-

croscopy in breast surgery: a pilot study," *BioMed Central Cancer*, vol. 15, no. 1, pp. 1–7, 2015.

[241] S. Zuo, M. Hughes, C. Seneci, T. P. Chang, and G.-Z. Yang, "Toward intraoperative breast endomicroscopy¡? brk?¿ with a novel surface-scanning device," *IEEE Transactions on Biomedical Engineering*, vol. 62, no. 12, pp. 2941–2952, 2015.

[242] K. J. Rosbach, D. Shin, T. J. Muldoon, M. A. Quraishi, L. P. Middleton, K. K. Hunt, F. Meric-Bernstam, T.-K. Yu, R. R. Richards-Kortum, and W. Yang, "High-resolution fiber optic microscopy with fluorescent contrast enhancement for the identification of axillary lymph node metastases in breast cancer: a pilot study," *Biomedical Optics Express*, vol. 1, no. 3, pp. 911–922, 2010.

[243] J. Dobbs, M. Kyrish, S. Krishnamurthy, B. Grant, H. Kuerer, W. Yang, T. Tkaczyk, and R. Richards-Kortum, "High resolution microendoscopy with structured illumination and lugol's iodine staining for evaluation of breast cancer architecture," in *Optical Biopsy XIV: Toward Real-Time Spectroscopic Imaging and Diagnosis*, vol. 9703, p. 97030E, International Society for Optics and Photonics, 2016.

[244] T. P. Chang, D. R. Leff, S. Shousha, D. J. Hadjiminas, R. Ramakrishnan, M. R. Hughes, G.-Z. Yang, and A. Darzi, "Imaging breast cancer morphology using probe-based confocal laser endomicroscopy: towards a real-time intraoperative imaging tool for cavity scanning," *Breast Cancer Research and Treatment*, vol. 153, no. 2, pp. 299–310, 2015.

[245] K. J. Pienta and D. S. Coffey, "Correlation of nuclear morphometry with progression of breast cancer," *Cancer*, vol. 68, no. 9, pp. 2012–2016, 1991.

[246] F. Crete, T. Dolmiere, P. Ladret, and M. Nicolas, "The blur effect: perception and estimation with a new no-reference perceptual blur metric," in *Human vision and electronic imaging XII*, vol. 6492, p. 64920I, International Society for Optics and Photonics, 2007.

[247] H. Bay, T. Tuytelaars, and L. Van Gool, "Surf: Speeded up robust features," in *European conference on computer vision*, pp. 404–417, Springer, 2006.

[248] J. Dobbs, M. Kyrish, N. Bedard, B. Grant, S. Krishnamurthy, W. Yang, T. Tkaczyk, and R. Richards-Kortum, "High resolution microendoscopy with structured illumination for evaluation of breast cancer architecture," in *Frontiers in Optics*, pp. FTu4F–6, Optical Society of America, 2014.

[249] F. S. Fuchs, S. Zirlik, K. Hildner, M. Frieser, M. Ganslmayer, S. Schwarz, M. Uder, and M. F. Neurath, "Fluorescein-aided confocal laser endomicroscopy of the lung," *Respiration*, vol. 81, no. 1, pp. 32–38, 2010.

[250] S. Paramsothy and R. W. Leong, "Endoscopy: Fluorescein contrast in confocal laser endomicroscopy," *Nature Reviews Gastroenterology and Hepatology*, vol. 7, no. 7, pp. 366–368, 2010.

[251] L. Thiberville, M. Salauun, S. Lachkar, S. Dominique, S. Moreno-Swirc, C. Vever-Bizet, and G. Bourg-Heckly, "Confocal fluorescence endomicroscopy of the human airways," *Proceedings of the American Thoracic Society*, vol. 6, no. 5, pp. 444–449, 2009.

[252] B. Obstoy, M. Salaun, L. Veresezan, R. Sesboüé, P. Bohn, F.-X. Boland, and L. Thiberville, "Safety and performance analysis of acriflavine and methylene blue for in vivo imaging of precancerous lesions using fibered confocal fluorescence microscopy (fcfm): an experimental study," *BioMed Central Pulmonary Medicine*, vol. 15, no. 1, p. 30, 2015.

[253] L. Zhang, M. Ye, P. Giataganas, M. Hughes, and G.-Z. Yang, "Autonomous scanning for endomicroscopic mosaicing and 3d fusion," in *2017 IEEE International Conference on Robotics and Automation (ICRA)*, pp. 3587–3593, IEEE, 2017.

[254] S. Zuo, M. Hughes, and G.-Z. Yang, "Novel balloon surface scanning device for intraoperative breast endomicroscopy," *Annals of Biomedical Engineering*, vol. 44, no. 7, pp. 2313–2326, 2016.

[255] S. Zuo and G.-Z. Yang, "Endomicroscopy for computer and robot assisted intervention," *IEEE Reviews in Biomedical Engineering*, vol. 10, pp. 12–25, 2017.

[256] P. Giataganas, M. Hughes, C. Payne, P. Wisanuvej, B. Temelkuran, and G.-Z. Yang, "Intraoperative robotic-assisted large-area high-speed microscopic imaging and intervention," *IEEE Transactions on Biomedical Engineering*, 2018.

[257] F. Reyes, M. Noelck, C. Valentino, L. Grasso-Lebeau, and J. Lang, "Complications of methylene blue dye in breast surgery: case reports and review of the literature," *Journal of Cancer*, vol. 2, p. 20, 2011.

[258] S. C. Park, M. K. Park, and M. G. Kang, "Super-resolution image reconstruction: a technical overview," *Signal Processing Magazine, IEEE*, vol. 20, no. 3, pp. 21–36, 2003.

[259] A. Shadfan, H. Darwiche, J. Blanco, A. Gillenwater, R. Richards-Kortum, and T. S. Tkaczyk, "Development of a multimodal foveated endomicroscope for the detection of oral cancer," *Biomedical Optics Express*, vol. 8, no. 3, pp. 1525–1535, 2017.

[260] E. R. Languirand and B. M. Cullum, "Large area super-resolution chemical imaging via rapid dithering of a nanoprobe," in *Smart Biomedical and Physiological Sensor Technology XII*, vol. 9487, p. 94870O, International Society for Optics and Photonics, 2015.

[261] M. R. Harris, "Fibre bundle confocal endomicroscope," Nov. 15 2011. US Patent 8,057,083.

[262] F. Berier and A. Perchant, "Method and system for super-resolution of confocal images acquired through an image guide, and device used for implementing such a method," Jan. 12 2010. US Patent 7,646,938.

[263] M. Kyrish, R. Kester, R. Richards-Kortum, and T. Tkaczyk, "Improving spatial resolution of a fiber bundle optical biopsy system," in *Endoscopic Microscopy V*, vol. 7558, p. 755807, International Society for Optics and Photonics, 2010.

[264] J. Shao, W.-C. Liao, R. Liang, and K. Barnard, "Resolution enhancement for fiber bundle imaging using maximum a posteriori estimation," *Optics Letters*, vol. 43, no. 8, pp. 1906–1909, 2018.

[265] J. Cheng, Y. Chang, and S.-C. Chen, "Real-time high-resolution fiber bundle based two-photon endomicroscope," *Endoscopic Microscopy X; and Optical Techniques in Pulmonary Medicine II.*, vol. 9304, no. 207, pp. 54–55, 2015.

[266] D. Berlincourt, "Piezoelectric ceramics: Characteristics and applications," *The Journal of the Acoustical Society of America*, vol. 70, no. 6, pp. 1586–1595, 1981.

[267] G. Binnig and D. P. Smith, "Single-tube three-dimensional scanner for scanning tunneling microscopy," *Review of Scientific Instruments*, vol. 57, no. 8, pp. 1688–1689, 1986.

[268] M. Taylor, "Dynamics of piezoelectric tube scanners for scanning probe microscopy," *Review of Scientific Instruments*, vol. 64, no. 1, pp. 154–158, 1993.

[269] N. Zhang, T.-H. Tsai, O. O. Ahsen, K. Liang, H.-C. Lee, P. Xue, X. Li, and J. G. Fujimoto, "Compact piezoelectric transducer fiber scanning probe for optical coherence tomography," *Optics Letters*, vol. 39, no. 2, pp. 186–188, 2014.

[270] K. Liang, Z. Wang, O. O. Ahsen, H.-C. Lee, B. M. Potsaid, V. Jayaraman, A. Cable, H. Mashimo, X. Li, and J. G. Fujimoto, "Cycloid scanning for wide field optical coherence tomography endomicroscopy and angiography in vivo," *Optica*, vol. 5, no. 1, pp. 36–43, 2018.

[271] Y. Zhao, H. Nakamura, and R. J. Gordon, "Development of a versatile two-photon endoscope for biological imaging," *Biomedical Optics Express*, vol. 1, no. 4, pp. 1159–1172, 2010.

[272] C. J. Chen, "Electromechanical deflections of piezoelectric tubes with quartered electrodes," *Applied Physics Letters*, vol. 60, no. 1, pp. 132–134, 1992.

[273] P. Vandewalle, S. Süsstrunk, and M. Vetterli, "A frequency domain approach to registration of aliased images with application to super-resolution," *EURASIP Journal on Applied Signal Processing*, vol. 2006, pp. 233–233, 2006.

[274] S. Lertrattanapanich and N. K. Bose, "High resolution image formation from low resolution frames using delaunay triangulation," *Image Processing, IEEE Transactions on*, vol. 11, no. 12, pp. 1427–1441, 2002.

[275] D. Capel and A. Zisserman, "Computer vision applied to super resolution," *IEEE Signal Processing Magazine*, vol. 20, no. 3, pp. 75–86, 2003.

[276] J. C. Cendán, D. Coco, and E. M. Copeland III, "Accuracy of intraoperative frozen-section analysis of breast cancer lumpectomy-bed margins," *Journal of the American College of Surgeons*, vol. 201, no. 2, pp. 194–198, 2005.

[277] N. Cabioglu, K. K. Hunt, A. A. Sahin, H. M. Kuerer, G. V. Babiera, S. E. Singletary, G. J. Whitman, M. I. Ross, F. C. Ames, B. W. Feig, *et al.*, "Role for intraoperative margin assessment in patients undergoing breast-conserving surgery," *Annals of Surgical Oncology*, vol. 14, no. 4, pp. 1458–1471, 2007.